Universidade Federal de Pernambuco
Centro de Ciências Exatas e da Natureza
Programa de Pós-Graduação em Física

Universiteit Antwerpen
Faculteit Wetenschappen
Departement Fysica

Raí Maciel de Menezes

Skyrmionics and Magnonics in Chiral Ferromagnets: from micromagnetic to atomistic control

Recife

2021

Raí Maciel de Menezes

Skyrmionics and Magnonics in Chiral Ferromagnets: from micromagnetic to atomistic control

Thesis presented to the Doctoral Study Program of the physics department of the Federal University of Pernambuco and the Doctoral Study Program of the University of Antwerp as partial requirement to award the joint degree of Doctor in Physics.

Supervisors: Prof. Dr. Clécio Clemente de Souza Silva and Prof. Dr. Milorad Vlado Milošević.

Recife

2021

Acknowledgements

To my supervisors, Clécio and Milorad, for their patience, dedication and friendship throughout my doctorate. To Clecio for my education since the bachelor's degree and to Milorad for the opportunity to study in Antwerp and for the great scientific discussions.

To my parents, Geraldo and Taciana, for all the support in my life.

To my brother, Raniere, for his inspiration as a scientist.

To Camila, for being part of my trajectory, for her understanding and encouragement.

To my friends in the Physics department at UFPE, and to the members of the vortex dynamics group.

To my friends in the CMT group at the University of Antwerp.

To my friends José, Filipe, Jeroen, Denis, Cihan, and to professors Leonardo Cabral and Edson Sardella for participation in publications throughout my doctorate.

To the Research Foundation–Flanders (FWO-Vlaanderen) and Brazilian Agencies FACEPE, CAPES and CNPq.

"The temptation to form premature theories upon insufficient data is the bane of our profession".

Sherlock Holmes in The Valley of Fear, by Sir Arthur Conan Doyle.

Abstract

The precise control of skyrmionics and magnonics in magnetic materials is key to the development of novel spin-based technology and information transport applications. Essentially, the inherent stability of magnetic skyrmions (provided by their topological charge) together with their extremely small size (down to a few nanometers) and the ultralow threshold current necessary to move them in nanostructures are the main advantages of skyrmionics. Not least, magnonics offers lower power consumption compared to electronics and the excitation of high frequency (sub-100 nm wavelength) magnons makes it possible for the creation of nanometric devices for ultrafast information transport. Even though extensive research has been carried out in recent years, the precise manipulation of skyrmions and spin waves (magnons) in nanostructures is not fully mastered and needs to be addressed before making functional skyrmionic and magnonic devices. In this thesis, we reveal multiple alternatives for the manipulation of skyrmions and spin-waves in different materials, such as bulk chiral magnets, heterochiral structures, magnet-supperconductor hybrids and two-dimentional magnetic materials. We make use of a multiscale model to numerically simulate the magnetic states at each considered material, from micromagnetic to atomistic control. We first explore the different nucleation mechanisms, activation energy, and the time evolution of the skyrmion formation in chiral magnetic films, crucial for the realization of skyrmion-based devices. We show that the skyrmion lattice is formed from the conical phase progressively, most probably by the formation of chiral bobbres, followed by the cylindrical growth of individual skyrmions from the film surface. That reflects a rod-like (one-dimensional) nucleation of the skyrmion phase, with an activation barrier of several electronvolts per skyrmion for the case of MnSi (Manganese monosilicide). In addition, we reveal the interesting blinking (creation-annihilation) behavior of skyrmions close to the phase boundary between the conical and skyrmion phases, where we recall that such switching between topologically distinct states has been proposed as a bit operation for information storage. Next, we discuss the motion of ferromagnetic and antiferromagnetic skyrmions in heterochiral magnets. We report the characteristic deflection of ferromagnetic skyrmions when moving across a heterochiral interface, where the extent of such deflection is tuned by the applied spin-polarized current and the magnitude of Dzyaloshinskii-Moriya interaction. Following, we show that the antiferromagnetic skyrmion achieves much higher velocities than its ferromagnetic counterpart, yet experiences far stronger confinement in nanoengineered heterochiral tracks, which reinforces antiferromagnetic skyrmions as a favorable choice for skyrmion-based devices. After that, we study the interesting coupling of magnetic skyrmions and superconducting vortices in magnet-superconductor heterostructures. We perform numerical simulations, based on experimental observations, to demonstrate that the stray

field of magnetic skyrmions can nucleate antivortices in an adjacent superconducting film, giving rise to a hybrid topological object, the skyrmion-vortex pair, which harbor promising features for skyrmionics and quantum computing applications. We then explore the manipulation of a single skyrmion-vortex pair when currents are applied into both superconducting and magnetic parts of the heterostructure, which is of importance for the facilitated skyrmion guidance in racetrack applications. Afterwards, we make use of the high tunability of magnetic parameters in two-dimensional magnetic materials to reveal the rich phase diagram of exotic magnetic configurations in magnetic monolayers with suppressed nearest-neighbour exchange, where we show that several unique cycloidal, checkerboard, row-wise and spin-ice states are stabilized by the competition between the second-nearest-neighbor exchange, Dzyaloshinskii-Moriya, and dipolar interactions. Additionally, we show the coexistence of ferromagnetic and antiferromagnetic spin-cycloids, as well as novel types of skyrmions and chiral domain walls. Finally, in the last part of the thesis, we present the spin wave properties in the two-dimensional magnetic materials $CrBr_3$ and CrI_3. Using spin-dynamics simulations parametrized from first principles, we reveal that the spin wave dispersion in such materials can be tuned in a broad range of frequencies by strain-engineering, and that a designed pattern of strain, as well as structural defects (halide vacancies) can be turned useful in the design of spin-wave guides. Lastly, we discuss the realization of magnonic crystals by moiré-periodic modulation of magnetic parameters in van der Waals heterostructures, where we show that the several nanometer small periodicities in such samples are ideal for the interference of terahertz spin waves. Recalling the wide range of possibilities for manipulating spin waves in such two-dimensional materials, we therefore suggest these systems as a front-runner for prospective terahertz magnonic applications.

Keywords: Magnetic skyrmions; Spin waves; Chiral magnets; Spintronics.

Resumo

O controle preciso da skyrmiônica e magnônica em materiais magnéticos é a chave para o desenvolvimento de novas tecnologias baseadas em spin e para aplicações de transporte de informações. Essencialmente, a estabilidade inerente dos skyrmions magnéticos (favorecida por sua carga topológica) junto com seu tamanho extremamente pequeno (podendo chegar até alguns nanômetros) e a corrente ultrabaixa necessária para movê-los em nanoestruturas são as principais vantagens da skyrmiônica. Não menos importante, a magnônica oferece menor consumo de energia em comparação à eletrônica e a excitação de magnons de alta frequência (com comprimento de onda abaixo de 100 nm) torna possível a criação de dispositivos nanométricos para o transporte de informação ultrarrápido. Mesmo com extensa pesquisa realizada nos últimos anos, a manipulação precisa de skyrmions e ondas de spin (magnons) em nanoestruturas não é totalmente dominada e precisa ser tratada antes da realização de dispositivos skyrmiônicos e magnônicos funcionais. Nesta tese, revelamos várias alternativas para a manipulação de skyrmions e ondas de spin em diferentes materiais, como magnetos quirais espessos, estruturas heteroquirais, híbridos de supercondutores e magnetos, assim como materiais magnéticos bidimensionais. Fazemos uso de um modelo de multiescala para simular numericamente os estados magnéticos em cada material considerado, desde o controle micromagnético ao atomístico. Primeiro exploramos os diferentes mecanismos de nucleação, energia de ativação e a evolução temporal da formação de skyrmions em filmes magnéticos quirais, cruciais para a realização de dispositivos baseados em skyrmions. Mostramos que a estrutura do skyrmion é formada a partir da fase cônica progressivamente, muito provavelmente pela formação de *bobbres* quirais, seguida pelo crescimento cilíndrico de skyrmions individuais da superfície do filme. Isso reflete uma nucleação unidimensional da fase de skyrmion, com uma barreira de ativação de alguns elétron-volts por skyrmion para o caso de MnSi (Silicato de manganês). Além disso, revelamos o comportamento interessante de criação-aniquilação de skyrmions perto do limite de fase entre as fases cônica e de skyrmions, onde lembramos que essa comutação entre estados topologicamente distintos foi proposta como uma operação de bits (dígitos binários) para armazenamento de informações. A seguir, discutimos o movimento de skyrmions ferromagnéticos e antiferromagnéticos em magnetos heteroquirais. Relatamos a deflexão característica de skyrmions ferromagnéticos ao se mover através de uma interface heteroquiral, onde a extensão de tal deflexão é ajustada pela corrente polarizada de spin aplicada e a magnitude da interação Dzyaloshinskii-Moriya. A seguir, mostramos que o skyrmion antiferromagnético atinge velocidades muito mais altas do que sua contraparte ferromagnética, mas experimenta um confinamento muito mais forte em nanoestruturas heteroquirais, o que reforça os skyrmions antiferromagnéticos como uma escolha favorável para dispositivos baseados em skyrmions. Depois disso, estudamos

o interessante acoplamento de skyrmions magnéticos e vórtices supercondutores em heteroestruturas magneto-supercondutoras. Realizamos simulações numéricas, com base em observações experimentais, para demonstrar que o campo magnético emitido pelos skyrmions pode nuclear antivórtices em um filme supercondutor adjacente, dando origem a um objeto topológico híbrido, o par skyrmion-vórtice, que abriga recursos promissores para skyrmiônica e aplicações em computação quântica. Em seguida, exploramos a manipulação de um único par skyrmion-vórtice quando correntes são aplicadas nas partes supercondutoras e magnéticas da heteroestrutura, o que é importante para o controle dos skyrmions em nanoestruturas. Em seguida, fazemos uso da alta gama de possibilidades de se manipular os parâmetros magnéticos em materiais bidimensionais para revelar um diagrama de fase rico de configurações exóticas em monocamadas magnéticas com interação de troca de primeiro vizinho suprimida, onde mostramos que configurações únicas são estabilizadas pela competição entre as interações de troca de segundos vizinhos, Dzyaloshinskii-Moriya, e a interação dipolar. Além disso, mostramos a coexistência de cicloides de spin ferromagnéticas e antiferromagnéticas, bem como novos tipos de skyrmions e paredes de domínio quirais. Finalmente, na última parte da tese, apresentamos as propriedades de ondas de spins nos materiais magnéticos bidimensionais $CrBr_3$ e CrI_3. Usando simulações de dinâmica de spin parametrizadas a partir de calculos de primeiros princípios, revelamos que a dispersão da onda de spin em tais materiais pode ser sintonizada em uma ampla gama de frequências por meio de deformações no material, e que um padrão de deformação, bem como de defeitos estruturais (vacâncias) pode ser útil no desenvolvimento de guias de onda de spin. Por fim, discutimos a realização de cristais magnônicos por modulação periódica dos parâmetros magnéticos em padrões de moiré em heteroestruturas de van der Waals, onde mostramos que a periodicidade nanométrica em tais amostras é ideal para a interferência de ondas de spins na frequência de terahertz. Relembrando a ampla gama de possibilidades de manipulação de ondas de spins em tais materiais bidimensionais, sugerimos, portanto, esses sistemas como promissores para aplicações em magnônica de alta frequência.

Palavras-chave: Skyrmions magnéticos; Ondas de spin; Magnetos quirais; Spintrônica.

Abstract

De precieze controle van skyrmionica en magnonica in magnetische materialen is de sleutel tot de ontwikkeling van nieuwe spin-gebaseerde technologieën en toepassingen voor informatietransport. In wezen zijn de inherente stabiliteit van magnetische skyrmionen (geleverd door hun topologische lading), samen met hun extreem kleine formaat (tot enkele nanometers) en de ultralage drempelstroom die nodig is om ze in nanostructuren te verplaatsen, de belangrijkste voordelen van skyrmionica. Niet in de laatste plaats biedt magnonica een lager stroomverbruik in vergelijking met elektronica en de excitatie van hoogfrequente (sub-100 nm golflengte) magnons maakt het mogelijk om nanometrische apparaten te creëren voor ultrasnel informatietransport. Hoewel er de afgelopen jaren uitgebreid onderzoek is gedaan, is de precieze manipulatie van skyrmionen en spingolven (magnonen) in nanostructuren nog niet volledig begrepen en moet deze worden aangepakt voordat functionele skyrmionische en magnonische apparaten kunnen worden gemaakt. In dit proefschrift onthullen we verschillende methodes voor de manipulatie van skyrmionen en spingolven in verschillende materialen, zoals bulk chirale magneten, heterochirale structuren, magneet-supergeleider hybriden en tweedimensionale magnetische materialen. We maken gebruik van een multischaal model om de magnetische toestanden van elk beschouwd materiaal numeriek te simuleren, van micromagnetische tot atomistische controle. We onderzoeken eerst de verschillende nucleatiemechanismen, de activeringsenergie en de tijdsevolutie van de vorming van skyrmion in chirale magnetische films, cruciaal voor de realisatie van op skyrmion gebaseerde apparaten. We laten zien dat het skyrmion-rooster progressief wordt gevormd uit de conische fase, hoogstwaarschijnlijk door de vorming van chirale bobbers, gevolgd door de cilindrische groei van individuele skyrmionen vanaf het filmoppervlak. Dit weerspiegelt een staafachtige (eendimensionale) nucleatie van de skyrmionfase, met een activeringsbarrière van meerdere elektronvolts per skyrmion voor het geval van MnSi (mangaanmonosilicide). Bovendien onthulden we het interessante knipperende (creatie-annihilatie) gedrag van skyrmionen dicht bij de fasegrens tussen de conische en skyrmion-fasen, waarbij we ons herinneren dat dergelijk schakelen tussen topologisch verschillende toestanden overeenkomt met een bitbewerking voor informatieopslag. Vervolgens bespreken we de beweging van ferromagnetische en antiferromagnetische skyrmionen in heterochirale magneten. We tonen de karakteristieke afbuiging van ferromagnetische skyrmionen wanneer ze over een heterochirale interface bewegen, waarbij de mate van een dergelijke afbuiging wordt afgestemd door de toegepaste spin-gepolariseerde stroom en de grootte van de Dzyaloshinskii-Moriya-interactie. Hierna laten we zien dat het antiferromagnetische skyrmion veel hogere snelheden bereikt dan zijn ferromagnetische tegenhanger, maar toch een veel sterkere opsluiting ervaart in nano-engineered heterochirale sporen, wat antiferromagnetische

skyrmionen versterkt als een gunstige keuze voor op skyrmion gebaseerde apparaten. Daarna bestuderen we de interessante koppeling van magnetische skyrmionen en supergeleidende wervels in magneet-supergeleider heterostructuren. We voeren numerieke simulaties uit, gebaseerd op experimentele waarnemingen, om aan te tonen dat het stray veld van magnetische skyrmionen antivortices kan vormen in een aangrenzende supergeleidende film, wat aanleiding geeft tot een hybride topologisch object, het skyrmion-vortex-paar, dat veelbelovende eigenschappen vertoont voor skyrmionica en quantum computing-toepassingen. Vervolgens onderzoeken we de manipulatie van een enkel skyrmion-vortex-paar wanneer stromen worden aangelegd in zowel supergeleidende als magnetische delen van de heterostructuur, wat van belang is voor gefaciliteerde skyrmion-geleiding in circuittoepassingen. Daarna maken we gebruik van de hoge afstembaarheid van magnetische parameters in tweedimensionale magnetische materialen om het rijke fasediagram van exotische magnetische configuraties in magnetische monolagen met onderdrukte naaste-buren uitwisseling te onthullen, waar we laten zien dat unieke configuraties worden gestabiliseerd door concurrentie tussen de uitwisselingsinteracties van de tweede buur, Dzyaloshinskii-Moriya, en de dipoolinteractie. Daarnaast tonen we het naast elkaar bestaan van ferromagnetische en antiferromagnetische spin-cycloïden, evenals nieuwe soorten skyrmionen en chirale domeinwanden. Ten slotte presenteren we in het laatste deel van het proefschrift de spingolfeigenschappen van de tweedimensionale magnetische materialen $CrBr_3$ en CrI_3. Met behulp van spin-dynamica-simulaties die zijn geparametriseerd op basis van eerste principes berekeningen, onthullen we dat de spingolfdispersie in dergelijke materialen kan worden afgestemd op een breed spectrum aan frequenties door middel van strain-engineering, en dat een ontworpen rekpatroon, evenals structurele defecten (halogenidevacatures) kan worden gebruikt bij het ontwerpen van spin-golfgeleiders. Ten slotte bespreken we de realisatie van magnonische kristallen door moiré-periodieke modulatie van magnetische parameters in van der Waals heterostructuren, waar we laten zien dat de korte periodiciteiten, van enkele nanometers, in dergelijke systemen ideaal zijn voor de interferentie van terahertz spingolven. Gebaseerd op het brede scala aan mogelijkheden voor het manipuleren van spingolven in dergelijke tweedimensionale materialen, stellen we deze systemen daarom voor als veelbelovende kandidaten voor toekomstige terahertz magnonische toepassingen.

Trefwoorden: Magnetische skyrmionen; Spin golven; Chirale magneten; Spintronica.

Contents

List of Figures

List of Tables

1 Introduction

We start this thesis with a short historical overview of magnetism, followed by an introduction of skyrmionic and magnonic states in magnetic materials. In this chapter, we will see how the magnetic skyrmions and spin waves can be detected experimentally and what is the relevance of such research field from the scientific and technological perspectives. We will discuss the recent advances in the field and provide the motivation and a detailed outline of the thesis.

1.1 Hystorical overview

The history of magnetism dates back to pre-Christian times. People in ancient Greece and China were familiar with the natural "magic" of some stones, which had the ability to attract some objects by remote control. In fact, the earliest observations on magnets are attributed to the Greek philosopher Thales of Miletus, in the sixth century BC. According to Aristotle, Thales thought some stones had souls, because iron is attracted to them [42]. The properties of the magnets were also used in China during the Han dynasty (206 BC – 220 AD), where the first compass ever has been reported [16, 43]. The ancient chinese compass, called *Si Nan*, which means the "South pointer", consisted in a magnetic stone carved in the shape of a Chinese spoon and placed on a flat square bronze or copper plate [Fig. 1.1 (a)]. The spoon turns on the base to align its handle with the Earth's magnetic field, thus pointing to the south after each rotation. The material that composed the compass was most probably the mineral **magnetite**, the iron oxide Fe_3O_4 [Fig. 1.1 (b)], which develops in a natural way by volcanic activity. When magnetized, the magnetite is also called **lodestone**. Pieces of lodestone, which served as compass needles, were of great importance to early navigation, paving the way for more precise instruments that allowed explorers to accurately navigate the seas, effectively changing the course of history. The importance for naviation is clear from the origin of the name lodestone, which in Middle English means "course stone" or "leading stone".

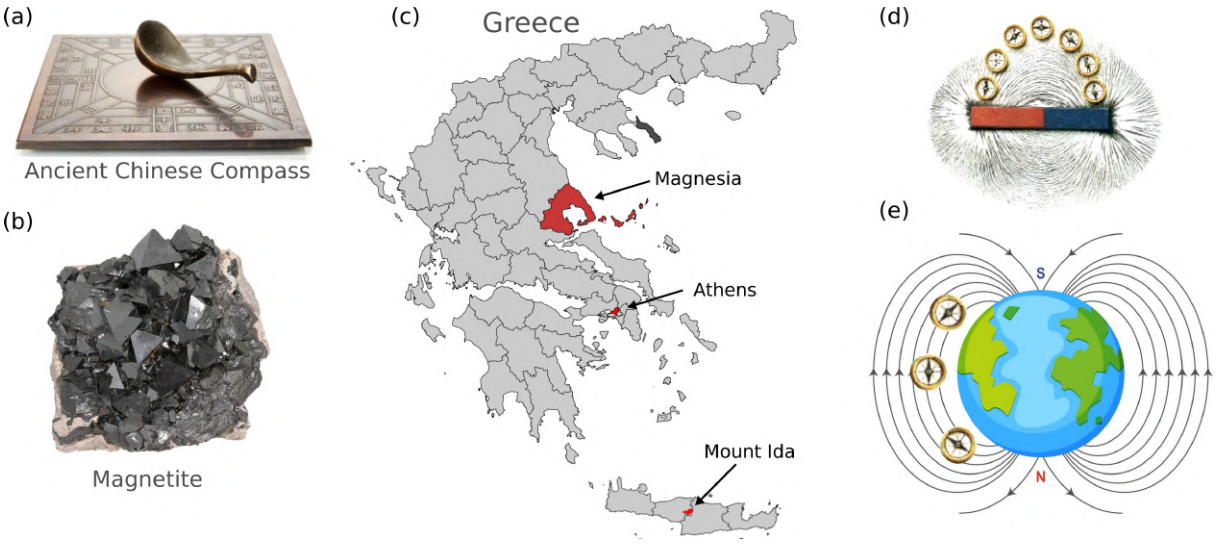

Figure 1.1 – (a) The "South pointer", ancient compass used for orientation in China. (b) A sample of Magnetite, or iron oxide Fe_3O_4. When magnetized, the Magnetite is also called Lodestone. (c) Map of Greece indicating the regions of Magnesia and Mount Ida, from where the name "magnet" may have originated. (d) Pierre de Maricourt (1269) discovered that the direction of a compass needle near a natural magnet formed lines that surrounded the material and that such lines passed through two points diametrically opposed to each other that he called "poles". (e) William Gilbert (1600) discovered that the Earth itself is a great magnet, which explains why magnetic needles point to the north/south direction. Adapted from Refs. [1–4].

Following the etymology, the word **magnet** originates from the ancient Greek term *magnetis lithos*, meaning "stone from Magnesia", which probably refers to the region of Magnesia, a famous locality of the magnetic stones in ancient Greece [Fig. 1.1 (c)]. The location of Magnesia is however debatable, some sources say the name was given after the city of Magnesia in Asia Minor (modern Manisa, in Turkey) [44]. On the other hand, Pliny the Elder in his encyclopedia *Naturalis Historia* [45], refers to the tale of a shepherd, named Magnes, who was pasturing his herds in Mount Ida (Crete) [Fig. 1.1 (c)] when he discovered that some stones in the ground were attracted by the iron nails in his sandals, and named the stones after himself. [45].

Regardless of the ancient knowledge of magnets, it was only in 1269 that scientists began to understand it, when Pierre de Maricourt (also known as Petrus Peregrinus in Latin language) discovered that the direction of a compass needle near a natural magnet formed lines that surrounded the material [Fig 1.1 (d)]. In his letter of 1269 [46], Pierre explained that such lines passed through two points diametrically opposed to each other. He was the first to use the word **pole** to describe those points. In the same work, he also reported that like poles repel each other while different poles attract, and that by breaking a magnet you get two smaller ones. However, the reason why compass needles pointed north/south was not fully understood by Pierre and the scientists of his time. The philosophy of magnetic directivity of the early thirteenth century proposed that

Figure 1.2 – Some of the most influential figures in the history of eletromagnetism.

the compass needle would point to the North Star (Polaris). In the same century, the idea of a large magnetic island on the north pole that attracted the compass has been proposed [43]. It was only in 1600 that William Gilbert, in his monograph *De Magnete* [44], presented experiments with his model earth called the "terella", and comparing it to the inclination of magnetic needles which had been measured at many points on the Earth's surface, He concluded that the Earth itself was a great magnet [Fig 1.1 (e)]. Therefore, the compass needle aligned to the Earth itself, rather than the stars as previously assumed.

Gilbert's monograph was arguably the first modern scientific text and inspired extended research in the following years. Remarkably, in 1819, the Danish physicist Hans Oersted eventually discovered a connection between electricity and magnetism. When performing a lecture demonstration for some students, He noticed that a current-carrying wire was capable of deflecting a compass needle nearby [47]. The electromagnetic revolution had begun [Fig 1.2]. Soon after Oersted reported his discovery, André-Marie Ampère and Dominique-François Arago (1822) showed that a current-carrying coil was equivalent to a magnet [48], and Jean-Baptiste Biot and Felix Savart investigated the forces exerted on magnets by currents [49]. A decade after Oersted's discovery, Michael Faraday (1831) found that the movement of a magnet near a metallic wire induced current in the wire. He had discovered the electromagnetic induction [50]. All this experimental work inspired James Clerk Maxwell's (1855) to publish his paper *On Faraday's lines of force* [51], where he reduced all of the current knowledge of electromagnetism into a linked set of differential equations.

Interestingly, the relation between a current-carrying coil and a magnet led Ampère to propose that matter contained tiny (vanishingly small) current loops that were somehow aligned when the material was magnetized. This model of permanent magnets was proposed almost a century before the description of the quantum nature of matter, from which we know that magnetization is actually created by aligning the intrinsic spin momentum of electrons [16], a situation quite similar to that proposed by Ampère. In chapter 2, we will present a detailed discussion of the origin of atomic

magnetic moments and how they can align to produce magnetic order in matter.

1.2 The study of spin waves

With the advance of quantum mechanics in the beginning of twentieth century, the scientific knowledge on magnetism has made substantial progress. It was in 1930 that Felix Bloch, who had already worked under the supervision of Werner Heisenberg in his doctoral thesis, theoretically proposed the concept of **spin waves** to explain the variation of spontaneous magnetization with temperature near the absolute zero, which resulted in the derivation of his famous formula known as Bloch's $T^{3/2}$ law [52, 53]. He also developed a description of boundaries between magnetic domains, now known as **Bloch walls** [16]. According to Bloch, the strong correlation between the atomic magnetic moments not only leads to magnetic order such as ferromagnetism, but also allows the propagation of magnetic excitations. When a magnetic moment is excited, e.g., by thermal fluctuations or some oscillating applied magnetic field, the neighbouring magnetic moments will also 'feel' the oscillation through the magnetic coupling, for example through the exchange interaction described earlier by Heisenberg, thus leading

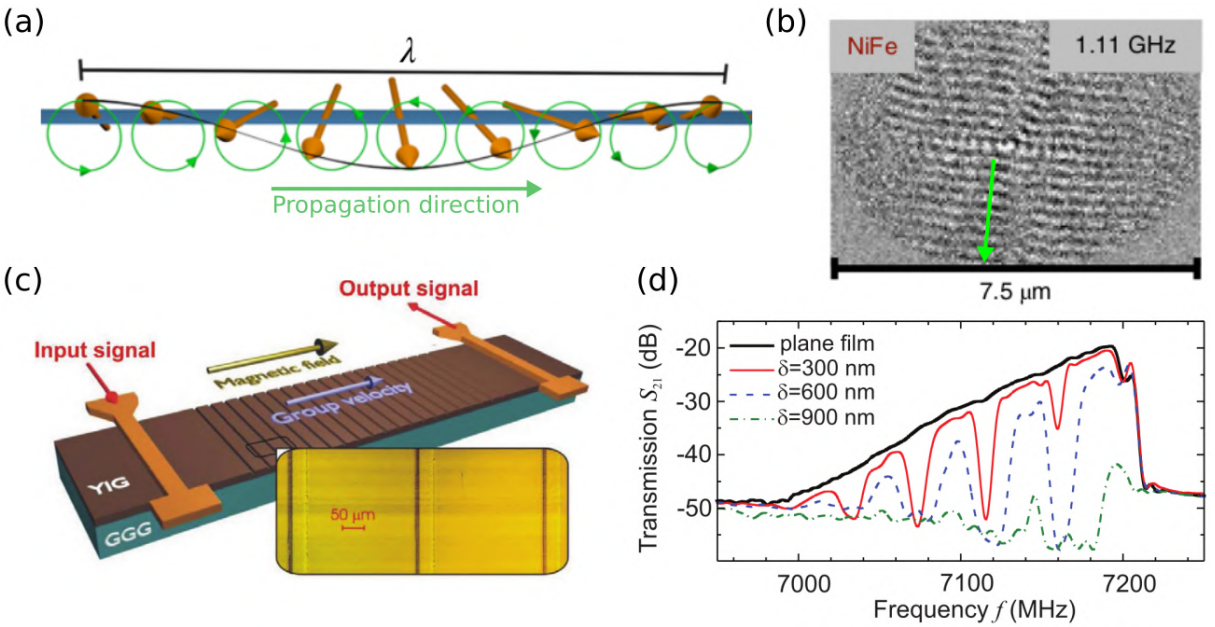

Figure 1.3 – (a) Illustration of a spin wave of wavelength λ propagating along the direction indicated by the green arrow. Orange arrows represent the magnetic moments of the atomic sites. (b) Scanning transmission X-ray microscopy (STXM) image of spin waves in a NiFe layer, excited using a.c. magnetic fields. (c) Schematic of a magnonic crystal structure comprising an array of shallow grooves on the surface of a YIG film. Here, the spin waves are excited by an input antenna and travel through the periodic modulation before being measured at the output antenna. (d) Spin wave transmission characteristics for the magnonic crystal in (c), for different values of the groove depths δ. Adapted from Refs. [5, 6].

to an excitation that propagates like a wave in the magnetic system, as illustrated in Fig. 1.3 (a). Later, Holstein and Primakoff (1940) [54], and Dyson (1956) [55], have made further development in the foundation of spin waves theory. Their quantum formulation showed that spin excitations are quantized, and the quanta of spin waves was called **magnon** [32].

Spin waves can be observed through different experimental techniques. The traditional methods used to detect spin waves are [56]: (*i*) inelastic neutron scattering (INS), which measures the energy loss of a neutron beam, resulting from the interaction of the spin 1/2 of the incoming neutrons with the electron's spin in the solid [57]. (*ii*) Inelastic light scattering, i.e., Brillouin scattering [58], Raman scattering [59] and X-ray scattering [5]. Similarly to the INS, light scattering techniques measure the energy loss of photons reflected from or transmitted through a magnetic material. Other common methods are: (*iii*) Ferromagnetic resonance [60], which measures the absorption of microwaves incident on a magnetic material, and (*iv*) Spin polarized electron energy loss spectroscopy (SPEELS), whose basic concepts are similar to those of INS, but has been shown to be able to excite high energy surface magnons [61]. Fig. 1.3 (b) illustrates one example of X-ray microscopy image of spin waves in a NiFe layer, where the spin waves are excited using a.c. magnetic fields.

Magnonics is the sub-field of magnetism that deals with the excitation, propagation, control and detection of spin waves. Magnonics offers lower power consumption compared to electronics, and the excitation of sub-100 nm wavelength magnons makes the creation of nanometric devices possible [62]. Fig. 1.3 (c) illustrates one example spin-wave based device, the so called magnonic crystal. Magnonic crystals are artificial materials designed in such a way that the magnetic properties of the media are characterized by periodic lateral variation[63]. The spin wave spectra in such materials exhibit features such as band gaps, where the waves are not allowed to propagate, as illustrated in Fig. 1.3 (d). Magnonic crystals have potential application in information transport and processing based on magnons. In addition, magnonic interferometers [64, 65] and Voltage-controlled logic gates [66] can serve as low-power signal processing devices [67, 68].

1.3 The study of magnetic skyrmions

Skyrmions are topologically stable configurations, originally proposed by the British physicist Tony Skyrme (1962) to describe elementary particles in a 4-dimensional vector field [69]. Interestingly, skyrmionic solutions have turned out to be relevant in several condensed matter systems such as in liquid crystals [70], quantum Hall systems [71] and Bose–Einstein condensates [72]. One particular form of skyrmions is

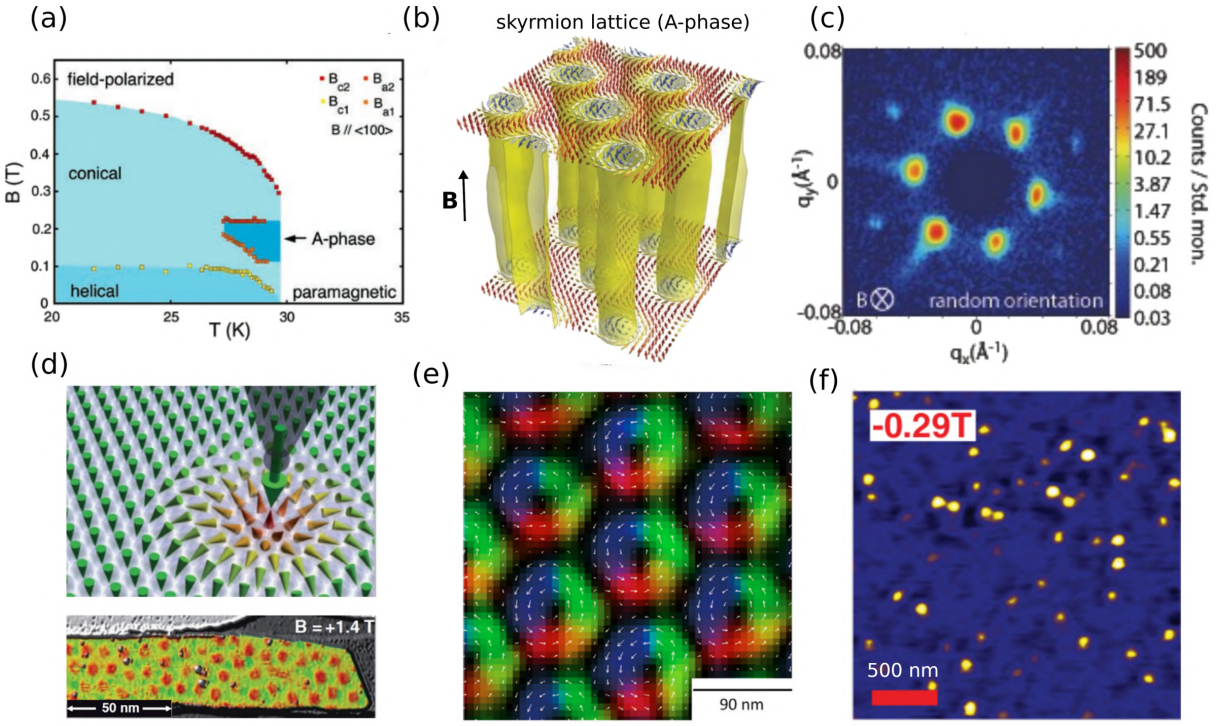

Figure 1.4 – Experimental observation of magnetic skyrmions. (a) Magnetic phase diagram of MnSi as a function of applied magnetic field and temperature. (b) Illustration of skyrmion lattice phase. (c) Typical neutron scattering diffraction pattern of the SkL in MnSi. (d) Top: illustration of STM tip used to detect skyrmions by spin-polarized tunneling current. Bottom: SP-STM image of nanometer scale skyrmions in a bilayer of FePd. (e) Skyrmion lattice state imaged by Lorentz TEM. The colors indicate the in-plane component of the magnetization, with spin orientation indicated by white arrows. (f) MFM image of skyrmions (yellow dots) in a Ir/Fe/Co/Pt multilayer film, where the colors indicate the MFM probe resonance shift, proportional to the out-of-plane component of the magnetization. Adapted from Refs. [7–11]

the **magnetic skyrmion**, found in chiral magnetic materials that exhibit spiral magnetism due to the Dzyaloshinskii–Moriya interaction (DMI), which in turn results from the spin-orbit coupling in asymmetric crystalline structures [73]. Extended lattices of magnetic skyrmions were first observed experimentally in 2009, in B20-type bulk systems such as MnSi [7] and $Fe_{1-x}Co_xSi$ [74], but they are also present in thin film chiral magnets [10], where the DMI is created at the interface between the magnetic thin film and a heavy metal material [25]. Fig. 1.4 (a) shows the magnetic phase diagram of MnSi as a function of applied magnetic field and temperature, where the magnetic phases were identified by neutron scattering experiments [7]. In particular, the skyrmion lattice (SkL), also known as the A-phase, is illustrated in Fig. 1.4 (b). In this phase, the magnetization swirls locally forming some kind of magnetic whirlpools, each one representing a single skyrmion on a ferromagnetic background, and the hexagonal modulation of the SkL can be observed as peaks in the neutron scattering diffraction pattern, as illustrated in Fig. 1.4 (c).

In addition to neutron scattering experiments, the spin texture of magnetic

skyrmions can also be observed in real-space by a variety of techniques. Some of the common methods used to detect magnetic skyrmions are: (*i*) spin-polarized scanning tunneling microscopy (SP-STM) [9], where an extremely sharp magnetic tip [Fig. 1.4 (d)] is moved systematically over the sample while a voltage is applied between the tip and the magnetic material, thus allowing electrons to tunnel between the two. Electrons with spins matching the tip's magnetization will have a higher chance of tunneling, thus giving information about the local spin configuration; (*ii*) Lorentz transmission electron microscopy (TEM) [10], where a high-energy electron beam is transmitted through a thin magnetic film. When the beam passes through a region of magnetic induction in the sample, the electrons are deflected by the Lorentz force, and the in-plane components of the magnetic texture can be imaged [Fig. 1.4 (e)]; (*iii*) Magnetic force microscopy (MFM) [11]. In this method, the interaction between the stray field generated by the sample and a magnetic tip (or MFM probe) is calculated. The tip-sample magnetic interactions are then used to reconstruct the magnetic structure of the sample surface [Fig. 1.4 (f)]. Other possibilities for the efficient detection of skyrmions are the Magneto-optic Kerr effect (MOKE) microscopy [75], as well as the electrical detection by Hall voltage measurements [76].

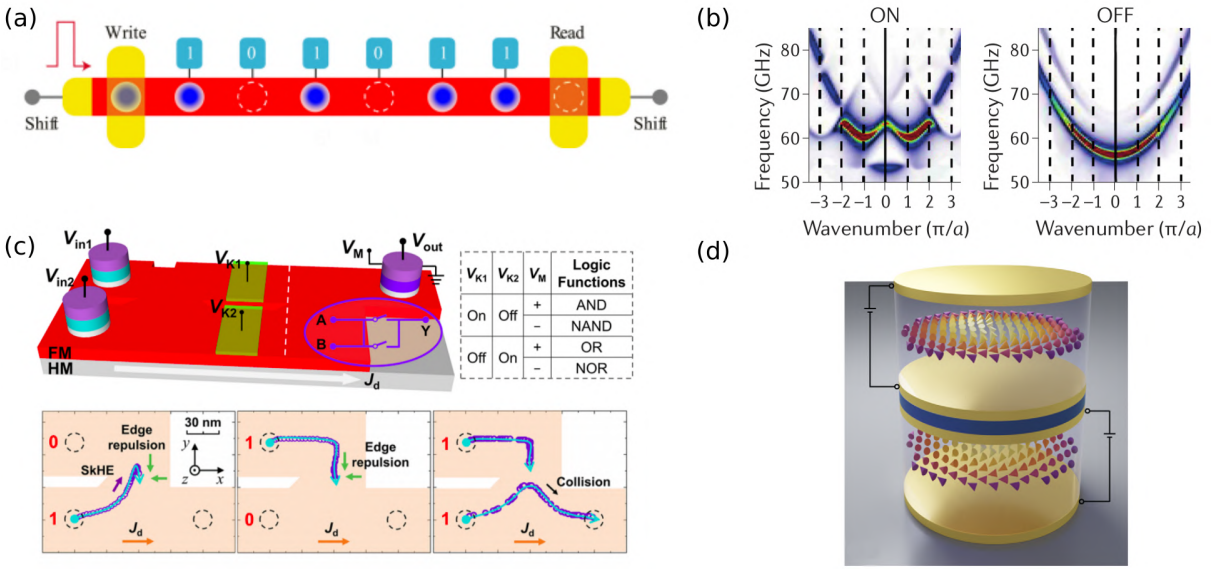

Figure 1.5 – Skyrmions for applications. (a) Train of skyrmions in a racetrack for memory devices. The skyrmions serve as memory bits, passing through magnetic read/write heads positioned on the racetrack. (b) Skyrmion lattice as magnonic crystal. The dispersion relation for spin-wave propagation along waveguide with and without skyrmions is shown, displaying gaps in frequency related to the skyrmion lattice periodicity. (c) Schematic of a reconfigurable skyrmion logic gate. Insets show some cases of inputs and their corresponding outputs and the evolution of the position of skyrmion. (d) Schematic of the two-layer magnetic material used as the platform for the skyrmion qubit coupling scheme. Qubit coupling is adjusted by a non-magnetic spacer (blue plate), and logic states are adjusted by electric fields (yellow plates). Adapted from Refs. [12–15].

A particularly interesting property of magnetic skyrmions is that they are topologically protected objects, which means that the skyrmionic texture cannot be destroyed into a trivial solution by continuous deformation. This property increases the stability of the skyrmions in such a way that they are able to move throughout the sample without losing their shape, and makes them promising candidates for technological applications, such as spin-based information processing and storage devices [12]. Nevertheless, the fact that spins are arranged in a discrete lattice rather than a continuous one, makes it possible for the skyrmions to be destroyed in a first-order phase transition, characterized by an energy barrier that determines the stability of the skyrmion phase. Generally, skyrmions are highly stable magnetic objects and can be observed even at room temperature in some materials [77].

Skyrmionics refers to the emerging technologies that deal with the creation and annihilation, propagation, control and detection of magnetic skyrmions. The remarkable stability, extremely small size (down to a few nanometers), and the ultralow threshold current necessary to move the skyrmions in nanostructures are the main advantages of skyrmionics. Fig. 1.5 shows some examples of skyrmion-based applications. Commonly suggested components for which skyrmionics can be used are: skyrmion racetrack memory [19]; magnonic crystals [78]; logic gates [79] and radio-frequency devices [80]. In addition, recent work has also suggested skyrmion qubits as logical elements for quantum computing [11, 15]. Advances in two-dimensional magnetic materials have also raised expectations towards skyrmionic and magnonic devices, as these systems offer a wide range of magnetic parameter manipulations and are therefore suggested as promising candidates for application in cutting-edge devices. Fig. 1.6 shows the number of scientific publications over the years including the keyword "magnetic skyrmion". Note that the relevance from both scientific and technological perspectives has created a great interest in the subject in the last decade, with a rapid increase in the number of

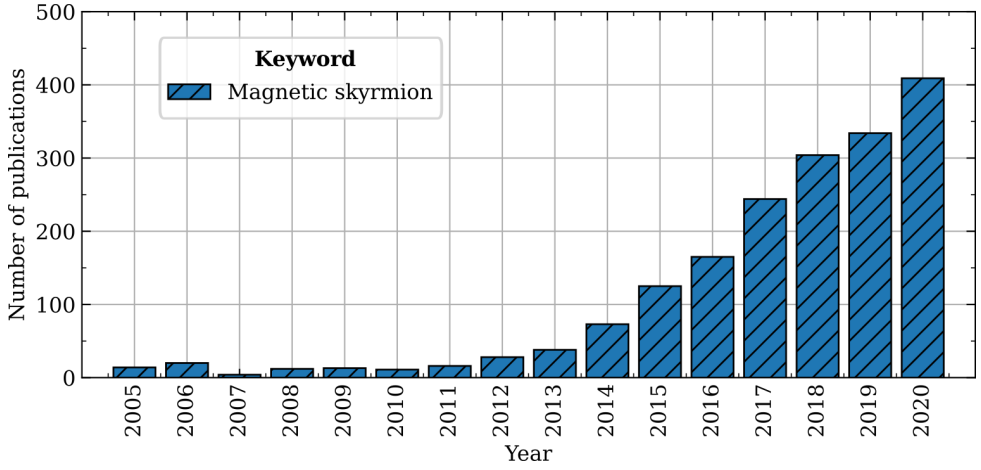

Figure 1.6 – Number of publications along the years including the keyword "magnetic skyrmion" obtained from the *Web of Science* from 2005 to 2020.

publications to date.

1.4 Structure of the thesis

After presenting a general introduction (chapters 2 and 3) of the theoretical approaches and numerical methods used to investigate skyrmionic and magnonic states in magnetic materials, we organize the results of the thesis in three parts: In Part I (chapter 4), we explore the nucleation mechanism and stability of magnetic skyrmions in bulk chiral magnetic films; Part II (chapters 5 and 6) is dedicated to the manipulation of magnetic skyrmions in thin film heterostructures; and in Part III (chapters 7 and 8) we explore the fundamental properties of spin-textures and magnonics in two-dimensional magnets. The chapters are organized as follows:

- In **Chapter 2**, we introduce the basic theoretical concepts of magnetic interactions. We provide a detailed description of magnetic states, from the atomic spin moments to skyrmionic and magnonic phases. The concepts presented in this chapter will be necessary for a complete understanding of the results presented in the next chapters of the thesis.

- In **Chapter 3**, we introduce the numerical approaches for simulating the considered magnetic textures. We discuss the multiscale modeling used to simulate the magnetic states, from the micrometer to nanometer length scales, as well as the methods used for finding minimal energy paths of magnetic phase transitions.

- In **Chapter 4**, we explore the nucleation mechanism and stability of magnetic skyrmions in chiral magnetic materials. We show how the skyrmion lattice is formed from the conical phase progressively in small domains, and study the different nucleation mechanisms and the time evolution of the skyrmion lattice formation in chiral magnetic films. Part of the results presented in this chapter are published in Ref. [39].

- In **Chapter 5**, we report the characteristic features of skyrmion motion in heterochiral magnets, for both the ferromagnetic (FM) and antiferromagnetic (AFM) skyrmions. We show that a heterochiral interface deflects the trajectory of FM skyrmions. Further analysis reveal that such deflection is completely absent in the AFM case, and that the AFM skyrmion achieves much higher velocities and stronger confinement in nanoengineered heterochiral tracks when compared to its FM counterpart, which reinforces AFM skyrmions as a favorable choice for skyrmion-based devices. The results presented in this chapter are published in Ref. [81].

- In **Chapter 6**, we study the coupling of magnetic skyrmions and superconducting vortices in magnet-superconductor (M-S) heterostructures. We discuss experimental observations of the skyrmion-vortex interaction in hybrid material, followed by numerical study of the nucleation of the skyrmion-vortex pair (SVP). Next, we provide an in-depth analysis and investigate the manipulation of the SVP correlations in a M-S hybrid. We combine micromagnetic and molecular dynamics simulations to investigate the behavior of skyrmions and vortices simultaneously when currents are applied into both S and M part of the heterostructure, which is of importance for the facilitated skyrmion guidance in racetrack applications. The results presented in this chapter are published in Refs. [11] and [82].

- In **Chapter 7**, we investigate the effects of suppressed nearest-neighbour exchange in magnetic monolayers. We report the rich phase diagram of exotic magnetic configurations, obtained for both square and honeycomb lattice symmetries, comprising coexistence of ferromagnetic and antiferromagnetic spin-cycloids, as well as multiple types of magnetic skyrmions. We also reveal that magnetic monolayers could be good candidates to host the antiferromagnetic skyrmions that are experimentally evasive to date. The results presented in this chapter are published in Ref. [83].

- In **Chapter 8**, we present the spin-wave (SW) properties in two-dimensional (2D) magnetic materials, such as monolayer chromium trihalides $CrBr_3$ and CrI_3. We reveal that the SW dispersion in 2D materials can be tuned in a broad range of frequencies by strain-engineering, paving the way towards flexo-magnonic applications, and that defect engineering these monolayers can be useful in design of spin-wave guides. We discuss the spectra of spin-waves propagating across a moiré-periodic modulation of magnetic parameters in a van der Waals heterostructure, and show that such structures hold the necessary nanometric modulation period for realization of a magnonic crystal in the terahertz frequency range.

- In **Chapter 9**, we summarize the results of this thesis and present future perspectives.

2 Theoretical background

In this chapter, we review the basic concepts of magnetostatics, magnetodynamics and the different theoretical approaches used to investigate skyrmionic and magnonic states in magnetic materials. We start introducing the magnetic moment and its response to external applied fields and collective interactions. We further provide a detailed description of the static and dynamical properties of magnetic skyrmions, as well as the main characteristics of spin waves. The purpose of this chapter is to provide the reader with the necessary knowledge to fully understand the results presented in the next chapters of the thesis.

2.1 The magnetic moment

The fundamental ingredient of magnetism is the so-called magnetic moment, which defines the strength and orientation of magnetic fields in matter. In the classical eletrodynamics, the elementary magnetic moment is equivalent to a tiny (vanishingly small) current loop [see Fig. 2.1 (a)] and can be expressed as

$$\boldsymbol{\mu} = \frac{1}{2}\int \mathbf{r}\times\mathbf{j}(\mathbf{r})dV, \tag{2.1}$$

where $\mathbf{j}(\mathbf{r})$ is the current density (per element of area) at the position $\mathbf{r}$, and dV is the volume element. For the case of a uniform current I circulating in a plane loop of area $\mathcal{A}$, the current density can be expressed as $\mathbf{j}(\mathbf{r})dV = Id\mathbf{l}$, where $d\mathbf{l}$ is the element of distance along the loop [see Fig. 2.1 (b)], and the Eq. (2.1) takes the simple form

$$\boldsymbol{\mu} = I\int d\boldsymbol{\mathcal{A}} = I\boldsymbol{\mathcal{A}}, \tag{2.2}$$

where $d\boldsymbol{\mathcal{A}} = \frac{1}{2}\mathbf{r}\times d\mathbf{l}$ points normal to the loop plane, in a sense determined by the direction of the circulating current, and $|\boldsymbol{\mathcal{A}}| = \mathcal{A}$. In the International System of Units (SI), the magnetic moment is expressed in Ampere-Square Meter [Am^2].

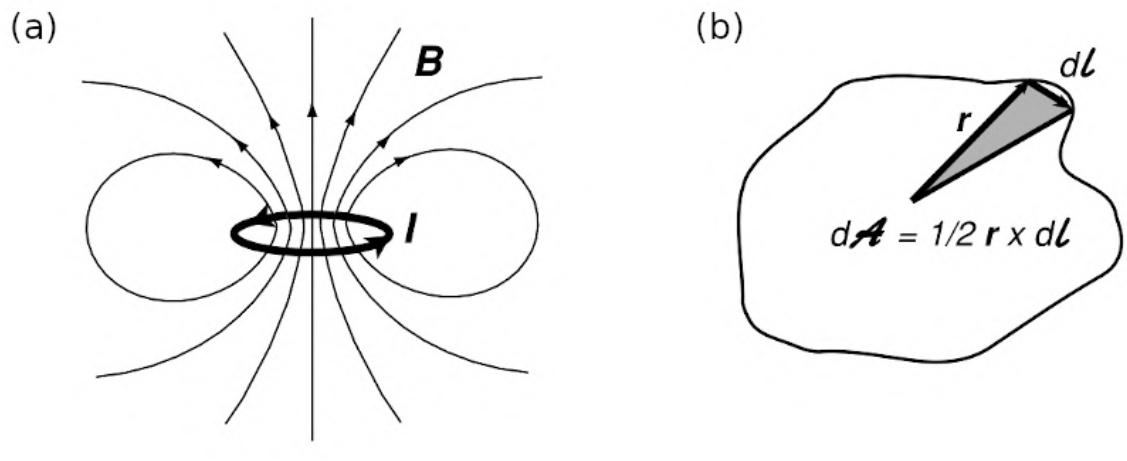

Figure 2.1 – (a) A circulating electric current I is equivalent to a magnetic moment, which defines the strength and orientation of the magnetic field **B**. (b) The area of a loop is obtained by summing the area of the elementary triangles. Retrieved from Ref. [16].

The magnetic field **B** created by the current loop is given by the Biot–Savart law [84]

$$\mathbf{B} = -\frac{\mu_0}{4\pi}\int \frac{\mathbf{r}' \times \mathbf{j}(\mathbf{r}')dV}{|r'|^3}, \tag{2.3}$$

where $\mathbf{r}'$ is the vector connecting dV to the observation point. The field of the magnetic moment has the same form as that of an electric dipole formed of positive and negative charges separated by a small distance. Consequently, the magnetic moment is generally referred to as a magnetic dipole moment.

In the atomic level, the magnetic moments emerge from the motion of electrons in the atomic orbitals and from the so-called intrinsic spin momentum. From the classical point of view [Eq. (2.2)], the magnetic moment created by an electron of mass m_e, moving with velocity v in a circular orbit of radius r_0, can be written as $\boldsymbol{\mu}_L = I\pi r_0^2$, where $I = -e/\tau$ is the current generated by the electron motion and $\tau = 2\pi r_0/v$ the rotation period. Notice that, since the charged particle has mass, the orbital magnetic moment $\boldsymbol{\mu}_L$ is always connected with the **orbital angular momentum** of the electron, which in the classical description is given by $\boldsymbol{\mathcal{L}} = m_e v r_0$, and we obtain

$$\boldsymbol{\mu}_L = -\frac{e}{2m_e}\boldsymbol{\mathcal{L}}. \tag{2.4}$$

The ratio of the magnetic moment and the angular momentum of a particle or system is known as the *gyromagnetic ratio*, and it is often represented by the Greek letter γ (Gamma). In the above relation for the electron in a circular orbit, $\gamma = -e/2m_e$. However, the quantum nature of the electron can not be captured by the classical approximation, and a correct understanding of the electron angular momentum requires the introduction of quantum mechanics.

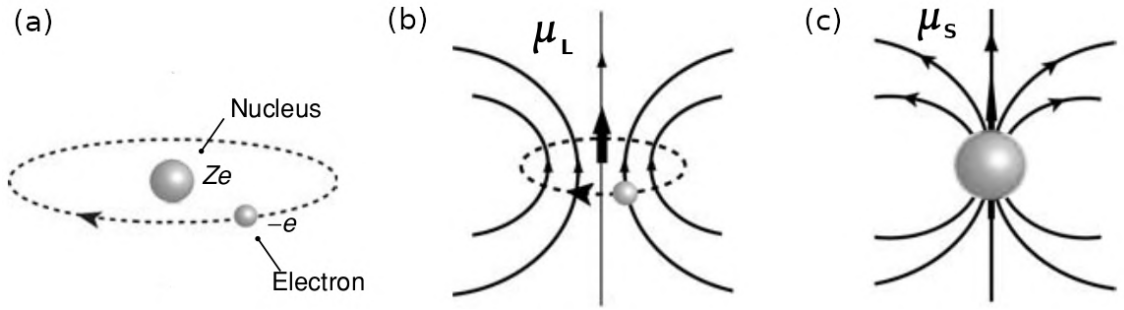

Figure 2.2 – (a) The Bohr model for the hydrogen atom. The electron moves in circular orbit around the nucleus of charge Ze. (b) Orbital magnetic moment $\boldsymbol{\mu}_L$ induced by the electron motion. (c) Intrinsic spin magnetic moment $\boldsymbol{\mu}_S$. Adapted from Ref. [16].

It is characteristic of angular momenta in quantum mechanics that its magnitude is quantized in terms of the orbital quantum number. In the semi-classical description of the hydrogen atom proposed by Niels Bohr [see Fig. 2.2 (a)], the electrons circulate around the nucleus with angular momentum that takes the form $\mathcal{L} = nh/2\pi$, with n a non-zero, positive integer and h the Planck constant. The Bohr atomic model was the first one to incorporate quantum theory and to successfully explain the radiation spectrum of atomic hydrogen. The angular momentum quantization was further corroborated by the application of the Schrödinger's equation to the atomic model, where the magnitude of the orbital angular momentum assumes the form $\mathcal{L} = \sqrt{l(l+1)}\hbar$ and its projection along z-direction satisfies $\mathcal{L}_z = m_l\hbar$, with $l = 0, 1, 2, ...$, and $m_l = l, (l-1), ... -l$, the azimuthal and magnetic quantum numbers, respectively. Therefore, Eq. (2.4) can be rewritten on its quantized form as follows

$$\boldsymbol{\mu}_L = -\mu_B \boldsymbol{L}, \tag{2.5}$$

where we define the **Bohr magneton** $\mu_B \equiv -e\hbar/2m_e$ and $\boldsymbol{L} \equiv \boldsymbol{\mathcal{L}}/\hbar$. Fig. 2.2 (b) illustrates the orbital magnetic moment induced by the electron motion.

In addition to the orbital momentum, elementary particles and nuclei have the so-called **spin angular momentum**, commonly represented by $\boldsymbol{\mathcal{S}}$. The spin momentum is a pure quantum phenomena, with no classical analogy, and it is an intrinsic property of fundamental particles, as is the case with the electric charge. The magnitude of the spin angular momentum is quantized in terms of the spin quantum number, s, and it is written as $\mathcal{S} = \sqrt{s(s+1)}\hbar$, with s a multiple of 1/2 (i.e. $s = 0, \frac{1}{2}, 1, \frac{3}{2}, ...$). The projection of $\mathcal{S}$ along z-direction satisfies $\mathcal{S}_z = m_s\hbar$, where m_s can only take one of $2s+1$ possible values: $m_s = s, (s-1), ..., -s$. Those particles with half-integer spin numbers are known as fermions and satisfies the Fermi-Dirac statistics, while those particles with integer spins are known as bosons and obey Bose–Einstein statistics [85]. For the case of an electron, $s = 1/2$ and the spin component can only assume one of the two values $\mathcal{S}_z = \pm\hbar/2$. The spin angular momentum is then associated with a magnetic moment, as illustrated in Fig. 2.2 (c). Similar to Eq. (2.5), the spin magnetic moment

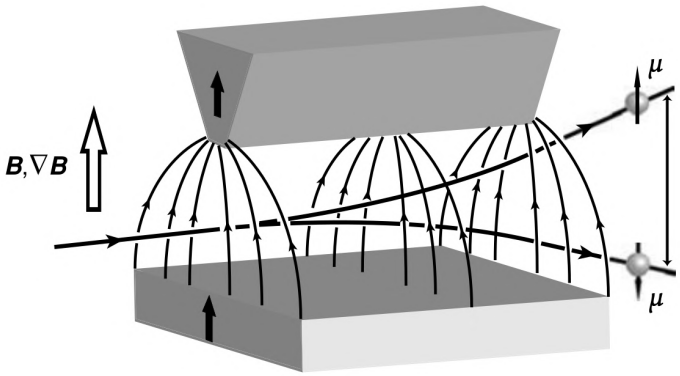

Figure 2.3 – Stern–Gerlach experiment, a beam of silver atoms enters a region where there is a strong magnetic field gradient. Although silver has no orbital angular momentum ($\boldsymbol{L} = 0$), the silver beam splits in two, indicating a magnetic moment associated with the spin angular momentum. Adapted from Ref. [16].

can be expressed as $\boldsymbol{\mu}_S = -g_S \mu_B \boldsymbol{S}$, where $\boldsymbol{S} \equiv \boldsymbol{\mathcal{S}}/\hbar$ and g_S is a correction factor known as the Landé g-factor. The value of $g_S \approx 2.0023192$ is derived naturally from Dirac's equation in the framework of relativistic quantum mechanics [86]. When both orbital and spin angular momentum are coupled, the total magnetic moment can be written as

$$\boldsymbol{\mu} = -\mu_B (g_L \boldsymbol{L} + g_s \boldsymbol{S}), \tag{2.6}$$

where $g_L = 1$ is the g-factor for the orbital angular momentum.

The electron spin angular momentum was observed experimentally for the first time in 1921 by Otto Stern and Walther Gerlach. In the Stern–Gerlach experiment, a beam of silver atoms enters a region where there is a strong magnetic field gradient [see Fig. 2.3]. Although silver has no orbital angular momentum ($\boldsymbol{L} = 0$), the silver beam splits in two, indicating a magnetic moment associated with the spin angular momentum. Notice that the spin and angular momentum of composite particles, such as atoms and ions, are given by the combination of their constituents. The magnetism is then inherently related to the electronic band structure, and the net unpaired spins in the valence band of an element will determine whether the material is magnetic or non-magnetic. For example, a helium-4 atom in the ground state has zero magnetic moment, even though the quarks and electrons which make it up are all fermions with non-zero spin. Generally, when several electrons are present on the same atom, the resultant quantum numbers can be expressed by the sum over the individual quantum numbers of all electrons,

$$\mathsf{S} = \sum_i s_i, \quad \mathsf{L} = \sum_i l_i, \quad \mathsf{M}_s = \sum_i m_{s_i}, \quad \mathsf{M}_l = \sum_i m_{l_i}. \tag{2.7}$$

The magnitudes of the spin and orbital moments become $|\boldsymbol{S}| = \sqrt{\mathsf{S}(\mathsf{S}+1)}$ and $|\boldsymbol{L}| =$

$\sqrt{\mathsf{L}(\mathsf{L}+1)}$, where the values of S and L will depend on how the electrons are distributed in the atomic orbitals.

Notice that so far we have considered the spin and orbital angular momenta separate since they are independent of one another. However, when both $\boldsymbol{S}$ and $\boldsymbol{L}$ are present, they do couple via the so-called spin-orbit interaction, and we have to introduce the concept of **total angular momentum**. In other words, due to the spin-orbit coupling, the moments $\boldsymbol{L}$ and $\boldsymbol{S}$ are not separately conserved quantities (there is the possibility for momentum transfer through spin-orbit coupling), but the total angular momentum $\boldsymbol{J} \equiv \boldsymbol{L} + \boldsymbol{S}$ is conserved. The magnitude of the total momentum can be expressed as $|\boldsymbol{J}| = \sqrt{\mathsf{J}(\mathsf{J}+1)}$, where the total quantum number J can take the following range of values, $|\mathsf{L}-\mathsf{S}| \leq \mathsf{J} \leq \mathsf{L}+\mathsf{S}$, jumping only in integer steps. Therefore, we rewrite Eq. (2.6) in the form

$$\boldsymbol{\mu} = -g_J \mu_B \boldsymbol{J}, \tag{2.8}$$

where, for $g_L = 1$ and $g_S = 2$,

$$g_J = \frac{3}{2} + \frac{\mathsf{S}(\mathsf{S}+1) - \mathsf{L}(\mathsf{L}+1)}{2\mathsf{J}(\mathsf{J}+1)}. \tag{2.9}$$

The gyromagnetic ratio (ratio of the magnetic moment to the angular momentum) can be extracted from Eq. (2.8), and it differs from the classical description by the introduction of the g-factor,

$$\gamma = -\frac{g_J \mu_B}{\hbar} = -g_J \frac{e}{2m_e}. \tag{2.10}$$

The combination of quantum numbers which minimize the energy of the (many-eletron) atom or ion can be estimated using **Hund's rules**. The empirical method proposed by Hund is to fill the atomic orbitals in a specific sequence. The first and second Hund's rules are: (*i*) first organize the electrons in a way to maximize S, and (*ii*) maximize L without changing S. The first rule is justified by the fact that electrons minimize their Coulomb interaction if they are separated, therefore, they tend to occupy different orbitals. The second rule is understood by imagining that electrons orbiting in the same sense can avoid each other during their motion, which again reduces Coulomb repulsion. Finally, the value of J is determined by the third Hund's rule: (*iii*) $\mathsf{J} = \mathsf{L} - \mathsf{S}$ if the valence shell is less than half full; $\mathsf{J} = \mathsf{L} + \mathsf{S}$ if the shell is more than half full, and $\mathsf{J} = \mathsf{S}$ if the valence shell is exactly half full. The third rule is an attempt to minimize the spin-orbit energy. The values of magnetic moment predicted by Hund's rules and Eq. (2.8), given by $\mu = g_J \mu_B \sqrt{\mathsf{J}(\mathsf{J}+1)}$, are in very good agreement with the magnetic moments obtained experimentally (via measurements of the susceptibility) for some ions, e.g., the $4f$ series. However, the Hund's rules do not always appear to agree with experiment. The reason for that is that the third rule fails when the crystal field interaction is much stronger than the spin-orbit interaction, which is the case, e.g.,

of most $3d$ ions. Experimental results suggest that, in the case of strong crystal field interaction, the Hund's rules can be fixed by taking $\mathsf{L} = 0$ (so that $\mathsf{J} = \mathsf{S}$ and $g_J = 2$). This effect is known as **orbital quenching**. For the case of $4f$ ions, the orbitals are much less extended away from the nucleus when compared with $3d$ orbitals, so that the crystal field terms are much less important and Hund's third rule is obeyed.

2.2 Magnetic moment dynamics

The orientation of the magnetic moment is sensitive to multiple magnetic interactions, which may arise from the exchange of electrons with neighboring ions, applied external fields, demagnetization fields, among other interactions. Let us first consider the simplest case where an isolated magnetic moment $\boldsymbol{\mu}$ is subjected to a uniform external magnetic field, $\mathbf{B}$. The energy is minimized when the magnetic moment aligns parallel to the magnetic field, according to the Zeeman energy

$$\mathcal{E}_{\text{Zeeman}} = -\boldsymbol{\mu} \cdot \mathbf{B}. \tag{2.11}$$

In the case where the moment is not aligned with the external field, it becomes subject to a torque given by

$$\boldsymbol{\tau} = \boldsymbol{\mu} \times \mathbf{B}, \tag{2.12}$$

which tends to turn the moment towards the minimal energy position. However, since the torque is equal to the rate of change of the total angular momentum, it can be expressed as $\boldsymbol{\tau} = \hbar(d\boldsymbol{J}/dt)$. On the other hand, the magnetic moment is associated with $\boldsymbol{J}$ by Eq. (2.8), and the torque is rewritten in the form $\boldsymbol{\tau} = -\frac{1}{\gamma}(d\boldsymbol{\mu}/dt)$. By substituting that into Eq. (2.12), we obtain the Landau-Lifshitz differential equation for the magnetic moment dynamics [16]

$$\frac{d\boldsymbol{\mu}}{dt} = -\gamma \boldsymbol{\mu} \times \mathbf{B}. \tag{2.13}$$

Notice that, according to Eq. (2.13), the change in $\boldsymbol{\mu}$ is perpendicular to both $\boldsymbol{\mu}$ and to $\mathbf{B}$. The magnetic moment therefore **precesses** around the applied field direction instead of turning towards $\mathbf{B}$, as illustrated in Fig. 2.4 (a). Considering that $\mathbf{B}$ is along the z-axis and $\boldsymbol{\mu}$ makes an angle of θ with respect to $\mathbf{B}$, Eq. (2.13) has solution

$$\begin{aligned} \mu_x(t) &= |\boldsymbol{\mu}| \sin\theta \cos(\omega_L t) \\ \mu_y(t) &= |\boldsymbol{\mu}| \sin\theta \sin(\omega_L t) \\ \mu_z(t) &= |\boldsymbol{\mu}| \cos\theta. \end{aligned} \tag{2.14}$$

where $\omega_L \equiv \gamma B$ is the so-called **Larmor frequency** (named after Joseph Larmor). It is important to notice that the Larmor frequency is independent of the angle θ between the applied magnetic field and the magnetic moment direction. This property is crucial for

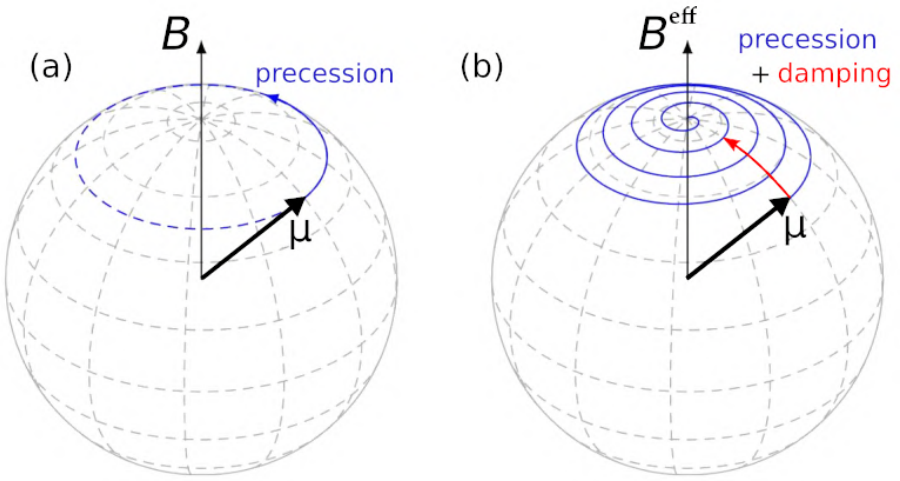

Figure 2.4 – (a) Free precession of a magnetic moment $\boldsymbol{\mu}$ around the magnetic field $\mathbf{B}$ (b) Damped precession relaxes the magnetic moment towards the effective field $\mathbf{B}^{\text{eff}}$. Adapted from Ref. [17].

applications such as in the nuclear magnetic resonance (NMR) and electron paramagnetic resonance (EPR) thechniques, since the precession rate gives access to details of the intramolecular magnetic field around an atom in a molecule, regardless the spatial orientation of the atomic spins.

The free precession is however an idealized situation in which there is no way for the system to dissipate energy, and the angular momentum remains constant. In the presence of energy dissipation, the precession amplitude decays in time, and the magnetic moment spirals about the field until it reaches the equilibrium position (parallel to the field) in a characteristic relaxation time, as illustrated in Fig. 2.4 (b). The energy loss can be included into Eq. (2.13) by the introduction of a damping term. One of the most widely used forms is that introduced by T. L. Gilbert, in the so-called Landau–Lifshitz–Gilbert (LLG) equation [87]

$$\frac{d\boldsymbol{\mu}}{dt} = -\frac{\gamma}{1+\alpha^2}\left[\boldsymbol{\mu}\times\mathbf{B}^{\text{eff}} + \alpha\boldsymbol{\mu}\times(\boldsymbol{\mu}\times\mathbf{B}^{\text{eff}})\right], \tag{2.15}$$

where α is the dimensionless, Gilbert damping factor and $\mathbf{B}^{\text{eff}}$ is the effective field acting on the magnetic moment, as we discuss below.

In a real material, the atomic magnetic moments are subjected to much complex collective interactions rather than a simple uniform external field. However, Eq. (2.15) can be generalized in terms of the effective field $\mathbf{B}^{\text{eff}}$ acting on the magnetic moment, which can be expressed as $\mathbf{B}^{\text{eff}} = \partial\mathcal{H}/\partial\boldsymbol{\mu}$, where $\mathcal{H}$ is the Hamiltonian that accommodates all magnetic interactions of the considered spin system.

In the macroscopic point of view, where the sample size is much larger than the interatomic distances, it is convenient to define the magnetic moment per unit volume,

M, also known as **magnetization**. For that purpose, the magnetic moments are averaged over small blocks of volume δV, which are large enough to have good macroscopic average, but small compared to the sample dimensions so that **M** represents a local quantity, given by

$$\mathbf{M} = \frac{1}{\delta V} \sum_i \boldsymbol{\mu}_i, \tag{2.16}$$

where the index i runs over all magnetic moments in the volume δV. The magnetization vector can be further expressed as $\mathbf{M} = M_s \boldsymbol{m}$, where $M_s = n\mu$ is the so-called **saturation magnetization**; n is the number of magnetic moments per unit volume, and $\boldsymbol{m}$ is the unit vector representing the magnetization direction. The LLG equation is then written in the macroscopic limit as

$$\frac{d\boldsymbol{m}}{dt} = -\frac{\gamma}{1+\alpha^2}\left[\boldsymbol{m} \times \mathbf{B}^{\text{eff}} + \alpha \boldsymbol{m} \times (\boldsymbol{m} \times \mathbf{B}^{\text{eff}})\right], \tag{2.17}$$

where $\mathbf{B}^{\text{eff}} = \frac{1}{M_s} \partial \mathcal{H} / \partial \boldsymbol{m}$.

2.3 Collective interactions

In this section, we discuss the different types of magnetic interactions that might contribute to the energy Hamiltonian of the magnetic moments. We will see that, a strong correlation between the magnetic moments can lead to long-range magnetic order, giving rise to important phenomena, such as ferromagnetism and topological spin-textures. The interaction between the magnetic moments also allows the propagation of information throughout the material, for example, in the form of spin waves.

2.3.1 Magnetic dipolar interaction

As we know from the previous sections, each magnetic moment is associated with a magnetic dipolar field. Therefore, the first interaction that we might expect to play a role when multiple magnetic moments are put together is the dipole-dipole interaction. In this case, the energy of the system is minimized when the magnetic moments are aligned "head to tail", with the magnetic poles facing their corresponding counterparts. The dipole-dipole contribution to the Hamiltonian can be written as

$$\mathcal{H}_{\text{dd}} = -\frac{1}{2}\frac{\mu_0 \mu^2}{4\pi} \sum_{i,j \neq i} \frac{3(\hat{\boldsymbol{\mu}}_i \cdot \hat{\boldsymbol{r}}_{ij})(\hat{\boldsymbol{\mu}}_j \cdot \hat{\boldsymbol{r}}_{ij}) - (\hat{\boldsymbol{\mu}}_i \cdot \hat{\boldsymbol{\mu}}_j)}{r_{ij}^3}, \tag{2.18}$$

where the sum runs over all pairs of magnetic moments in the system; $\boldsymbol{r}_{ij}$ is the distance between sites i and j, and μ_0 is the vacuum permeability.

From this point of view, one might question if the dipolar interactions are the responsible for the long-range magnetic order observed in some materials, such as in

permanent magnets. To answer that question we can estimate the order of magnitude of the dipolar energy. Consider two magnetic moments, each one with $\mu \approx 1\mu_B$, separated by $r \approx 1$ Å. In this case, $\mu^2/4\pi r^3 \approx 10^{-4}$ eV, which corresponds to 1 K in temperature (i.e., $K_B T \approx 10^{-4}$ eV, with $T = 1$ K and K_B the Boltzmann constant). Therefore, the order imposed by dipolar interaction is too weak, and can be easily destroyed by thermal fluctuations. This can not explain most magnetic materials, which order at much higher temperatures. As we shall see in the next section, the exchange interaction between neighbouring ions is the one responsible for magnetic order in most magnetic materials.

In the continuous limit, where the magnetic moments can be expressed in terms of the magnetization function [Eq. (2.16)], the dipolar field is commonly referred to as **demagnetization field**. The dipolar energy is then determined by the integral over the volume V of the magnet,

$$\mathcal{H}_{\mathrm{dd}} = -\frac{\mu_0}{2}\int_V \mathbf{M}(\mathbf{r}) \cdot \mathbf{H}_{\mathrm{d}}(\mathbf{r}) d^3\mathbf{r}, \tag{2.19}$$

where

$$\mathbf{H}_{\mathrm{d}}(\mathbf{r}) = -\frac{1}{4\pi}\int_V \left[\frac{3[\mathbf{M}(\mathbf{r}') \cdot \widehat{(\mathbf{r}-\mathbf{r}')}]\widehat{(\mathbf{r}-\mathbf{r}')} - \mathbf{M}(\mathbf{r}')}{||\mathbf{r}-\mathbf{r}'||^3}\right] d^3\mathbf{r}' \tag{2.20}$$

is the demagnetization field at the position $\mathbf{r}$. Notice that, the analytical solutions for the integrals in the above equations can be very difficulty in the case of arbitrary magnetization profile and sample geometry. Therefore, the demagnetization field is commonly solved by numerical integration.

2.3.2 Exchange interaction

The so-called exchange interaction is the one responsible for the phenomenon of long range magnetic order in most magnetic materials, and it arises from the sharing of electrons in the atomic bonds. The overlap of two or more electron wavefunctions in the atomic bonds has to satisfy certain conditions which strongly affect the preferential orientation of neighbouring magnetic moments. The fact that electrons are **identical particles** implies that the exchange of two electrons must give the same electronic density. For example, let us consider a system of two electrons (one from each atom in the bond) with spatial coordinates $\mathbf{r}_1$ and $\mathbf{r}_2$ respectively. The first electron is in the quantum state $\psi_a(\mathbf{r}_1)$ and the second electron is in state $\psi_b(\mathbf{r}_2)$, where the wave functions ψ_a and ψ_b are the solutions of Schrödinger's equation for each individual atom. The joint wave function Ψ has to be invariant with respect to particle exchange, i.e., $|\Psi(1,2)|^2 = |\Psi(2,1)|^2$. In addition, since electrons are fermions, and according to the **Pauli exclusion principle**, two or more identical fermions can not occupy the same quantum state simultaneously, the total eletronic wavefunction must be antisymmetric $\Psi(1,2) = -\Psi(2,1)$.

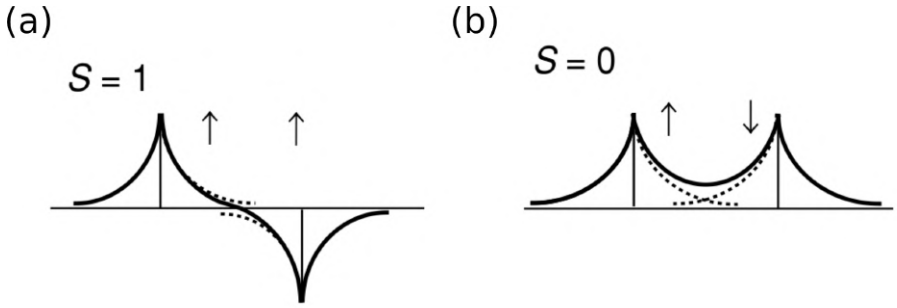

Figure 2.5 – The joint wave function of two electrons, for (a) antisymmetric spatial part (solid line) and symmetric spin state (arrows), and (b) symmetric spatial part and antisymmetric spin state. Dashed lines show the individual wavefunctions. Retrieved from Ref. [16].

The joint wave function can be written as the product of functions of space and spin coordinates, given by

$$\Psi(1,2) = \phi(\mathbf{r}_1,\mathbf{r}_2)\chi(s_1,s_2).$$

In this way, when the spatial part ϕ of the wave function is symmetric (antisymmetric), the spin part χ must be antisymmetric (symmetric), as illustrated in Fig. 2.5. The antisymmetric spin state is characterized by spin number $S = 0$, and it has only one possible configuration ($m_S = 0$). This state is called **spin singlet**, and it is given by

$$\chi_S = \frac{1}{\sqrt{2}}\left[|\uparrow_1,\downarrow_2\rangle - |\downarrow_1,\uparrow_2\rangle\right], \tag{2.21}$$

where $|\uparrow_1,\downarrow_2\rangle$ represents the state where the first electron has spin $s = 1/2$ and the second one has $s = -1/2$. On the other hand, the symmetric spin state has $S = 1$, and three different possible configurations ($m_S = 1, 0, -1$), and it is called **spin triplet**, given by

$$\chi_T = |\uparrow_1,\uparrow_2\rangle;\quad \frac{1}{\sqrt{2}}\left[|\uparrow_1,\downarrow_2\rangle + |\downarrow_1,\uparrow_2\rangle\right];\quad |\downarrow_1,\downarrow_2\rangle. \tag{2.22}$$

The total wave functions for the singlet and triplet cases are written as

$$\begin{aligned}\Psi_S &= \frac{1}{\sqrt{2}}\left[\psi_a(\mathbf{r}_1)\psi_b(\mathbf{r}_2) + \psi_a(\mathbf{r}_2)\psi_b(\mathbf{r}_1)\right]\chi_S \\ \Psi_T &= \frac{1}{\sqrt{2}}\left[\psi_a(\mathbf{r}_1)\psi_b(\mathbf{r}_2) - \psi_a(\mathbf{r}_2)\psi_b(\mathbf{r}_1)\right]\chi_T.\end{aligned} \tag{2.23}$$

Notice that both expressions satisfy the antisymmetric condition $\Psi_{S,T}(1,2) = -\Psi_{S,T}(2,1)$. The energies of the two possible states can be evaluated from the Hamiltonian operator $\hat{\mathcal{H}}$,

$$\begin{aligned}E_S &= \int \Psi_S^* \hat{\mathcal{H}} \Psi_S d^3\mathbf{r}_1 d^3\mathbf{r}_2 \\ E_T &= \int \Psi_T^* \hat{\mathcal{H}} \Psi_T d^3\mathbf{r}_1 d^3\mathbf{r}_2,\end{aligned} \tag{2.24}$$

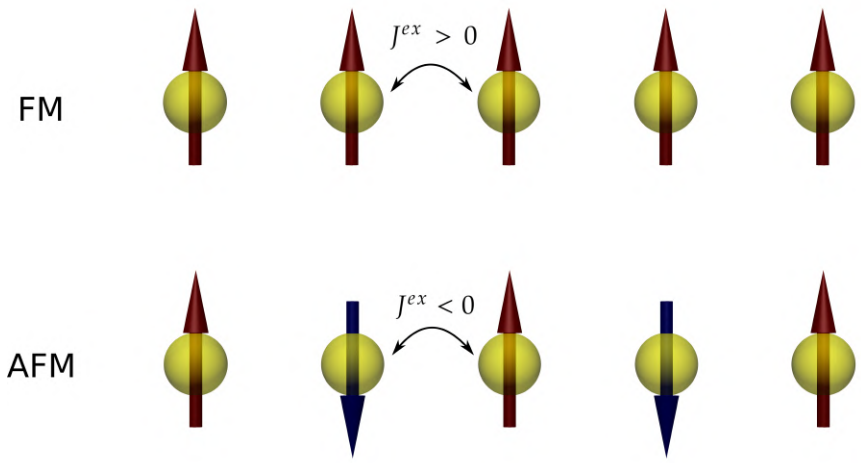

Figure 2.6 – Illustration of ferromagnetic (top) and antiferromagnetic (bottom) configurations. Here, the spheres represent the atoms and the arrows represent the direction of the magnetic moments.

and the energy difference between the two states is [16, 21]

$$E_S - E_T = 2 \int \psi_a^*(\mathbf{r}_1)\psi_b^*(\mathbf{r}_2)\hat{\mathcal{H}}\psi_a(\mathbf{r}_2)\psi_b(\mathbf{r}_1)d^3\mathbf{r}_1 d^3\mathbf{r}_2, \tag{2.25}$$

where we assume that the spin parts of the wave function χ_S and χ_T are normalized.

Since the triplet and singlet states favor the alignment and anti-alignment of spins, respectively, the spin-dependent term of the Hamiltonian can be parametrized using the expression

$$\mathcal{H}_{\text{ex}} = -J_{\text{ex}}\hat{\mathbf{n}}_1 \cdot \hat{\mathbf{n}}_2, \tag{2.26}$$

where $\hat{\mathbf{n}}_1$ and $\hat{\mathbf{n}}_2$ are the directions of the two spins, respectively, and $J_{\text{ex}} \equiv E_S - E_T$ is the so-called **exchange constant** (or exchange integral), which defines the energy cost of flipping the spin (and consequently, the magnetic interaction of the atomic bond). Therefore, if $J_{\text{ex}} > 0$, the triplet state is the ground state of the system and the energy is minimized when $\hat{\mathbf{n}}_1$ is parallel to $\hat{\mathbf{n}}_2$. On the other hand, if $J_{\text{ex}} < 0$ the singlet is the ground state and the energy is minimized for $\hat{\mathbf{n}_1}$ antiparallel to $\hat{\mathbf{n}}_2$. The Heisenberg model (named after Werner Heisenberg) generalizes this magnetic interaction for a spin-lattice system by assuming that it applies between all neighbouring atoms, giving rise to the Heisenberg Hamiltonian

$$\mathcal{H}_{\text{ex}} = -\frac{1}{2}\sum_{i,j} J_{ij}^{\text{ex}}\hat{\mathbf{n}}_i \cdot \hat{\mathbf{n}}_j, \tag{2.27}$$

where J_{ij}^{ex} is the exchange constant between the i^{th} and j^{th} spins. The factor of 1/2 is included because the summation runs over each pair of spins twice. Within this model, $J^{ex} > 0$ indicates a ferromagnetic interaction, where all spins in the lattice tend to align along the same direction [see Fig. 2.6], while $J^{ex} < 0$ indicates a antiferromagnetic

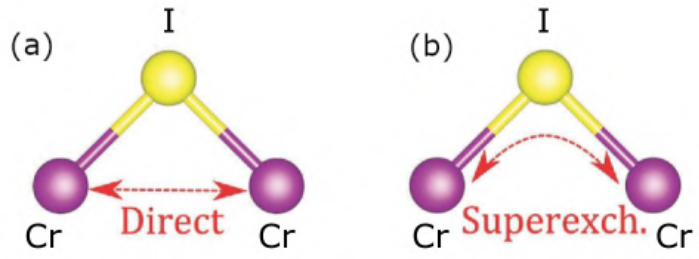

Figure 2.7 – Illustration of (a) direct exchange and (b) superexchange between chromium atoms in the van der Waals magnetic material CrI_3. Adapted from Ref. [18].

interaction, where the spins tend to align antiparallel. Usually, the energy contribution of exchange interaction is a few orders of magnitude higher than that of the dipolar interaction, and can therefore stabilize long-range magnetic order at much higher temperatures.

Note, however, that Eq. (2.25) was derived for the system of two electrons, but such calculation can be much more complicated to solve for the case of many-electron atomic spins, where competing exchange interactions may coexist with different signs of coupling. In addition, in some cases, the exchange coupling between two magnetic ions may not be given by the direct overlap of their electronic orbitals, as considered above, but mediated through a non-magnetic ion, in the so-called **superexchange** interaction [see, e.g., Fig. 2.7], which exchange calculations involve the electronic orbitals of the ligand ion, and J^{ex} depends sensitively on the interatomic separation, and on the bonding angle between orbitals. Therefore, the exchange parameter is commonly calculated by numerical methods, such as *ab initio* calculations []. In a general scenario, the exchange Hamiltonian can be expressed as

$$\mathcal{H}_{\text{ex}} = -\frac{1}{2}\sum_{i,j} \hat{\mathbf{n}}_i \mathcal{J}_{ij} \hat{\mathbf{n}}_j, \tag{2.28}$$

with the tensorial exchange coupling

$$\mathcal{J}_{ij} = \begin{bmatrix} J_{ij}^{xx} & J_{ij}^{xy} & J_{ij}^{xz} \\ J_{ij}^{yx} & J_{ij}^{yy} & J_{ij}^{yz} \\ J_{ij}^{zx} & J_{ij}^{zy} & J_{ij}^{zz} \end{bmatrix}, \tag{2.29}$$

which takes into account anisotropic interactions, and can be applied to different atomic structures. Eq. (2.28) is reduced to Eq. (2.27) for the case of isotropic exchange coupling: $\mathcal{J}_{ij} = J_{ij}^{\text{ex}}\mathcal{I}$, with $\mathcal{I}$ the identity matrix.

Let us now consider, for example, the case of uniform ferromagnetic interaction, and that the angles between nearest neighbour spins are very small. In this case, we can assume $\hat{\mathbf{n}}_i \cdot \hat{\mathbf{n}}_j \approx 1 - \phi_{ij}^2/2$, where ϕ_{ij} is the angle between the i^{th} and j^{th} spins. In the continuous limit, we can write $\phi_{ij}^2 \approx |(\mathbf{r}_{ij} \cdot \nabla)\mathbf{m}|^2$, where $\mathbf{m} = (m_x, m_y, m_z)$ is the

magnetization function and $\mathbf{r}_{ij}$ the distance vector connecting sites i and j. Therefore, in the continuum approximation, the exchange Hamiltonian is given by the integral over the sample volume

$$\mathcal{H}_{\text{ex}} = A_{\text{ex}} \int_V \left[(\nabla m_x)^2 + (\nabla m_y)^2 + (\nabla m_z)^2 \right] d^3\mathbf{r}, \tag{2.30}$$

where the exchange stiffness coefficient, A_{ex}, represents the strength of exchange interactions per unit distance. In the International System of Units (SI), the exchange stiffness is expressed in Joules per meter [J/m].

2.3.3 Dzyaloshinsky-Moriya interaction

In chiral magnetic materials, where space inversion symmetry is broken, the indirect exchange mechanism that couples two atomic spins to a neighbor atom with large spin-orbit coupling (SOC) results in antisymetric terms in the exchange matrix [Eq. (2.29)]. The antisymetric (AS) exchange, commonly referred to as the **Dzyaloshinskii-Moriya interaction** (DMI) [73, 88, 89], can be extracted from the exchange matrix as follows

$$\mathcal{J}_{ij}^{\text{AS}} = \frac{1}{2}\left(\mathcal{J}_{ij} - \mathcal{J}_{ij}^{T}\right), \tag{2.31}$$

and the DMI contribution to the magnetic Hamiltonian is given by

$$\mathcal{H}_{\text{dmi}} = -\frac{1}{2}\sum_{i,j} \hat{\mathbf{n}}_i \mathcal{J}_{ij}^{\text{AS}} \hat{\mathbf{n}}_j = -\frac{1}{2}\sum_{i,j} \mathbf{D}_{ij} \cdot (\hat{\mathbf{n}}_i \times \hat{\mathbf{n}}_j), \tag{2.32}$$

where $\mathbf{D}_{ij}$ is the Dzyaloshinsky-Moriya (DM) vector defined as

$$D_{ij}^{x} = \frac{1}{2}\left(J_{ij}^{yz} - J_{ij}^{zy}\right), \quad D_{ij}^{y} = \frac{1}{2}\left(J_{ij}^{xz} - J_{ij}^{zx}\right), \quad D_{ij}^{z} = \frac{1}{2}\left(J_{ij}^{xy} - J_{ij}^{yx}\right). \tag{2.33}$$

The direction of the DM vector is perpendicular to the plane of the triangle composed of the two magnetic sites and the atom with a large SOC, as illustrates in Fig. 2.8.

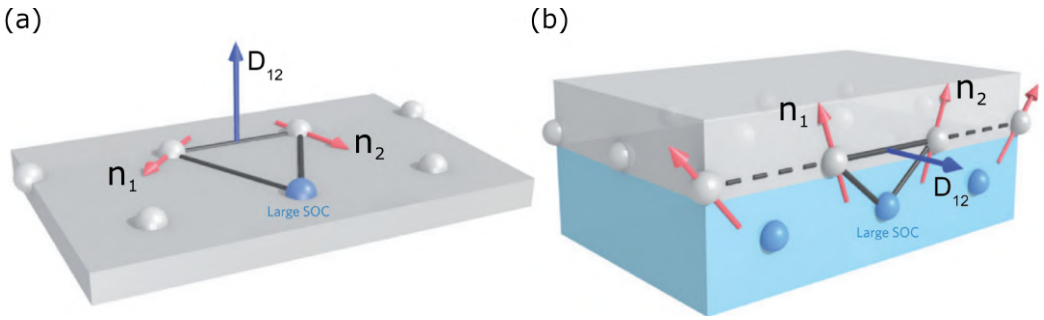

Figure 2.8 – Illustration of a DMI generated by (a) indirect exchange for the triangle composed of two atomic spins, $\hat{\mathbf{n}}_1$ and $\hat{\mathbf{n}}_2$, and an atom with a strong SOC, and (b) at the interface- Such topological protection increases the stability between a ferromagnetic metal (grey) and a metal with a strong SOC (blue). The DMI vector $\mathbf{D}_{12}$ is perpendicular to the plane of the triangle composed of two magnetic sites and an atom with a large SOC. Adapted from Ref. [19].

In contrast to the symmetric exchange interaction, the DMI is characterized by a vectorial product of the magnetic moments and the tendency is to couple the two spins perpendicularly. As we shall see in Sec. 2.5, the competition of the symmetric exchange and DM interactions favors the rotation of magnetization at short length scales, giving rise to chiral spin structures such as cycloids and magnetic skyrmions. The orientation of the DM vector, therefore, defines the plane in which the magnetization rotates and whether it rotates clockwise or counterclockwise. The DMI is also responsible for the effect of **weak ferromagnetism** observed in some antiferromagnets, such as MnF_2 and $MnCO_3$, where the spins may be canted away from the antiferromagnetic axis by about 1^o, which results in a small ferromagnetic moment in the perpendicular direction.

In the case of magnetic thin films with an interfacially induced DMI (case that will be considered in some parts of this thesis), the contribution of DMI to the Hamiltonian can be expressed in the continuous limit as [90]

$$\mathcal{H}_{\text{dmi}} = -\int_V D\left[m_x\partial_x m_z - m_z\partial_x m_x + m_y\partial_y m_z - m_z\partial_y m_y\right] d^3\mathbf{r}, \tag{2.34}$$

where D represents the strength of DM interaction and $\mathbf{m} = (m_x, m_y, m_z)$ is the magnetization function. In the SI, D is expressed in Joules per square-meter [J/m^2].

2.3.4 Magnetocrystalline anisotropy

The magnetocrystalline anisotropy arises from the interaction of atomic spin orbitals with the local crystal environment, which tends to orient the magnetization along certain crystallographic axes (known as easy magnetization axes). The form of the anisotropy and its magnitude, therefore, depend on the crystal symmetry and the chemical composition of the material. For example, a pure iron crystal exhibits easy axes along the $\langle 100\rangle$ crystallographic directions and hard axes along $\langle 111\rangle$ and $\langle 110\rangle$, as illustrated in Fig. 2.9. The sources of magnetocrystalline anisotropy can be separated into two distinct cases: the **Single-ion anisotropy** (SIA) and the **Two-ion anisotropy** (TIA). The SIA originates from the electrostatic interaction of the orbitals containing the valence electrons with the crystal-field created by the neighbouring atomic sites. The crystal-field, combined with the spin-orbit interaction, tends to stabilize a particular orbital and forces the magnetic moment to align itself along well-defined crystallographic axes. The SIA contribution to the magnetic Hamiltonian can be writen as

$$\mathcal{H}_{\text{sia}} = \sum_i \hat{\mathbf{n}}_i \mathcal{A}_i \hat{\mathbf{n}}_i, \tag{2.35}$$

with the SIA matrix given by

$$\mathcal{A}_i = \begin{bmatrix} A_i^{xx} & A_i^{xy} & A_i^{xz} \\ A_i^{yx} & A_i^{yy} & A_i^{yz} \\ A_i^{zx} & A_i^{zy} & A_i^{zz} \end{bmatrix}. \tag{2.36}$$

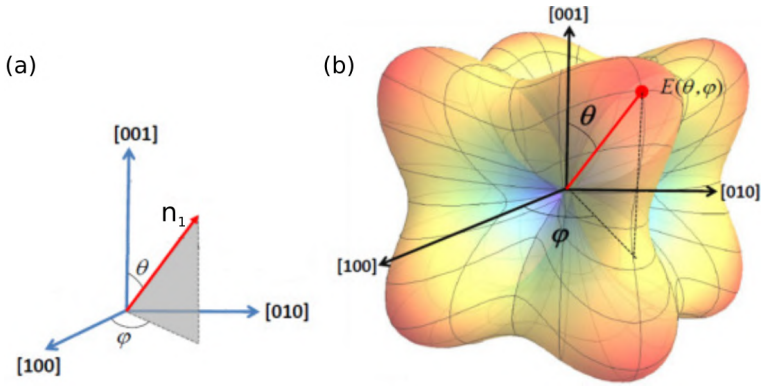

Figure 2.9 – (a) Definition of magnetic moment direction with respect to the crystallographic axes in a cubic system. (b) Example of the anisotropy energy surface for pure iron crystal, which exhibits easy axes along the ⟨100⟩ crystallographic directions and hard axes along ⟨111⟩ and ⟨110⟩. Adapted from Ref. [20].

In the simple case of uniaxial anisotropy along $\hat{z}$ direction, the only non-zero element of SIA matrix is A_i^{zz}, and Eq. (2.35) becomes

$$\mathcal{H}_{\text{sia}} = \sum_i A_i^{zz} (\hat{\mathbf{n}}_i \cdot \hat{z})^2. \tag{2.37}$$

The TIA contribution reflects the anisotropy of the dipole–dipole interaction (DDI) as well as the anisotropic exchange between magnetic sites. As discussed in Sec. 2.3.1, the DDI tends to align the magnetic moments in a head-to-tail configuration, which preferential direction is sensitive to the atomic distances in the crystal structure. On the other hand, the contribution of the anisotropic exchange to the magnetic Hamiltonian was already included in the exchange matrix discussed in Eq. (2.29), which anisotropic part can be further separate as

$$\mathcal{J}_{ij}^{\text{ani}} = \frac{1}{2}\left(\mathcal{J}_{ij} + \mathcal{J}_{ij}^T\right) - J_{ij}\mathcal{I}\,, \tag{2.38}$$

where $J_{ij} = \frac{1}{3}\text{Tr}(\mathcal{J}_{ij})$ represents the isotropic exchange interaction and $\mathcal{I}$ is the identity matrix. The anisotropic exchange is crucial to stabilize long-range order in two-dimensional magnetic materials, such as in the few-atom-thick van der Waals heterostructures.

In the continuum limit, the energy contribution of a uniaxial anisotropy, with an easy axis $\hat{\mathbf{u}}$, can be expressed as

$$\mathcal{H}_{\text{ani}} = -\int_V K\,(\mathbf{m}\cdot\hat{\mathbf{u}})^2\, d^3\mathbf{r}, \tag{2.39}$$

where K is the anisotropy constant, often expressed in units of Joule per cubic-meter [J/m^3], and $\mathbf{m}$ is the magnetization function.

2.4 Magnetic ordering

When the magnetic moments are strongly coupled, long-range magnetic order may arise throughout the material. For example, let us consider the case where the interaction between magnetic moments is dominated by the ferromagnetic exchange. The Weiss model [21] describes the **spontaneous magnetization** induced due to the ferromagnetic exchange by approximating the Heisenberg Hamiltonian [Eq. (2.27)] in terms of an effective molecular field $\mathbf{B}_{\mathrm{mf}}$, where the exchange Hamiltonian for the i^{th} spin becomes

$$\mathcal{H}_{\mathrm{ex}}^{i} = -\hat{\mathbf{n}}_i \cdot \sum_j J_{ij}^{\mathrm{ex}} \hat{\mathbf{n}}_j \equiv -\hat{\mathbf{n}}_i \cdot \mu \mathbf{B}_{\mathrm{mf}}. \tag{2.40}$$

The assumption underlying this approach is that all magnetic ions experience the same molecular field (stemming from the exchange interaction with neighbouring spins), which may be not applicable in the case of strongly nonuniform magnetization profiles and at temperatures close to a magnetic phase transition, but it is enough to demonstrate the spontaneous magnetization that emerges from the coupling between the magnetic moments. The molecular field approximation allows us to treat the exchange coupling analogous to the Zeeman interaction [Eq. (2.11)] between the magnetic moment and an external applied field, so the total Hamiltonian becomes

$$\mathcal{H} = -\mu \sum_i \hat{\mathbf{n}}_i \cdot (\mathbf{B} + \mathbf{B}_{\mathrm{mf}}), \tag{2.41}$$

where $\mathbf{B}$ is the external magnetic field. We are now able to treat this problem as if the magnetic moments were independent parts (i.e., there is no interaction between them), which is known as a **paramagnetic** system.

In a paramagnetic system, there is no long-range magnetic order in the absence of external fields, but an applied magnetic field induces a magnetization which aligns parallel with the field direction. The induced magnetization M in the system is determined by the average moment along the field direction (say $\mathbf{B} = B\hat{z}$) $M = n\langle \mu_z \rangle$, where n is the number of magnetic ions per unit volume. The expected value of $\langle \mu_z \rangle$ as a function of field and temperature T can be obtained by means of statistical mechanics calculations [16, 21], which results in the following expression for the magnetization of the paramagnetic system

$$\frac{M}{M_s} = \mathcal{B}_J(y), \tag{2.42}$$

where $\mathcal{B}_J$ is the Brillouin function [21] and

$$y = \frac{g_J \mu_B \mathsf{J} B}{k_B T}, \tag{2.43}$$

with g_J and J the g-factor and the total quantum number associated with the magnetic moment, respectively [see Sec. 2.1].

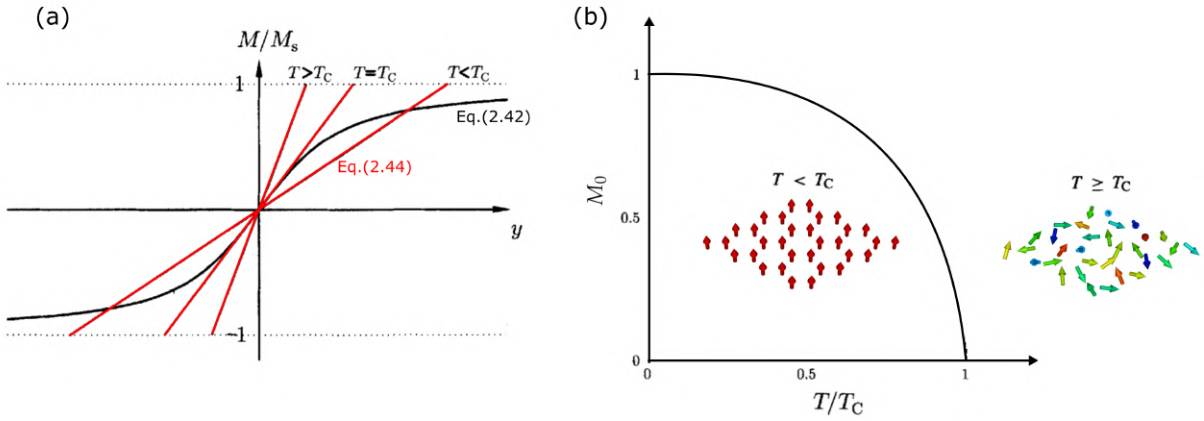

Figure 2.10 – (a) The graphical solution of Eqs. (2.42) and Eq. (2.44) for $B = 0$. A non-zero solution exists only for $T < T_C$. (b) The spontaneous magnetization as a function of temperature. The magnetization is zero for $T \geq T_C$ (the magnetic state is paramagnetic) and is non-zero for $T < T_C$ (the magnetic state is ferromagnetic). Adapted from Ref. [21].

Let us now include the molecular field in the paramagnetic system, for what we replace B by $B + B_{\text{mf}}$ in Eq. (2.43). Since the molecular field measures the effect of the ordering of the system, one can assume that $B_{\text{mf}} = \lambda M$, where the constant λ defines the strength of the molecular field as a function of the sample magnetization. Therefore, for $\lambda \neq 0$, Eq. (2.43) can be rewritten as

$$\frac{M}{M_s} = \frac{k_B T y}{g_J \mu_B \mathsf{J} \lambda M_s} - \frac{B}{\lambda M_s}. \tag{2.44}$$

The solution for this model is obtained by solving simultaneously Eq. (2.42) and Eq. (2.44). These equations can be solved graphically. The case of $B = 0$ is illustrated in Fig. 2.10 (a). Notice that, for high temperatures, the only simultaneous solution of Eqs. (2.42) and (2.44) is at $y = 0$, which implies $M = 0$. However, below a critical temperature, two new solutions emerge: $M/M_s = \pm M_0$, where M_0 is some non-zero value that grows when the material is cooled, as illustrated in Fig. 2.10 (b). The material thus becomes magnetized, even in the absence of an external field, which is the characteristic of long-range ferromagnetic order. The transition temperature, known as the **Curie temperature** T_C, is obtained when the gradient of Eq. (2.44) is equal to that of the Brillouin function [Eq. (2.42)] at the origin. For the case of small y, the Brillouin function can be approximated as $\mathcal{B}_J(y) \approx (\mathsf{J}+1)y/3\mathsf{J}$, which results in the following expression for the Curie temperature

$$T_C \approx \frac{g_J \mu_B (\mathsf{J}+1) \lambda M_s}{3k_B} = \frac{n \lambda \mu^2}{3k_B}, \tag{2.45}$$

where $M_s = n g_J \mu_B \mathsf{J}$ and $\mu = g_J \mu_B \sqrt{\mathsf{J}(\mathsf{J}+1)}$ [see Sec. 2.1]. The Weiss's molecular field theory was the first mean field theory to describe a magnetic phase transition, and one that remains useful today.

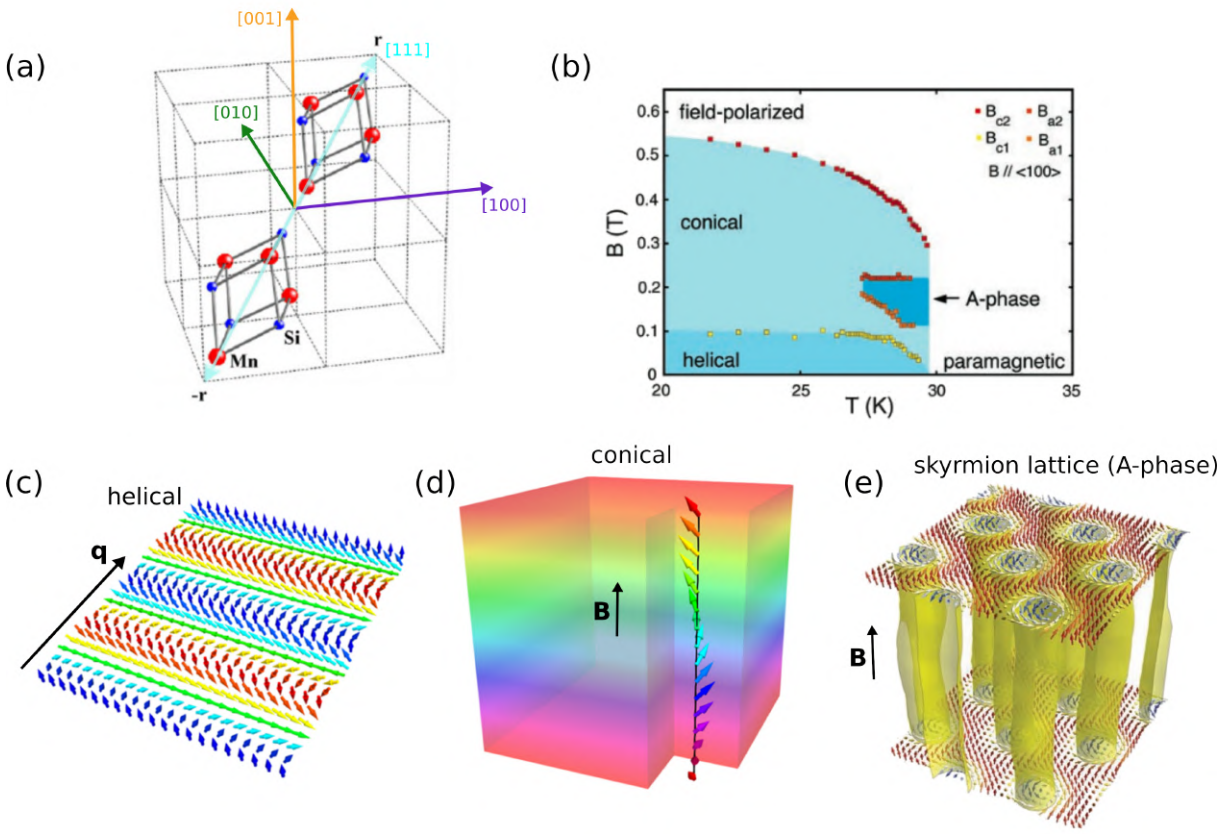

Figure 2.11 – (a) Crystal structure of MnSi with B20 cubic symmetry. (b) Phase diagram of MnSi as a function of temperature T and field B. (c-e) Illustration of chiral magnetic states: the helical phase (c), the conical phase (d), and skyrmion phase (e). Adapted from Refs. [7, 8, 22, 23].

2.5 Chiral magnetic states

The competition between the symmetric exchange and DM interactions in chiral magnetic materials favors the rotation of magnetization at short length scales. This gives rise to the so-called **chiral magnetic states** (CMS). A common example of a chiral magnet is the MnSi (manganese silicide) compond, which crystallizes in the B20 structure that lacks inversion symmetry, as illustrated in Fig. 2.11 (a). Therefore, let us now consider the MnSi as an example to illustrate the CMS. The magnetic phase diagram of MnSi as a function of applied magnetic field and temperature is shown in Fig. 2.11 (b), where the magnetic phases were identified by neutron scattering experiments [7]. The most familiar phases in Fig. 2.11 (b) are the field-polarized and paramagnetic ones, which are also observed in basic ferromagnetic materials, as discussed in the previous section. However, three different CMS emerge due to DM interaction in MnSi, which are: the **helical phase**, the **conical phase** and the **skyrmion phase** (also known as the A-phase).

For small, or in the absence of applied magnetic fields, the equilibrium spin-configuration below the Curie temperature in MnSi is the helical phase. In this state, the magnetization precesses around an easy axes **q** determined by the crystalline

anisotropies [91], where the local magnetization is perpendicular to the helix pitch. The helical phase is illustrated in Fig. 2.11 (c). Upon increasing the external magnetic field, the system transitions from the helical to the conical phase, where the magnetization now precesses around the magnetic field direction, with a non-zero magnetization component parallel to the field, as illustrated in Fig. 2.11 (d). At higher fields, the system finally saturates in the field-polarized state. The skyrmion phase, on the other hand, appears at intermediate magnetic field values and at temperatures just below T_C. At this phase, the magnetization swirls locally, forming some kind of magnetic whirlpools, known as skyrmions, where the magnetization at the center of each skyrmion is flipped from the background magnetization, as illustrated in Fig. 2.11 (e).

2.6 The magnetic skyrmion

Extended lattices of magnetic skyrmions were first observed in B20-type bulk systems, such as MnSi, but they are also present in thin film chiral magnets [25], where the DMI is created at the interface between the magnetic thin film and a heavy metal material. The sense at which the magnetization rotates differ between the two cases. The Néel-type skyrmion texture [Fig. 2.12 (a)] is stabilized in thin magnetic films with interface induced DMI, while the Bloch-type skyrmions [Fig. 2.12 (b)] are found in bulk materials. The different rotation senses of the magnetization in such systems are defined by the direction of the DM vector [see Sec.2.3.3], which in the bulk case points along the vector connecting the magnetic moments, $\hat{\mathbf{r}}_{ij}$, while in the case of interface induced DMI it points along $\hat{\mathbf{n}} \times \hat{\mathbf{r}}_{ij}$, where $\hat{\mathbf{n}}$ is the unit vector normal to the interface.

2.6.1 Topological properties

A particularly interesting property of magnetic skyrmions is the fact that they are topologically protected objects, which means that the skyrmion texture can not be destroyed into a trivial solution by a continuous deformation. In order to determine

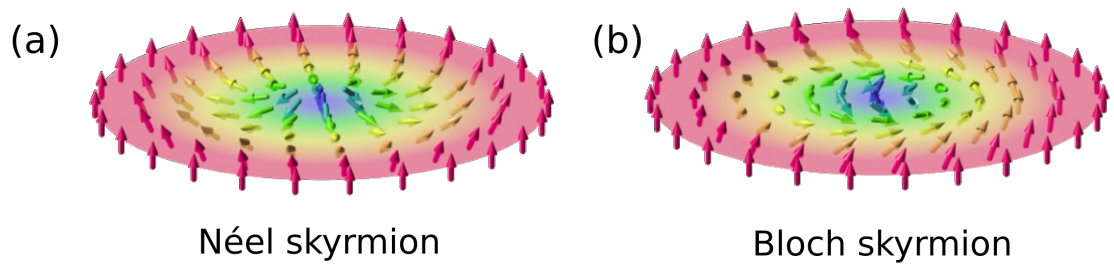

Figure 2.12 – (a) Néel-type skyrmion, observed in thin film chiral magnets. (b) Bloch-type skyrmion, observed in bulk chiral magnets. In both cases, the spin at the center of the skyrmion points down, while the spins at the perimeter point up. Retrieved from Ref. [24].

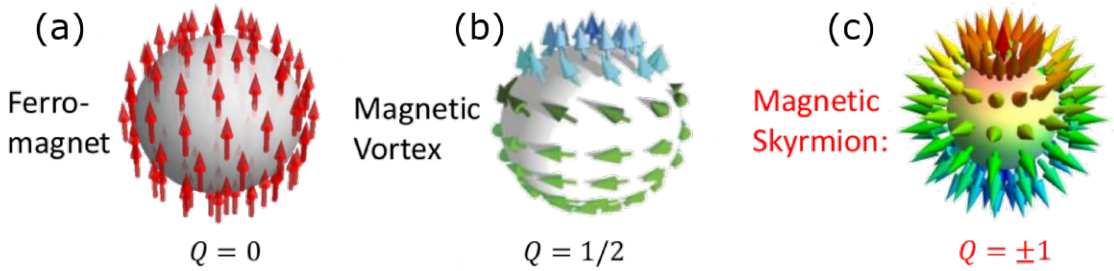

Figure 2.13 – The topological presentation of a magnetic phase by wrapping each individual spin onto a unit sphere, for (a) ferromagnetic state, (b) magnetic vortex and (c) magnetic skyrmion. The topological charge Q counts how many times the spins wind around the unit sphere.

whether a given spin structure is a skyrmion one needs to calculate the **topological charge** Q, defined as

$$Q = \frac{1}{4\pi} \int \mathbf{m} \cdot \left(\partial_x \mathbf{m} \times \partial_y \mathbf{m} \right) dx dy, \tag{2.46}$$

where $\mathbf{m}$ is the magnetization function. The topological charge, also known as the **skyrmion number**, counts how many times the spins wind around the unit sphere, as illustrated in Fig. 2.13. The skyrmions are characterized by an integer topological charge, and can not be continuously deformed into, e.g., the ferromagnetic state, where $Q = 0$. Such topological protection increases the stability of the magnetic skyrmions in such a way that they are able to move throughout the magnetic material without losing their shape, similar to vortices in superconductors [92], property that makes them promising candidates for technological applications such as magnetic memory devices. However, the fact that spins are arranged in a discrete lattice rather than a continuous one, makes it possible for the skyrmions to be destroyed in a first-order phase transition, characterized by an energy barrier that determines the stability of the skyrmion phase. Generally, skyrmions are highly stable magnetic objects and can be observed even at room temperature in some materials [77].

2.6.2 Helicity and vorticity

The skyrmion spin-texture can be characterized by assuming the rotational symmetry of the magnetization around the skyrmion core, so we can write

$$\mathbf{m}(r,\phi) = \sin\Theta(r)\cos\Phi(\phi)\hat{x} + \sin\Theta(r)\sin\Phi(\phi)\hat{y} + \cos\Theta(r)\hat{z}, \tag{2.47}$$

where $\Theta(r)$ and $\Phi(\phi)$ give the direction of the magnetization at the position $\mathbf{r} = r\cos\phi\hat{x} + r\sin\phi\hat{y}$, as illustrated in Fig. 2.14 (a). The center of the skyrmion coincides with the origin of the coordinate system ($r = 0$). Note that, due to the symmetry, the value of Φ does not depend on the distance r, and Θ is independent on the angle ϕ. By

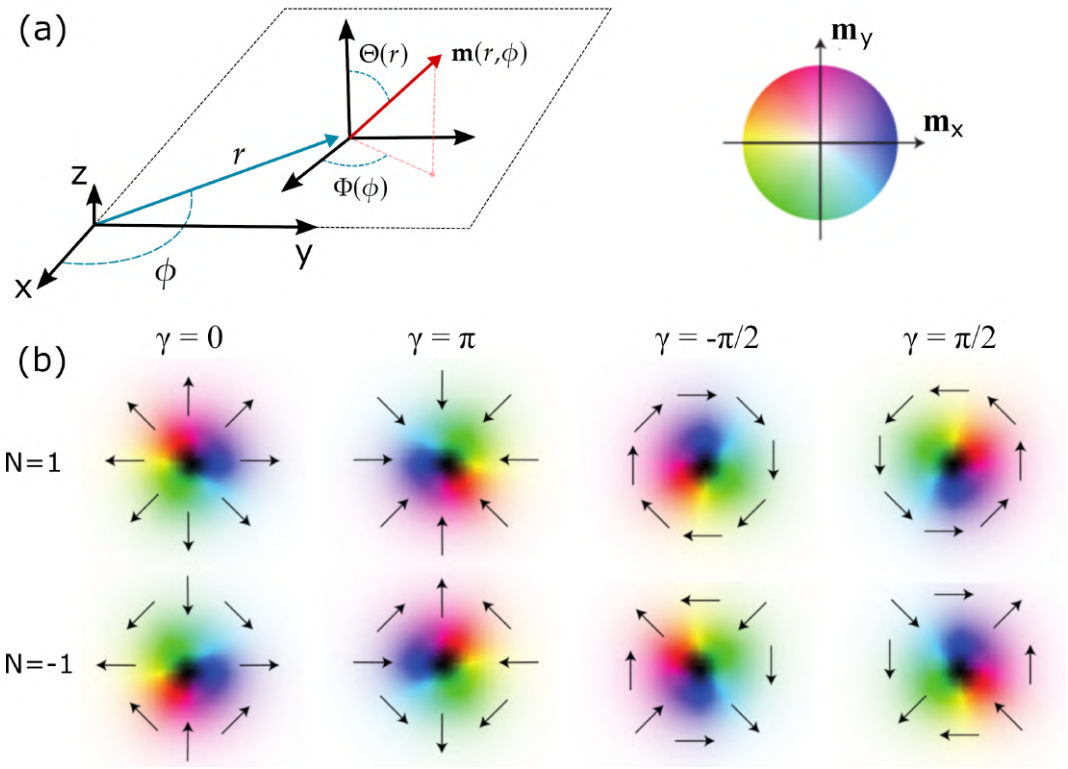

Figure 2.14 – (a) Illustration of coordinate system considered in Eq. (2.47). (b) Skyrmion structures for different vorticities N and helicities γ. The arrows indicate the direction of the in-plane spin component. Adapted from Ref. [25].

substituting Eq. (2.47) into Eq. (2.46), we obtain

$$Q = \frac{1}{4\pi}\int_0^{\infty} dr \int_0^{2\pi} d\phi \frac{d\Theta}{dr}\frac{d\Phi}{d\phi}\sin\Theta(r) = \frac{1}{4\pi}\Big[\cos\Theta(r)\Big]_{r=0}^{r=\infty}\Big[\Phi(\phi)\Big]_{\phi=0}^{\phi=2\pi}. \tag{2.48}$$

If we assume that the spins point up at $r \to \infty$ while they point down at $r = 0$ (skyrmion core), we obtain $\Big[\cos\Theta(r)\Big]_{r=0}^{r=\infty} = 2$. The skyrmion structure is then classified by the definition of two parameters: (*i*) the skyrmion **vorticity**, represented by the integer N, which counts how many times, and the sense at which Φ rotates in a full cycle from $\phi = 0$ to 2π, defined as

$$N = \frac{\Big[\Phi(\phi)\Big]_{\phi=0}^{\phi=2\pi}}{2\pi}, \tag{2.49}$$

such that the topological charge becomes $Q = N$, and (*ii*) the skyrmion **helicity**, represented by the phase γ, which defines the value of Φ at $\phi = 0$, i.e.,

$$\Phi(\phi) = N\phi + \gamma. \tag{2.50}$$

Fig. 2.14 (b) shows the skyrmion structures obtained for different values of N and γ. Notice that the Néel-type skyrmion [Fig. 2.12] is represented by $\gamma = 0$ or π while the Bloch-type skyrmion is represented by $\gamma = \pm\pi/2$. The case where $N = -1$ is also known as the anti-skyrmion.

2.7 Skyrmions in motion

2.7.1 Spin-transfer-torque

When a spin polarized current is applied to the magnetic material, it can drive the magnetic skyrmions throughout the sample. A spin-polarized electric current is obtained when most of the spins of the moving electrons are aligned in the same direction, as illustrated in Fig. 2.15 (a). Therefore, a spin-polarized current does not only carry charge, but also angular momentum, and its interaction with the localized magnetic moments results in a torque on the magnetization, called a **spin-transfer-torque** (STT). The STT in a thin magnetic film can be induced in two different scenarios: (i) by an in-plane spin-polarized current (CIP) applied into the magnetic layer [see Fig. 2.15 (b)], or (ii) by an electric current applied into an adjacent heavy metal (HM) layer, which due to the spin Hall effect gives rise to a spin-polarized current perpendicular to the film plane (CPP) [93–96] [see Fig. 2.15 (c)]. In both scenarios, the effects of STT to the magnetization dynamics can be included into the LLG equation [Eq. (2.17)] as follows. For the CIP scenario, the Zhang and Li STT term [97]

$$\boldsymbol{\tau}_{ZL} = \frac{b}{1+\alpha^2}\left[\mathbf{m}\times(\mathbf{m}\times(\mathbf{j}\cdot\nabla)\mathbf{m}) + (\beta-\alpha)\mathbf{m}\times(\mathbf{j}\cdot\nabla)\mathbf{m}\right], \tag{2.51}$$

is added to the right hand side of the LLG equation, where $\mathbf{j}$ is the current density; β is the non-adiabatic factor; α is the Gilbert damping factor and $b = P\mu_B/eM_s(1+\beta^2)$, with

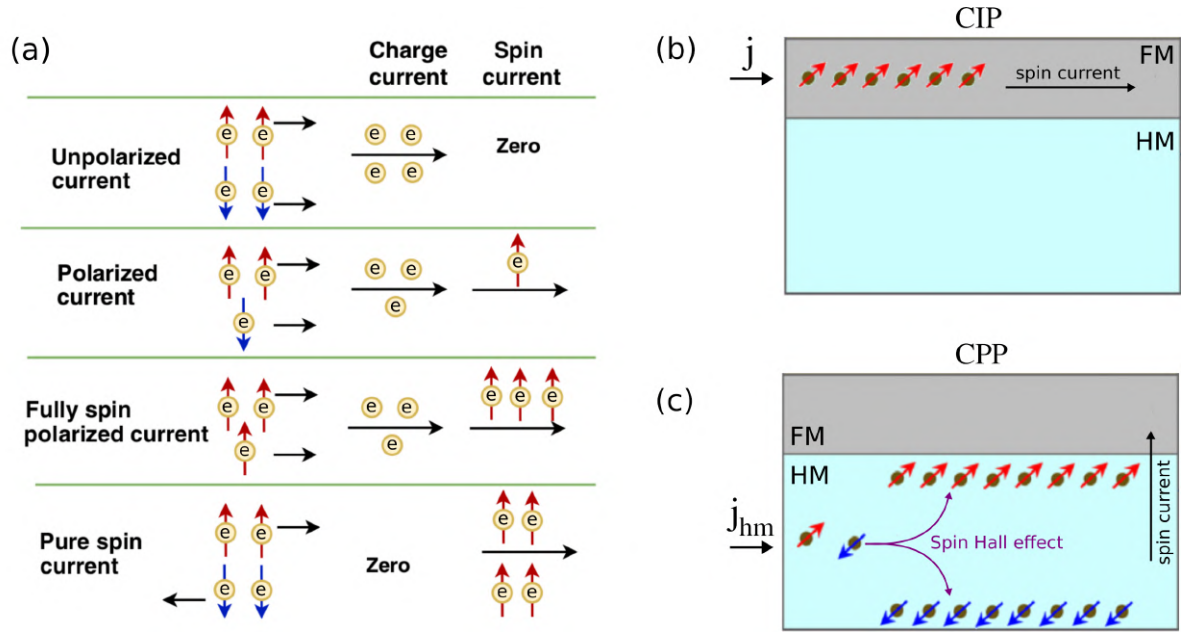

Figure 2.15 – (a) Illustration of spin currents. When most of the spins of the moving electrons are aligned in the same direction, the current is said to be spin polarized. (b-c) Illustration of spin-polarized currents in a ferromagnet (FM)-heavy metal (HM) heterostructure, for (b) in-plane spin-polarized current (CIP) applied into the FM layer, and (c) spin-polarized current perpendicular to the film plane (CPP), induced by an electric current applied into the HM layer. Adapted from Refs. [26, 27].

P the polarization of the current density, μ_B the Bohr magneton, e the electron charge, and M_s the saturation magnetization. On the other hand, in the CPP scenario the electric current applied into the HM layer results in a spin current injected into the magnetic film along the out-of-plane direction, with $\mathbf{m}_p = -\text{sgn}\theta_{SH}(\hat{z} \times \hat{j}_{\text{hm}})$ the orientation of the injected spins [93, 94, 98, 99], where θ_{SH} is the spin-Hall angle characteristic of the heavy metal and $\mathbf{j}_{\text{hm}}$ is the current density flowing through the HM layer. In this situation, the STT is described by the Slonczewski term [100, 101]

$$\boldsymbol{\tau}_{SL} = \frac{1}{1+\alpha^2}\frac{j_z \hbar P}{2eM_s d}\left[\mathbf{m} \times (\mathbf{m}_p \times \mathbf{m}) + \alpha \mathbf{m} \times \mathbf{m}_p\right] \tag{2.52}$$

where d is the thickness of the magnetic layer and $j_z = \theta_{SH} j_{\text{hm}}$ the spin current density induced along the out-of-plane direction.

2.7.2 Skyrmion Hall effect

When charged particles move in the presence of a perpendicular magnetic field, they experience a transverse deflection, as a result of the Lorentz force [16], and eventually accumulate at the sample edges, thus creating a voltage difference across the sample. This effect is known as the Hall effect, and it is named after the American physicist Edwin Hall, who first observed this phenomenon in 1879 [102]. Interestingly, a similar effect occurs for magnetic skyrmions, where their topological, rather than electrical charge causes them to travel with curved trajectories in the presence of applied currents. When a spin-polarized current is applied into the magnetic material, it drives the skyrmion by means of the spin-transfer torque mechanism, as discussed in the previous section. The electrons are deflected by the Lorentz force due to the emergent magnetic field of the skyrmion, while the skyrmion experiences a curved trajectory, where the velocity of the skyrmion has a component perpendicular to the electron flow, as illustrated in Fig. 2.16 (a). Several studies have demonstrated the so-called **skyrmion Hall-effect** (SkHE) [29, 103]. For instance, Fig. 2.16 (b) shows experimental observations of magnetic skyrmions in a Ta/CoFeB/TaO_x trilayer by magneto-optical Kerr effect (MOKE) microscopy [29]. The experiment consists of applying spin-polarized current pulses to a thin-film magnetic device containing several skyrmions. The applied current causes the skyrmions to accumulate at the edge of the sample, similar to the charged particles in the classical Hall-effect. The side of the sample at which skyrmions accumulate depends on the sign of the topological charge Q [Eq. (2.46)]. Fig. 2.16 (c) shows the trajectory of an isolated skyrmion after applying several current pulses. Observe that the skyrmion trajectory is characterized by a Hall-angle with respect to the electron flow direction, defined as

$$\theta_{sk} = \arctan\left(\frac{\dot{y}}{\dot{x}}\right), \tag{2.53}$$

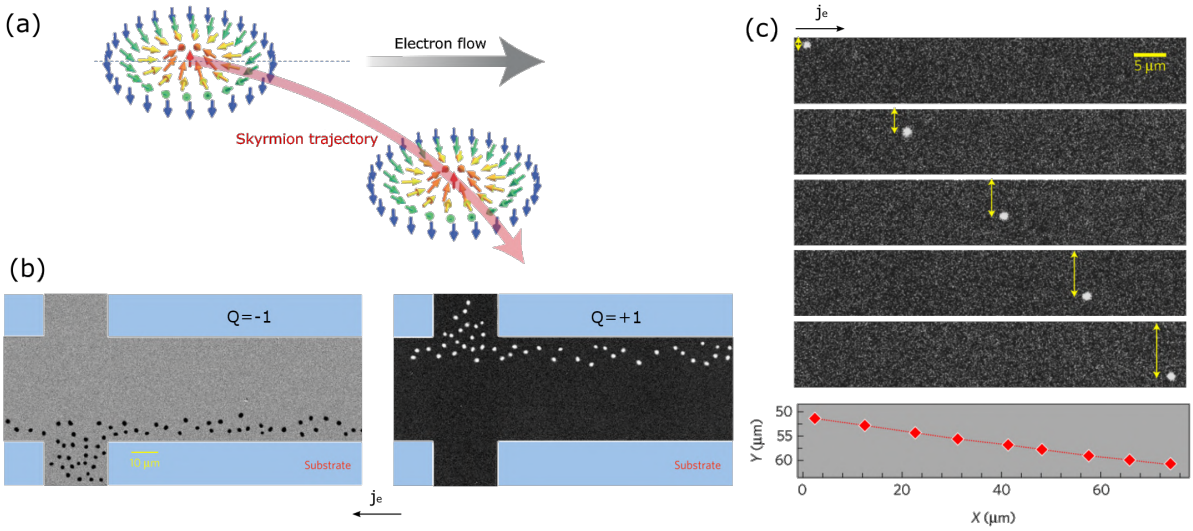

Figure 2.16 – (a) Illustration of the skyrmion Hall effect, the skyrmion experience a curved trajectory with respected to the electron flow. (b) MOKE microscopy images demonstrating skyrmion ($Q = +1$) and anti-skyrmion ($Q = -1$) accumulation at the edges of the device. (c) Skyrmion motion after applying several current pulses. The skyrmion trajectory is illustrated in the bottom panel. Adapted from Refs. [28, 29].

where $\dot{\mathbf{r}} = \dot{x}\hat{x} + \dot{y}\hat{y}$ is the drift velocity of the skyrmion. In order to derive the skyrmion velocity and understand the origin of the SkHE, one can analyze the dynamics of an isolated skyrmion based on the Thiele equation.

2.7.3 Thiele equation for skyrmion motion

The Thiele equation describes the dynamics of the center-of-mass of the skyrmion by assuming a rigid body motion of the spin texture [93, 95, 96, 104, 105]. The translational motion of the skyrmion is obtained by projecting the LLG equation [Eq. (2.17)], with spin-transfer-torque included [Eqs. (2.51) and (2.52)], onto the relevant translational modes [104]. The magnetization profile for the Néel skyrmion is considered to follow the general form of Eq. (2.47) and the LLG equation is integrated over the skyrmion area. The resultant dynamical force equation can be derived for both CIP and CPP scenarios. The Thiele equation for the CIP scenario reads

$$\mathbf{G} \times (\boldsymbol{\nu} - \dot{\mathbf{r}}) + \mathcal{D}(\beta\boldsymbol{\nu} - \alpha\dot{\mathbf{r}}) - \nabla V(\mathbf{r}) = 0, \tag{2.54}$$

where $\mathbf{G} = \mathcal{G}\hat{z} = 4\pi Q\hat{z}$ is the gyromagnetic coupling vector, with Q the topological charge [Eq. (2.46)]; $\dot{\mathbf{r}} = \dot{x}\hat{x} + \dot{y}\hat{y}$ is the drift velocity of the skyrmion; $\boldsymbol{\nu} = \nu_x\hat{x} + \nu_y\hat{y}$ is the velocity of the conduction electrons associated to the spin-polarized current; β is the non-adiabatic factor; α is the Gilbert damping factor; V is the potential stemming from external forces, boundaries or impurities, and $\mathcal{D}$ represents the dissipative tensor, with components $\mathcal{D}_{ij} = \int d^2r\, \partial_i\mathbf{m} \cdot \partial_j\mathbf{m}$. The first term in Eq. (2.54) is also known as the

Magnus force term due to the resemblance with the force generated when a spinning body travels through a viscous fluid, which acts perpendicular to the velocity of the body.

In the case where a spin-polarized current is applied along the x direction, i.e. $v_y = 0$, the Thiele equation can be separated into its two components, which for the case of $V = 0$ yields

$$\dot{x} = \left(\frac{\mathcal{G}^2 + \mathcal{D}^2\alpha\beta}{\mathcal{G}^2 + \alpha^2\mathcal{D}^2}\right) v_x, \tag{2.55a}$$

$$\dot{y} = \left(\mathcal{G}\mathcal{D}\frac{\alpha - \beta}{\mathcal{G}^2 + \alpha^2\mathcal{D}^2}\right) v_x. \tag{2.55b}$$

The above equations describe the velocity of the center-of-mass of the skyrmion due to the applied current in the absence of external forces and impurities, where the skyrmion velocity is constant for a fixed applied current. Notice that the skyrmion undergoes a transverse motion, $\dot{y} \neq 0$ (when α differs from β), because it carries a non-zero skyrmion number ($\mathcal{G} \neq 0$). The skyrmion Hall-effect therefore originates from the effective gyrotropic force related to the topological character of the skyrmion.

Similarly, for a Néel skyrmion driven by the CPP scenario, the skyrmion motion is described by the modified Thiele equation [93, 95, 96]:

$$-\mathbf{G} \times \dot{\mathbf{r}} - \alpha\mathcal{D}\dot{\mathbf{r}} + 4\pi\mathcal{B}\mathbf{j}_{\text{hm}} - \nabla V(\mathbf{r}) = 0, \tag{2.56}$$

where $\mathbf{j}_{\text{hm}}$ is the current density flowing through the heavy metal, which gives rise to a spin-polarized current perpendicular to the plane. The parameter $\mathcal{B}$ quantifies the efficiency of the spin-Hall effect. If we consider $\mathbf{j}_{\text{hm}} = j_{\text{hm}}\hat{x}$. For the case of $V = 0$, Eq. (2.56) yields

$$\dot{x} = \frac{\alpha\mathcal{D}}{\mathcal{G}^2 + \alpha^2\mathcal{D}^2} 4\pi\mathcal{B} j_{\text{hm}}, \tag{2.57a}$$

$$\dot{y} = \frac{\mathcal{G}}{\mathcal{G}^2 + \alpha^2\mathcal{D}^2} 4\pi\mathcal{B} j_{\text{hm}}. \tag{2.57b}$$

Note that, for $\alpha \ll 1$, the Magnus term dominates $\dot{y} \gg \dot{x}$, and the relevant motion is perpendicular to the current direction.

The skyrmion Hall-angle is therefore obtained by substituting Eqs. (2.55a) and (2.55b) (in case of CIP) or Eqs. (2.58) and (2.59) (in case of CPP) into Eq. (2.53), which yields

$$\theta_{sk} = \arctan\left(\frac{\mathcal{G}\mathcal{D}(\alpha - \beta)}{\mathcal{G}^2 + \alpha^2\mathcal{D}^2}\right), \tag{2.58}$$

for the case of CIP, and

$$\theta_{sk} = \arctan\left(\frac{\mathcal{G}}{\alpha\mathcal{D}}\right), \tag{2.59}$$

for the CPP scenario. Notice that θ_{sk} is a constant, determined by the material parameters and skyrmion profile.

2.8 Antiferromagnetic skyrmion

Antiferromagnetic (AFM) skyrmions are expected to combine the advantages of antiferromagnets with those of skyrmions regarding spintronic applications. AFM skyrmions have zero net topological charge and simulations of their current-induced motion have shown that accordingly they move straight along the direction imposed by the applied current [30, 94, 106, 107], i.e., the AFM skyrmion does not experience a Hall-effect. This is considered advantageous for applications, because as opposed to ferromagnetic skyrmions their antiferromagnetic counterparts are not driven towards the boundary of the hosting magnetic structures, where they can collapse. Additional benefits arise from their antiferromagnetic nature, e.g. their insensitivity to parasitic stray fields [30]. The AFM skyrmion comprises a two-sublattice structure, where each sublattice (indexed 1 and 2) contains half of the spins of the system and has the opposite magnetization of the other sublattice [see Fig. 2.17 (a)]. In this way, the topological numbers projected to each sublattice satisfy $Q_1 = -Q_2$. The opposing topological index of two sublattices causes the exact cancellation of the Magnus force in the presence of spin-polarized current [Fig. 2.17 (b)], so the antiferromagnetic skyrmion moves along the direction of the applied current.

The trajectory of the center-of-mass of the AFM skyrmion can also be described in the CPP scenario within the modified Thiele equation [Eq. (2.56)] by assuming the cancellation of the Magnus force, i.e., $G = 0$. In this case, assuming $\mathbf{j}_{\mathrm{hm}} = j_{\mathrm{hm}}\hat{x}$, the Thiele equation for the AFM skyrmion reads

$$-\alpha\mathcal{D}\dot{x} + 4\pi\mathcal{B}j_{\mathrm{hm}} - \frac{dV}{dx} = 0, \tag{2.60}$$

and $\dot{y} = 0$. Notice the velocity of the AFM skyrmion driven by a current density is inversely proportional to the damping factor α, and the AFM skyrmion can move much

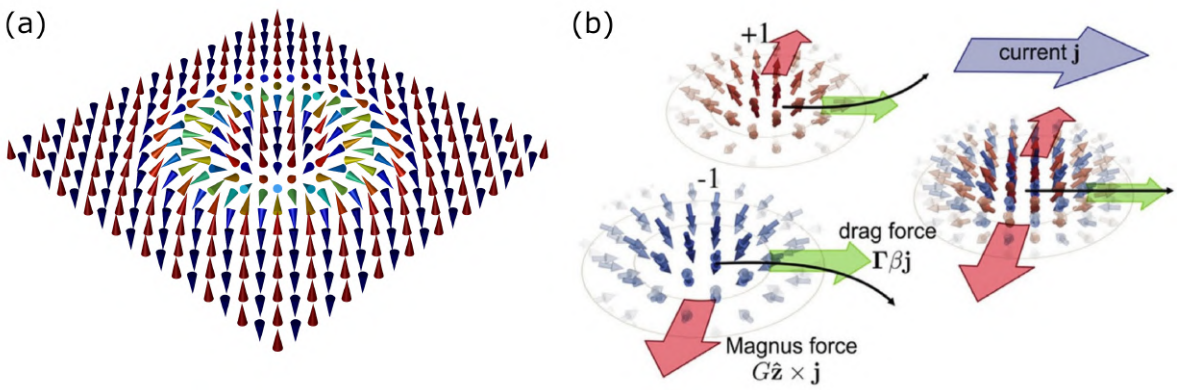

Figure 2.17 – (a) Illustration of AFM skyrmion. (b) The opposing topological charges of two sublattices causes the exact cancellation of the Magnus force in the presence of spin-polarized current. Adapted from Ref. [30].

faster than the FM one for weak damping, possibly reaching km/s while remaining stable [30, 94, 106–108].

2.9 Spin waves

The strong correlation between the magnetic moments not only leads to magnetic order such as ferromagnetism and topological spin-textures, but also allows the propagation of magnetic excitations. When a magnetic moment is excited, e.g., by some oscillating magnetic field, the neighbouring magnetic moments will also 'feel' the oscillation through the magnetic coupling, such as the exchange interaction, leading to a collective excitation that propagates as a wave in the crystal lattice. In 1930 Felix Bloch showed that such excitations, which he called **spin waves**, dominate the magnetic thermodynamics at low temperatures [52]. Furthermore, a quantum formulation shows that spin excitations are quantized, and the quanta of spin waves are called **magnons** [32]. In this thesis, we focus on the semiclassical representation of spin waves in a ferromagnet.

In order to review the basic properties of spin waves, let us now consider the simple case of a linear chain of semiclassical spins interacting via nearest-neighbour ferromagnetic exchange, as illustrated in Fig. 2.18 (a). The magnetic Hamiltonian of the i^{th} spin-site is given by

$$\mathcal{H}_i = -J_{\text{ex}} S^2 \left(\hat{\mathbf{n}}_i \cdot \hat{\mathbf{n}}_{i+1} + \hat{\mathbf{n}}_i \cdot \hat{\mathbf{n}}_{i-1}\right) - \mu \mathbf{B} \cdot \hat{\mathbf{n}}_i, \tag{2.61}$$

where $\mathbf{B}$ is the external applied field. A magnetic excitation in the spin-system will induced a precession of the magnetic moments around the effective field $\mathbf{B}^{\text{eff}} = \frac{1}{\mu}\partial\mathcal{H}_i/\partial\mathbf{n}_i$ [see Sec. 2.2]. Consider $\mathbf{B} = B_0\hat{z}$ such that the magnetic moments saturate along the $\hat{z}$ direction. The spin dynamics can be described by the Landau-Lifshitz equation [see Eq. (2.13)], which for the in-plane spin components results in

$$\frac{dn_i^x}{dt} = -\gamma \left[n_i^y (B^{\text{eff}})^z - n_i^z (B^{\text{eff}})^y\right], \tag{2.62a}$$

$$\frac{dn_i^y}{dt} = -\gamma \left[n_i^z (B^{\text{eff}})^x - n_i^x (B^{\text{eff}})^z\right]. \tag{2.62b}$$

Substituting the effective field into Eq. (2.62a), it becomes

$$\frac{dn_i^x}{dt} = -\frac{\gamma}{\mu}\left[n_i^y(-J_{\text{ex}}S^2(n_{i+1}^z + n_{i-1}^z) - \mu B_0) - n_i^z(-J_{\text{ex}}S^2(n_{i+1}^y + n_{i-1}^y))\right]. \tag{2.63}$$

Considering that the amplitude of the spin excitation is small, we linearize this equation by assuming $n^x, n^y \ll n^z \approx 1$, which results in

$$\frac{dn_i^x}{dt} \approx \gamma B_0 n_i^y - \frac{\gamma J_{\text{ex}} S^2}{\mu}\left[-2n_i^y + n_{i+1}^y + n_{i-1}^y\right]. \tag{2.64}$$

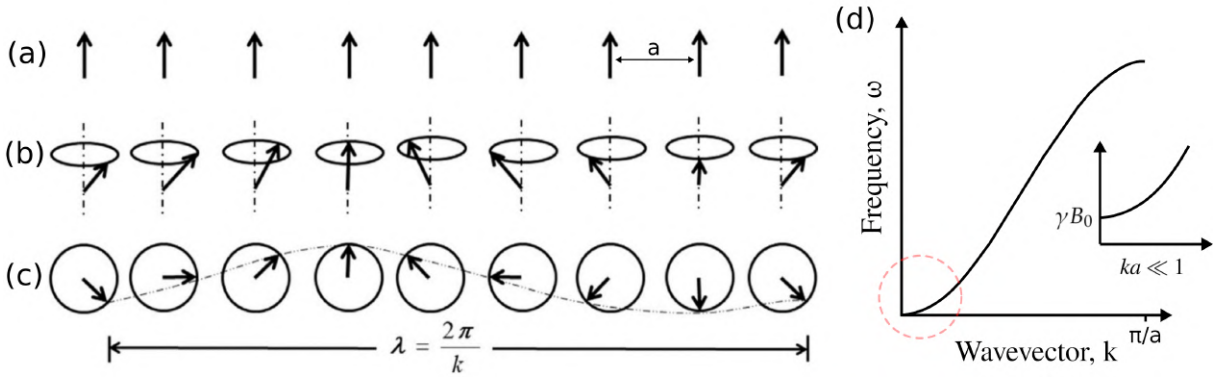

Figure 2.18 – (a) Illustration of linear chain of spins in the ferromagnetic ground state. (b) Side and (c) top views of spin wave in the linear chain of spins. (d) Dispersion relation for spin waves in a linear chain. The inset shows a zoom near the origin (red circle), where $ka \ll 1$. Adapted from Ref. [31].

The equation above shows that the movement of a spin at any location is coupled with the movement of neighboring spins, thus indicating that a collective motion is induced when we have a spin excitation. Therefore, as a possible solution for Eq. (2.64), one can consider that the magnetic excitations assume the form of harmonic travelling waves

$$n_i^x = A_x e^{i(kx_i - \omega t)}, \tag{2.65a}$$

$$n_i^y = A_y e^{i(kx_i - \omega t)}, \tag{2.65b}$$

where A_x and A_y are the amplitudes of the spin oscillation, with A_x,$A_y \ll 1$. Here, x_i is the position of the i^{th} spin-site; ω is angular frequency and k is the wavenumber. Substituting that into Eq. (2.64), we obtain

$$-i\omega A_x = A_y \left[\gamma B_0 - \frac{\gamma J_{ex} S^2}{\mu}\left(-2 + e^{ika} + e^{-ika}\right)\right], \tag{2.66}$$

where we used $x_{i+1} - x_i = a$ and $x_{i-1} - x_i = -a$, with a the lattice constant [see Fig. 2.18 (a)]. Eq. (2.66) can be rewritten as

$$i\omega A_x = -A_y \left[\gamma B_0 + \frac{2\gamma J_{ex} S^2}{\mu}(1 - \cos ka)\right]. \tag{2.67}$$

Similarly, doing the same analysis for Eq. (2.62b) results in

$$i\omega A_y = A_x \left[\gamma B_0 + \frac{2\gamma J_{ex} S^2}{\mu}(1 - \cos ka)\right]. \tag{2.68}$$

Note that Eqs. (2.67) and (2.68) can be rewritten in the matrix form

$$\begin{bmatrix} i\omega & -\left[\gamma B_0 + \frac{2\gamma J_{ex} S^2}{\mu}(1 - \cos ka)\right] \\ \left[\gamma B_0 + \frac{2\gamma J_{ex} S^2}{\mu}(1 - \cos ka)\right] & i\omega \end{bmatrix} \begin{bmatrix} A_x \\ A_y \end{bmatrix} = 0, \tag{2.69}$$

Sample shape and field direction	Demagnetizing factors	ω_0/γ
	$N_x = N_y = N_z = 4\pi/3$	H_0
	$N_x = N_y = 0$ $N_z = 4\pi$	$H_0 - 4\pi M$
	$N_z = N_x = 0$ $N_y = 4\pi$	$[H_0(H_0 + 4\pi M)]^{1/2}$
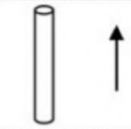	$N_z = 0$ $N_x = N_y = 2\pi$	$H_0 + 2\pi M$
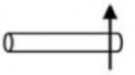	$N_y = 0$ $N_x = N_z = 2\pi$	$[H_0(H_0 - 2\pi M)]^{1/2}$

Figure 2.19 – Demagnetization effects to the FMR frequency (in CGS units) for different shapes of the magnetic sample. The magnetic field direction is indicated by the black arrow. Retrieved from Ref. [32].

which solution is obtained by equating the main determinant to zero, from where we obtain the angular frequency

$$\omega = \gamma B_0 + \frac{2\gamma J_{\text{ex}} S^2}{\mu}(1 - \cos ka)\,. \tag{2.70}$$

This equation describes the relation between the spin wave frequency ω and the wavenumber k, and it is called **dispersion relation**. Using this solution into Eqs. (2.67) and (2.68), we obtain $A_x = iA_y \equiv A_0$, and the real part of the spin wave solution becomes

$$n_i^x = A_0 \cos(kx_i - \omega t), \quad n_i^y = A_0 \sin(kx_i - \omega t). \tag{2.71}$$

Fig. 2.18 (b) and (c) illustrates the spin wave in the linear chain of spins, with wavelength defined as $\lambda = 2\pi/k$. Notice that, for $k = 0$ all spins precess in phase and there is no contribution from the exchange energy, i.e., $\omega_0 = \omega(k = 0) = \gamma B_0$. This is known as the **magnetic resonance frequency**, or zero-momentum spin wave (magnon) mode. As the wavenumber increases, the phase difference of precession for neighboring spins increases and so does the exchange energy. In the limit of $ka \ll 1$, Eq. (2.70) becomes

$$\omega \approx \omega_0 + \frac{\gamma J_{\text{ex}} a^2 S^2}{\mu} k^2, \tag{2.72}$$

and the spin wave frequency has a quadratic dependence on the wavevector. Fig. 2.18 (d) shows the dispersion relation for the spin waves in a linear chain, where the inset

shows the case of $ka \ll 1$. Generally, the spin wave dispersion can take different forms depending on the material shape and magnetic interactions involved. For instance, the effects of demagnetization fields to resonance frequency ω_0 in bulk ferromagnetic samples was derived by Charles Kittel [109], in the so-called Kittel equation

$$\omega_0 = \gamma \mu_0 \left[H_0 + (N_x - N_z)M\right]^{1/2} \left[H_0 + (N_y - N_z)M\right]^{1/2}, \tag{2.73}$$

where N_x, N_y and N_z are the diagonal components of the demagnetizing tensor, with z corresponding to the direction of the applied field, and M is the sample magnetization. The Kittel equation shows that the **ferromagnetic resonance frequency** (FMR), ω_0, depends on the sample shape and on the direction of the applied field, as illustrated in Fig. 2.19.

3 Numerical simulations

To simulate the magnetic states resulting from the collective interactions in magnetic materials, one can make use of multiple numerical techniques. In this chapter, we present the methods used for solving spin dynamics in different scales, as well as the minimum energy path analysis used to calculate activation energies of magnetic phase transitions.

3.1 Multiscale modeling

A multiscale approach for the magnetic system can be done by combining first-principles (*ab initio*) simulations of the quantum origin of magnetic interactions with the semiclassical atomistic spin-dynamics and micromagnetic simulations. First-principles electronic structure calculations are based on the laws of quantum mechanics and provide detailed insight into the origin of magnetic properties within the subnanometer length scale, while the atomistic spin-dynamics rely on the Heisenberg spin model to simulate the effective local moments of atomic sites. The micromagnetic model, on the other hand, is applied in the case where magnetization changes over large length scales, and the magnetic energy can be treated in the continuous approximation. Fig. 3.1 illustrates the time and length scales accessible by the different numerical methods used to simulate the magnetic materials.

3.1.1 First-principles calculations

Ab initio calculations, based on **density functional theory** (DFT) approaches, make use of the Hohenberg–Kohn–Sham (HKS) theory [110] to state that the total energy of a system can be described by the electron density. For many materials the local spin density approximation (LSDA) to the DFT is known to provide a reliable description of the ground state atomic structure and electronic structure of the solid [111], from where we are able to accurately infer the equilibrium lattice constants, as well as the localized

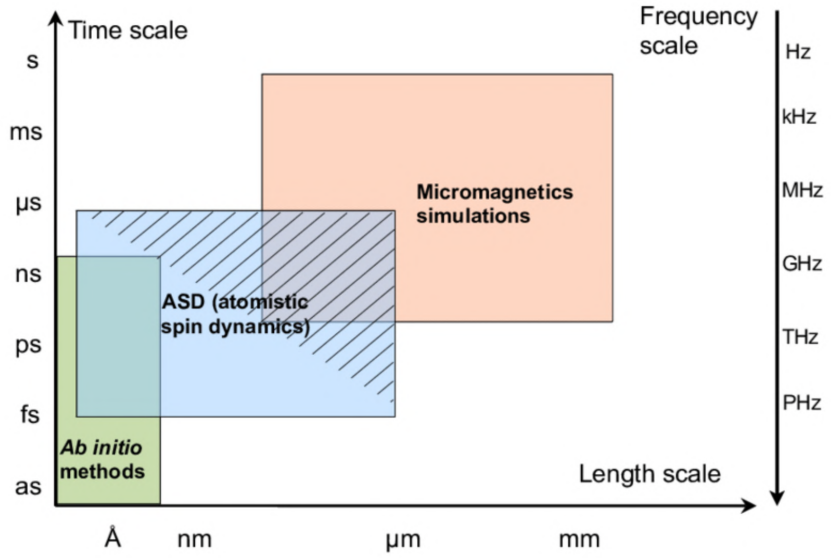

Figure 3.1 – Schematic of time and length scales accessible by the different numerical methods used to simulate the magnetic materials. The atomistic spin dynamics makes the connection between the *ab initio* calculations and micromagnetic simulations. Retrieved from Ref. [33].

spin moments and magnetic interactions between neighbouring spins. The method consists in calculating the total energies of different magnetic configurations, and the magnetic parameters between atomic sites are obtained by fitting these energies under the supposition that the change in energy is only related to the magnetic interactions. This procedure requires at least as many calculated magnetic configurations as the number of parameters of the Hamiltonian [112]. Fitting these parameters is, however, often very complicated and requires a case-by-case construction. Difficulties may arise, for example, in the calculation of the electronic structure in some transition metal oxides, where the conventional DFT-LSDA is not appropriate to describe the strong Coulomb repulsion between $3d$ electrons localized on metal ions and it can predict metallic ground states instead of experimentally observed insulating ones [113, 114]. In this case, it is necessary to go beyond the LSDA. An improved method is obtained by combining the DFT-LSDA with the unrestricted Hartree-Fock (UHF) approximation in the so-called LSDA+U method [115]. *Ab initio* calculations generally requires high computational effort, and applications of such method are limited to short length scales, generally in the order of several hundred atoms. In addition, thermal effects are typically difficult to incorporate into standard DFT approaches and a semiclassical treatment of atomic magnetic moments might be required. Standard software packages such as the VASP (Vienna Ab-initio Software Package) [116] and the FLEUR (Full-potential Linearised augmented plane wave in EURope) [117] are examples of codes that solve the HKS

equations iteratively and make DFT calculations easily accessible. Other examples of simulation packages that provide DFT calculations include ABINIT [118], Quantum ESPRESSO [119], SIESTA [120], Wien2K [121], TB2J [122], among others. Fig. 3.2 (a) shows the example of bonding charge distribution calculated by *ab initio* simulations of the Van der Waals magnetic material CrI_3, from where magnetic parameters can be extracted.

3.1.2 Atomistic spin dynamics

In the nanometer to micrometre length scale, the magnetic parameters obtained in the *ab initio* calculations can be incorporated onto a Heisenberg spin model with effective local moments, where the Landau-Lifshitz-Gilbert (LLG) equation [Eq. (2.15)] is solved numerically in order to describe the time evolution of the magnetic system. This method is commonly called **atomistic spin dynamics** (ASD), and can solve the magnetic state for different crystalline structures, with the resolution of a single atomic-site. Fig. 3.2 (b) shows an example of crystalline structure considered in the ASD simulations, where the magnetic interactions between neighbouring moments are extracted from the *ab initio* electron density calculation.

The magnetic Hamiltonian that describes the spin system is given by the summation of energy contributions of the relevant inter-atomic magnetic interactions. For the case of magnetic interactions discussed in Sec. 2.3, the Hamiltonian of the spin system can be written as

$$\mathcal{H} = \mathcal{H}_{\text{dd}} + \mathcal{H}_{\text{ex}} + \mathcal{H}_{\text{dmi}} + \mathcal{H}_{\text{ani}} + \mathcal{H}_{\text{zeeman}}, \tag{3.1}$$

which, for each magnetic moment $\boldsymbol{\mu}_i = \mu\hat{\mathbf{n}}_i$, results in the effective field $\mathbf{B}_i^{\text{eff}} = \frac{1}{\mu}\delta\mathcal{H}/\delta\hat{\mathbf{n}}_i$. The spin-dynamics is then simulated by the numerical integration of the LLG equation. The simplest integration scheme for the dynamical equation is the Euler method [123], which updates the spin direction in discretized time steps, given by

$$\hat{\mathbf{n}}_i' = \hat{\mathbf{n}}_i^t + \delta t \Delta\hat{\mathbf{n}}_i^t, \tag{3.2}$$

where $\hat{\mathbf{n}}_i'$ represents the new spin direction after a single time step δt and $\Delta\hat{\mathbf{n}}_i^t \equiv \frac{\partial\hat{\mathbf{n}}_i^t}{\partial t}$. An improved integration scheme can be obtained by higher order Runge-Kutta methods [124]. For instance, the Heun's solver [125], which falls into the Runge-Kutta category, makes use of Euler's iteration [Eq. (3.2)] as a predictor step before calculating the revised spin position

$$\hat{\mathbf{n}}_i^{t+\delta t} = \hat{\mathbf{n}}_i^t + \frac{\delta t}{2}\left(\Delta\hat{\mathbf{n}}_i^t + \Delta\hat{\mathbf{n}}_i'\right), \tag{3.3}$$

where $\Delta\hat{\mathbf{n}}_i' \equiv \frac{\partial\hat{\mathbf{n}}_i'}{\partial t}$. Notice, however, that one must ensure the conservation of the magnitude of the spin, for example by the renormalization of the spin vector after each

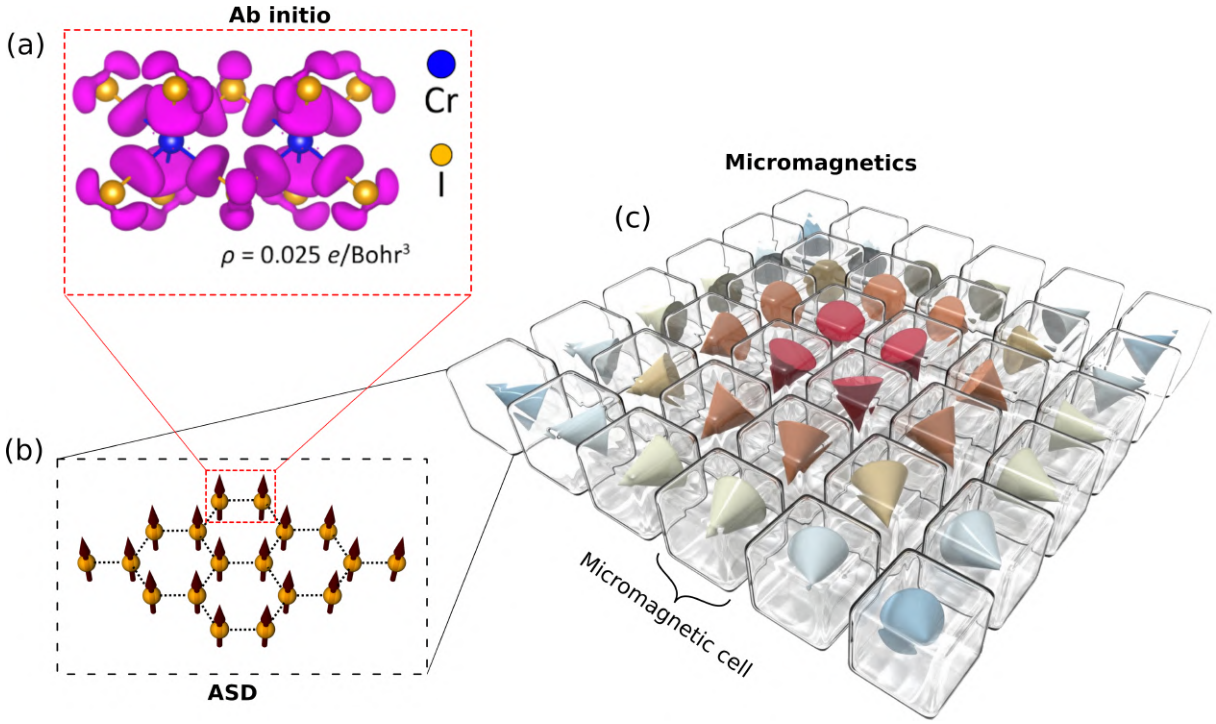

Figure 3.2 – Multiscale modeling. (a) Bonding charge distribution (purple clouds) calculated by *ab initio* simulations of the Van der Waals magnetic material CrI_3, from where magnetic parameters can be calculated. (b) Example of possible crystalline structure considered in the ASD simulations, where the spheres represent the magnetic atoms and arrows are the effective magnetic moments. (c) Schematic illustration of micromagnetic approach. The continuous magnetization function is discretized into a grid of small blocks of volume ΔV (micromagnetic cells), each one carrying an effective magnetic moment (cones) of magnitude $M_s \Delta V$. Adapted from Refs. [34, 35]

time step. Some integration methods, such as the *semi-implicit scheme B* (SIB) [126] intrinsically preserve the spin length, and are commonly used for solving ASD simulations. Simulation packages such as *SPIRIT* [38], *VAMPIRE* [127] and *UppASD* [128] are examples of well-tested tools that provide atomistic spin dynamics and other important functionalities beyond LLG simulations.

In principle, the LLG equation describes the motion of magnetic moments at zero temperature. However, temperature-dependent simulations can be implemented by the introduction of a stochastic thermal field $\mathbf{B}^{\text{th}}$, which is added as a contribution to the effective field acting on the localized spin-sites, i.e., $\mathbf{B}_i^{\text{eff}} \rightarrow \frac{1}{\mu}\delta\mathcal{H}/\delta\hat{\mathbf{n}}_i + \mathbf{B}_i^{\text{th}}$. The magnitude of the thermal field is obtained by the fluctuation-dissipation theorem, and is given by

$$\mathbf{B}_i^{\text{th}}(T,t) = \boldsymbol{\eta}_i(t)\sqrt{2\mathcal{D}/\delta t} = \boldsymbol{\eta}_i(t)\sqrt{\frac{2\alpha k_B T}{\gamma \mu \delta t}}, \tag{3.4}$$

where T is the temperature, k_B is the Boltzmann constant, α is the Gilbert damping, γ is the gyromagnetic ratio and $\boldsymbol{\eta}_i(t)$ is a Gaussian white noise that represents the thermal fluctuations on each atomic site i. The ensemble average and variance of the thermal

field satisfies $\langle \mathbf{B}_i^{\text{th}}(t) \rangle = 0$ and $\langle \mathbf{B}_{ia}^{\text{th}}(t) \mathbf{B}_{jb}^{\text{th}}(t') \rangle = 2\mathcal{D}\delta_{ij}\delta_{ab}\delta(t-t')$, respectively, where a,b indicate the components of the vector $\mathbf{B}_i^{\text{th}}$. The stochastic LLG, as it is called, provides equivalent results for the magnetic ground state as those obtained by Monte Carlo methods [38].

3.1.3 Micromagnetic simulations

In the limit where the direction of the magnetic moments varies slowly along the lattice sites, i.e., on a length scale much larger than the atomic distances, the magnetic system can be expressed in terms of the magnetization function $\mathbf{M}(\mathbf{r},t)$ [Eq. (2.16)]. In this case, the magnetic energy [Eq. (3.1)] is treated in the continuous approximation, as discussed in Sec. 2.3. The **micromagnetic model**, therefore, consists of discretizing the continuous magnetization function in a grid of small blocks of volume ΔV, called **micromagnetic cells**, each one carrying an effective magnetic moment of magnitude $M_s \Delta V$. The micromagnetic cells are large enough to average several atomic magnetic moments, but small compared to the characteristic length scale at which the magnetization changes. Fig. 3.2 (c) illustrates the micromagnetic approach. The spin-dynamics is then simulated by the numerical integration of the LLG equation, as discussed in the previous section for the atomistic spin-dynamics. Notice, however, that the discretization of the magnetization function implies that the derivatives of $\mathbf{M}(\mathbf{r},t)$ have to be treated by finite-difference approximations [129]. The fact that the micromagnetic model averages atomic moments in larger blocks makes it useful for simulating large magnetic systems. Furthermore, the size of the micromagnetic cells can be chosen according to the characteristic length scale at which the magnetization changes, which makes micromagnetic simulations adaptable to different length scales. Several software packages provide micromagnetic simulations, two of the most impactful and widely known ones are MUMAX3 [129] and OOMMF [130]. Another option of open-source code is the simulation package *FIDIMAG* [35], which provides both atomistic and finite-difference micromagnetic simulations. Lastly, the atomistic model can interface directly with micromagnetism by the implementation of adaptive finite-difference mesh, which allows, e.g., the calculation of interface properties at the atomic level, while treating the bulk of the material with a micromagnetic description [131].

The basic assumption of the micromagnetic framework is that the magnetic system can be expressed in terms of a continuous magnetization function. Consequently, the micromagnetic method is not, a priori, suitable for studying magnetic states that fluctuate on small length scales, such as antiferromagnets and frustrated magnets. Furthermore, even when magnetic states satisfy the continuous approximation, it is still possible that transitions between states require a strong spatial variation of magnetization during the process, which is the case, for example, with the creation and annihilation

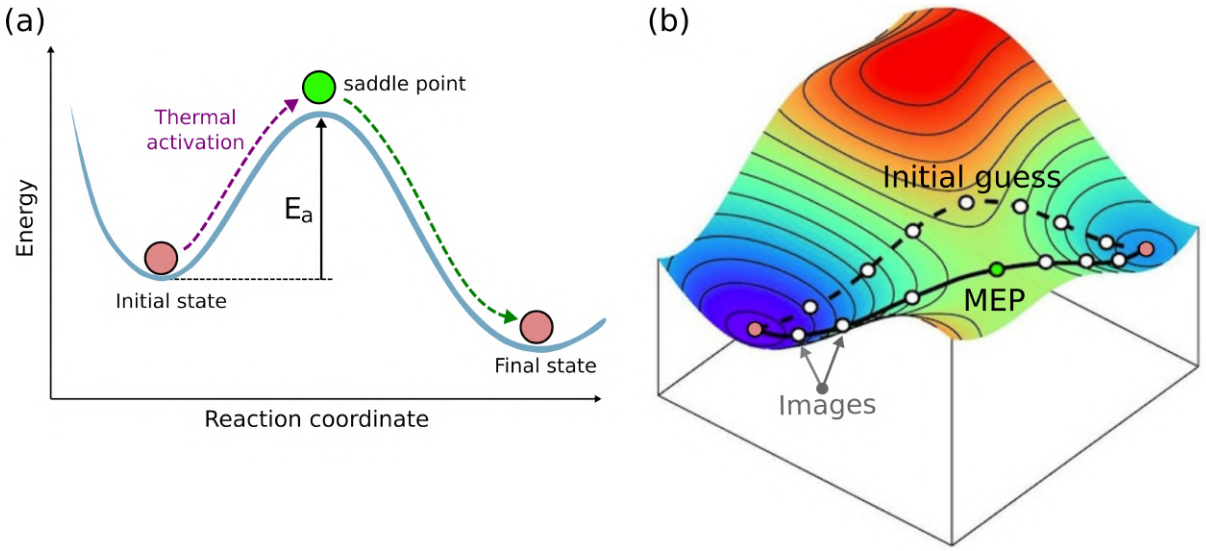

Figure 3.3 – (a) Illustration of energy path for the phase transition between two magnetic states. The activation energy E_a is determined by the highest-energy configuration, or saddle point (SP), along the transition. (b) Illustration of the GNEB initial guess and the MEP connecting the two minima in the energy landscape. Adapted from Ref. [36]

of magnetic skyrmions. In these situations, an atomistic model of the magnetic system must be resorted to.

3.2 Minimum energy paths for magnetic phase transition

The stability of a magnetic phase can be estimated by calculating the activation energy necessary to destroy such a configuration. The transition between two phases can be driven, e.g., by thermal fluctuations, and the activation energy for the phase transition is determined by the highest-energy configuration, or saddle point (SP), along the **minimum energy path** (MEP) connecting the two magnetic states, as illustrated in Fig. 3.3 (a) and (b). MEPs for magnetic phase transition can be numerically calculated by the **geodesic nudged elastic band** (GNEB) method [132], which involves taking some initial guess for the path connecting the two minima in the energy landscape [see Fig. 3.3 (b)], and then using an iterative procedure to bring that to the nearest MEP. Since transitions between magnetic states may require a strong spatial variation of magnetization during the process, the GNEB method has to be treated in the atomistic framework. Some simulation packages, such as *SPIRIT* [38] and *FIDIMAG* [35], have the GNEB method implemented in their codes.

In the GNEB method, a path is represented by a discrete chain of magnetic configurations, called "images" of the system, between the initial and final states. The initial guess of the path is then represented by the set of images $[\boldsymbol{\mathcal{M}}^1,\ldots,\boldsymbol{\mathcal{M}}^Q]$, where Q is the number of images along the path; $\boldsymbol{\mathcal{M}}^\nu = (\hat{\mathbf{n}}_1^\nu,\hat{\mathbf{n}}_2^\nu,\ldots,\hat{\mathbf{n}}_N^\nu)$ represents the magnetic

configuration of the ν^{th} image of the system with N spins, and $\hat{\mathbf{n}}_i$ is the orientation of the i^{th} spin. In order to converge from the initial guess to the nearest MEP, the effective force at each image is calculated by the negative energy gradient $-\nabla E^{\nu}$, where E^{ν} is the energy of the ν^{th} magnetic configuration and $\nabla_i = \partial/\partial\hat{\mathbf{n}}_i$. The force component along the local tangent to the path is then substituted by an artificial spring force $\mathbf{F}_{\text{spring}}$ between the images, forming an **elastic band** [see Fig. 3.4 (a)], which ensures uniform distribution of the images along the path, while the energy gradient forces orthogonal to the path tangents, $\mathbf{F}_{\perp}$, are applied, thus moving the images towards the minimum energy position in a process termed **nudging**. The first and last images of the chain are fixed and given by the local minima corresponding to the initial and final states. This procedure is therefore called nudged elastic-band (NEB). Fig. 3.4 (a) illustrates the forces acting on the NEB method, where the total force on the ν^{th} image reads

$$\mathbf{F}^{\nu} = \mathbf{F}^{\nu}_{\perp} + \mathbf{F}^{\nu}_{\text{spring}}. \tag{3.5}$$

The force orthogonal to the path can be obtained by subtracting the component of the energy gradient parallel to the tangent vector $\hat{\boldsymbol{\tau}}^{\nu}$, i.e.,

$$\mathbf{F}^{\nu}_{\perp} = -\nabla E^{\nu} + (\nabla E^{\nu} \cdot \hat{\boldsymbol{\tau}}^{\nu})\,\hat{\boldsymbol{\tau}}^{\nu}, \tag{3.6}$$

and the spring forces are defined as follows

$$\mathbf{F}^{\nu}_{\text{spring}} = k(l_{\nu-1,\nu} - l_{\nu,\nu+1})\hat{\boldsymbol{\tau}}^{\nu}, \tag{3.7}$$

where k is a spring constant and $l_{\nu,\mu}$ is a measure of distance between images ν and μ. In order to use the NEB method for spin systems, it is necessary to consider the fact that spin lengths are constants. The configuration of a system of N spins therefore contains N constraints on the magnitude of the vectors. The constrained problem can be avoided by projecting the spin system on a curved space, where each spin vector $\hat{\mathbf{n}}_i$ is represented by a point on a 2D unit sphere, S^2. The spin configuration is then described in the two-dimensional Riemannian manifold $\mathcal{R} = \prod_{i=1}^{N} S_i^2$, which corresponds to the direct product of N unit spheres (S_1^2,...,S_N^2). In this formalism, $l_{\nu,\mu}$ denotes the **geodesic** distance between images in the curved space, and can be written as

$$l_{\nu,\mu} = \sqrt{\left(d_1^{\nu,\mu}\right)^2 + \ldots + \left(d_N^{\nu,\mu}\right)^2}, \tag{3.8}$$

where

$$d_i^{\nu,\mu} = \arccos\left(\hat{\mathbf{n}}_i^{\nu} \cdot \hat{\mathbf{n}}_i^{\mu}\right) \tag{3.9}$$

is the geodesic distance for the i^{th} spin between images ν and μ, and is determined by the great-circle distance in the unit sphere S_i^2 [133]. This procedure is therefore called geodesic-NEB.

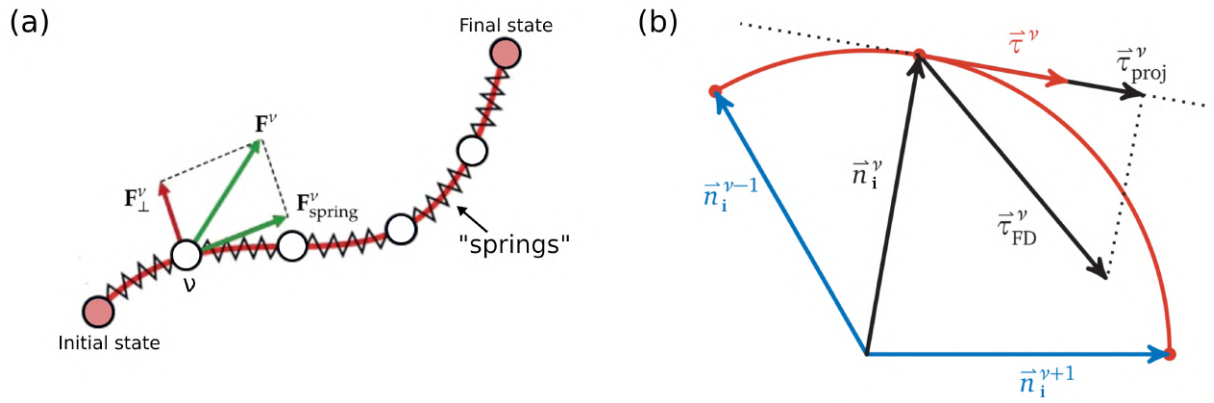

Figure 3.4 – (a) Illustration of nudged elastic-band method. Force vectors acting on the ν^{th} image are indicated. (b) Schematic illustration of the projection of the tangent vector for a single-spin system. Addapted from Refs. [37, 38]

The simplest estimate for the tangent vector is given by the forward-difference between adjacent images

$$\hat{\boldsymbol{\tau}}^{\nu}_{\text{FD}} = \frac{\boldsymbol{\mathcal{M}}^{\nu+1} - \boldsymbol{\mathcal{M}}^{\nu}}{\left|\boldsymbol{\mathcal{M}}^{\nu+1} - \boldsymbol{\mathcal{M}}^{\nu}\right|}. \tag{3.10}$$

Fig. 3.4 (b) illustrates the tangent vector for a single-spin system. Notice that, for the GNEB method, $\hat{\boldsymbol{\tau}}^{\nu}_{\text{FD}}$ has to be projected onto the tangent space so that it correctly points along the geodesic path. A given vector $\mathbf{A} = (\mathbf{A}_1,\ldots,\mathbf{A}_N)$ in $3N$ dimensions can be projected onto the tangent space by applying the projection operator $\mathcal{P}_{\mathcal{T}}$ [132], where

$$\mathcal{P}_{\mathcal{T}}\mathbf{A} = \left(\mathbf{A}^{\mathcal{T}}_1,\ldots,\mathbf{A}^{\mathcal{T}}_N\right), \tag{3.11}$$

with

$$\mathbf{A}^{\mathcal{T}}_i = \mathbf{A}_i - (\mathbf{A}_i \cdot \hat{\mathbf{n}}_i)\,\hat{\mathbf{n}}_i. \tag{3.12}$$

The projected tangent vector is then written as

$$\hat{\boldsymbol{\tau}}^{\nu}_{\text{proj}} = \mathcal{P}_{\mathcal{T}}\hat{\boldsymbol{\tau}}^{\nu}_{\text{FD}}, \tag{3.13}$$

which needs to be re-normalized after projection, resulting in $\hat{\boldsymbol{\tau}}^{\nu} = \hat{\boldsymbol{\tau}}^{\nu}_{\text{proj}}/|\hat{\boldsymbol{\tau}}^{\nu}_{\text{proj}}|$, as illustrated in Fig. 3.4 (b). Moreover, an improved tangent estimate can be calculated by using, e.g., both forward or backward difference of the two adjacent images, as discussed in Ref. [134]. Finally, the resultant force acting on the ν^{th} image is obtained by projecting Eq. (3.5), onto the tangent space

$$\mathbf{F}^{\nu}_{\text{GNEB}} = \mathcal{P}_{\mathcal{T}}\left(\mathbf{F}^{\nu}_{\perp} + \mathbf{F}^{\nu}_{\text{spring}}\right). \tag{3.14}$$

Notice that, since the GNEB provides a discrete representation of the MEP, the highest energy image may not be placed exactly on top of the SP, and the activation energy needs to be obtained through interpolation. In order to determine the maximum

energy accurately, the highest energy image can be treated separately, in the so-called **climbing image** (CI) method [135]. In the CI method, the spring forces acting on the highest energy image are deactivated during the iterative optimization, and the energy gradient force is inverted to point along the path. The resultant force acting on the CI becomes

$$\mathbf{F}^{CI}_{\text{GNEB}} = \mathcal{P}_{\mathcal{T}} \left[-\nabla E^{CI} + 2 \left(\nabla E^{CI} \cdot \hat{\boldsymbol{\tau}}^{CI} \right) \hat{\boldsymbol{\tau}}^{CI} \right]. \tag{3.15}$$

This procedure makes the image to move uphill in the energy landscape along the path. After the CI-GNEB calculation has converged, the position of the CI coincides with the SP along the MEP and gives an accurate value of the activation energy.

Part I

Skyrmionics in bulk chiral magnets

4 Nucleation of magnetic skyrmions from the conical phase

The inherent stability of magnetic skyrmions provided by their topological charge makes the study of skyrmionics feasible, and understanding the nature of their stability is key to the development of novel skyrmion-based devices. In this chapter, we explore the nucleation mechanism and stability of magnetic skyrmions in chiral magnetic materials. We perform minimum energy path (MEP) analysis [Sec. 3.2] and Atomistic Spin Dynamics (ASD) simulations [Sec. 3.1.2], based on experimental observations of the skyrmion formation, in order to understand the nucleation and spatial growth of the skyrmion phase. The results reveal that the skyrmion lattice (SKL) is formed from the conical (Con) phase progressively in small domains, with an activation barrier of several eV for the case of MnSi. Furthermore, we study the different nucleation mechanisms and the time evolution of the SkL formation in chiral magnetic thin films. We show that the Con → SkL phase transition is characterized by a rod-like (one-dimensional) nucleation, in agreement with experimental observations reported in literature, and reveal the interesting blinking (creation-annihilation) behavior of skyrmions close to the phase boundary between the two phases.

Part of the results presented in this chapter are published in Physical Review B, **102**, 104416. (2020).

4.1 Motivation

Magnetic skyrmions have garnered much attention as they show promise as bits in next generation memory devices [136]. A key ingredient for their stabilization is broken inversion symmetry, either in the underlying crystal lattice of bulk magnetic materials or in the interfaces of thin film heterostructures. This broken symmetry, combined with a strong spin-orbit coupling, produces the Dzyaloshinskii-Moriya interaction (DMI) [Sec. 2.3.3]. In chiral helimagnets such as MnSi and FeGe, the DMI competes

with the exchange interaction to produce three distinct magnetic phases below the Curie temperature, including the skyrmion lattice (SkL) [137–139]. The magnetic phase diagram of MnSi is illustrated in Fig. 2.11 (b). As discussed in Sec. 2.5, the SkL phase is bounded by first order transitions to the paramagnetic phase on the high temperature side and to the conical phase in all other directions of the field-temperature phase diagram.

Due to the skyrmions' inherent topological structure, there is an energy barrier for both the creation and destruction of the SkL from any non-topological phase (e.g. the conical, helical, or field-polarized ferromagnetic phases). As a result, the conical and the SkL phases are local minima of the free energy over a finite region of parameter space, giving rise to phenomena such as quench metastability and field history dependence [140–145]. The metastability gives rise to activated behavior reported for $Fe_{1-x}Co_xSi$ [146] and Zn-doped Cu_2OSeO_3 [147], and the activation barrier for the destruction of a metastable SkL in the latter compound was previously determined from time-dependent measurements [148]. Similarly, the activation barrier for single skyrmions in magnetic thin films have been predicted from theoretical calculations [149–152]. Understanding the nature of this topological energy barrier is an important step to the development of skyrmion-based applications.

Furthermore, time-dependent measurements of the SkL nucleation from the conical phase have been reported for $Co_8Zn_{10}Mn_2$ thin plates [153, 154], however, a complete description of the nucleation mechanism of the SkL in chiral magnets has not yet been fully established. Therefore, in the next sections, we employ a numerical analysis, based on experimental observations of the skyrmion formation, to both understand and quantify the activation energy for skyrmion nucleation and the microscopic dynamics of the phase transition itself.

4.2 Topological energy barrier for skyrmion formation

In this section, we will investigate the phase transition between the conic phase, which is a non-topological state, and the SkL phase, a topologically protected state. For this study, we will compare our numerical calculations with recent experimental observations of SkL nucleation in MnSi. As we will see below, experimental observations reveal an energy barrier for SkL phase nucleation, which our simulations will demonstrate to be directly related to the creation of the topological charge.

4.2.1 Experimental observations in MnSi

The formation of the skyrmion phase can be observed experimentally, for example, by means of small-angle neutron scattering (SANS) [155], where the hexagonal

modulation of the SkL is observed as peaks in the diffraction pattern. In this section, we focus in the SANS measurements of the SkL formation in MnSi reported in Ref. [39]. In the experiments, a sample of MnSi crystal was aligned with the [110] crystallographic direction parallel to both the applied field (which defines the orientation of skyrmion tubes) and the incident neutron beam. Fig. 4.1(a) illustrates a typical diffraction pattern observed in the experiments. This shows the sum of the scattered intensity as both the sample and applied field are rotated together to satisfy the Bragg condition for each of the six peaks [for extended discussion on the SANS technique we refer to Ref. [155]]. Essencialy, the diffraction pattern reveals a hexagonal modulation in the magnetic state, with periodicity of approximately 16 nm ($q \approx 0.38$ nm^{-1}), thus indicating the presence of the SkL phase. The total integrated Bragg peak intensity is proportional to the fraction of the sample volume within the SkL phase. Bragg peaks associated with the conical phase are not visible in this geometry, and therefore do not contribute to the scattering.

Figures 4.1(b) and 4.1(c) shows respectively a major and a minor hysteresis loop as a function of applied magnetic field observed in the experiments at $T = 28.1$ K. In both cases, the intensity was normalized by the maximal observed intensity, which corresponds to the entire sample being in the SkL phase. In the major hysteresis loop, the field was swept from 130 mT to 240 mT and back. Both end points are well inside the conical phase, and this loop covers the entire SkL phase. Here, a clear separation of the two sweep directions is observed, with the SkL volume fraction lagging in the direction the field is changing. Therefore, the hysteresis indicates that there is an energy barrier between the two magnetic phases, which is related to the creation and destruction of magnetic skyrmions. Such energy barrier characterizes the topological protection of the skyrmion phase.

To confirm hysteretic behavior, a series of minor loops were measured, each of which was centered on the high field phase transition into the conical state. Prior to each minor loop, the sample was cooled from the paramagnetic state to the measurement temperature in a constant field (205 mT), followed by a reduction of the field to the starting point. From here, minor hysteresis loops were recorded by raising the field to partially leave the SkL phase and then decreasing it to reenter. An example of a minor loop is show in Fig. 4.1(c). The minor loops show a clear nesting, quantified by the loop area which grows superlinearly as the loops become longer as shown in Fig. 4.1(d). Here the horizontal axis is the effective field sweep range ΔH_{eff}, defined as the separation between the two crossing points of the different field sweep directions illustrated in the inset of Fig. 4.1(c). Values for ΔH_{eff} and the loop area were determined by fits to the data described below, and the area was found to grow as a power law $\propto (\Delta H_{\text{eff}})^{1.45\pm0.1}$.

To quantify the activation barrier for skyrmion formation and destruction, the SANS hysteresis loops were analyzed using an adapted Preisach model. This is suitable

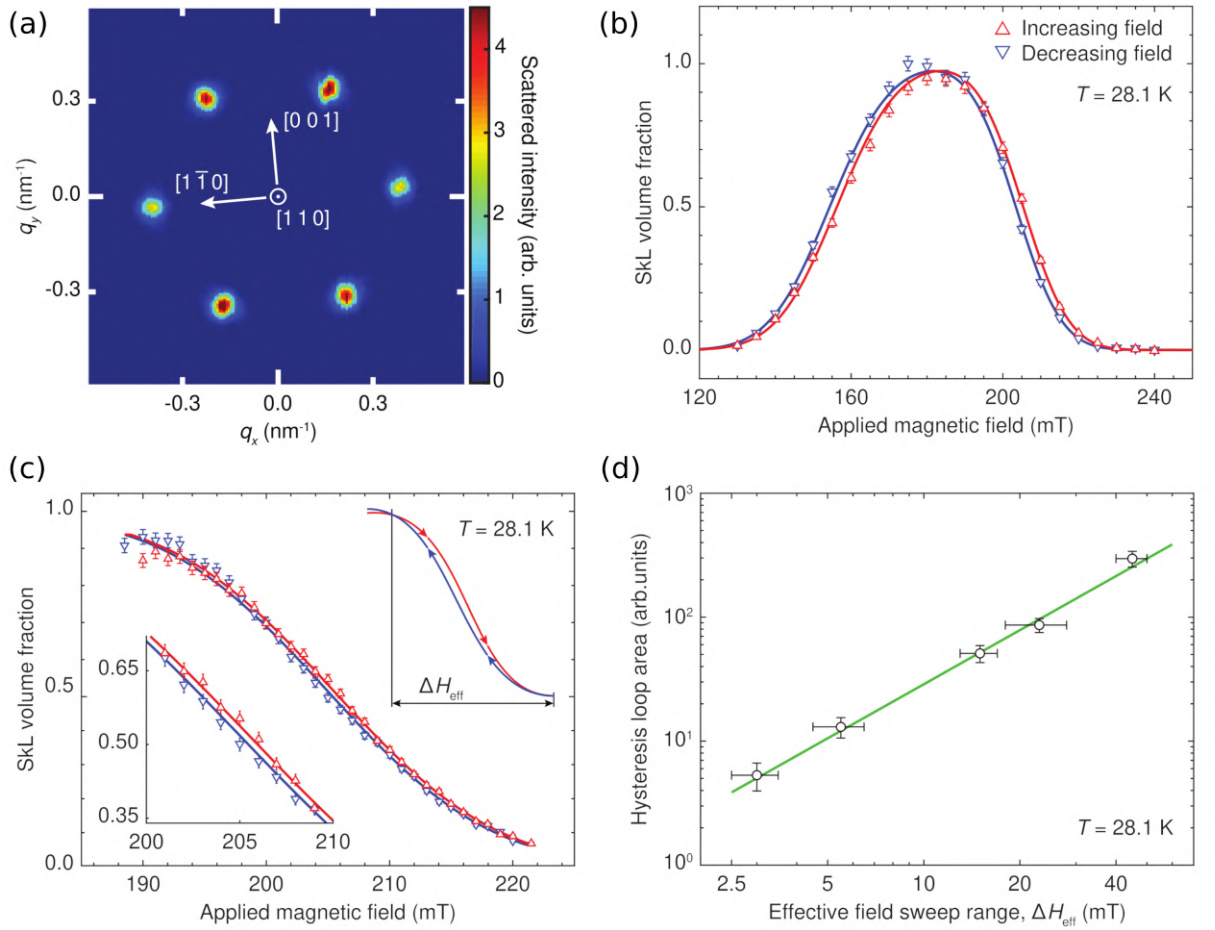

Figure 4.1 – (a) SANS diffraction pattern of the SkL of MnSi at $H = 195$ mT. This is a sum of measurements at different incident angles, with peaks on the horizontal axis appearing fainter as they were, on average, further from the Bragg condition. Background scattering near the detector center ($q = 0$) is masked off. (b) Major hysteresis loop for $T = 28.1$ K. (c) Minor hysteresis loop at the same temperature, centered around 205 mT and with an field sweep range of 33 mT. Symbols are the same as in panel (b). Bottom left inset: Expanded view of the central part of the loop. Top right inset: Schematic showing field sweep direction and effective sweep range ΔH_{eff}. Curves in (b) and (c) are fits to an adapted Preisach model described in the text. (d) Area of hysteresis loops as a function of the effective sweep range. Retrieved from Ref. [39].

for transitions in bistable systems, where two phases coexist as local free energy minima over some range of the external field [156]. In the region of bistability, the free energy F is assumed to be linearly proportional to the magnetic field B:

$$F(B,T,\ldots) = F(B_c,T,\ldots) \mp (X - X_0/2)(B - B_c). \tag{4.1}$$

Here, X is an order parameter with dimensions of a magnetic moment, used to distinguish the conical ($X = 0$) and skyrmion ($X = X_0$) phases. The sign of the second term in Eq. (4.1) corresponds to respectively the lower (-) and upper (+) transition between the SkL and conical phases. The Preisach free energy as a function of applied field is shown in Fig. 4.2 (a). A similar picture was previously proposed to describe

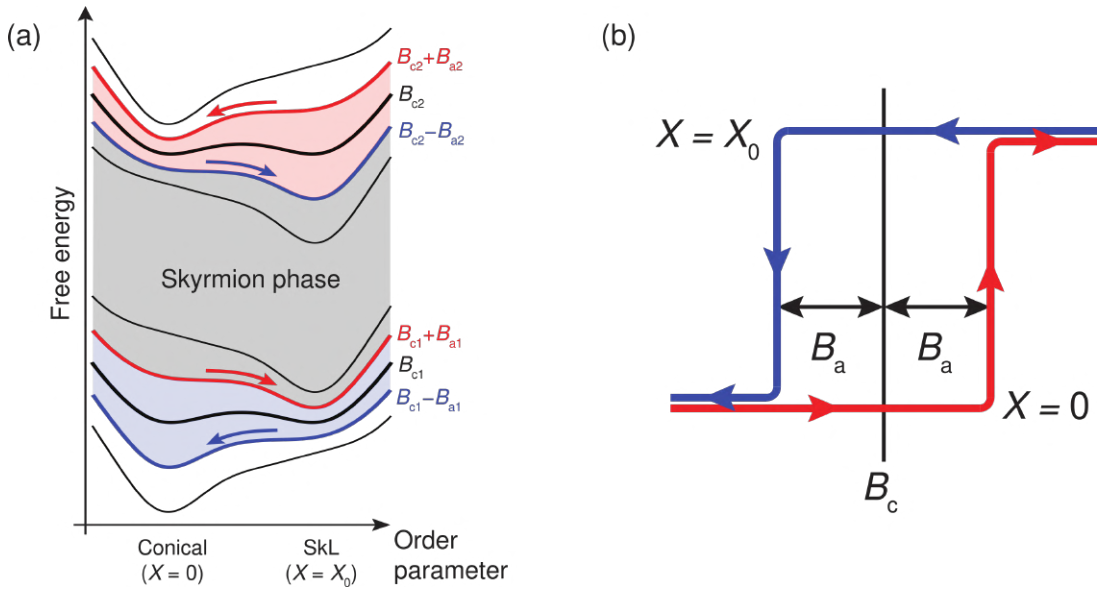

Figure 4.2 – Behavior of an individual Preisach unit. (a) Free energy for different values of the applied field. Black curves correspond to fields where the conical and SkL phases have the same energy. Red (blue) curves indicate the location of the phase transition for increasing (decreasing) field. (b) Hysteretic response of the order parameter. Retrieved from Ref. [39].

temperature-quenched metastable SkL phases in MnSi [143].

The low- and high-field transitions are treated independently, with each one governed by a pair of parameters: the critical field ($B_{c1/c2}$) where the two phases have the same free energy, and the height of the activation barrier ($B_{a1/a2}$) that inhibits the transition. As the external magnetic field is increased from zero and approaches the lower conical-to-SkL phase transition, the conical state free energy increases and the SkL state free energy decreases. At $B = B_{c1} + B_{a1}$, the conical phase minimum vanishes and the system transitions to the skyrmion phase. For decreasing fields, the transition occurs at $B = B_{c1} - B_{a1}$. Similarly, the upper SkL-to-conical transition occurs at $B = B_{c2} \pm B_{a2}$, where the situation is reversed and the conical and SkL free energies respectively decrease and increase with increasing field. The Preisach model is an inherently zero-temperature model, and a transition between the states only occur when one minima disappears and the system is no longer bistable. This is appropriate for the SkL as reported activation barriers are much greater than $k_B T$ [148] for $T \leq T_c$.

Preisach free energy curves produce perfectly rectangular hysteresis loops, centered around B_c and with width $2B_a$, as shown in Fig. 4.2(b). Rounded loops are obtained by considering the sample to be composed of microscopic, independently-acting, "Preisach units", each with its own $B_{c1/c2}$ and $B_{a1/a2}$. Since the magnetization is approximately linear across both the upper and lower field phase transitions [138], $B_{c1/c2}$ and $B_{a1/a2}$ are expressed in terms of the corresponding applied fields $H_{c1/c2}$ and $H_{a1/a2}$. To model the SANS hysteresis loops, Preisach units are assumed to follow a Gaussian

T (K)	$\overline{H}_{c1}$ (mT)	σ_{c1} (mT)	$\overline{H}_{a1}$ (mT)	$\overline{H}_{c2}$ (mT)	σ_{c2} (mT)	$\overline{H}_{a2}$ (mT)
27.8	188 ± 8	19 ± 2	1.1 ± 0.3	211 ± 3	14 ± 1	1.0 ± 0.2
28.1	155.3 ± 0.2	12.5 ± 0.2	0.94 ± 0.14	204.4 ± 0.2	9.5 ± 0.2	0.96 ± 0.12
28.4	168 ± 9	21 ± 3	1.0 ± 0.3	200 ± 6	19 ± 2	0.7 ± 0.3

Table 1 – Preisach parameters obtained from fits to major hysteresis loops. Uncertainties indicate the one sigma confidence interval provided by the fitting algorithm. Retrieved from Ref. [39].

distribution in both critical and activation fields. These distributions are characterized by their mean values ($\overline{H}_{c1/c2}, \overline{H}_{a1/a2}$) and standard deviations ($\sigma_{c1/c2}, \sigma_{a1/a2}$).

A fit to the major hysteresis loop for $T = 28.1$ K is shown in Fig. 4.1(b), and the resulting parameter values are summarized in Table 1. Values of $\sigma_{a1/a2}$ converge to zero during the fit, and this parameter was therefore eliminated. Differences between the fit and the data near the maximum SkL volume fraction [see Fig. 4.1(b)] are due to the Gaussian Preisach distribution used. A skewed distribution, introducing additional degrees of freedom, could improve the overall fit. However, the values of $\overline{H}_a$, which is the principal variable of interest, would most likely remain unchanged as they depend on the width of the hysteresis (separation of up- and down-sweeps) at half SkL volume fraction, where the current fits are very good.

As the two transitions are treated independently some Preisach units could, in principle, return to the conical phase before others have entered the SkL phase. At 28.1 K, where the separation of the transition fields is much greater than $\sigma_{c1/c2}$, this rarely occurs. However, at 27.8 K and 28.4 K the transitions overlap significantly, preventing the intensity from reaching the maximum at 28.1 K, which is reflected in the increased values of σ_{c1}/σ_{c2} [see Table 1]. More importantly, the good agreement between $\overline{H}_{a1}$ and $\overline{H}_{a2}$ supports a topological origin for the activation barrier which should be similar for both phase transitions. Further support for this conclusion comes from the comparable values of the activation fields at different temperatures. This indicates that the finite temperature range of the SKL phase is not due to a significant reduction of the activation barrier, but rather a convergence of the two critical fields as the energy separation between the conical and SkL phases is reduced.

While applying the Preisach model does not require prior knowledge about the nature of individual units, it is nonetheless relevant to consider their nature. In the original application to ferromagnetic hysteresis, magnetic domains behave sufficiently independent to be treated as Preisach units. By analogy, we anticipate that in the present case they correspond to microscopic SkL domains, within which the cascade of individual skyrmion formation occurs much faster than the measurement time. In this way, each domain experiences the phase transition quasi-instantaneously and independent of other domains [the time evolution of the SkL formation will be discussed

ΔH_{eff} (mT)	$\overline{H}_{c2}$ (mT)	σ_{c2} (mT)	$\overline{H}_{a2}$ (mT)
5.5 ± 1.0	203.6 ± 0.2	11.5 ± 0.2	0.18 ± 0.05
15 ± 2	204.8 ± 0.1	10.5 ± 0.1	0.16 ± 0.05
23 ± 5	205.1 ± 0.2	10.5 ± 0.1	0.25 ± 0.04

Table 2 – Preisach parameters obtained from minor hysteresis loops at $T = 28.1$ K (PSI). Retrieved from Ref. [39].

in more detail later in this chapter]. In such a scenario, variations of the local magnetic field due to crystal inhomogeneities and demagnetization effects give rise to a range of different transition fields and therefore a non-zero σ_c.

It is likely that both the distribution of SkL domains throughout the sample as well as their sizes depend on the field and temperature history, which may affect the activation barriers observed in the SANS experiments. To explore this possibility, Preisach model fits were performed on the minor hysteresis loops, where the initial configuration was obtained by a field cooling to the midpoint of the SkL-conical transition. In contrast, the major loop has a starting point entirely within the conical phase. The results of the minor loop fits are summarized in Table 2. While the values of $\overline{H}_{c2}$ agree with those obtained from the major loop, $\overline{H}_{a2}$ is reduced significantly, confirming that the barrier to create or destroy SkL domains depends on the field history. We return to this point later.

4.2.2 Theoretical modeling for the nucleation of the skyrmion-lattice

To complement the SANS data, we next perform atomistic spin dynamics simulations to investigate the transition between the conical and SkL states using a homemade simulation code [151] as well as the *Spirit* package [38]. The extended Heisenberg Hamiltonian that describes the system of classical spins can be written as [Sec. 3.1.2]

$$\begin{aligned}\mathcal{H} = &- J_{\text{ex}} \sum_{\langle i,j \rangle} \mathbf{n}_i \cdot \mathbf{n}_j - \sum_{\langle i,j \rangle} \mathbf{D}_{ij} \cdot (\mathbf{n}_i \times \mathbf{n}_j) \\ &- \sum_i \mu \mathbf{B} \cdot \mathbf{n}_i,\end{aligned} \tag{4.2}$$

where $\boldsymbol{\mu}_i$ is the magnetic moment of the i^{th} atomic site with $|\boldsymbol{\mu}_i| = \mu$, and $\mathbf{n}_i = \boldsymbol{\mu}_i/\mu$ is the i^{th} spin orientation. Here J_{ex} represents the first-neighbours exchange coupling, $\mathbf{D}_{ij}$ is the DMI vector, $\mathbf{B}$ is the perpendicular external magnetic field, and $\langle i,j \rangle$ denotes pairs of nearest-neighbour spins i and j. For the simulations we adopt parameters $J_{\text{ex}} = 1$ meV and $D = 0.18 J_{\text{ex}}$, which are reasonable values for MnSi [157, 158]. Although intrinsic exchange and cubic anisotropies [159] may define a preferential direction for the spin rotation in MnSi at zero field, such high-order contributions are much weaker than the energy terms in Eq. (4.2) and are therefore neglected in the calculations. Similarly, the

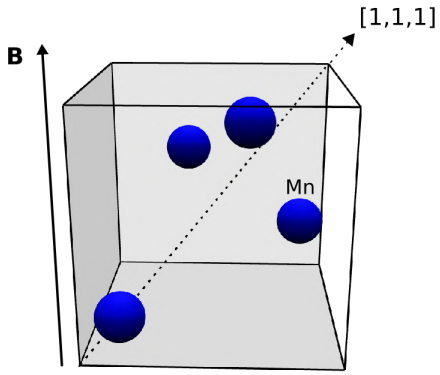

Figure 4.3 – Unit cell of the B20-structure of MnSi showing only the location of the Manganese atoms. The magnetic field **B** is applied along the [001] direction.

small contribution from a dipolar interaction is also not included [160, 161]. The dynamics of the spin system is governed by the Landau-Lifshitz-Gilbert equation [Sec. 2.2]

$$\frac{\partial \mathbf{n}_i}{\partial t} = -\frac{\gamma}{(1+\alpha^2)\mu_i}\left[\mathbf{n}_i \times \mathbf{B}_i^{\text{eff}} + \alpha \mathbf{n}_i \times (\mathbf{n}_i \times \mathbf{B}_i^{\text{eff}})\right], \tag{4.3}$$

where γ is the electron gyromagnetic ratio, α is the damping parameter and $\mathbf{B}_i^{\text{eff}} = -\partial\mathcal{H}/\partial\mathbf{n}_i$ is the effective field.

The MnSi crystal, shown in Fig. 4.3, consists of a B20 structure (space-group $P2_13$) with four Mn atoms and four Si atoms located at the 4(a)-type sites of the simple-cubic unit cell with position coordinates (u, u, u), $(0.5+u, 0.5-u, -u)$, $(-u, 0.5+u, 0.5-u)$, and $(0.5-u, -u, 0.5+u)$, where $u_{\text{Mn}} = 0.137$ and $u_{\text{Si}} = 0.845$ [162]. For the simulations, only Mn magnetic moments are considered. The spin dynamics simulations were performed in a mesh of $N \times \sqrt{3}N \times N$ unit cells with $N = 26$, which fits a periodic cell of a triangular lattice of skyrmions, consisting of two skyrmion tubes located at respectively the center and corners of the simulation box. The choice of N was verified to minimizes the SkL energy. Periodic boundary conditions are considered along the three dimensions. To obtain the ground state of the spin model, the energy of the considered states are minimized for different values of the applied field $\mathbf{B} \parallel [001]$. The choice of field direction parallel to one of the unit cell main axes ensures that skyrmions form as uniform tubes within the simulation box. However, the direction of the applied field is not expected to have much impact on the energetics as long as a high-symmetry direction of the crystal is chosen. Figure 4.4(a) shows the energy obtained in the simulations for the field-polarized ferromagnetic, conical and SkL states, from where the ground state is found to be conical for $\mu B < 0.007 J_{\text{ex}}$ and $0.018 J_{\text{ex}} < \mu B < 0.028 J_{\text{ex}}$, SkL for $0.007 J_{\text{ex}} < \mu B < 0.018 J_{\text{ex}}$, and field-polarized ferromagnetic for $\mu B > 0.028 J_{\text{ex}}$.

Next, the transition between conical and SkL states is considered. At the critical fields $\mu B_{c1} = 0.007 J_{\text{ex}}$ and $\mu B_{c2} = 0.018 J_{\text{ex}}$, both states have approximately the same energy. The activation barrier between the two states can be calculated by the geodesic

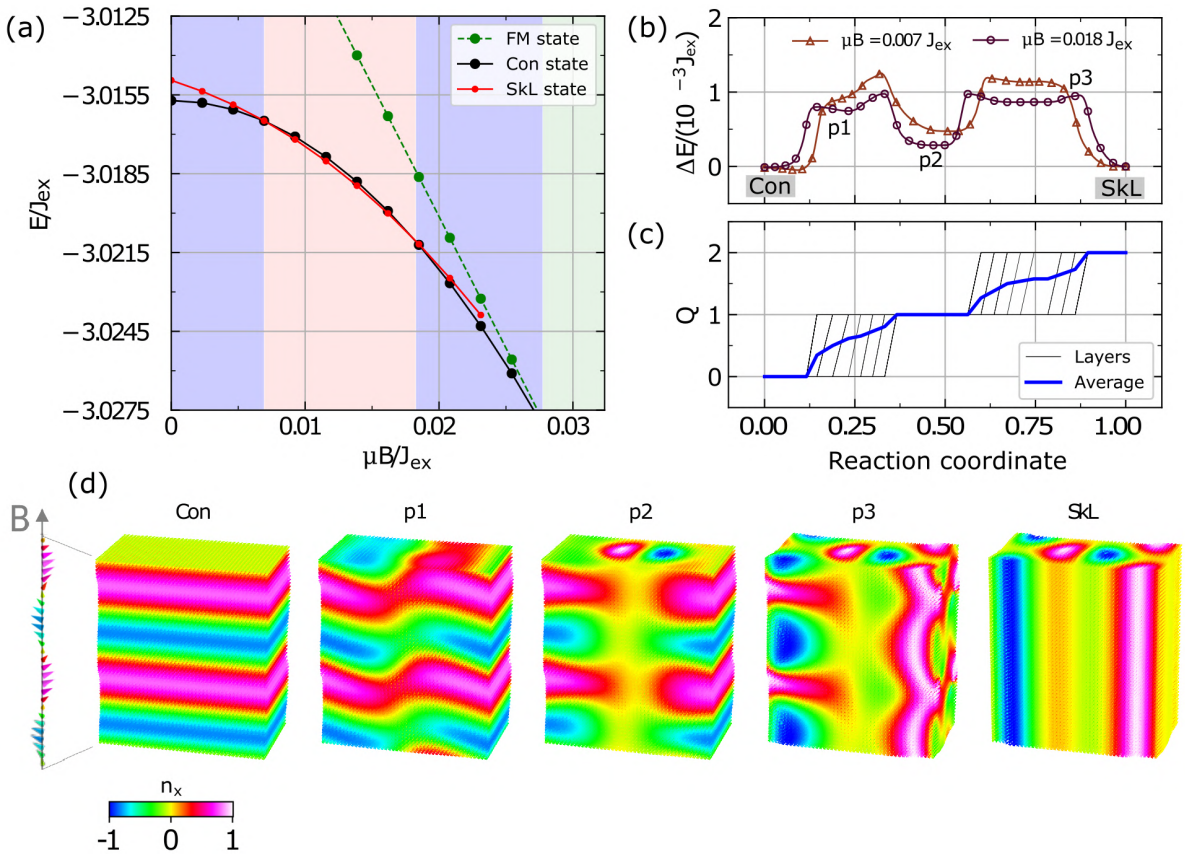

Figure 4.4 – (a) Energy per spin vs applied field for each state. The ground state is indicated by the colored shading with blue for the conical (Con) state, red for the SkL and green for the field-polarized ferromagnetic (FM) state. (b) Minimal energy path between conical and SkL states for $\mu B = 0.007 J_{ex}$ and $\mu B = 0.018 J_{ex}$. (c) Topological charge as a function of the reaction coordinate for $\mu B = 0.018 J_{ex}$. (d) Spin configurations in a $N \times \sqrt{3}N \times 2N$ mesh along the formation path for $\mu B = 0.018 J_{ex}$, as indicated in panel (b). Retrieved from Ref. [39].

nudged elastic band (GNEB) method [see Sec. 3.2] and a climbing image method [134], allowing a precise determination of the highest energy saddle point along the minimal energy path connecting the two states. Here, the reaction coordinate defines the normalized (geodesic) displacement along the formation path. Figure. 4.4(b) shows the activation barrier calculated between the two states in both critical fields. From this one finds that it is energetically favorable to break the conical state locally in different stages, nucleating the skyrmions individually instead of the whole lattice at once. Figure 4.4(c) shows the topological charge, given by [136]

$$Q = \frac{1}{4\pi} \int \mathbf{n} \cdot \left(\frac{\partial \mathbf{n}}{\partial x} \times \frac{\partial \mathbf{n}}{\partial y} \right) dx\, dy, \tag{4.4}$$

calculated along the formation path for each xy-layer of the sample for $B = B_{c2}$. Notice that the tube of the first skyrmion is formed gradually, layer-by-layer, in a conical background and the average topological charge approaches $Q = 1$, giving rise to the first elongated maximum in the minimal energy path. This is consistent with previous

works suggesting that skyrmions are nucleated or annihilated by the formation and subsequent motion of Bloch points (magnetic monopoles) [163–165]. After that, the second skyrmion is formed in a similar way, after which the average topological charge approaches $Q = 2$ and the transition is complete. Energetically equivalent paths were obtained for the first skyrmion nucleating either at the center or the corners.

As recognized previously, the transitions between the SkL and conical states are not expected to occur in a spatially homogeneous fashion. As a result, the average energy per spin necessary to nucleate a single skyrmion depends on the lateral size of the domains. An estimate of the activation barrier can be obtained by comparing the energy separation $\Delta E_a = |E_{\mathrm{SkL}} - E_{\mathrm{Con}}|$ of the SkL and conical states near the critical field, due to an activation field B_a equivalent to the one obtained from the SANS experiments. Adjusting for the difference between the transition fields obtained experimentally and from the simulations one finds $B_a \approx (B_{c2} - B_{c1})/50 \approx 2 \times 10^{-4} J_{\mathrm{ex}}/\mu$, and from there $\Delta E_a \approx 10^{-5} J_{\mathrm{ex}}$. This value is roughly two orders of magnitude smaller than the activation energy calculated in the GNEB simulation where the SkL was formed in two steps. Therefore, to nucleate one skyrmion with a 100 times smaller activation field in the simulations we need to consider a phase transition that occurs in 100 times as many steps as previously. This is exactly equivalent to using a 100 times larger simulation box, as the activation energy is given by the number of skyrmion nucleations per area. Considering the SkL periodicity of 19 nm in MnSi [137], this corresponds to skyrmion domains of order $\sim 0.05\ \mu\mathrm{m}^2$. This is the same order of magnitude as the correlation length determined directly from the SANS experiments [39].

As the formation barrier for the individual skyrmions along the reaction coordinate are all roughly the same height (see Fig. 4.4(b)), once the system has sufficient energy to overcome the initial barrier skyrmions will continue to nucleate until defects or demagnetization makes it energetically unfavorable. This limits the size of the SkL domains, and we speculate that this mechanism is responsible for the discrete Preisach units observed in the SANS measurements. In contrast, the change of SkL volume fraction for the minor hysteresis loops is due to the expansion/reduction of already present domains formed during the field cooling. This results in a smaller activation barrier, which persists since the crystal never reaches a fully saturated conical or SkL phase throughout the minor loop. Spatially resolved measurements would be required to confirm this picture.

The topological energy barrier for each skyrmion can be estimated by multiplying ΔE_a by the number of spins within a SkL unit cell, and increasing the length of the skyrmions in the simulations to the thickness of the single crystal used in the SANS experiments. Using the above relationship between B_a and J_{ex}/μ with $\mu = 0.4\mu_B$ [166], this yields $\Delta E_a \approx 7$ eV per skyrmion. By the nature in which it was obtained, the

activation energy above should be considered as an estimate rather than an exact value.

4.3 Kinetics of skyrmion nucleation from the conical phase

As discussed in the previous section, it is well known that magnetic skyrmions can emerge from the conical phase as the system is excited by the appropriate applied field and temperature. The ultrafast spin rotation along the phase transition is, however, a challenge for experimental observations. Recent work has shown the time evolution of skyrmion nucleation from the conical phase in thin plates of $Co_8Zn_{10}Mn_2$ [153, 154], nevertheless, the kinetics of such a phase transition is not fully understood. Therefore, in this section we investigate the dynamical mechanism for the magnetic skyrmion nucleation from the conical phase in chiral magnetic films.

To investigate the different stages of the phase transformation in more detail, we perform spin dynamics simulations of the transition between the conical and SkL states. For that purpose we make use of the extended Heisenberg Hamiltonian that describes the system of classical spins, as written in Eq. (4.2). For the simulations we adopt a spin-system parametrized by the exchange interaction $J_{\text{ex}} = 1$ meV. The helix period at zero field L_D is defined by the ratio $D/J_{\text{ex}} = \tan(2\pi/N_s)$, where N_s is the number of spin sites along one period. For the simulations, we consider $N_s = 16$, which leads to $D = 0.41 J_{\text{ex}}$. The dynamics of the spin system is governed by the Landau-Lifshitz-Gilbert (LLG) equation [Eq. (4.3)]. In addition to LLG, fast energy minimizations are performed using the Verlet-like velocity projection method, as explained in Refs. [38, 132], which accelerates convergence towards local minima and avoids overstepping due to momentum considered in the standard LLG equation [167, 168]. In this method the spins are treated as massive particles moving on the surfaces of spheres, where the velocity at each time step is damped by projecting it along the force $\mathbf{F}_i = -\partial\mathcal{H}/\partial\mathbf{n}_i$ and $\mathbf{n}_i$ is renormalized after each iteration in order to conserve the magnitude of the spins. For the simulations we make use of the simulation package *Spirit* [38].

4.3.1 Mechanisms for skyrmion nucleation

Before investigating the nucleation mechanisms of the skyrmion phase, let us first calculate the magnetic ground states of the considered spin-system. For the simulations, we consider a sample of $160 \times 138 \times 16$ spin sites, with periodic boundary conditions along x and y directions. Contrary to Sec. 4.2.2, open boundary conditions are set along the z direction, such that the thickness of the magnetic film corresponds to $d = L_D$. Fig. 4.5(a) shows the energy density profiles obtained in the simulations for the considered magnetic phases: helix (HL), conical (Con), skyrmion lattice (SkL) and out-of-plane ferromagnetic (FM). The magnetic ground state was found to be HL

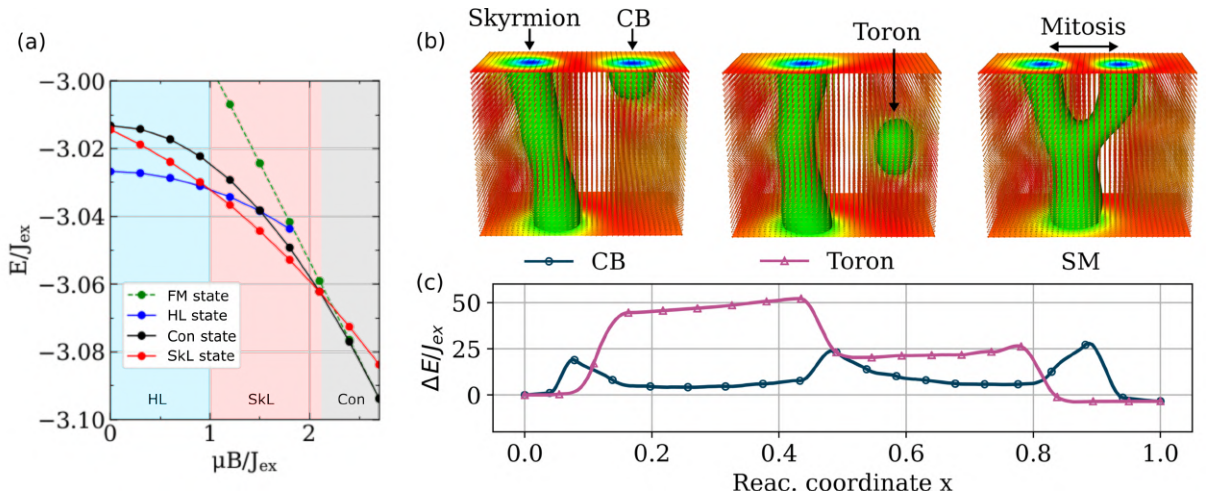

Figure 4.5 – (a) Energy per spin site obtained in the simulations for the four considered magnetic phases: helix (HL), conical (Con), skyrmion lattice (SkL), and out-of-plane ferromagnetic (FM), as a function of the out-of-plane applied field. (b) Snapshots of three distinct nucleation mechanisms for the skyrmion formation [chiral bobber (CB), toron, and the skyrmion mitosis (SM)]. (c) Minimal energy paths for different nucleation mechanisms, for magnetic film thickness $d = 2L_D$. Here, $x = 0$ corresponds to a single skyrmion-tube and $x = 1$ corresponds to two fully formed skyrmions. The three peaks along the formation path in the CB case correspond to the nucleation of CB at the top surface, nucleation of CB at the bottom surface, and the connection of bobbers into the new skyrmion-tube, respectively. The path along SM state was found to be unstable. Results obtained for $\mu B/J_{ex} = 2$.

for $\mu B/J_{ex} < 1$, SkL for $1 < \mu B/J_{ex} < 2.3$, Con for $2.3 < \mu B/J_{ex} < 2.6$, and FM for $\mu B/J_{ex} > 2.6$.

Next, we focus on the transition between conical and SkL states. To model the SkL growth from the conical phase, we fixed the applied field at $\mu B/J_{ex} = 2$, where the Con phase is metastable and the SkL is the ground state. The rate at which skyrmions nucleate is related to the activation energy between the states before and after nucleation. The activation energy can be calculated by the geodesic nudged elastic band (GNEB) method [132, 151] together with the climbing image method [134], both implemented in the *Spirit* package. Such methods allow the precise determination of the highest energy saddle point along the minimal energy path connecting the two states, where the reaction coordinate, x, defines the normalized (geodesic) displacement along the formation path. In general, the transition between the two phases can be mediated by different intermediate states. Here, we have considered the following: (i) the formation of chiral bobbers (CB) [153, 169, 170], (ii) the formation of torons [169], and (iii) the formation of Y-shaped skyrmion tubes during skyrmion mitosis (SM) [153]. Fig. 4.5 (b) illustrates the considered intermediate states. For the magnetic film of thickness $d = L_D$, as considered above, only the CB mechanism is stable along the minimal energy path. However, as discussed in Ref. [169], the surface effects play important role in the stabilization of skyrmion tubes in a conical background. Particularly, the formation

of torons is favored by increasing the ratio d/L_D. Therefore, we considered a thicker magnetic film, with $d = 2L_D$. In this case, toron nucleation path can be stabilized, but the CB nucleation is still the energetically favorable mechanism for skyrmion formation, as shown by the lower activation energy in the minimal energy paths in Fig. 4.5 (c). The path along the skyrmion mitosis (the Y-shaped skyrmion) was unstable for the two considered thicknesses, where in both cases the formation path collapsed into CB formation. Therefore, for magnetic films of thickness $d \leq 2L_D$, as that considered in Refs. [153, 154], we expect the preferential intermediate state for skyrmion nucleation to correspond to CBs instead of torons or Y-shaped skyrmion tubes. For now on, we therefore focus on the formation of CBs to study the mechanism for skyrmion nucleation in chiral magnetic thin films.

4.3.2 Activation energy for chiral bobber nucleation

The activation energy for the skyrmion formation depends on both the applied magnetic field and on the material parameters such as film thickness. Fig. 4.6 (a) shows the minimal energy paths for the nucleation of a single skyrmion from the conical phase for different film thickness d, at fixed field $\mu B/J_{ex} = 2.0$. The first and second peak along the formation paths correspond to the nucleation of the Bloch points of CBs at the top and bottom surfaces. Each CB can be represented as a hemisphere [169] of diameter L_D and thickness $L_D/2$, therefore, for $d/L_D > 1$ a third peak along the formation path corresponds to the connection of the chiral bobbers into the skyrmion tube. Fig. 4.6 (b) shows the minimal energy paths for skyrmion nucleation for fixed film thickness $d/L_D = 1.5$, but at different values of applied field. Notice that by varying either the film thickness or applied field one can cross the phase boundary between the

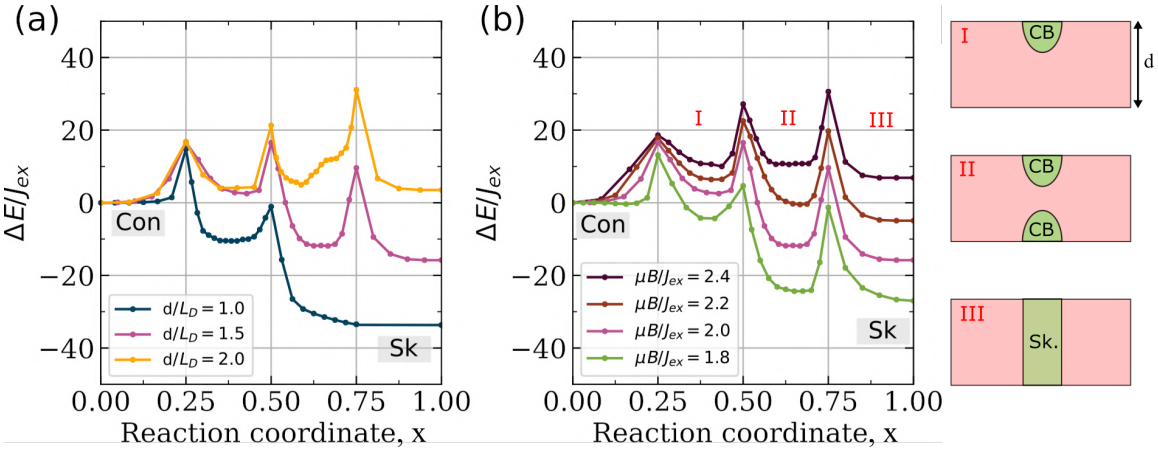

Figure 4.6 – (a,b) Minimal energy path for the nucleation of a single skyrmion from the conical phase for (a) different film thickness d, at fixed field $\mu B/J_{ex} = 2.0$, and (b) different values of the applied field, for fixed film thickness $d/L_D = 1.5$. Insets show the stages of the phase transition, with chiral bobbers (CBs) nucleating at the top and bottom surfaces before connecting to form the skyrmion (Sk) tube.

conical ($x = 0$) and skyrmion ($x = 1$) phases, i.e., $E_{\mathrm{Con}} - E_{\mathrm{sk}}$ changes sign.

4.3.3 Time evolution of skyrmion-lattice nucleation

When the conical spin-system is subjected to thermal excitation high enough to overcome the activation energy for the skyrmion nucleation, the phase transition takes place. The SkL phase grows with the nucleation of multiple skyrmions, and a collective dynamics governs the evolution of the phase transition. In our numerical study, to simulate the SkL phase growth, the spin system is therefore initialized in the conical phase, and by performing spin dynamics simulations based on stochastic Landau-Lifshitz-Gilbert (LLG) equation [38], the skyrmions are allowed to nucleate and occupy the sample. For the simulations, we consider a magnetic film of thickness $d = L_D$, which activation energies for skyrmion nucleation are shown in Fig. 4.7 (a), for different values of the applied field. Fig. 4.7 (b-c) shows the topological charge $Q = \frac{1}{4\pi}\int \mathbf{n}\cdot\left(\frac{\partial \mathbf{n}}{\partial x}\times\frac{\partial \mathbf{n}}{\partial y}\right)dxdy$ calculated at the film surface as a function of the simulation time, for (b) different values of applied field and fixed temperature, and (c) different temperatures and fixed field. Observe that the SkL phase growth is characterized by the fast nucleation of skyrmions at the beginning of the transformation followed by a reduction of nucleation rate until saturation at the optimal skyrmion-density for the considered parameters.

In fact, in Ref. [154] the authors show, by means of *in situ* Lorentz transmission electron microscopy (LTEM) images of the magnetic states in a $Co_8Zn_10Mn_2$ thin plate, that the SkL growth from the conical phase satisfy the Johnson-Mehl-Avrami-Kolmogorov (JMAK) model for phase transitions [171, 172]. The JMAK formula that describes the time evolution of the SkL phase fraction F_{sk} can be written as

$$F_{sk}(t) = 1 - \exp(-[k(t - t_0)]^n), \tag{4.5}$$

where t_0 is the time at which the phase transition starts, k is the overall reaction rate and n is the so-called Avrami constant. The value of n represents the dimensionality of the crystal growth, with $n = 1$, 2, and 3 corresponding to rod-like (1D), disc-like (2D), and spherical (3D) crystal growth, respectively. By taking the logarithm on both sides of the above equation, we obtain

$$\ln[-\ln(1 - F_{sk}(t))] = n\ln(k) + n\ln(t - t_0), \tag{4.6}$$

from where the Avrami number can be estimated by calculating the slope of $\ln[-\ln(1 - F_{sk}(t))]$ *vs* $\ln(t - t_0)$.

In our simulations, the SkL phase fraction can be defined as $F_{\mathrm{sk}}(t) \equiv Q(t)/Q_{\mathrm{sat}}$, where Q_{sat} is the saturation topological charge and gives the maximum number of skyrmions in the sample. Fig. 4.7 (d) shows the plot of $\ln[-\ln(1 - F_{\mathrm{sk}})]$ *vs* $\ln(t - t_0)$, with

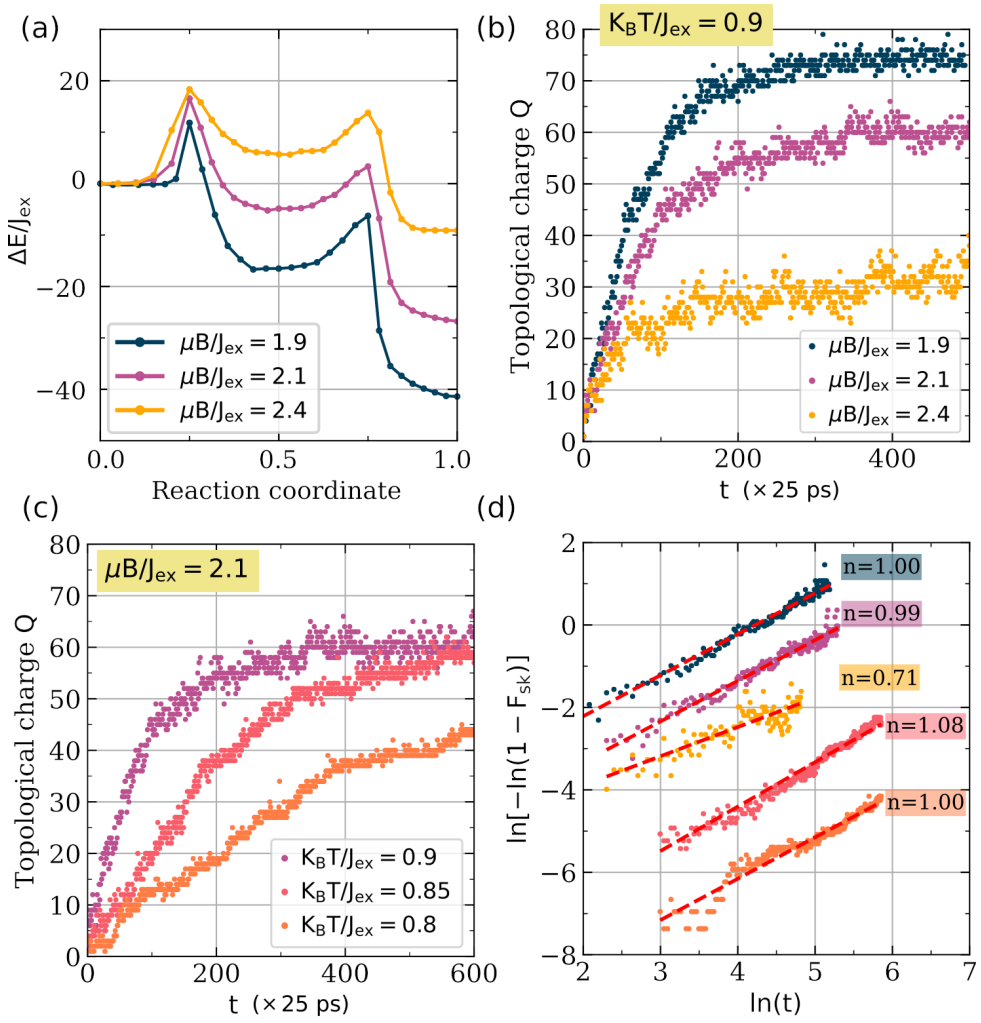

Figure 4.7 – Numerical simulation of SkL phase growth from conical phase. (a) Activation energy for skyrmion nucleation at different values of applied field, for $d = L_D$. (b-c) Topological charge Q at the film surface as a function of time, for the simulation of SkL nucleation from the conical phase, for (b) different values of applied field and fixed temperature $K_BT/J_{ex} = 0.9$, and (c) different temperatures and fixed field $\mu B/J_{ex} = 2.1$. (d) Correspondent avrami number n obtained by linear fitting of $\ln[-\ln(1 - F_{sk})]$ *vs* $\ln(t)$.

$t_0 = 0$, obtained in the simulations, from where we can extract the Avrami constant $n \approx 1$ for most of the considered parameters, which is in agreement with the experimentally observed in Ref. [154]. The SkL growth is therefore characterized by a rod-like (1D) nucleation that can be attributed to the cylindrical growth of individual skyrmions from the film surface, and the speed of the phase transition is limited by the formation of individual skyrmion-tubes.

Observe that for $K_BT/J_{ex} = 0.9$ and $\mu B/J_{ex} = 2.4$ the obtained Avrami number ($n = 0.71$) is significantly lower than unity. The reduced value of Avrami number indicates a sluggish nature of the nucleation process, which in this case we attribute to the consecutive nucleation and collapse of the skyrmions. Such process is favored when the system is close to the phase boundary between the SkL and Con states, as discussed

in more detail in the following sections.

4.3.4 Nonuniform nucleation rates

When the value of activation energy for skyrmion nucleation is not uniform throughout the sample, either due to nonuniformity of magnetic parameters, or due to some extra phenomena that takes place during the SkL growth, e.g., the rearrangement of already-nucleated skyrmions, a change in the overall SkL nucleation rate can occur. In fact, in Ref. [154] the authors report a reduced value of Avrami number at later stages of the Con → SkL transformation. Here we show that the growth mechanism of the SkL phase can be treated as rod-like (1D) in all stages of the transformation. In fact, in the JMAK formula, the reaction rate is represented by the parameter k. Therefore, a reduction in the skyrmion nucleation rate, or skyrmion formation driving force (out of the expected saturation) implies that k is not constant. Therefore, let us now assume that the dimentionality of the phase growth is 1D, i.e. $n = 1$ along the whole phase transition, but the value of k changes during the prosess. The JMAK formula with $n = 1$ and for the phase growth starting at $t_0 = 0$ is given by

$$F_{sk} = 1 - \exp(-kt). \tag{4.7}$$

If the value of k changes from k_1 to k_2 at a time $t = t_1$ along the growth process, Eq. (4.7) can be rewritten as

$$F_{sk}(t) = \begin{cases} 1 - \exp(-k_1 t) & \text{, if } t < t_1 \\ 1 - \exp(-k_1 t_1 - k_2(t - t_1)) & \text{, if } t \geq t_1. \end{cases} \tag{4.8}$$

Fig. 4.8 (a) shows the plot of $F_{sk}(t)$ obtained from Eq. (4.8) with $k_1 = 0.5$, $k_2 = 0.1$ and $t_1 = 2$ s. Notice that the change in k induces a reduction in the overall slope of

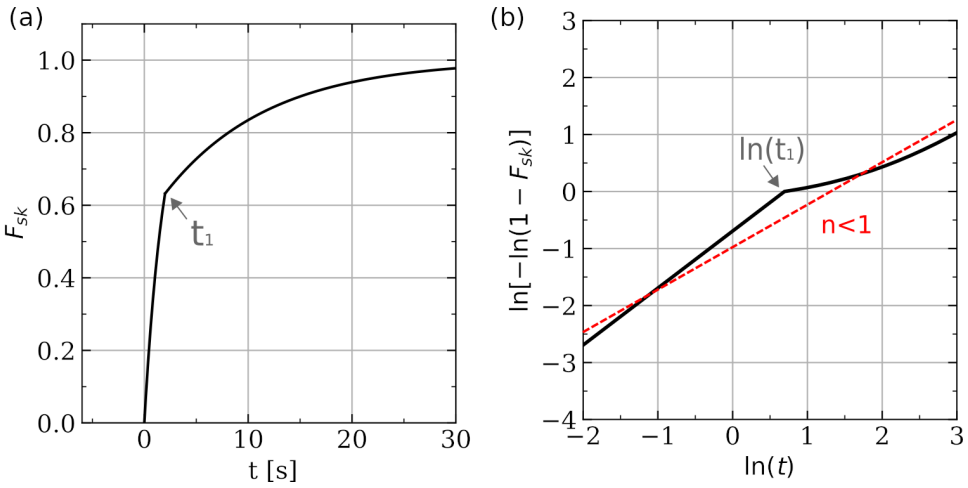

Figure 4.8 – (a) Plot of F_{sk} *vs* t obtained from Eq. (4.8) with $k_1 = 0.5$, $k_2 = 0.1$ and $t_1 = 2$ s. (b) Plot of $\ln[-\ln(1 - F_{sk}(t))]$ *vs* $\ln(t)$ correspondent to (a). Here, the dashed line represents the linear fitting, which results in $n < 1$, even though 1D nucleation is assumed.

$\ln[-\ln(1-F_{sk}(t))]$ *vs* $\ln(t)$ [Fig. 4.8 (b)], similar to that observed in Ref. [154], even though 1D nucleation is assumed. Therefore, extracting the Avrami constant from the slope of $\ln[-\ln(1-F_{sk}(t))]$ *vs* $\ln(t)$ can be misleading when the phase transition experiences a change in the nucleation rate, either due to nonuniformities in the sample or due to some extra phenomena that takes place during the transformation.

4.3.5 Skyrmion blinking

Notice that the SkL formation process can be characterized by a combination of skyrmions (and/or chiral bobbers) nucleation and collapse as shown, e.g., by the oscillations of the topological charge in Fig. 4.7 (b-c). This blinking behavior (creation-destruction process) is favored by the local stability of an intermediate state between the conical and skyrmion phase, which breaks the nucleation process into stages with lower energy cost when compared to the homogeneous nucleation. Once at the intermediate state, the energy barrier for the system to transit to the skyrmion phase can be similar to the barrier to return to the conical phase, as indicated in Fig. 4.9 (a). This leads to sequential instances of formation and collapse of CBs and skyrmions during the formation of the lattice, seen in the simulations and illustrated in Fig. 4.9 (b). Such blinking behavior is favored when the system is close to the phase boundary between the SkL and Con states.

To investigate the nucleation process in more detail, we consider a smaller simulation box which can accommodate a maximum of two skyrmions only. The spin system is initialized in the conical phase and, by performing spin dynamics simulations based on stochastic LLG, the skyrmions are allowed to nucleate and occupy the sample. Fig. 4.9 (c) shows the topological charge calculated at the film surface as a function of the simulation time for different values of applied field. Notice that, for $\mu B/J_{ex} = 2.4$ all the nucleated CBs collapse [in the considered time window], and the system can not develop to the full SkL phase. On the other hand, for $\mu B/J_{ex} = 1.8$ the nucleated CBs rarely collapse and the system quickly transitions to the SkL phase. The number of CB nucleations therefore increases with respect to the number of collapses as soon as we change the applied field from $\mu B/J_{ex} = 2.4$ to 1.8, favouring the SkL formation, as shown by the histograms in Fig. 4.9 (c). A high number of CB collapses therefore results in a sluggish nature of the nucleation process, as observed for $\mu B/J_{\mathrm{ex}} = 2.4$ in Fig. 4.7 (b).

The switching between skyrmionic and non-topological states has been proposed as a bit operation for information storage [173]. Understanding the temperature-, thickness- and field-dependence of the blinking behavior of magnetic skyrmions may be crucial to the development of novel technological applications. We therefore expect that the results presented in this section can motivate new research in the topic.

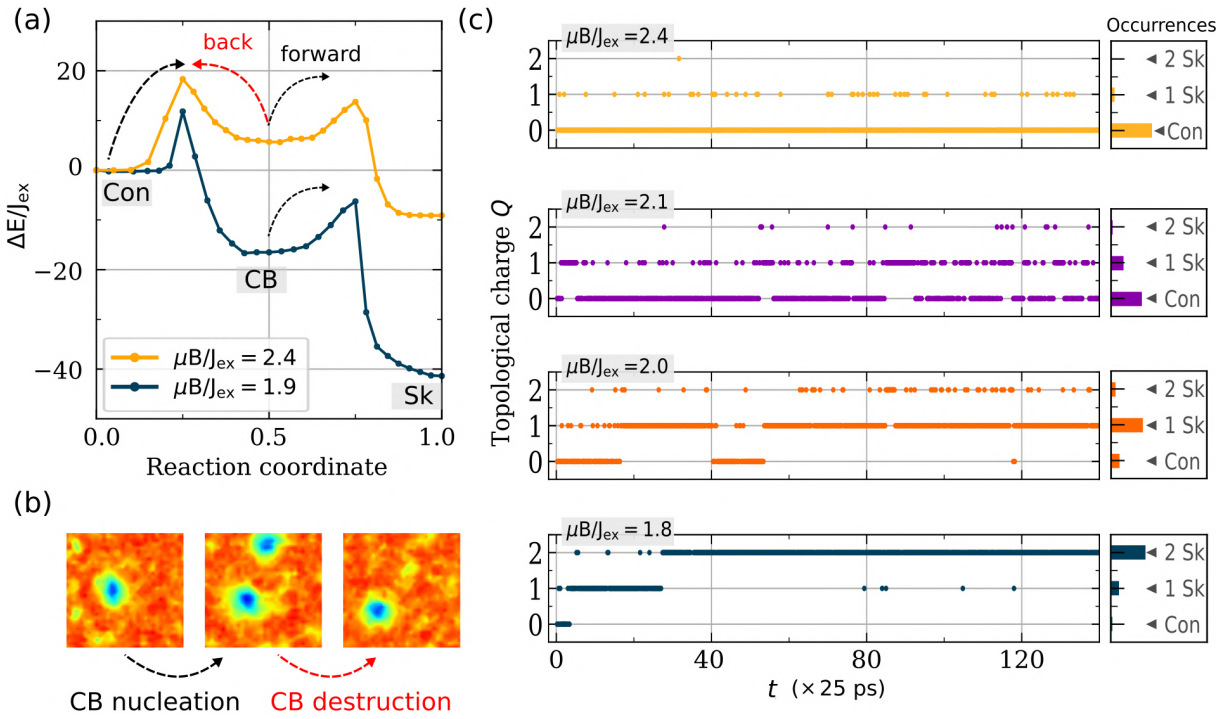

Figure 4.9 – (a) Activation energy for skyrmion nucleation at different values of applied field, for $d/L_D = 1.0$. At higher field, the energy barrier for the CB to transit to the skyrmion phase is similar to the barrier to return to the conical phase. (b) Snapshots of blinking behavior of a chiral bobber, obtained in the spin-dynamics simulations for $\mu B/J_{ex} = 2.0$. (c) Topological charge Q calculated at the film surface as a function of the simulation time, for different values of applied field. Histograms in the right show the number of occurrences of the states $Q = 0$ (Con phase), $Q = 1$ (single skyrmion) and $Q = 2$ (two skyrmions). Here $d/L_D = 1.0$ and $K_BT/J_{ex} = 1.0$.

4.4 Conclusion of the chapter

We performed atomistic spin simulations to study the Conical (Con) to Skyrmion-lattice (SkL) phase transition in chiral magnetic films. Comparing the simulations with experimental data for MnSi, we reveled that the skyrmion lattice is formed progressively in smaller domains, containing hundreds of skyrmions, with an activation barrier of several eV/mm for a single skyrmion in MnSi. Further, we studied the different nucleation mechanisms and the time evolution of the SkL formation in chiral magnetic thin films. We showed that the Con → SkL phase transition is characterized by a rod-like (one-dimensional) nucleation that can be attributed to the formation and growth of chiral bobbers from the film surface, and reveal the interesting blinking (creation-annihilation) behavior of skyrmions close to the phase boundary between the two phases. Our results advance the understanding of the nucleation mechanism of the SkL in chiral magnets, and we expect that our findings will instigate further measurements of topological energy barriers between different (chiral) magnetic states. Such studies are an important step to understanding the evolution of magnetic states in bulk and ultrathin materials and will establish definitively the feasibility of high-density devices based on topological

spin structures.

Part II

Skyrmionics in thin film heterostructures

5 Deflection of ferromagnetic and antiferromagnetic skyrmions at heterochiral interfaces

Devising magnetic nanostructures with spatially heterogeneous Dzyaloshinskii-Moriya interaction (DMI) is a promising pathway towards advanced confinement and control of magnetic skyrmions in potential devices. In this chapter, we discuss theoretically how a skyrmion interacts with a heterochiral interface using micromagnetic simulations and analytic arguments. We show that a heterochiral interface deflects the trajectory of ferromagnetic (FM) skyrmions and that the extent of such deflection is tuned by the applied spin-polarized current and the difference in DMI across the interface. Further, we show that this deflection is characteristic for the FM skyrmion, and is completely absent in the antiferromagnetic (AFM) case. In turn, we reveal that the AFM skyrmion achieves much higher velocities than its FM counterpart, yet experiences far stronger confinement in nanoengineered heterochiral tracks, which reinforces AFM skyrmions as a favorable choice for skyrmion-based devices.

The results presented in this chapter are published in Physical Review B, **99**, 104409. (2019).

5.1 Motivation

The interfacially induced Dzyaloshinskii-Moriya interaction (DMI) [Sec. 2.3.3] is a chiral interaction observed in ferromagnetic thin films, e.g., a Co layer, when coupled to nonmagnetic layers with a strong spin-orbit coupling, e.g., the heavy metal Pt [174–176]. The interfacially-induced DMI favors the rotation of the magnetization at short length scales, giving rise to chiral spin structures of the Néel-type, such as cycloids and magnetic skyrmions [177–180]. Particularly, magnetic skyrmions are promising candidates for technological applications, such as spin-based information processing and computing devices [180–183]. Most recently, the suggestion of skyrmions in antiferromagnetic

(AFM) systems has also increased the expectation on skyrmion-based devices, since in those systems the skyrmions are not sensitive to stray fields, move straight along the direction imposed by the applied current, and present better mobility with lower energy costs [30, 94, 106–108, 184, 185].

The confinement of ferromagnetic (FM) skyrmions in mesoscopic chiral films and tracks has already been thoroughly studied in recent years [186–189]. As a latest development, spatial engineering of DMI has been suggested as an alternative manner of skyrmion guidance and manipulation. Such heterochiral samples have been demonstrated to strongly confine magnetic skyrmions [190], pin them or manipulate their size [191], and increase their lifetime [192], in the regions where the DMI is higher. The interest in these results is reinforced by the fact that heterochiral structures can indeed be fabricated experimentally, via engineering of the substrate and/or the capping layer of the thin ferromagnetic film [193, 194]. Bearing in mind the potential of heterochiral systems for the development of skyrmion-based devices, the last piece of the puzzle is to understand the skyrmion dynamics in such samples. However, the dynamics of a single magnetic skyrmion while e.g. crossing the regions with different DMI strengths remains mostly unexplored, while the confinement effects in AFM heterochiral films have not been studied at all to date.

In the next sections we address theoretically the dynamics of FM and AFM skyrmions in heterochiral films, and particularly their interaction with a heterochiral interface (where DMI changes, see e.g. a suggested realization in Fig. 5.1). The DMI strength can be modified along the sample using, e.g., lithographic techniques to correspondingly pattern the heavy metal (HM) layer(s) and thereby adjust the interfacially-induced DMI [190, 193, 194]. Note that by altering the HM configuration and/or thickness one might also induce changes in other material parameters, such as the magnetic anisotropy. In this chapter, we are focusing exclusively on the effects of the spatially varied DMI, and therefore consider the other material parameters homogeneous throughout the sample to avoid ill interpretations of the results. We proceed by employing micromagnetic simulations to show that local canting of the magnetization at the heterochiral interface [190] can be seen as an imposed potential barrier in the Thiele formalism for the center-of-mass of the skyrmion, that causes a characteristic deflection in the trajectory of the FM skyrmion when crossing the heterochiral interface. After verifying it in full micromagnetic simulations, we show that such deflection is completely absent in an analogous antiferromagnetic sample, and that the AFM skyrmion: (i) moves much faster than the FM skyrmion, as already predicted in the literature [30], but (ii) experiences far stronger confinement in heterochiral films, so that the critical current needed to push it over a heterochiral interface is much larger than in the FM case. These results promote antiferromagnetic heterochiral films as an advanced platform for skyrmion-based devices.

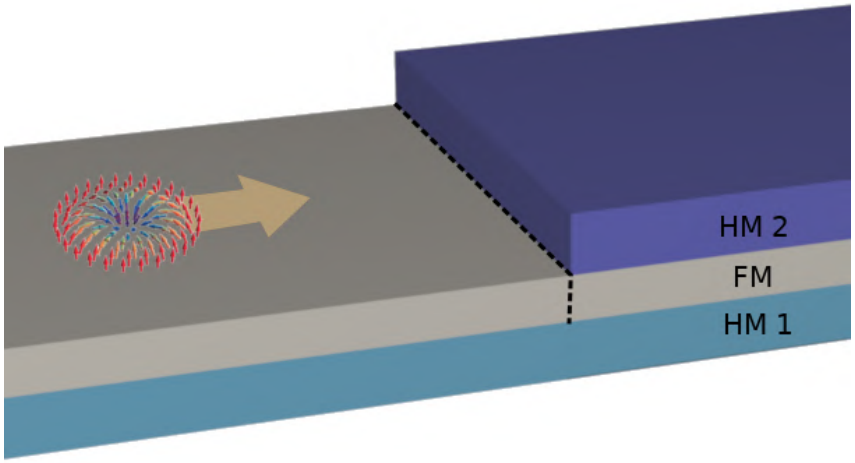

Figure 5.1 – Schematic representation of an experimental analogue of the considered system, a ferromagnetic layer between two heavy metal (HM) layers, with a suitably patterned top layer. In the depicted sample, the heterochiral interface is created at the lateral end of the top layer. The dashed line indicates the interface where the DMI changes.

5.2 Theoretical formalism

5.2.1 Micromagnetic model

The dynamics of the magnetization is governed by the Landau-Lifshitz-Gilbert (LLG) equation [see Sec. 2.2 and Eq. 2.17]

$$\frac{d\mathbf{m}}{dt} = \frac{\gamma}{1+\alpha^2}\left(\mathbf{m}\times\mathbf{H}_{\text{eff}} + \alpha\left[\mathbf{m}\times(\mathbf{m}\times\mathbf{H}_{\text{eff}})\right]\right), \tag{5.1}$$

where γ is the gyromagnetic ratio and α the damping factor. $\mathbf{H}_{\text{eff}}$ is the effective magnetic field given by the functional derivative of the free energy $E = \int(\mathcal{E}_{\text{ex}} + \mathcal{E}_{\text{anis}} + \mathcal{E}_{\text{dmi}})dV$ with respect to the magnetization: $\mathbf{H}_{\text{eff}} = -\frac{1}{M_{\text{s}}}\delta E/\delta\mathbf{m}$.

For the micromagnetic simulations, we employ the simulation package *Mumax*^{3} [195], on an ultrathin ferromagnetic film with perpendicular magnetic anisotropy and with spatially inhomogeneous DMI. The local free energy density $\mathcal{E}$, related to the magnetization $\mathbf{M}(x,y) = M_{\text{s}}\mathbf{m}(x,y)$, where M_{s} is the saturation magnetization and $|\mathbf{m}| = 1$, has multiple contributions, and we consider the following: exchange, anisotropy, DMI, and demagnetization. We approximate the demagnetization energy by using an effective anisotropy $K_{\text{eff}} = K - \frac{1}{2}\mu_0 M_{\text{s}}^2$, with K the perpendicular magnetic anisotropy and μ_0 the vacuum permeability. This approximation is justified by the fact that we are interested in ultrathin films, where dipolar coupling becomes local in the zero-thickness limit [16]. In this chapter we do not consider the effects of an external magnetic field, therefore, the Zeeman term of the energy-density is zero. The expressions for the remaining energy-density terms are

$$\mathcal{E}_{\text{ex}} = A\left[(\partial_x \mathbf{m})^2 + (\partial_y \mathbf{m})^2\right],$$
$$\mathcal{E}_{\text{anis}} = K_{\text{eff}}(1 - m_z^2),$$
$$\mathcal{E}_{\text{dmi}} = -D\left[m_x\partial_x m_z - m_z\partial_x m_x + m_y\partial_y m_z - m_z\partial_y m_y\right].$$

For the simulations of the ferromagnetic case, we consider the following parameters: saturation magnetization: $M_{\text{s}} = 580$ kAm^{-1}, exchange stiffness: $A = 15$ pJm^{-1}, and perpendicular anisotropy $K = 0.8$ MJm^{-3} ($K_{\text{eff}} = 0.6$ MJm^{-3}), stemming from the experimental results on Co/Pt systems [196, 197]. The used values of the DMI constant, D, will be specified in the sections below. For all simulations, we consider a system discretized into cells of size $1 \times 1 \times 0.4$ nm^3.

The Néel skyrmion in a chiral magnetic film can be driven by two different scenarios [see Sec. 2.7.1]: (i) by an in-plane spin-polarized current (CIP) applied into the ferromagnetic layer, or (ii) by an electrical current applied into the HM layer, which due to the spin Hall effect gives rise to a spin-polarized current perpendicular to the plane (CPP) [93–96]. In this chapter we explore both scenarios. For simulations of the spin transfer torque (STT) associated with the CIP and CPP scenarios, the Zhang and Li STT [Eq. (2.51)] and the Slonczewski STT [Eq. (2.52)] terms were added to the LLG equation, respectively, as explained in Sec. 2.7.1. In *Mumax*^{3} one can simulate the CPP scenario by considering a fixed layer, with polarization vector $\mathbf{m}_p$, on top of the film and the applied current injected along the $\hat{z}$ direction. For both the CIP and the CPP scenarios, the polarization rate of the spin-polarized current was fixed at $P = 0.4$.

For the antiferromagnetic samples, we consider the same parameters of the FM case, except for the negative exchange stiffness $A = -15$ pJm^{-1}. Note that *Mumax*^{3} was originally developed for simulations of FM systems in the continuous field approximation. However, once we consider the AFM system, which comprises two sublattices of reversely-aligned spins, we end up performing an atomistic simulation (albeit with a large lattice parameter), where the finite-differences derivatives performed by *Mumax*^{3} are mathematically equivalent to the classical Heisenberg model (see, e.g., Appendix A.1). The STT can be applied also to the AFM system provided one considers an ultra-small mesh size in the micromagnetic simulations [94, 106, 107, 198, 199]. In this chapter, we simulate only the CPP-driven AFM skyrmion. Note that one can not straightforwardly use the CIP scenario in the micromagnetic simulations since spatial derivatives are involved in the STT term and the reversely-aligned magnetization of the AFM system can no longer be described by a differentiable field.

5.2.2 Thiele equation for skyrmion dynamics in the presence of external forces

As discussed in Sec. 2.7.3, the Thiele equation describes the dynamics of the center-of-mass of the skyrmion by assuming a rigid body motion of the spin texture , and can be written out for both CIP and CPP scenarios.

The Thiele equation for the CIP scenario reads

$$\mathbf{G} \times (\boldsymbol{\nu} - \dot{\mathbf{r}}) + \mathcal{D}(\beta\boldsymbol{\nu} - \alpha\dot{\mathbf{r}}) - \nabla V(\mathbf{r}) = 0, \tag{5.3}$$

where $\mathbf{G} = \mathcal{G}\hat{z} = 4\pi Q\hat{z}$ is the gyromagnetic coupling vector, with Q the skyrmion number; $\dot{\mathbf{r}} = \dot{x}\hat{x} + \dot{y}\hat{y}$ is the drift velocity; $\boldsymbol{\nu}$ is the velocity of the conduction electrons associated to the spin-polarized current; V is the potential stemming from an external force, such as boundaries or impurities; and $\mathcal{D}$ represents the dissipative tensor, with components $\mathcal{D}_{ij} = \int d^2r \partial_i\mathbf{m} \cdot \partial_j\mathbf{m} = \mathcal{D}\delta_{ij}$. For the range of parameters considered in this chapter, $\mathcal{D} \approx 4\pi$–8π, as discussed in appendix A.2. When the spin-polarized current is applied along the x direction, i.e. $\nu_y = 0$, and $V(\mathbf{r}) = 0$, the Thiele equation can be separated into its two components given by Eqs. 2.55a and 2.55b. On the other hand, if we consider $V(\mathbf{r}) = V(x)$, the Thiele equation leads to

$$\dot{y} = \frac{\mathcal{G}}{\mathcal{D}\alpha}(\nu_x - \dot{x}), \tag{5.4a}$$

$$\left(\frac{\mathcal{G}^2}{\mathcal{D}\alpha} + \mathcal{D}\beta\right)\nu_x - \left(\frac{\mathcal{G}^2}{\mathcal{D}\alpha} + \mathcal{D}\alpha\right)\dot{x} = \frac{dV}{dx}. \tag{5.4b}$$

Note that the x component of the skyrmion velocity is directly affected by the external potential and, consequently, the Magnus force (represented by the $\mathcal{G}$ term), which drives the skyrmion along the y direction, is also affected. Indeed, taking the variation $\delta\dot{y} \equiv \dot{y}(t + dt) - \dot{y}(t)$ of Eq. (5.4a), for a fixed current density, we obtain

$$\delta\dot{y} = -\frac{\mathcal{G}}{\mathcal{D}\alpha}\delta\dot{x}, \tag{5.5}$$

which means that, if the external potential is attractive ($dV/dx < 0$), or repulsive ($dV/dx > 0$), the skyrmion trajectory is deflected to the $-\mathcal{G}\hat{y}$ or $+\mathcal{G}\hat{y}$ direction respectively, depending on the skyrmion number.

In the case of a repulsive external potential, the critical current for the skyrmion to overcome such energy barrier is given by choosing $\dot{x} = 0$ for the maximal value of $F = dV/dx$ in Eq. (5.4b), i.e.

$$\nu_x^c = \frac{F_{\max}}{\frac{\mathcal{G}^2}{\mathcal{D}\alpha} + \mathcal{D}\beta}. \tag{5.6}$$

For the limit of small α and β ($\alpha \sim \beta \ll 1$), the critical current can be approximated as $\nu_x^c = \frac{F_{\max}\mathcal{D}\alpha}{\mathcal{G}^2}$. In the same way, Eq. (5.4b) results in $(\nu_x - \dot{x}) \approx \frac{\mathcal{D}\alpha}{\mathcal{G}^2}\frac{dV}{dx}$. Substituting this

expression into Eq. (5.4a), we obtain the velocity of the skyrmion in the y direction:

$$\dot{y} \approx \frac{1}{\mathcal{G}} \frac{dV}{dx}, \tag{5.7}$$

which depends only on the external potential V. The maximal velocity can be written as $\dot{y}_{\max} = F_{\max}/\mathcal{G}$.

Similar results are obtained for a Néel skyrmion driven by the CPP scenario. In this case, the skyrmion motion is described by the modified Thiele equation [93, 95, 96]:

$$-\mathbf{G} \times \dot{\mathbf{r}} - \alpha \mathcal{D} \dot{\mathbf{r}} + 4\pi \mathcal{B} \mathbf{j}_{\text{hm}} - \nabla V(\mathbf{r}) = 0, \tag{5.8}$$

where $\mathbf{j}_{\text{hm}}$ is the current density flowing through the heavy metal, which gives rise to a spin-polarized current perpendicular to the plane. The parameter $\mathcal{B}$ quantifies the efficiency of the spin-Hall effect. Now we consider $\mathbf{j}_{\text{hm}} = j_{\text{hm}} \hat{y}$. For the case of $V = 0$, Eq. (5.8) can be separated into its two components given by Eqs. 2.58 and 2.59. In this scenario, for $\alpha \ll 1$, the Magnus term dominates $\dot{x} \gg \dot{y}$, and the relevant motion is perpendicular to the direction of the applied current. If we consider $V(\mathbf{r}) = V(x)$, the modified Thiele equation leads to

$$\dot{y} = \frac{1}{\mathcal{D}\alpha}(4\pi \mathcal{B} j_{\text{hm}} - \mathcal{G}\dot{x}), \tag{5.9a}$$

$$-\left(\frac{\mathcal{G}^2}{\mathcal{D}\alpha} + \mathcal{D}\alpha\right)\dot{x} + \frac{4\pi \mathcal{B}\mathcal{G}}{\mathcal{D}\alpha} j_{\text{hm}} = \frac{dV}{dx}. \tag{5.9b}$$

Taking the variation $\delta\dot{y}$ of Eq. (5.9a), for a fixed current density, we recover Eq. (5.5). Therefore, the presence of a external potential deflects the skyrmion trajectory in the same direction as in the CIP scenario. In the same way, the critical current for the skyrmion to overcome a repulsive potential is obtained by choosing $\dot{x} = 0$ in Eq. (5.9b), i.e.

$$4\pi \mathcal{B} j^c_{\text{hm}} = \frac{\mathcal{D}\alpha}{\mathcal{G}} F_{\max}. \tag{5.10}$$

Finally, for the limit of $\alpha \ll 1$, Eq. (5.9b) becomes $(4\pi \mathcal{B} j_{\text{hm}} - \mathcal{G}\dot{x}) \approx \frac{\mathcal{D}\alpha}{\mathcal{G}} \frac{dV}{dx}$. By substituting this expression into Eq. (5.9a), we recover Eq. (5.7) for the skyrmion velocity in y direction.

5.3 Results and discussion

5.3.1 Ferromagnetic skyrmion

5.3.1.1 Skyrmion trajectory when facing nonuniform canting of the background magnetization

In this chapter, we are interested in the skyrmion motion in heterochiral systems, particularly the behavior of the skyrmion trajectory while crossing an interface where

DMI changes. As the simplest case of a heterochiral film, we consider a system where the DMI strength, D, varies only in the x direction as: $D = D_1$, for $x < x_0$, and $D = D_2$ for $x > x_0$, with D_1 and D_2 constant. For this geometry, it was shown in Ref. [190] that canting of the magnetization is induced at the interface $x = x_0$, and that the magnetization profile is given by:

$$\theta(x) = 2\arctan\left(e^{-|(x-x_0)/\xi|}\tan\frac{\theta_0}{2}\right), \tag{5.11}$$

where $\theta(x)$ is the angle of the spins with respect to the z axis, i.e., $\mathbf{m} = (\sin\theta, 0, \cos\theta)$, $\xi = \sqrt{A/K_{\text{eff}}}$, and

$$\theta_0 = \arcsin\frac{D_2 - D_1}{\pi D_c} \tag{5.12}$$

is the canting angle at the interface, with $D_c = 4\sqrt{AK_{\text{eff}}}/\pi$. Notice that in Ref. [190] the DMI parameter takes opposite sign to the one used here. The canting of the magnetization at the interface can be either positive or negative, depending on the difference between the DMI strengths D_1 and D_2.

It now becomes of interest to first understand what happens to the skyrmion trajectory when encountering such nonuniform canting of the background magnetization.

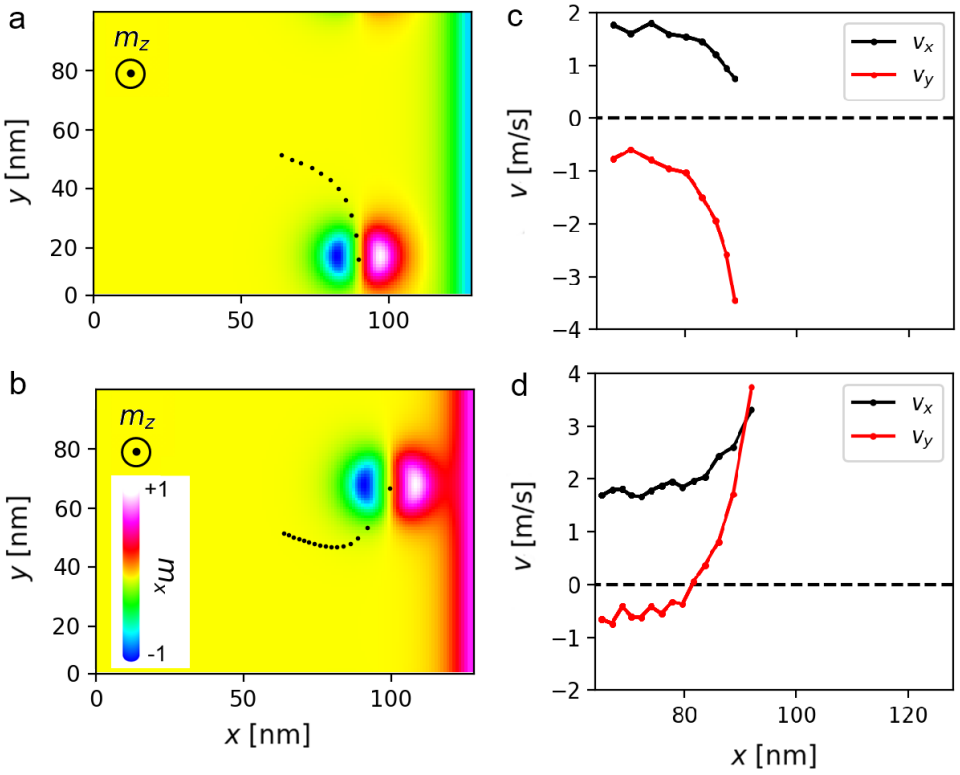

Figure 5.2 – Skyrmion trajectories (trail of black dots) in the presence of (a) negative and (b) positive canting of the background magnetization at the right edge of the sample. (c) Center-of-mass velocities of the skyrmion in plot (a). (d) Center-of-mass velocities of the skyrmion in plot (b). Here $j = 5 \times 10^{10}\text{Am}^{-2}$, $\alpha = 0.3$ and $\beta = 0$. The center of mass is calculated as the mean point of the region where $m_z = 0$.

In Fig. 5.2 we show the result of a simulation performed in the micromagnetic framework for the skyrmion trajectory in a thin ferromagnetic film with uniform DMI, here fixed at $D = 0.8D_c$, and artificially imposed canting of spins on the right sample boundary. We consider a sample of size $128 \times 96 \times 0.4$ nm^3, with periodic boundary conditions in the y direction. The skyrmion is initialized in the center of the simulated region and the energy is minimized numerically. An in-plane polarized current is then applied in the $-\hat{x}$ direction (CIP scenario). The skyrmion undergoes a transverse motion due to the Magnus force. To address the effect of nonuniform canting of the magnetization (as expected at a heterochiral interface), we fix a column of spins at the right side of the sample as $\mathbf{m}_{\text{fixed}} = (-\sin\theta_{\text{edge}}, 0, \cos\theta_{\text{edge}})$ in Fig. 5.2 (a), and $\mathbf{m}_{\text{fixed}} = (\sin\theta_{\text{edge}}, 0, \cos\theta_{\text{edge}})$ in Fig. 5.2 (b), with canting angle $\theta_{\text{edge}} = \frac{\pi}{4}$. The fixed columns spread the canting of the magnetization in the vicinity of the edge, which then affects the skyrmion trajectory. Although these examples are not ideally realistic, they will be useful to understanding the results of the next section. Fig. 5.2 (c,d) shows that the induced canting can be seen as either repulsive (c) or attractive (d) external potential for the skyrmion. In those two cases the Magnus force pushes the skyrmion in different directions ($-\hat{y}$ and $+\hat{y}$). These results are in accordance with Eq. (5.5) if one considers the local canting of the magnetization as an external potential for the center of mass of the skyrmion, which is a reasonable assumption, since the energy cost for the skyrmion to flip the background spins during its motion is higher if the background spins are in the opposite direction [Fig. 5.2 (a)] than if those have the same polarity as the skyrmion [Fig. 5.2 (b)]. We have obtained analogous results for the CPP scenario.

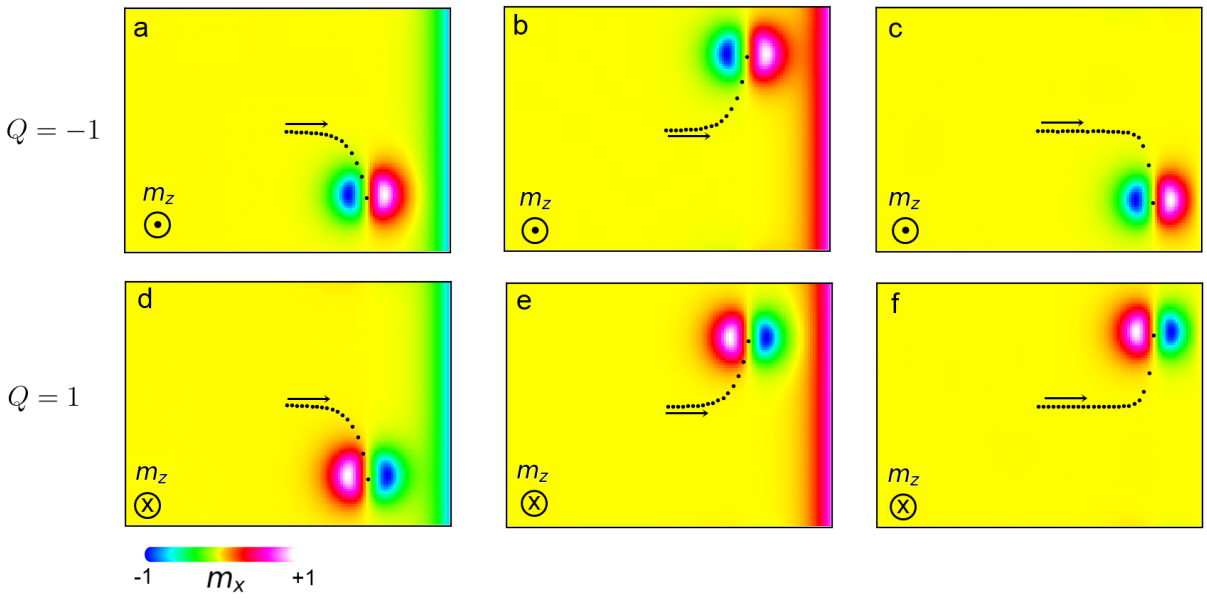

Figure 5.3 – Skyrmion trajectories (given as a trail of black dots) for $Q = -1$ (a-c) and $Q = 1$ (d-f), for different canting of the magnetization at the edge, $m^x_{\text{fixed}} = -\sin\theta_{\text{edge}}, +\sin\theta_{\text{edge}}$ and 0, respectively from top to bottom, with $\theta_{\text{edge}} = \frac{\pi}{4}$. The applied current density is $j = 5 \times 10^{10}\text{Am}^{-2}$.

In order to provide a better comparison of the simulations with the analytic results, we next consider the case $\alpha \ll 1$ and $\beta = 0$. In this case, the relevant motion in the y direction will be given solely by the effect of the external potential [see Eq. (5.7)]. In Fig. 5.3 we take $\alpha = 0.02$ (within the typical range $\alpha \sim 10^{-3}$–10^{-2} for skyrmion-hosting materials [93, 200–203]), and perform the same simulation of Fig. 5.2, but now for six different situations: for the skyrmion numbers $Q = \pm 1$, and the fixed magnetizations at the right edge $m^x_{\text{fixed}} = -\sin\theta_{\text{edge}}, +\sin\theta_{\text{edge}}$ and 0, with $\theta_{\text{edge}} = \frac{\pi}{4}$. In the last case, the fixed spins do not induce any canting of the magnetization, but increase the necessary energy to flip their neighbours and must act as a repulsive potential for both considered skyrmion numbers. With such examples, we look for the corroboration of Eq. (5.5) for predicted deflection of the skyrmion trajectory. Comparing Fig. 5.3(a,b) to (d,e), we change the skyrmion number [consequently the sign of $\mathcal{G}$ in Eq. (5.5) as well], but we also change the canting effect from repulsive to attractive and vice versa. Therefore, the skyrmion is deflected *in the same direction* for both $Q = \pm 1$. Comparing Fig. 5.3(c) to (f), the skyrmion number changes, but the fixed spins act as a repulsive barrier in both situations, hence, the skyrmion is deflected *in opposite directions* for opposite topological charge. These results are in complete accordance with Eq. (5.5) and will be useful to understanding the results of the next sections. For the CPP scenario, we obtained similar results when choosing $\alpha = 0.02$.

5.3.1.2 Skyrmion trajectory while crossing an interface where DMI changes

The examples of the previous subsection illustrate the strong interaction of skyrmions with nonuniform canting, moreover, as we saw before, similar canting of the magnetization is intrinsic to the DMI interface(s) in a heterochiral ferromagnetic film. Therefore, we study next the trajectory of a single skyrmion while crossing an interface where DMI changes. In the simulations, we consider a sample of size $256 \times 256 \times 0.4\ \text{nm}^3$, with DMI strength D_1 for $x < x_0$ and D_2 for $x > x_0$, where $x_0 = 128$ nm. The skyrmion is initialized at the position $x = 64$ nm, $y = 128$ nm (see Fig. 5.4) and we consider periodic boundary conditions in the y direction. An in-plane current is applied along $-\hat{x}$ (CIP scenario), with $\alpha = 0.02$ and $\beta = 0$, such that the relevant motion in the y direction will be given solely by the effect of the heterochiral interface (the effects of the non-adiabatic parameter, β, to the skyrmion trajectory are shown in Appendix A.3). As expected from the previous discussion, the skyrmion is deflected at the interface along $\pm\hat{y}$, depending on the canting direction, which in turn depends on the DMI strengths D_1 and D_2.

To illustrate the role of different parameters, we calculate the skyrmion deflection Δy after the skyrmion reaches the position $x = 192$ nm (as shown in Fig. 5.4), for selected values of DMI strengths and applied currents. Fig. 5.5 shows the skyrmion deflection after crossing the interface as a function of $\Delta D = D_2 - D_1$, with $D_1 = 0.8 D_c$ fixed. For high currents, the deflections are smaller than those observed for low currents, and

anti-symmetric for ΔD positive or negative, since the energy barrier induced by the interface is small when compared to the kinetic energy induced by the applied current. On the other hand, for low currents, the skyrmion motion can be completely blocked by the repulsive potential induced by $\Delta D < 0$, if $j < j_c(\Delta D)$, where j_c is the critical current for the skyrmion to overcome the interface. The more negative ΔD is, the higher is the necessary current for the skyrmion to overcome the interface. For example, for $j = 2\times10^{10}$ Am^{-2} in Fig. 5.5, the skyrmion can not cross the interface for $\Delta D \leq -0.05D_c$, and continues the motion purely in the y direction, along the interface. Notice that for the considered parameters the y component of the skyrmion velocity *does not depend on the applied current* [see Eq. (5.7)]. The maximal velocity of the skyrmion in the y direction, for a fixed ΔD, is the same for all current values, as confirmed by the graph in the inset of Fig. 5.5. However, for low currents the skyrmion takes longer time to cross the interface, which translates into a larger deflection. The largest deflections are observed when the applied current is just above j_c, e.g., for the case of $j = 5\times10^{10}$ Am^{-2} in Fig. 5.5, where the skyrmion overcomes the interface with $\Delta D = -0.1D_c$ after a rather extreme deflection of $\Delta y = -18.5$ μm.

Comparing the graph in the inset of Fig. 5.5, where $\dot{y}_{\max}$ varies linearly with ΔD, with Eq. (5.7) and Eq. (5.12), we obtain

$$F_{\max} \approx c\mathcal{G}\Delta D = c\pi D_c \mathcal{G} \sin\theta_0, \tag{5.13}$$

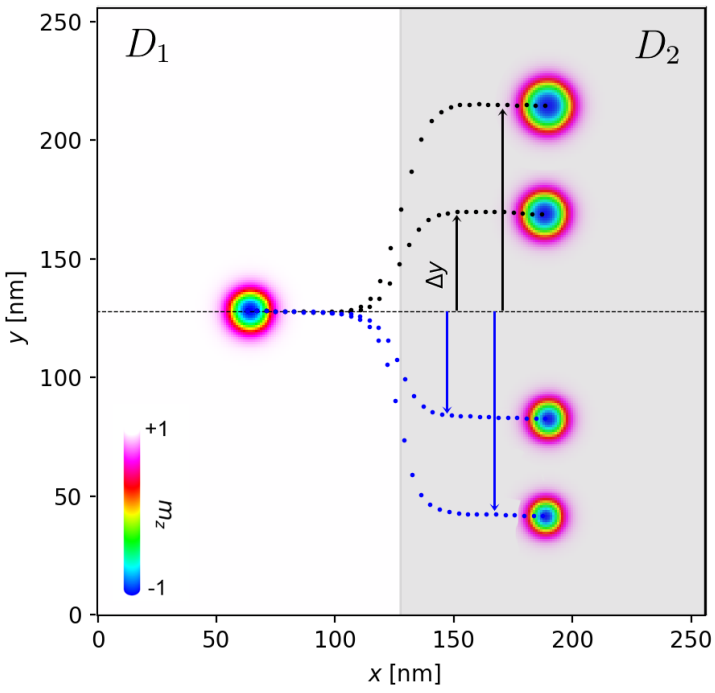

Figure 5.4 – The skyrmion is initialized on the left side of the diagram. Depending on the difference of the DMI strengths, D_1 and D_2, the skyrmion deflection is positive ($\Delta y > 0$, black arrows) or negative ($\Delta y < 0$, blue arrows). The dots show the respective trajectories of the skyrmion, for $j = 2\times10^{11}$Am^{-2} and $\Delta D/D_c = 0.05, 0.025, -0.025, -0.05$, respectively top-to-bottom.

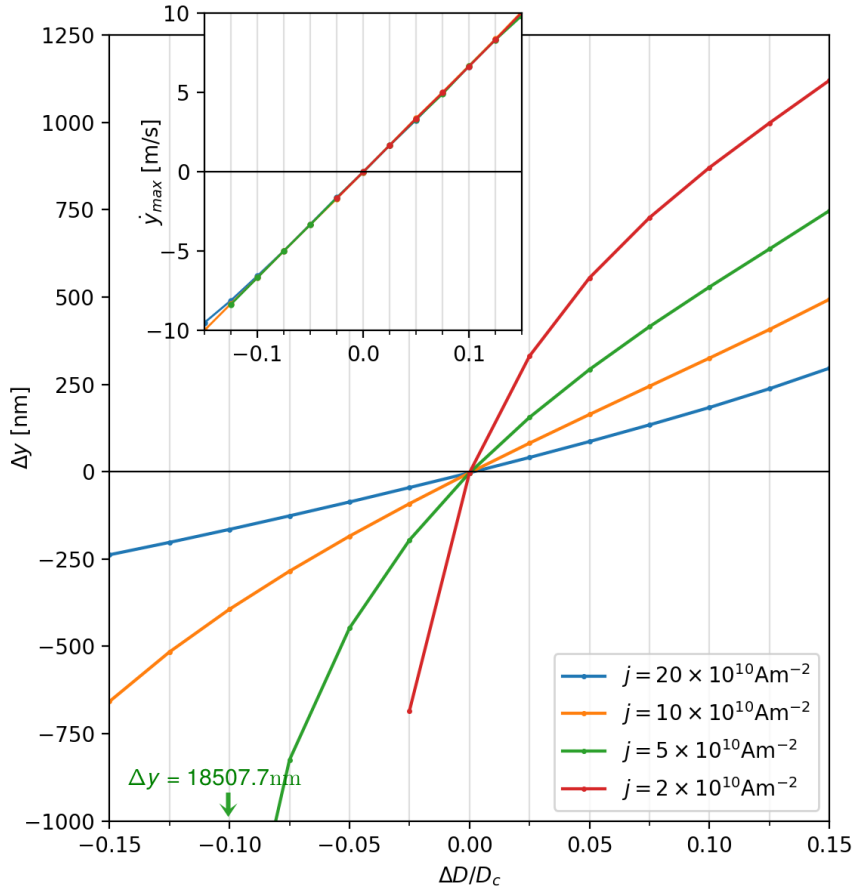

Figure 5.5 – Main panel exhibits the deflection in the skyrmion trajectory, Δy, for different values of applied current j and the change in DMI across the interface $\Delta D = D_2 - D_1$, with $D_1 = 0.8D_c$ fixed. The inset shows the maximal velocity of the skyrmion in the y direction (along the interface) as a function of ΔD, for different values of j.

where c is the slope of $\dot{y}_{\max}(\Delta D)$ characteristic in the inset of Fig. 5.5, and θ_0 is the canting angle at the interface (from the graph, we obtained $c \approx 67/D_c$ ms^{-1}). Note that, since the external potential V does not depend on the applied current scenario and Eq. (5.7) is valid for both CIP and CPP scenarios, the graph in the inset of Fig. 5.5 and consequently Eq. (5.13) are general results for a ferromagnetic skyrmion. Therefore, the critical current, given by Eqs. (5.6) and (5.10), depends linearly on ΔD for both CIP and CPP scenarios. Note that the dissipative factor $\mathcal{D}$ in Eqs. (5.6) and (5.10) depends on the skyrmion size, which in turn depends on the material parameters, e.g., the DMI strength. However, as will be shown in Fig. 5.9 of the next section, for the considered range of parameters, such linear dependence is preserved in the CPP scenario for different values of α.

5.3.1.3 Multi-channel skyrmion bit sequencer

Based on our findings, the heterochiral interface can be used to very precisely guide the skyrmion motion in a more complex circuitry, for example to selectively "write" skyrmions in one of multiple nanotracks, or to selectively direct a skyrmion to

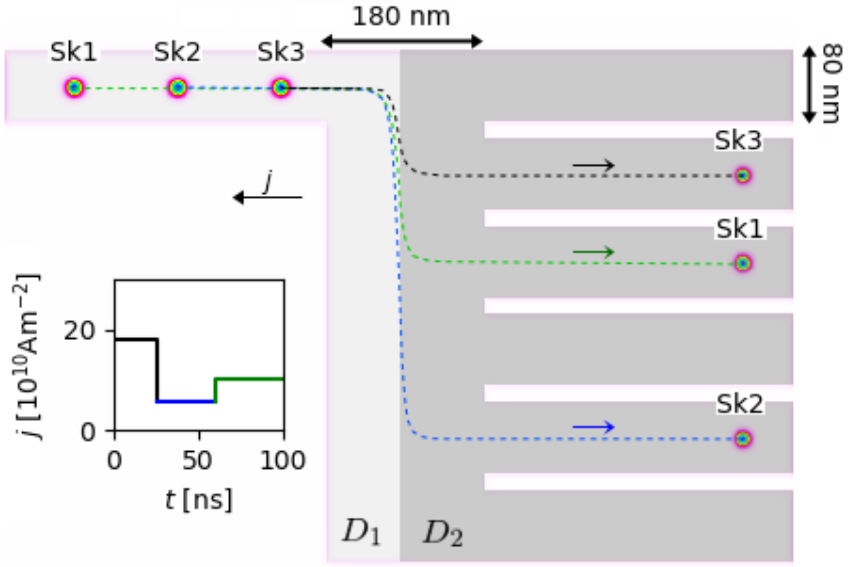

Figure 5.6 – Selective deflection of a skyrmion chain into multiple nanotracks, using the properties of a heterochiral interface. Dashed lines indicate the trajectory of each skyrmion during the simulation, for a series of current pulses of $j = 18 \times 10^{10}$ Am^{-2} for $0 < t < 25$ ns, $j = 5.5 \times 10^{10}$ Am^{-2} for $25 < t < 60$ ns, and $j = 10 \times 10^{10}$ Am^{-2} for $t > 60$ ns, in a sample with $\alpha = 0.02$, $\beta = 0$, $D_1 = 0.8D_c$ and $D_2 = 0.75D_c$ ($\Delta D/D_c = -0.05$).

one of the many logical gates in a larger skyrmion microprocessor. We here exemplify such an application of a heterochiral interface, for the targetted manipulation of a chain of skyrmions by pulsed current. Although simplistic, this example is intended for the reader to creatively visualize other possible uses of heterochiral systems.

In this example, we consider a rectangular ferromagnetic film of size $880 \times 634 \times 0.4$ nm^3, where high-DMI tracks are engineered (by a suitable heavy-metal capping layer, see Fig. 5.6) with DMI strengths of $D_1 = 0.8D_c$ (single track on the left) and $D_2 = 0.75D_c$ (six tracks on the right side). A skyrmion chain, containing skyrmions labeled Sk1, Sk2 and Sk3 and separated by 115 nm, is initialized in the D_1 track on the left side of the sample. A current pulse is then applied along the $-\hat{x}$ direction (CIP scenario), which induces motion of skyrmions along $+\hat{x}$ direction. The duration and intensity of subsequent current pulses is designed in such a manner that each skyrmion reaches the heterochiral interface under a different current density, and thereby experiences different deflection of its trajectory. Moreover, the intensity of the pulses is chosen according to Fig. 5.5, so that the deflection of the skyrmions exactly corresponds to the entry point of one of the six tracks on the right side of the sample [204].

Obviously, the exact duration and intensity of the current pulses has to be precisely engineered for a particular realization of the sample, depending on the separation of skyrmions in the initial chain and the values of all relevant parameters including the change of DMI across the interface. Nevertheless, once optimized, such an interface can

be very reliably used to write skyrmions in multiple channels in any desired sequence, as we show in the animated data in Supplementary Material [204]. We remind the reader that current-induced deflection of a FM skyrmion at a heterochiral interface can easily exceed ten micrometers (as shown in the previous section), hence a large number of nanotracks could be very controllably accessed in this manner. We stress that such controlled manipulation is needed for more complex skyrmion-based computing and storage circuits. For instance, it could be used to selectively place the skyrmions in the input branches of (many) skyrmion-based logic gates [79], or to precisely write information in multi-bit memory cells.

5.3.2 Antiferromagnetic skyrmion

Antiferromagnetic (AFM) skyrmions are expected to combine the advantages of antiferromagnets with those of skyrmions regarding spintronic applications. AFM skyrmions have zero net topological charge and simulations of their current-induced motion have shown that accordingly they move straight along the direction imposed by the applied current [30, 94, 106, 107]. This is considered advantageous for applications, because as opposed to ferromagnetic skyrmions their antiferromagnetic counterparts are not driven towards the boundary of the hosting magnetic structures, where they can collapse. Additional benefits arise from their antiferromagnetic nature, i.e. their insensitivity to parasitic stray fields [30]. In what follows, we address in more detail the behavior of AFM skyrmions in heterochiral samples.

Antiferromagnetic skyrmions have been recently intensively studied regarding their spin structure, their stability, and their motion [30, 94, 106, 107, 185, 205–207]. The AFM skyrmion comprises a two-sublattice structure, where each sublattice (indexed 1 and 2) contains half of the spins of the system and has the opposite magnetization of the other sublattice. In this way, the topological numbers projected to each sublattice satisfy $Q_1 = -Q_2$. The opposing topological index of two sublattices causes the exact cancellation of the Magnus force in the presence of current, so the antiferromagnetic skyrmion moves along the direction of the current. The velocity of the AFM skyrmion driven by a current density is inversely proportional to the damping factor α, and the AFM skyrmion can move much faster than the FM one for weak damping, possibly reaching km/s while remaining stable [30, 94, 106–108].

To understand the dynamics of the AFM skyrmion while crossing an interface where the DMI changes, we first simulate, in the micromagnetic framework, the AFM ground state in the presence of such an interface. Here, we consider a sample of size $256 \times 100 \times 0.4\,\mathrm{nm}^3$ with DMI strength D_1 for $x < x_0$ and D_2 for $x > x_0$, with $x_0 = 128$nm. Fig. 5.7(b) shows a snapshot zoom of the configuration obtained after minimizing the energy numerically. Notice that the induced canting ($m_x = \sin\theta$) points in opposite

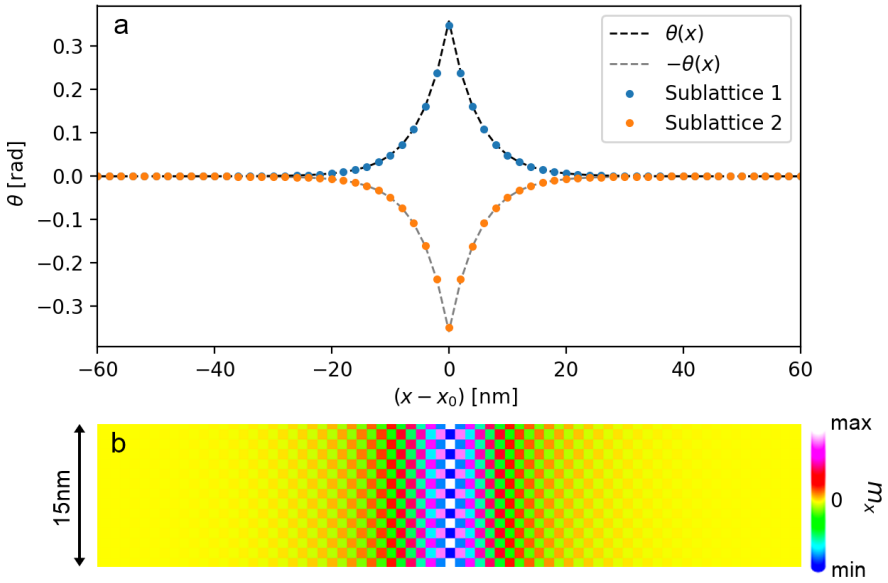

Figure 5.7 – (a) Canting of the magnetization $\theta(x)$ at a DMI interface of a heterochiral AFM system, plotted separately for each sublattice, for $D_2 - D_1 = 1.1D_c$. Dashed lines represent the analytic result for the FM system, given by Eq. (5.11). (b) Snapshot zoom of the configuration obtained after minimizing the energy numerically.

directions in each sublattice. As shown in Fig. 5.7(a), the canting induced at each sublattice follows the analytic result for the FM system (dashed lines), given by Eq. (5.11). In the presence of canting induced by the DMI interface, we expect skyrmion scattering at each sublattice to follow the FM result of Fig. 5.3. We recall that the sublattices have opposite topological charge and induce opposite canting at the interface, hence the effective motion of the AFM skyrmion, given by a combination of the two sublattices, is a combination of either Fig. 5.3 (a) and (e), or Fig. 5.3 (b) and (d). Therefore, the characteristic deflection observed for the FM skyrmion while crossing the interface is completely absent (cancelled out) in the AFM system. However, the attractive or repulsive effect in the x direction is still expected.

The dynamics of the magnetization in the micromagnetic simulations is controlled by applying a spin current perpendicular to the plane (CPP scenario). Since the DMI interface is always either attractive in both sublattices [combination of Fig. 5.3 (b) and (d)] or repulsive in both sublattices [combination of Fig. 5.3 (a) and (e)], the DMI interface can be seen as an external potential in the modified Thiele equation [Eq. (5.8)], for a single lattice with $G = 0$. Since the AFM skyrmion moves along the direction of the current, now we assume $\mathbf{j}_{\mathrm{hm}} = j_{\mathrm{hm}}\hat{x}$, and the Thiele equation for the AFM skyrmion reads

$$-\alpha\mathcal{D}\dot{x} + 4\pi\mathcal{B}j_{\mathrm{hm}} - \frac{dV}{dx} = 0, \tag{5.14}$$

with $\dot{y} = 0$. In the same way as in the FM case, the critical current for the AFM skyrmion to overcome a repulsive potential is obtained by choosing $\dot{x} = 0$ in Eq. (5.14), for the

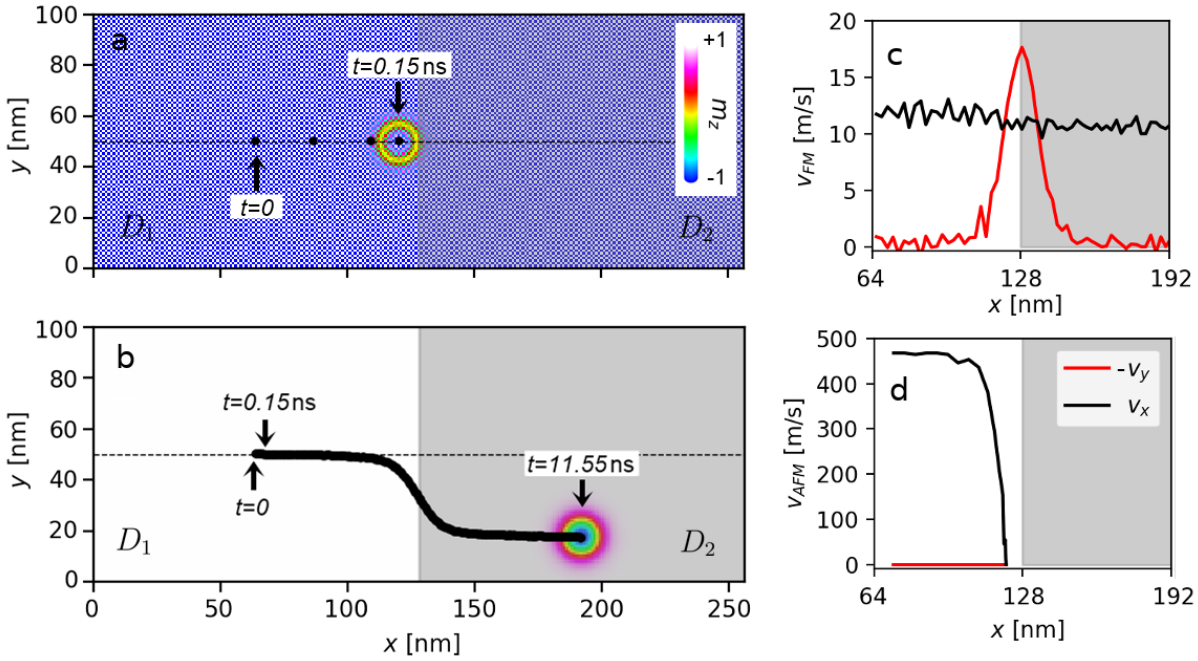

Figure 5.8 – Snapshots of the calculated spin configurations during simulation for the AFM (a) and FM (b) skyrmion driven by the CPP scenario. The trail of black dots indicates the skyrmion trajectory, plotted at intervals of 0.05 ns. (a) The AFM skyrmion reaches the interface after $t = 0.15$ ns, where its movement is completely blocked. (b) The FM skyrmion moves slower than the AFM one, but can cross the interface after sufficiently long time. (c) Center-of-mass velocities of the FM skyrmion, during motion shown in (b). (d) Center-of-mass velocities of the AFM skyrmion, during motion shown in (a). The spin current is applied along the $\hat{z}$ direction but polarized along $+\hat{y}$ ($\hat{j}_{\rm hm} = -\hat{x}$), for the AFM case, and $-\hat{x}$ ($\hat{j}_{\rm hm} = -\hat{y}$) for the FM case, with current density $j = 2 \times 10^{10}$ Am^{-2}, DMI strengths $D_1 = 0.8D_c$ and $D_2 = 0.775D_c$, and damping parameter $\alpha = 0.02$. The center of mass is calculated as the mean point of the region where $m_z = 0$.

maximal value of $F = dV/dx$, i.e.

$$4\pi\mathcal{B}j^c_{\rm hm} = F_{\rm max}, \tag{5.15}$$

which means that the critical current does not depend on α [similar result is obtained for the CIP scenario if one considers $\mathcal{G} = 0$ in Eq. (5.3)]. Therefore, for $\alpha \ll 1$, not only that AFM skyrmion travels faster than the corresponding FM one, but the critical current for the AFM skyrmion to overcome the same energy barrier is much higher than that expected for the FM skyrmion [see Eq. (5.10)]: $j^c_{\rm AFM} = (\mathcal{G}/\mathcal{D}\alpha)j^c_{\rm FM}$. Fig. 5.8 shows the comparison between the AFM and FM skyrmion driven by the CPP scenario in the presence of a DMI interface. The skyrmion is initialized on the left side of the interface, and for the same current density ($j = 2 \times 10^{10}$ Am^{-2}), the AFM skyrmion moves much faster than the FM one, as shown in Fig. 5.8 (c,d), but only the FM skyrmion can cross the interface. This means that the enhanced skyrmion confinement reported in ferromagnetic high-DMI racetracks due to spatially engineered DMI [190] is even more effective for the antiferromagnetic racetracks.

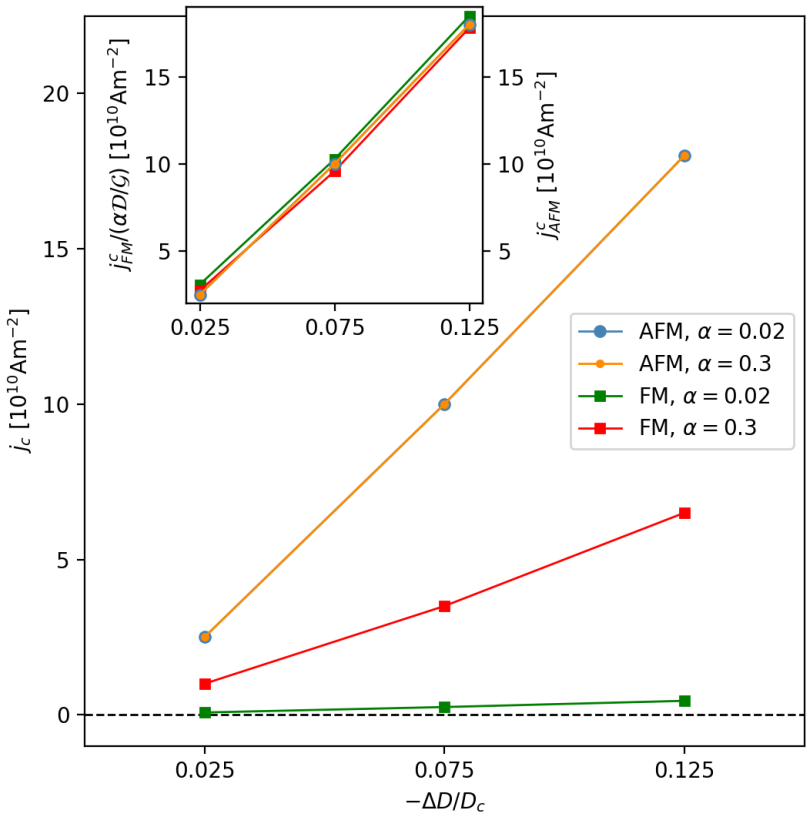

Figure 5.9 – Critical current for the skyrmion to overcome a heterochiral interface in the AFM and FM cases, as a function of ΔD, with $D_1 = 0.8D_c$ fixed. Inset shows that all data collapses on the same curve with appropriate scaling, following Eq. (5.15).

Fig. 5.9 shows the numerically calculated critical current for the skyrmion to overcome the heterochiral interface in the AFM and FM cases, as a function of the difference in DMI across the interface. For the FM case, for lowered damping parameter, the skyrmion moves faster, but the efficiency of the confinement also decreases, which may be a drawback for racetrack applications. However, in the AFM case, the critical current is very large for the considered values of α, as expected from Eq. (5.15). In other words, our results indicate that the AFM skyrmion indeed moves *faster*, yet experiences *stronger* confinement than the FM skyrmion in heterochiral films, especially for systems with weak damping. Both these (seemingly contradictory) features establish AFM skyrmions as a favorable choice for skyrmion-based devices. The values of α considered here are similar to those obtained from experimental results on CoFeB/W systems [93, 202, 208] and Co/Pt layers [196] ($\alpha \approx 0.015$ and $\alpha \approx 0.3$, respectively). The inset in Fig. 5.9 demonstrates the scaling of the critical current of the FM cases to the AFM results, with factor $(\mathcal{D}\alpha/\mathcal{G})$, as expected from the analytic formulae. Here $\mathcal{G} = 4\pi$ and the dissipative term is calculated from the simulations as specified in Appendix B. For the inset in Fig. 5.9 we use $\mathcal{D} = 4.87\pi$, calculated for the skyrmion at rest, in the region with $D_1 = 0.8D_c$. Note that similar results can be obtained from the Thiele equation by considering the external potential due to a "boundary" instead of the heterochiral

interface (as done in Sec. 5.3.1.1).

5.4 Conclusion of the chapter

Recent advances in atomically controlled growth of heterostructures have opened the door to heterochiral structures with spatially engineered DMI, with precisely defined interfaces where DMI changes. In this chapter, we have addressed the expected behavior of skyrmions in such systems, by studying the dynamics of both ferromagnetic and antiferromagnetic skyrmions when encountering a heterochiral interface during their motion. We demonstrated that a local canting of the magnetization, characteristic for the interface where the DMI changes, can strongly deflect the trajectory of a FM skyrmion. We explored the thresholds of this phenomenon both analytically and numerically, and quantified its dependence on the relevant material parameters. These findings are very useful for the controlled manipulation of either single skyrmions or skyrmion chains in skyrmion-based devices (switches, logic gates, memory elements, to name a few) where depending on the applied current one can control which path the skyrmion will take in the corresponding nanoengineered circuit, as exemplified in Sec. 5.3.1.3.

In addition, we showed that such a deflection characteristic for the ferromagnetic skyrmion is completely absent in the antiferromagnetic case. Although this finding is detrimental for the applications of the above effect in AFM systems, we demonstrated that the AFM skyrmion holds other advantages to the FM one - it travels much faster for the given applied current, yet is far better confined in heterochiral films even at high driving currents. This makes AFM skyrmions favorable for skyrmion-based devices in which very fast transfer of information and reliable guidance within specified tracks are essential.

6 Skyrmion-vortex coupling in chiral magnet-superconductor heterostructures

In this chapter, we discuss the coupling of magnetic skyrmions and superconducting vortices in magnet-superconductor heterostructures. First, the effects of skyrmion stray field on a superconducting film is explored by numerical simulations in order to explain experimental observations of the skyrmion-vortex interaction in hybrid material. Next, we use numerical simulations and analytic arguments within London and Thiele formalisms to reveal broader possibilities for manipulating the skyrmion-vortex dynamic correlations in the hybrid system, that are not possible in its separated constituents. We explore the thresholds of particular dynamic phases, and quantify the phase diagram as a function of the relevant material parameters, applied current and induced magnetic torques. Finally, we demonstrate the broad and precise tunability of the skyrmion Hall-angle in presence of vortices, with respect to currents applied to either or both the superconductor and the ferromagnet within the heterostructure. The realization of a strongly interacting skyrmion-vortex system opens a path toward controllable topological hybrid materials, unattainable to date.

The results presented in this chapter are published in Physical Review Letters, **126**, 117205. (2021) and Physical Review B, **100**, 014431. (2019).

6.1 Motivation

The ability to trap and manipulate magnetic skyrmions is of great recent importance for cutting-edge memory devices and information technology [180–183]. Heterostructures often present nontrivial phenomena enabled by the competition or hybridization of the physical properties of its parts. Particularly, magnet-superconductor heterostructures have received much attention in recent years [209–212], either for their possible applications in spintronics [213] and Josephson devices [214–217], or for the rich emergent physics in such systems [218–222]. Recently, theoretical works on chiral

magnet (CM)-superconductor (SC) heterostructures have demonstrated that the stray magnetic field of superconducting vortices may be able to create [223] skyrmions in the magnetic layer, also to trap or repel the preexisting skyrmions [224, 225], depending on vortex polarity. First insights in the dynamic properties of such hybrid systems were also recently provided in Ref. [224]. Furthermore, the combination of the Zeeman field with spin-orbit coupling (SOC) in such systems is suggested for the creation of a topological superconductor hosting Majorana fermions at its boundaries and vortex cores [226–233]. Majorana fermions have great utility in quantum computation. In this way, controlling the nucleation and dynamics of vortices in the presence of skyrmions is an important step to unlocking the potential of SC-CM hybrids for topological [234, 235] and fluxonic [236] quantum computation.

In the following sections we discuss experimental observations of the skyrmion-vortex interaction in SC-CM heterostructures, followed by numerical study of the effects of skyrmion stray field on a superconducting film, where we demonstrate the nucleation of the skyrmion-vortex pair in engineered hybrid material. Next, we provide an detailed analysis and investigate the manipulation of an isolated skyrmion-vortex pair in a SC-CM hybrid, in case of independently biased films (current applied to either CM or SC part). We study the dependence of the net motion of skyrmions and vortices on the viscosities of the host materials, the exerted Lorentz force and magnetic torques by applied current(s), and calculate the skyrmion Hall-angle with respect to currents applied into both superconductor and magnetic films. The results reveal that the skyrmion Hall-angle with respect to current applied into the magnetic film is always greater than that observed in the absence of vortices. We stress the possibility of compensating the skyrmion Hall effect (SHE) in such systems by applying combined currents into both constituent materials of the heterostructure, which is of importance for the facilitated skyrmion guidance in racetrack applications, where the SHE can cause skyrmion to annihilate at the sample edges.

6.2 Stray field and flux of magnetic skyrmions

As we shall see along this chapter, the magnetic stray fields of skyrmions and vortices play crucial role in their interaction. Therefore, in what follows, we introduce the main characteristics of the stray fields for each system.

Let us first consider a single magnetic skyrmion in a chiral magnetic film of thickness d_m. The local magnetic free-energy density is related to the magnetization $\mathbf{M}(x, y) = M_s\mathbf{m}(x, y)$, with M_s the saturation magnetization and $|\mathbf{m}| = 1$. The magnetization profile $\theta = \cos^{-1}(m_z)$ along the skyrmion have approximated solution [237]

$$\theta(r) \approx \pi - \sum_{+,-} \sin^{-1}\left[\tanh\left(\frac{r \pm r_0}{\sigma}\right)\right], \tag{6.1}$$

where r is the distance from the skyrmion center and r_0 and σ represent the domain wall position and width, respectively. The values of r_0 and σ can be obtained by fitting Eq. 6.1 into the magnetization profile obtained from micromagnetic simulations.

The skyrmion stray field at a distance h above the magnetic film surface can be described by means of multipole expansion, and can be written as [238]

$$\begin{aligned} B_z(w,r) &\approx b_0\left[\frac{P}{R^3} - \frac{(2Q+3Pw)w}{R^5} - \frac{5Q}{2}\frac{(r^2-2w^2)w}{R^7}\right], \\ B_r(w,r) &\approx b_0\left[\frac{(Q-3Pw)r}{R^5} - \frac{5Q}{2}\frac{(r^2-2w^2)r}{R^7}\right], \end{aligned} \tag{6.2}$$

where B_z and B_r are the out-of-plane and in-plane components of the stray field respectivelly, and $b_0 = -\mu_0 M_s d_m/2$, $w = h + d_m/2$ and $R = \sqrt{r^2+w^2}$. P and Q are given by

$$\begin{aligned} P &= \int_0^\infty r(\cos\theta - 1)dr, \\ Q &= \cos\gamma \int_0^\infty r^2 \sin\theta dr, \end{aligned} \tag{6.3}$$

where γ is the skyrmion helicity (in our case, $\gamma = 0$ for the Néel skyrmion). Note that for a given skyrmion profile, $\theta(r)$, P and Q are constants.

The magnetic flux ϕ_{sk} generated by the skyrmion can be calculated by integrating the magnetic field [Eq.(6.2)] over the area above the skyrmion, i.e., $\phi_{sk}(w) = 2\pi\int_0^{r_c} B_z(w,r)rdr$, where r_c is the radius of the considered area, from where we obtain

$$\begin{aligned} \phi_{sk}(w) =& 2\pi\left[\Omega_0\left(\frac{1}{R_c} - \frac{1}{w}\right) + \Omega_1(w)\left(\frac{1}{R_c^3} - \frac{1}{w^3}\right)\right. \\ &\left. + \Omega_2(w)\left(\frac{1}{R_c^5} - \frac{1}{w^5}\right)\right], \end{aligned} \tag{6.4}$$

where $R_c = \sqrt{r_c^2 + w^2}$ and

$$\begin{aligned} \Omega_0 &= -b_0 P, \\ \Omega_1(w) &= b_0\left(Pw^2 + \frac{3}{2}Qw\right), \\ \Omega_2(w) &= -\frac{3}{2}b_0 Q w^3. \end{aligned} \tag{6.5}$$

Note that the magnetic flux generated by the skyrmion above the magnetic material depends strongly on the skyrmion size, and it rapidly decreases with the distance from the magnetic film surface.

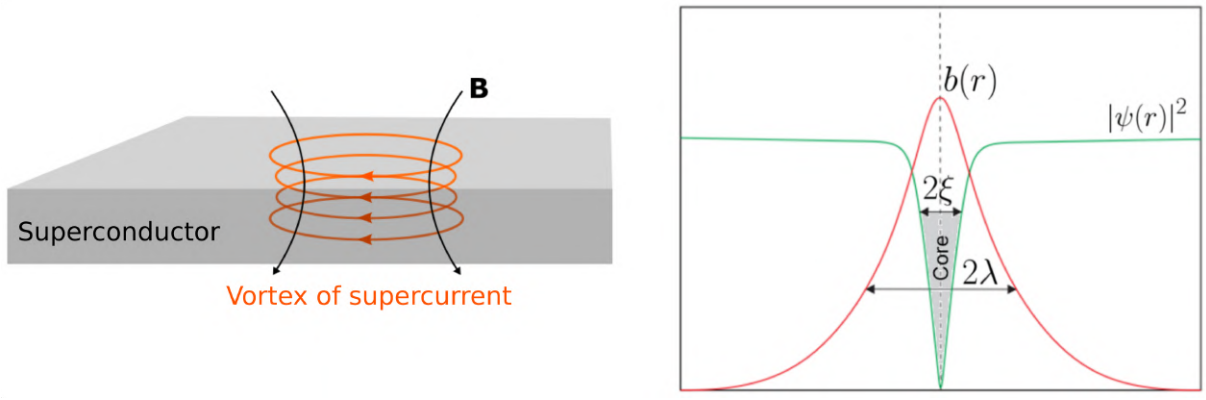

Figure 6.1 – Left: Schematic of a single vortex in the superconducting film. The magnetic field **B** crossing the vortex is shown as black lines. Right: Isolated vortex structure, showing the spatial variations of the induced magnetic field density $b(r)$ and Cooper-pair density $|\Psi|^2$ near the vortex core. Adapted from Ref. [40].

6.3 Stray field of superconducting vortices

When a type II superconductor is subjected to an applied external magnetic field, vortices of supercurrent (also called Abrikosov vortices) [239] emerge in the sample to drive magnetic flux lines across the superconductor [Fig. 6.1]. Each vortex carries a quantum of magnetic flux and, similar to magnetic skyrmions, can move throughout the sample without losing its shape. The stray field of the superconducting vortex can be calculated analytically in the London limit, $\lambda \gg \xi$, where λ and ξ are the superconductor penetration depth and the coherence length, respectively [239]. The general solution for the stray field produced outside the superconducting film of thickness d_s by a straight vortex reads [240]

$$B_r(r,z>0) = \frac{\phi_0}{2\pi\lambda^2}\int_0^\infty dk \frac{kJ_1(kr)}{k^2+\lambda^{-2}} f(k,z), \tag{6.6a}$$

$$B_z(r,z>0) = \frac{\phi_0}{2\pi\lambda^2}\int_0^\infty dk \frac{kJ_0(kr)}{k^2+\lambda^{-2}} f(k,z), \tag{6.6b}$$

where

$$f(k,z) = \tau e^{-kz}\frac{(k+\tau)e^{\tau d_s} + (k-\tau)e^{-\tau d_s} - 2k}{(k+\tau)^2 e^{\tau d_s} - (k-\tau)^2 e^{-\tau d_s}},$$

and $\tau = \sqrt{k^2+\lambda^{-2}}$. Here, $z = 0$ represents the superconductor surface and $r = \sqrt{x^2+y^2}$ the distance from the center of the vortex core. As discussed in Ref. [240], for the case of $d_s \gg \lambda$, the stray field of a single vortex can be approximated, near the superconductor surface, by the field of a magnetic monopole of "charge" $2\phi_0$, where ϕ_0 is the magnetic flux quantum, located at a distance $d_p = 1.27\lambda$ below the superconductor surface. In

this case, the stray field takes the simple form

$$B_r(r,z>0) = \frac{\phi_0}{2\pi}\frac{r}{R^3}, \tag{6.7a}$$

$$B_z(r,z>0) = \frac{\phi_0}{2\pi}\frac{z+d_\mathrm{p}}{R^3}, \tag{6.7b}$$

where $R = \sqrt{r^2+(z+d_\mathrm{p})^2}$ is the distance from the monopole. In Sec. 6.8 we use this approximation in our calculations for the case of thick superconducting films, $d_\mathrm{s} \gg \lambda$, while for small or moderate thicknesses we use the full expression given by Eq. 6.6. For more details, refer to Appendix A.4.

6.4 Experimental observations in [IrFeCoPt]/Nb heterostructures

The skyrmion-vortex interaction in the SC-CM hybrid material can be observed via magnetization and transport measurements in magnetic and superconducting films. In this section, we focus on the experimental observations reported in Ref. [11] for the [IrFeCoPt]/Nb heterostructures, which are the first SC-CM hybrids reported to host stable skyrmions in low fields and temperatures below the superconducting transition. The interaction between skyrmions and vortices can be mediated by two mechanisms: (*i*) exchange coupling, where the skyrmion exchange field combined with interfacial SOC induces circulating spin-polarized supercurrents j_{ex} that interfere with vortex currents [2,3,21–23]; and (*ii*) the interaction between their stray fields. In the first case, the direct contact between superconductor and magnet is required. In the second case, the magnitude of the interaction depends on the material thickness, skyrmion size, and the separation distance between SC and CM layers [24]. These interactions can be further modulated by adjusting the skyrmion/vortex length scales [see Fig. 6.2 (a)]. For example, the stray field coupling is enhanced by increasing skyrmion size, whereas proximity coupling requires j_{ex} and vortex currents j_s to circulate with similar radii, which corresponds to the condition $\xi < r_{sk} < \lambda$, where ξ, λ are the superconducting coherence and penetration lengths [239], and r_{sk} is the skyrmion radius. Since the skyrmion core polarization is antiparallel to the applied magnetic field H, it repels the superconducting vortices which carry magnetic flux-lines parallel with H. However, as we shall see in the following sections, a sufficiently large skyrmion can nucleate an antivortex in the superconductor, thus creating a bound pair of topological states.

Fig. 6.2 (b) shows the SC-CM hybrid samples considered in the experiments. To investigate the different interaction mechanisms, two types of heterostructures are considered: a chiral magnet-superconductor (MS) sample comprised of a Nb layer deposited directly onto a $[Ir_1Fe_{0.5}Co_{0.5}Pt_1]^{10}$ magnetic film (subscripts, e.g. in Ir_1 and $Fe_{0.5}$,

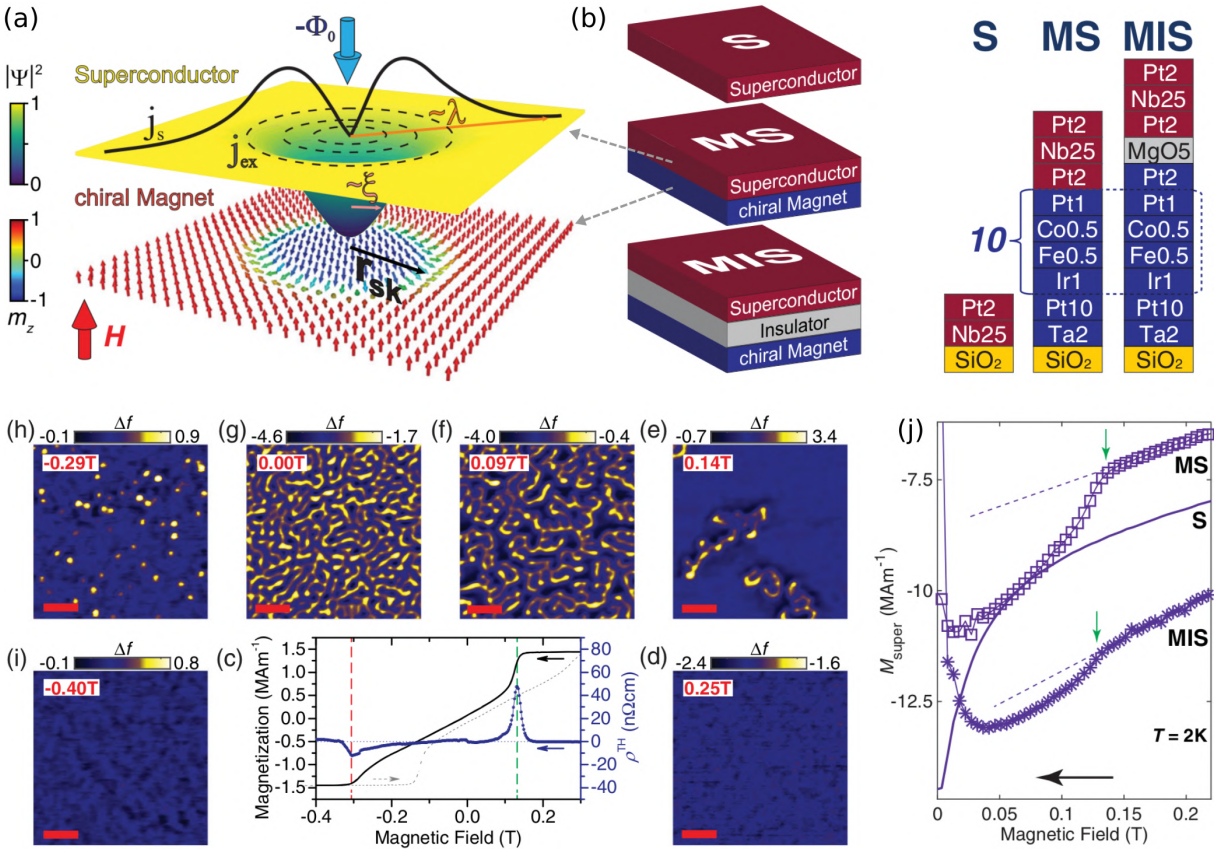

Figure 6.2 – (a) Schematic of a Néel skyrmion in the chiral magnet (bottom layer) in the presence of a (anti)vortex in the superconductor (top layer) with flux $-\Phi_0$ antiparallel to the external magnetic field H. Vortex currents j_s flow at radii up to λ; exchange currents j_{ex} are maximal at r_{sk}, where the local out-of-plane magnetic moment $m_z = 0$. The superconducting order parameter $|\Psi|$ is suppressed over a length ξ in the vortex core. (b) Sample compositions: numbers (e.g., Ir1, Pt2) indicate layer thicknesses in nm and there are 10 stacked repeats of the $[Ir_1Fe_{0.5}Co_{0.5}Pt_1]$ unit. (c) Magnetization $M(H)$ and topological Hall resistivity $\rho^{TH}(H)$ at temperature $T = 5$ K for a $[Ir_1Fe_{0.5}Co_{0.5}Pt_1]^{10}$ film. Arrows indicate field sweep directions; green/red dashed lines indicate skyrmion nucleation/annihilation fields H_{nuc}/H_{ann}, respectively, and the saturation magnetization $M_s = 1.45\,MAm^{-1}$. (d–i) MFM images at $T = 5.5$ K in a bare $[Ir_1Fe_{0.5}Co_{0.5}Pt_1]^{10}$ film during a $H = 0.25\,T \rightarrow -0.4\,T$ sweep. Scale bars are 500 nm; color bars indicate the MFM probe resonance shift Δf in Hz, proportional to m_z. (j) Evolution of the superconducting magnetization $M_{super}(H)$ through H_{nuc}. Data from a reference 25 nm Nb film are labeled S. Green arrows and dashed lines highlight the change in $M_{super}(H)$ below H_{nuc}. Adapted from Ref. [11].

indicate layer thicknesses in nm and there are 10 stacked repeats of the $[Ir_1Fe_{0.5}Co_{0.5}Pt_1]$ unit); and a chiral magnet-insulator-superconductor (MIS) sample, which include a 5 nm insulating MgO layer between SC and CM layers to suppress exchange coupling.

The magnetic properties of the isolated $[Ir_1Fe_{0.5}Co_{0.5}Pt_1]^{10}$ film are summarized in Fig. 6.2 (c). The sample is subjected to applied magnetic field, and by reducing the field from ferromagnetic saturation, a drop in magnetization $M(H)$ coincides with an increase in topological Hall resistivity $\rho^{TH}(H)$, signifying skyrmion nucleation at

$H_{\text{nuc}} \approx 0.14$ T [11, 241]. Magnetic force microscopy (MFM) images taken from descending field scans [Figs. 6.2 (d-i)] reveal isolated skyrmions in fields near the peaks in $\rho^{TH}(H)$ [Fig. 6.2 (e)]. At lower fields, skyrmions proliferate and agglutinate into worm-like structures [Fig. 6.2 (f)], merging into labyrinthine stripes near zero field [Fig. 6.2 (g)]. After field inversion, the stripes eventually split into individual skyrmions [Fig. 6.2 (h)] with a concomitant peak in $\rho^{TH}(H)$, before annihilation at H_{ann} according to previous studies [60–62]. Detailed analysis of the MFM image indicates a typical $r_{sk} = 51 \pm 6$ nm [11]. The thickness $d_s = 25$ nm of the superconducting Nb layer is therefore chosen to optimize skyrmion-vortex coupling by adjusting the superconductor length scales according to the observed skyrmion radius [11].

Fig. 6.2 (j) shows the field dependence of the superconducting magnetization, defined as $M_{\text{super}}(H) = M(H, T < T_c) - M(H, T = 10\text{ K})$, where $T_c = 6.05$ K is the critical temperature of the superconductor. Below H_{nuc}, the chiral film minimizes its free energy by nucleating (negatively magnetized) skyrmionic domains. This coincides with a sharp change in $M_{\text{super}}(H)$ becoming increasingly negative in both MS and MIS samples. In contrast, $M_{\text{super}}(H)$ of a bare 25 nm Nb film (S) evolves smoothly through this field range. The change in M_{super} below H_{nuc} indicates two possible processes in the heterostructures: (*i*) the ejection of vortices (with positive magnetic moment) at the sample edges and (*ii*) antivortex formation with negative moment (parallel to the skyrmion cores).

A threshold for antivortex formation by zero-field skyrmions was derived in Ref. [225], and is given by $M_s \geq \phi_0 \ln(\lambda^2/d_s\xi)/(0.86\pi^2 d_m r_{sk})$, where M_s and d_m are the saturation magnetization and thickness of the magnetic layer, respectively; and ϕ_0 is the magnetic flux quantum. The skyrmions in the [IrFeCoPt]^{10}/Nb heterostructures exceed this threshold by 34% at 2 K. In fact, as we shall see in the following sections, numerical simulations of the hybrid material indicate that the skyrmion stray fields create antivortices in the superconductor, strongly coupling spin and flux topologies in the SC-CM heterostructure.

6.5 Simulated magnetic states in [IrFeCoPt]/Nb heterostructures

To understand the effects of the skyrmion stray field on superconducting film reported in experimental observations in Sec. 6.4, we next perform micromagnetic simulations of the [IrFeCoPt]^{10} multilayers. The stray field of the skyrmionic textures calculated in our simulations can be later used as input for numerical experiments within the Ginzburg–Landau theory, which simulates the response of the superconducting Nb layer.

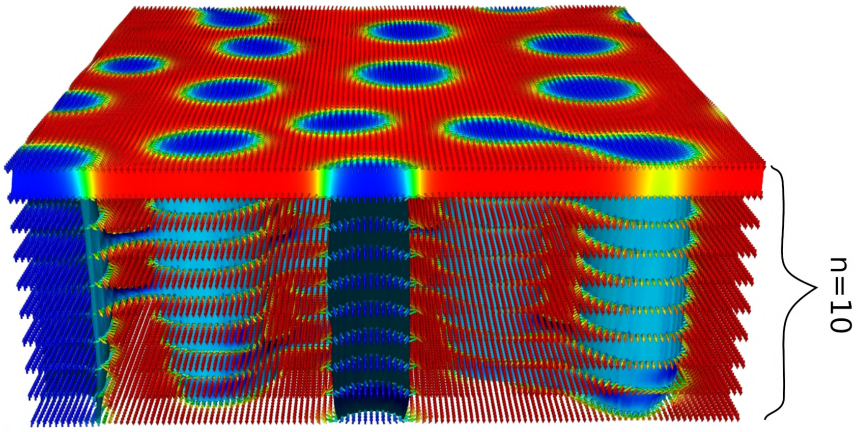

Figure 6.3 – Schematic of a stack of $n = 10$ magnetic layers considered in the simulations. The layers are allowed to interact with each other only by the demagnetizing field.

In the micromagnetic simulations of the chiral ferromagnetic multilayer, we consider a stack of $n = 10$ magnetic layers, each one of thickness 1 nm (representing the Co/Fe layers in the $[IrFeCoPt]^{10}$ system) and separated by 2 nm of vacuum (representing the nonmagnetic I and Pt layers). The layers are allowed to interact with each other only by the demagnetizing field and are discretized in micromagnetic cells of size $4 \times 4 \times 1$ nm^3 [see Fig. 6.3]. For the simulations we consider the parameters: saturation magnetization $M_s = 1.45$ MA/m (determined from experimental data in Ref. [11]); exchange stiffness $A = 13.9$ pJ/m and DMI strength $D = 2.1$ mJ/m^2 (determined by fitting simulated magnetizations to experimental zero-field MFM data; see Ref. [241] for details). The out-of-plane anisotropy $K = 1.4$ MJ/m^3 was determined as the best fitting value which matched the skyrmion nucleation field to the experimental observations.

Fig. 6.4 (a) shows the simulated magnetic phase diagram of the chiral multilayer as a function of applied field H, where the ground state is shaded blue for the helical phase (HL), red for skyrmions (SK) and green for saturated ferromagnetism (FM). The optimal configurations were determined by calculating the free energy for a broad range of HL and SK periodicities at each applied field value. A typical simulated magnetization in the skyrmion phase at $H = 100$ mT is shown in Fig. 6.4 (b). Notice that, even though DMI in the considered system favors skyrmion helicity of $\gamma = 0$ [see, e.g., Sec 2.6.2], the stray field of the multilayer system (which looks like a dipole pointing down) forces the top layer to change its helicity to $\gamma = \pi$, as illustrated in Fig. 6.4 (c), which shows the magnetic texture in a cut through skyrmion core. This indicates that demagnetizing fields play an important role in the magnetic texture, as well as in the skyrmion size (in this case $r_{sk} \approx 46$ nm).

For a better comparison between our simulations and experiments, it is important to subject the simulated superconducting film to a realistic stray field from the chiral magnet. Therefore, for the micromagnetic simulations, we have extracted the magnetic

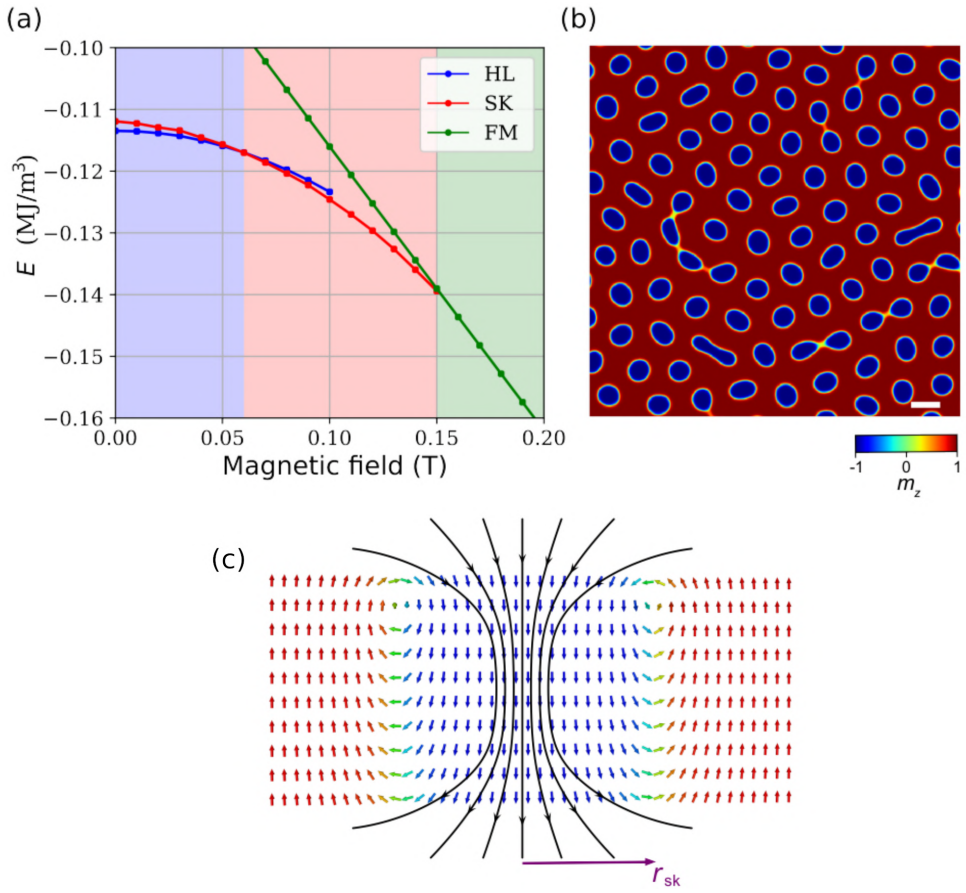

Figure 6.4 – (a) The energy of the magnetic states of a $n = 10$ multilayer as a function of applied field H, as obtained in the simulations. The ground state is indicated by colored shading, with blue for the HL state, red for the SkL state and green for the FM state. (b) Typical ground state magnetic texture obtained in simulations at $H = 0.1$ T. The color bar depicts the out-of-plane magnetic moment m_z averaged over all 10 layers and the white scale bar is 100 nm. (c) Cross-section of the magnetic texture inside the skyrmion core, with the skyrmion stray field shown by black lines.

states from MFM images [see Sec. 6.4] at correspondent applied fields and use those states as initial condition before relaxing magnetization. Fig. 6.5 shows the average magnetization and correspondent magnetic textures obtained in the simulations as a function of applied field. Black solid line in Fig. 6.5 (a) corresponds to the average magnetization obtained experimentally, as shown in Sec. 6.4, which is well reproduced by the simulations.

6.6 Antivortices induced by skyrmions

The response of the superconducting Nb layer to the stray field of the skyrmionic textures can be calculated by numerical experiments within the Ginzburg–Landau (GL) theory [Ref. [11] gives details on the GL calculations]. For that purpose, we calculate the stray field of spin-textures in our magnetic multilayer, at a distance of 7 nm (2 nm Pt + 5 nm MgO) above the film surface, i.e., at the plane of the superconducting

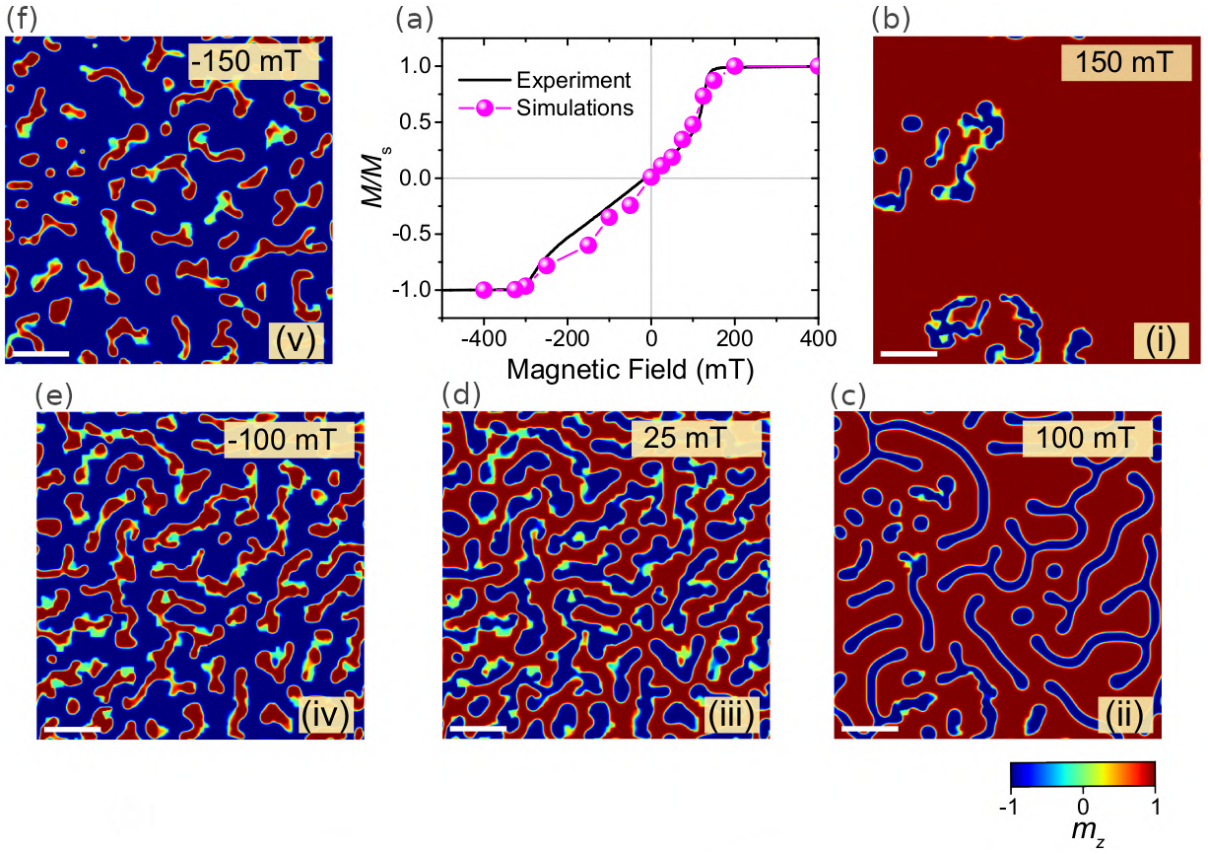

Figure 6.5 – (a) Average magnetization and (b-f) magnetic textures obtained in the simulations as a function of applied field. Black solid line in (a) corresponds to the average magnetization obtained experimentally, as shown in Sec. 6.4, and white scale bars in (b-f) correspond to 250 nm.

layer, according to the fabricated MIS samples [see Sec. 6.4]. Fig. 6.6 (a) shows an oblique view of two skyrmions in the magnetic film and the superconducting film above them, in presence of perpendicular external magnetic field of 125 mT, illustrating the stray field of the skyrmions and its effect on the superconducting film. Both skyrmions generate sufficient flux through the superconductor to induce antivortices there, as indicated by the depreciation of the Cooper-pair density $|\Psi|^2$ (GL simulations are performed for the superconducting parameters referring to the 25 nm thick Nb layer [11]).

Generally speaking, each skyrmion domain carries negative flux, and therefore induces vortex-like screening currents in the superconducting film. Those screening currents are maximal above the domain wall of the skyrmion, and remain visible even upon nucleation of the antivortex within the domain. Moreover, the screening currents keep the antivortex above the skyrmion, separated from the surrounding vortices induced by external magnetic field, as illustrated in Fig. 6.6 (b) (bottom row), where vortices and antivortices are seen as red and blue dots, respectively. The vortex states are obtained by GL simulations, with gradually decreasing the applied field B_{ext} from 150 mT to 0 mT, and using the stray fields of magnetic states corresponding to

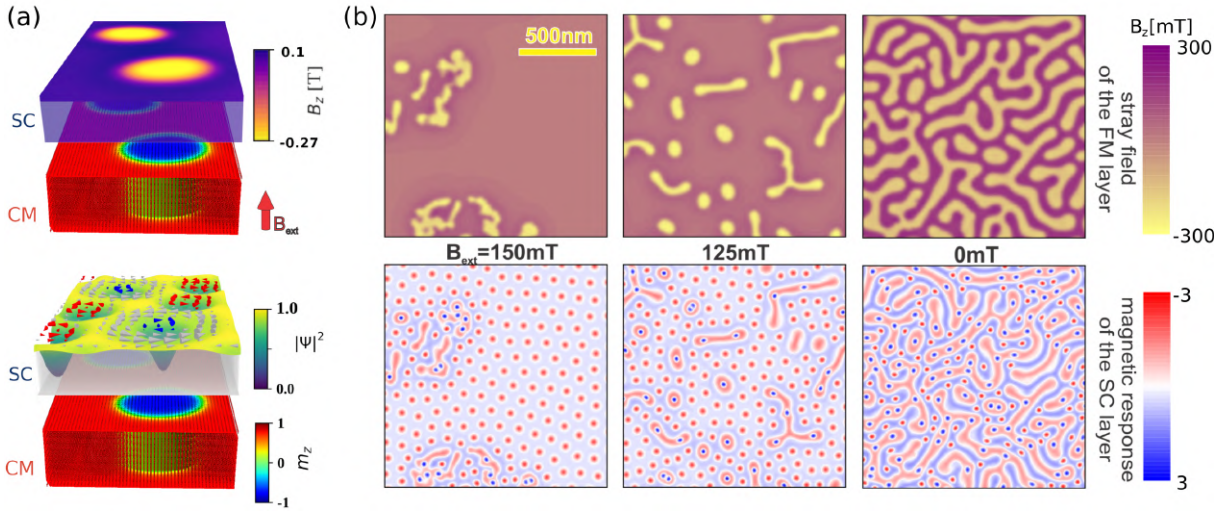

Figure 6.6 – (a) Oblique view of skyrmions in the chiral magnetic (CM) film, bellow the superconducting (SC) film. The top panel illustrates the piercing stray field of skyrmions through the superconducting layer and the bottom panel shows the resulting distribution of the Cooper-pair density ($|\Psi|^2$) and the supercurrents (arrows) in the superconductor. The color of the arrows differentiates the supercurrent of a vortex (red), antivortex (blue), and the screening currents (grey). (b) Top row: the out-of-plane component of the stray field of the magnetic multilayer, calculated at a distance of 7 nm above the film surface, corresponding to the plane of the superconducting layer (according to the fabricated MIS samples). Bottom row: the corresponding magnetic response of the superconducting layer, calculated in the GL simulations for superconducting parameters referring to the 25 nm thick Nb layer. Vortices and antivortices are seen as red and blue dots, respectively. The magnetic states correspond to Fig. 6.5, and the superconducting states are obtained for sequentially decreased B_{ext}.

Fig. 6.5 [see top row of Fig. 6.6 (b)]. At all considered B_{ext}, antivortices are preserved and localized above the skyrmions and stripe domains. Similar behavior is seen in the GL simulations of the MS samples, only with more antivortices nucleated per skyrmion due to larger stray field of the magnetic layer in the plane of the superconductor. In this way, both experiments and simulations indicate that skyrmion stray fields create antivortices in the superconductor.

6.7 Effect of the skyrmion stray field on vortex dynamics

In what follows, we briefly discuss the scenario where direct (dc) current is applied to the superconducting film in the above considered heterostructure. It is well known that under applied current the vortices in the superconductor are moved by Lorentz force, which acts perpendicularly to the direction of the applied current [239]. Interestingly, the stray field of magnetic skyrmions significantly affects the vortex dynamics. When skyrmions are present, the vortex flow interacts with the induced antivortices. As discussed earlier, vortices avoid the negative field of skyrmions while

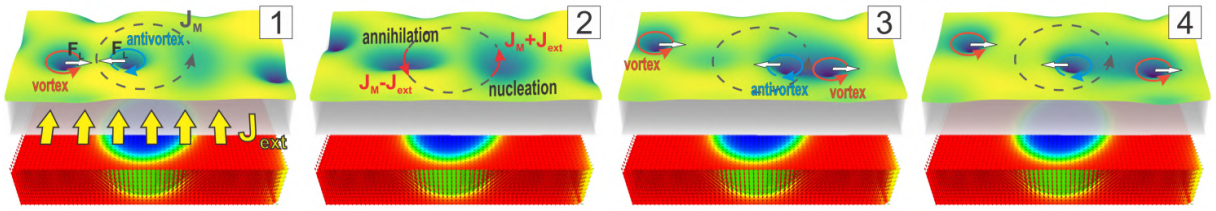

Figure 6.7 – Effect of the skyrmion stray field on vortex dynamics, showing sequential snapshots of the simulated Cooper-pair density as a function of time, for $H = 100$ mT. In each snapshot the lower layer shows the magnetic moments in the chiral magnetic layer, while the upper layer shows the Cooper-pair density in the superconducting film. The dashed line indicates the position and direction of maximal supercurrent flow.

simultaneously repelling each other. This makes it difficult for the vortices to find the optimal path to move through the sample, and they end up having to pass through the skyrmions, which results in the scenario shown in Fig. 6.7. That is, the applied current j_{ex} superimpose on the screening currents j_M that are maximal above the domain wall of a skyrmion, lowering the screening currents on one side (from which the vortex is approaching) and enlarging it on the other (snapshot 1). That leads to the annihilation of the skyrmion-induced antivortex and the incoming vortex (snapshot 2). On the opposite side of the skyrmion, as the current density exceeds the depairing current, a vortex-antivortex pair is created (snapshot 3). The antivortex remains under the skyrmion while the vortex takes the role of the incoming vortex and continues the journey (snapshot 4).

6.8 Manipulation of isolated skyrmion-vortex pair

In order to provide an in-depth analysis and investigate the manipulation of skyrmion-vortex pair (SVP) correlations, from now on through the end of this chapter, we consider a single magnetic skyrmion interacting with a single superconducting vortex in a magneto-superconducting bilayer. Fig. 6.8 illustrates the considered system, an ultrathin ferromagnetic (FM) film of thickness d with perpendicular magnetic anisotropy, e.g., a Co layer, coupled to a heavy metal (HM) layer (with a strong spin-orbit coupling, thus inducing interfacial DMI) e.g., the heavy metal Pt (neither Co nor Pt are superconductors at ambient pressure), placed on top of a superconducting film of thickness d_s, and separated by an insulating layer of thickness d_I. The interaction between the superconducting material and the FM film is solely through the magnetic stray fields.

In this section, we do not consider the creation of (anti)vortices in the superconductor, as discussed in the previous sections. Instead, we focus on a pre-existing skyrmion-vortex pair and explore the dynamics of the magnetic skyrmion when coupled

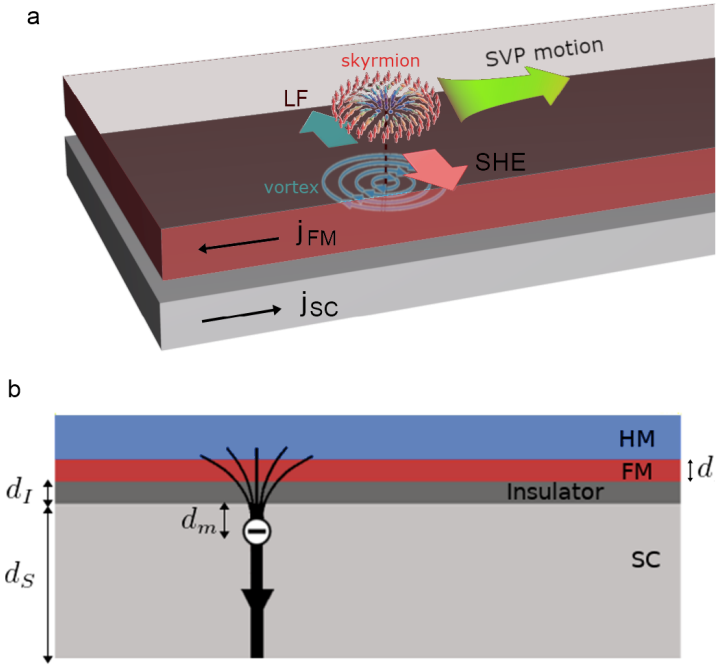

Figure 6.8 – (a) Oblique view of the considered heterostructure. By tuning the competition between the Lorentz force (LF), acting on the superconducting vortex, and the magnetic torques acting on the skyrmion, one can control the resultant skyrmion Hall effect (SHE) and the net direction of the skyrmion-vortex pair (SVP) motion. (b) Schematic details of the considered system, a thin ferromagnetic (FM) film of thickness d with perpendicular magnetic anisotropy, coupled to a heavy metal (HM) layer with a strong spin-orbit coupling, placed on top of a superconducting (SC) film of thickness d_s, separated by an insulating layer of thickness d_I, such that the interaction between the superconducting and the ferromagnetic film is restricted to only the magnetic stray fields.

to the superconducting vortex. We rely on the London approximation [Sec. 6.3] and molecular dynamics simulations to describe the vortex behavior in the superconducting layer, and the stray magnetic field of the (moving) vortices is used in the micromagnetic framework to understand the static and dynamic response of the ferromagnetic layer and skyrmion therein. For a description of the dynamic phases of the heterostructure as a whole, we couple the molecular dynamics of vortices with the Thiele equation of motion of skyrmions [Sec. 2.7.3]. In what follows, we give a short description of the key ingredients in our theoretical analysis.

6.8.1 Micromagnetic model

For the micromagnetic simulations of the chiral ferromagnetic layer, we consider the free energy resulting from the following magnetic interactions [Sec. 3.1.3]: exchange interaction, perpendicular anisotropy, DMI, Zeeman interaction and demagnetization. We approximate the demagnetization energy by using an effective anisotropy $K_{\text{eff}} = K - \frac{1}{2}\mu_0 M_s^2$, with K the perpendicular magnetic anisotropy and μ_0 the vacuum permeability,

which is justified for the case of ultrathin ferromagnetic films [16]. For the simulations of the ultrathin ferromagnetic film We consider the following parameters: saturation magnetization $M_s = 580\ \mathrm{kAm^{-1}}$, exchange stiffness $A_{ex} = 15\ \mathrm{pJm^{-1}}$, and perpendicular anisotropy $K = 0.8\ \mathrm{MJm^{-3}}$ ($K_{eff} = 0.6\ \mathrm{MJm^{-3}}$), stemming from the experimental results on Co/Pt systems [196, 197]. The used values of the DMI constant, D, will be specified in the sections below, for what is useful to define the critical DMI strength $D_c = 4\sqrt{A_{ex}K_{eff}}/\pi$ above which spin-cycloids become the ground-state in the ferromagnetic sample [186]. The Zeeman interaction accounts for the external magnetic field $\mathbf{B}$, which in this case will be given by the vortex stray field. For all simulations, we consider a system discretized into cells of size $1 \times 1 \times 0.4\ \mathrm{nm^3}$, with $d = 0.4$ nm the thickness of the FM film, and the dynamics of the magnetization is governed by the LLG equation [Eq. 2.17].

6.8.2 Equation of motion for the center-of-mass of the skyrmion

Thiele equation describes the dynamics of the center-of-mass of the skyrmion by assuming a rigid body motion of the spin texture [81, 93, 95, 96]. For the case of in-plane applied current the Thiele equation reads [see Sec. 2.7.3]

$$\mathbf{G} \times (\boldsymbol{\nu} - \dot{\mathbf{r}}_{sk}) + \mathcal{D}(\beta\boldsymbol{\nu} - \alpha\dot{\mathbf{r}}_{sk}) - \nabla V = 0, \tag{6.8}$$

where $\mathbf{G} = \mathcal{G}\hat{z} = 4\pi Q(dM_s/\gamma)\hat{z}$ is the gyromagnetic coupling vector, with Q the skyrmion number (in all simulations we consider $Q = -1$); $\dot{\mathbf{r}}_{sk} = \dot{x}_{sk}\hat{x} + \dot{y}_{sk}\hat{y}$ is the skyrmion drift velocity; V is the potential induced by the vortex field; $\boldsymbol{\nu} = \nu_x\hat{x} + \nu_y\hat{y}$ is associated to the velocity of the conduction electrons in the spin-polarized current, and $\mathcal{D}$ represents the dissipative tensor, with components $\mathcal{D}_{ij} = (dM_s/\gamma)\int d^2r\,\partial_i\mathbf{m}\cdot\partial_j\mathbf{m} = \mathcal{D}\delta_{ij}$ (see Appendix A.2). Eq. (6.8) can be rewritten into its two components, which yields

$$\begin{aligned}
\dot{x}_{sk} &= \frac{1}{\sigma_{\alpha\alpha}^2}\left[\sigma_{\alpha\beta}^2\nu_x + \mathcal{D}\mathcal{G}(\beta-\alpha)\nu_y + \alpha\mathcal{D}F_{sv}^x + \mathcal{G}F_{sv}^y\right], \\
\dot{y}_{sk} &= \frac{1}{\alpha\mathcal{D}}\left[\mathcal{G}(\nu_x - \dot{x}_{sk}) + \beta\mathcal{D}\nu_y + F_{sv}^y\right],
\end{aligned} \tag{6.9}$$

where $\sigma_{ab} = \sqrt{\mathcal{G}^2 + ab\mathcal{D}^2}$, $F_{sv}^x = -\partial V/\partial x$, and $F_{sv}^y = -\partial V/\partial y$.

6.8.3 Static properties of the hybrid system

6.8.3.1 Effects of the vortex field on the uniform ferromagnetic state

Let us first consider the effects of the magnetic field of the vortex in the superconductor to the uniform ferromagnetic state in the adjacent magnetic film. Fig. 6.9 shows the magnetization profile obtained from micromagnetic simulations of a ferromagnetic film in the presence of the stray field of a single vortex [see Sec. 6.3] in a thick superconducting film ($d_s \gg \lambda$), for different values of the penetration depth λ of the

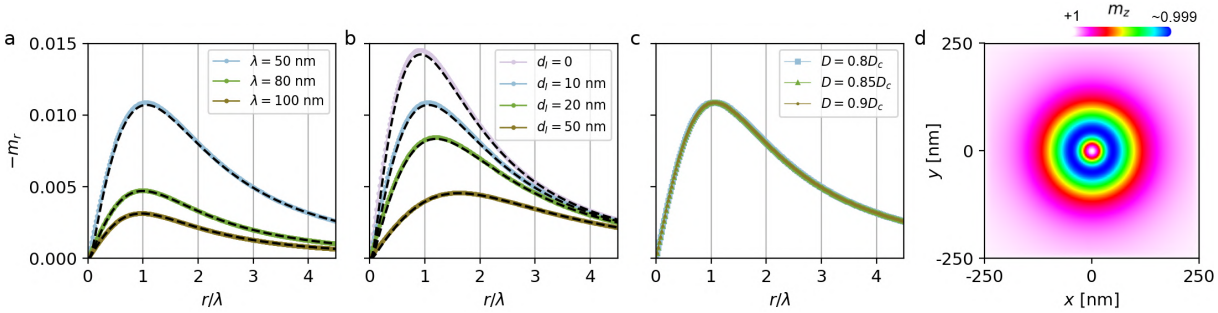

Figure 6.9 – Canting induced in the uniform ferromagnetic state of the FM film due to the stray field of the nearby superconducting vortex, as a function of the distance from the vortex core. (a) For different values of penetration depth λ of the superconductor, with $d_I = 10$ nm and $D = 0.8D_c$ fixed. (b) For different values of d_I, with $\lambda = 50$ nm and $D = 0.8D_c$ fixed. (c) For different values of D, with $\lambda = 50$ nm and $d_I = 10$ nm fixed. Dashed lines indicate the corresponding magnetization profiles obtained analytically using Eq. (6.13). (d) Contourplot of the z-component of the magnetization in the vicinity of the vortex core (centered at $(x,y) = (0,0)$), for $\lambda = 50$ nm, $d_I = 10$ nm, and $D = 0.8D_c$.

superconductor, thickness of the insulating layer d_I, and DMI strength D. The polarity of the magnetic field of the vortex is taken to be negative (pointing along the $-\hat{z}$ direction).

Note that for small values of λ, where the magnetic flux induced by the vortex is more localized, the corresponding canting of the magnetization in the FM film is more pronounced. Also notice that, for the parameters considered in this section, the presence of the superconducting vortex does affect the ferromagnetic ground state, but it is not sufficient to nucleate a skyrmion as e.g. considered in Ref. [223]. In fact, assuming weak variations of the local spin tilt angle θ, the magnetization profile induced by the stray field of the vortex can be calculated by considering the micromagnetic energy density in polar coordinates [242]

$$\begin{aligned} E^{2D}[\theta(r)] =& 2\pi \int_0^\infty \Bigg[A_{\text{ex}} \left(\frac{d\theta}{dr}\right)^2 + A_{\text{ex}} \frac{\sin^2\theta}{r^2} \\ & - D\left(\frac{d\theta}{dr} + \frac{\cos\theta \sin\theta}{r}\right) \\ & + K_{\text{eff}} \sin^2\theta - M_s B_r \sin\theta - M_s B_z \cos\theta \Bigg] r dr, \\ =& \int_0^\infty \mathcal{E}\left(\theta, \frac{d\theta}{dr}, r\right) dr, \end{aligned} \tag{6.10}$$

where we assumed $\mathbf{m} = \sin\theta\hat{r} + \cos\theta\hat{z}$, and $\mathbf{B}_v = B_r\hat{r} + B_z\hat{z}$ is the stray field of a vortex located at $r = 0$. In the limit of weak variations of the angle θ ($\frac{d\theta}{dr} \ll 1$ and $\theta \ll 1$), the energy density can be written as

$$\begin{aligned}\mathcal{E}(\theta,\theta',r) = 2\pi r \Bigg[& -D\theta' + \theta^2 \left(\frac{A_{\text{ex}}}{r^2} + K_{\text{eff}} + \frac{M_s B_z}{2} \right) \\ & + \theta \left(-\frac{D}{r} - M_s B_r \right) - M_s B_z + \mathcal{O}(\theta^3) + \mathcal{O}(\theta'^2) \Bigg],\end{aligned} \tag{6.11}$$

where $\theta' = d\theta/dr$. The Euler-Lagrange equation

$$\frac{\partial \mathcal{E}}{\partial \theta} - \frac{d}{dr}\left(\frac{\partial \mathcal{E}}{\partial \theta'} \right) = 0 \tag{6.12}$$

minimizes the energy functional and yields the following expression for the magnetization profile:

$$\theta(r) = \frac{B_r(r) M_s}{\frac{2A_{\text{ex}}}{r^2} + 2K_{\text{eff}} + B_z(r) M_s}. \tag{6.13}$$

Fig. 6.9(a,b) shows that the above expression (dashed lines) nicely agrees with the magnetization profile obtained in the micromagnetic simulations. Fig. 6.9(c) shows that, as suggested by Eq. (6.13), $\theta(r)$ does not depend on the DMI parameter. Notice that this expression is valid for any radial field such as that created by superconducting vortices, magnetic dots, or nearby magnetic tips, provided that the uniform magnetic order is only weakly perturbed. It will be useful now to define the radius of maximal canting, $r_\theta^{\max}$, as given by $\theta(r_\theta^{\max}) = \max[\theta(r)]$. For the case of $d_I = 10$ nm and $\lambda = 50$ nm, we find $r_\theta^{\max} \approx \lambda$. From here on, $d_I = 10$ nm will be used in all remaining calculations, unless stated otherwise.

6.8.3.2 Effects of the vortex field on the skyrmion size

The stray field of the vortex can affect the skyrmion size by favoring the rotation of the spin texture in the direction of the flux lines, where the competition with other magnetic interactions is relevant. For simplicity, we will only consider variation of the DMI strength and fix all the remaining parameters of the ferromagnetic material. By increasing the DMI strength one favors the rotation of the magnetization at short length scales and reduces the energy barrier for the vortex field to flip the spins along its direction, resulting in an increase of the skyrmion size. Fig. 6.10 shows how the skyrmion size, calculated by micromagnetic simulations, is affected by the stray field of a single vortex in a thick superconducting film ($d_s \gg \lambda$), for different values of D and λ, where skyrmion and vortex are on top of each other and concentric. For each λ, if $D \leq D_\lambda^*$, the skyrmion radius ξ_{sk} is confined in a region $\xi_{\text{sk}} < r_\theta^{\max}$, and increases its size abruptly to $\xi_{\text{sk}} > r_\theta^{\max}$ when D exceeds D_λ^*. The threshold state, where $\xi_{\text{sk}} \approx r_\theta^{\max}$, is unstable. From the simulations we calculate $D_\lambda^* \approx 0.882 D_c$, $0.9275 D_c$ and $0.945 D_c$ for $\lambda = 50$, 80 and 100 nm respectively. Notice that there is a range of DMI ($D < 0.85 D_c$ for all considered λ's) where the skyrmion size is weakly affected by the presence of the superconducting vortex and ξ_{sk} approximately corresponds to the

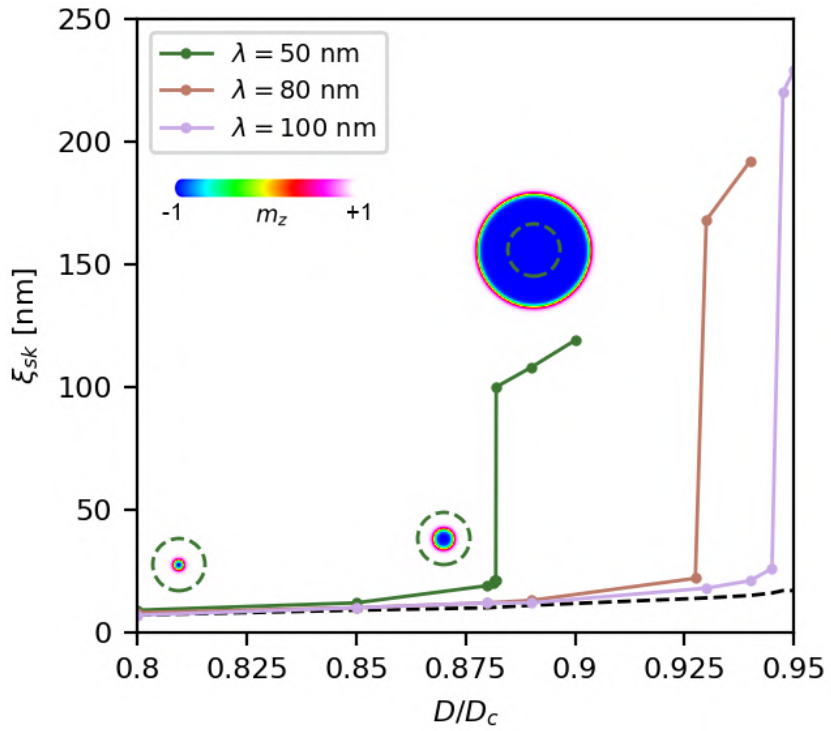

Figure 6.10 – Skyrmion radius when on top of a superconducting vortex, extracted from the micromagnetic simulations, as a function of the DMI strength D. Dashed line shows the skyrmion size in the absence of an external magnetic field. The insets show the z component of the magnetization for $\lambda = 50$ nm, where dashed circles represent $r = r_\theta^{\max}$ i.e. area where vortex core has strongest influence on the ferromagnetic state.

skyrmion size in the absence of any magnetic field (dashed line in Fig. 6.10). In this case, the interaction energy is dominated by the difference in Zeeman energy due to the presence of the vortex stray field. Nevertheless, the other terms are highly sensitive to the change in the skymion shape and thereby give a non-negligible contribution to the total vortex-skyrmion interaction energy (see Appendix A.4).

6.8.3.3 Skyrmion-vortex interaction

As shown in the previous section, the skyrmion-vortex interaction is stronger when the domain wall of the skyrmion faces the maximal background canting, i.e., when the skyrmion core is at a distance $r_c \approx |r_\theta^{\max} - \xi_{\text{sk}}|$ from the vortex core. To numerically calculate the spatial profile of the interaction energy between the skyrmion and the superconducting vortex, we relax the magnetization in the micromagnetic simulation for different positions of the vortex stray field, while keeping the magnetic moment at the center of the skyrmion fixed, at a fixed location. This approach is similar to the method used in Refs. [243–245] to calculate the interaction of the skyrmion with holes, sample edges, or material defects. We consider the case of $D \leq 0.85 D_c$, where the skyrmion profile is weakly perturbed by the presence of the vortex field (see Fig. 6.10). In such a

situation we are sure that the fixed core will indeed represent the center of mass of the skyrmion after relaxing the magnetization. Fig. 6.11(a,b) shows the interaction energy calculated in these simulations, as a function of the distance between the skyrmion and vortex cores, r_{sv}, for different values of λ and DMI strength D, with $d_s \gg \lambda$. Notice that the obtained energy profile can be fitted numerically by the expression

$$E = \frac{a}{(r_{sv}^2 + b\lambda^2)^2}, \tag{6.14}$$

with a and b the fitting parameters. The fitted curves are shown as dashed lines in Fig. 6.11(a,b). Insets show the corresponding interaction forces derived from Eq. (6.14).

For further analysis, we fix $\lambda = 50$ nm and $D = 0.8D_c$ in the simulations, unless specified otherwise.

The vortex in the superconducting film is assumed to be stabilized by an external, perpendicular magnetic field, which also should be considered in the free energy of the magnetic spin texture. In this section, we consider a sparse vortex lattice, hence small fields, of the order 0.1 mT or smaller. In this limit, the induced vortices are separated by distances larger than 5 μm (see, e.g., Ref. [246]), which is much larger than the length scale λ of the skyrmion-vortex interaction. This situation therefore closely approaches the idealized case of an isolated skyrmion-vortex pair considered in our calculations. In addition, we have verified that external magnetic fields up to 5 mT produce a negligible change in the skyrmion morphology for the considered magnetic parameters of the sample, justifying our analysis in absence of the external magnetic field.

6.8.4 Skyrmion dynamics in the presence of a superconducting vortex

6.8.4.1 Vortex at rest

We start by describing the motion of the skyrmion induced by the interaction with a pinned vortex in a thick superconducting film ($d_s \gg \lambda$), without any other applied drive. Fig. 6.11(c) shows the center-of-mass trajectories of the skyrmion in the presence of the vortex field, calculated in the micromagnetic simulations with damping parameter $\alpha = 0.02$ and 0.3, where the vortex position is fixed at the center of the simulation box and the skyrmion is initialized at a distance $r_{sv} = 2.4\lambda$ from the vortex core. As shown in energetic considerations of the previous section, the skyrmion is indeed attracted to the vortex core. A deflection in the azimuthal φ direction is induced by the Magnus force (φ is the angular cylindrical coordinate with origin at the vortex core position), and the skyrmion follows a spiral trajectory towards the center of the vortex. Damping factor α controls the magnitude of the Magnus force relative to the viscous drag and consequently the shape of the spiral trajectory. Similar trajectories are observed, e.g., for the skyrmion approaching a pinning center [244, 247].

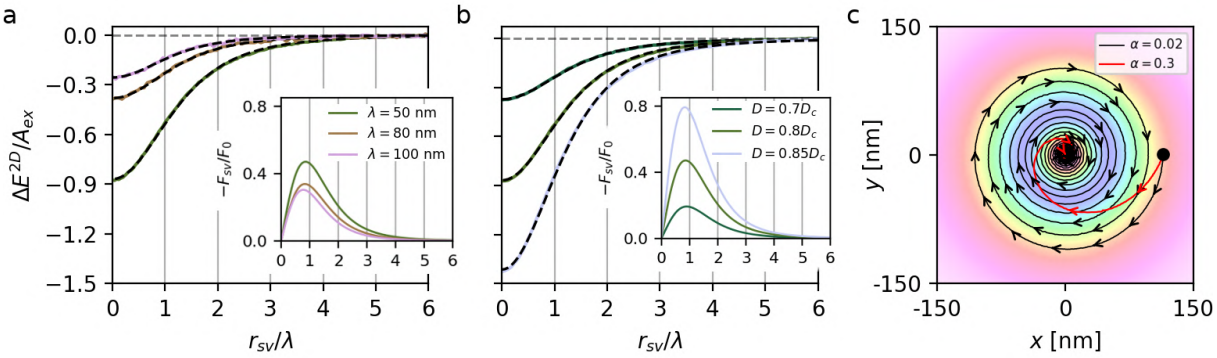

Figure 6.11 – Skyrmion-vortex interaction energy calculated in the micromagnetic simulations as a function of the distance between the skyrmion and vortex cores for (a) different values of λ and fixed $D = 0.8D_c$, and (b) different values of D and fixed $\lambda = 50$ nm. The curves fitted by Eq. (6.14) are shown as dashed lines. Insets show the corresponding interaction force calculated as the derivative of the fitted curves, where $F_0 = dA_{ex}/\lambda_0 = 0.12$ pN, with $\lambda_0 = 50$ nm. (c) Trajectory of a skyrmion dynamics in the presence of the vortex field, for $\alpha = 0.02$ and 0.3, $\lambda = 50$ nm, and $D = 0.8D_c$. Black dot indicates the initial position of the skyrmion and the arrows the center-of-mass trajectories. Background colors show the z component of the magnetization induced by the vortex in absence of a skyrmion, as shown in Fig. 6.9(d).

6.8.4.2 Vortex at constant speed

Let us next consider that a uniform current density, j_{SC}, is applied into a conventional superconducting material. The current induces a Lorentz force $\mathbf{F}_L = d_s\phi_0\mathbf{j}_{SC} \times \hat{z}$, which acts on the vortex core, thus forcing the vortex to move and, consequently, inducing the skyrmion motion as well. As a first approximation, in this section we neglect the effects of the skyrmion to the vortex motion and consider the vortex to move straight along the Lorentz force at a constant speed given by $v = F_L/\eta$, where η is the vortex viscous drag coefficient. As we shall discuss in more detail in Sec. 6.8.4.3, this is a good approximation only when both the driving force and the viscous drag acting upon the vortex are much stronger than the vortex-skyrmion force.

We performed micromagnetic simulations initializing the magnetic skyrmion concentric to the vortex core and then moving the vortex field, in a rigid body motion, along the $+\hat{x}$ direction, with constant velocity v. Fig. 6.12(a) shows the corresponding trajectories of the skyrmion for different values of v and for damping constant $\alpha = 0.02$. The skyrmion moves in cycloidal arcs created by the competition between the movement along the $\hat{x}$ direction imposed by the driven vortex and the deflection along the φ direction with respect to the vortex. The maximal amplitude of the cycloidal trajectory is approximately λ, which coincides with the maximal canting region defined by $r_\theta^{\max}$. For v higher than an escape velocity, v_c, the skyrmion crosses the $r = r_\theta^{\max}$ region and escapes from the confinement by the vortex field. The maximal amplitude Δy of the skyrmion trajectory as a function of the vortex velocity is shown in Fig. 6.12(c) for

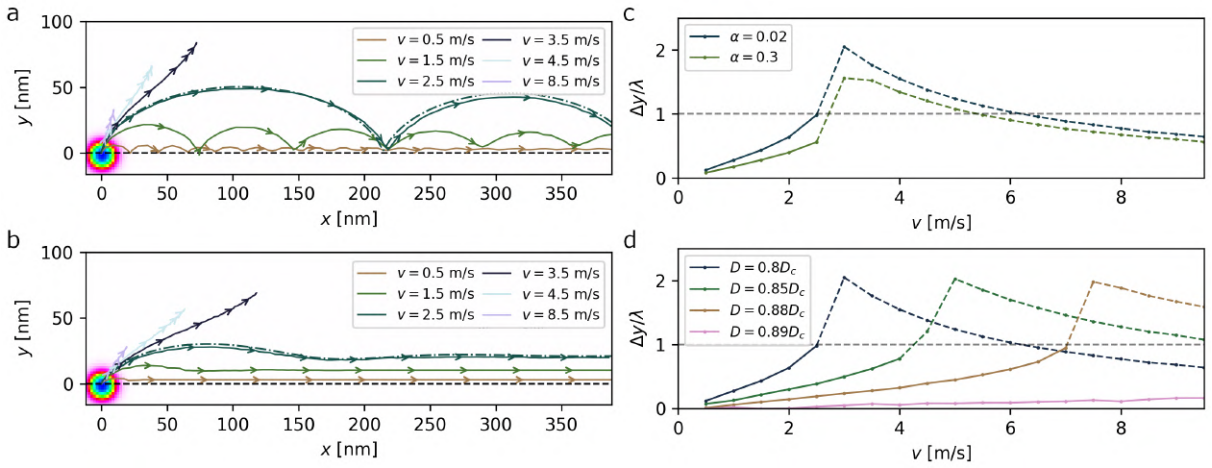

Figure 6.12 – Trajectories of the center of mass of the skyrmion calculated in the micromagnetic simulations for different values of the driven vortex velocity v, with damping factor $\alpha = 0.02$ (a), or $\alpha = 0.3$ (b). (c) Maximal amplitude of the skyrmion trajectory as a function of v, for different values of α, with fixed $D = 0.8D_c$. (d) Maximal amplitude of the skyrmion trajectory as a function of v for different values of the DMI strength and $\alpha = 0.02$ fixed. Transition from solid to dashed line indicates the escape velocity. Dash-dotted lines in (a) and (b) correspond to solutions of the Thiele equations for the case $v = 2.5$ m/s (see text).

$\alpha = 0.02$ and 0.3, with $D = 0.8D_c$ fixed, and in Fig. 6.12(d) for different values of D and $\alpha = 0.02$ fixed. In the latter case, for $D > D^*_\lambda$ one has $\xi_{sk} > r^{max}_\theta$ and the skyrmion trajectory no longer presents periodic arcs during the motion. Notice that the escape velocity does not change considerably by changing from low to high damping regime, however it strongly depends on the DMI parameter, as expected from the interaction force in Sec. 6.8.3.3.

Similar cycloidal motion has been observed in Ref. [248] for a moving magnetic field, where the authors stated that the skyrmion follows a periodic motion. However, notice from Fig. 6.12(a) that the amplitude of the cycloidal arcs decreases as the skyrmion moves further. In fact, by increasing the damping factor the dynamics changes from underdamped to overdamped motion, as show in Fig. 6.12(b) for $\alpha = 0.3$. Therefore, the cycloidal motion is a transient motion, after which the trajectories converge to a situation where the skyrmion moves along with the vortex, keeping a constant nonzero distance from the vortex core position (thick dashed lines in Figs. 6.12(a,b)). This indicates that the vortex core is no longer the minimal energy position for the skyrmion in the dynamical system as it is for the system with a stationary vortex ($v = 0$).

The above behavior is better understood in the frame of reference of the moving superconducting vortex. Fig. 6.13 shows the trajectories (indicated by arrows) of the center-of-mass of the skyrmion calculated in the micromagnetic simulations for different values of the vortex velocity, v, for $\alpha = 0.02$ or 0.3, in the frame of reference of the moving vortex. Each trajectory corresponds to a different initial position of the skyrmion

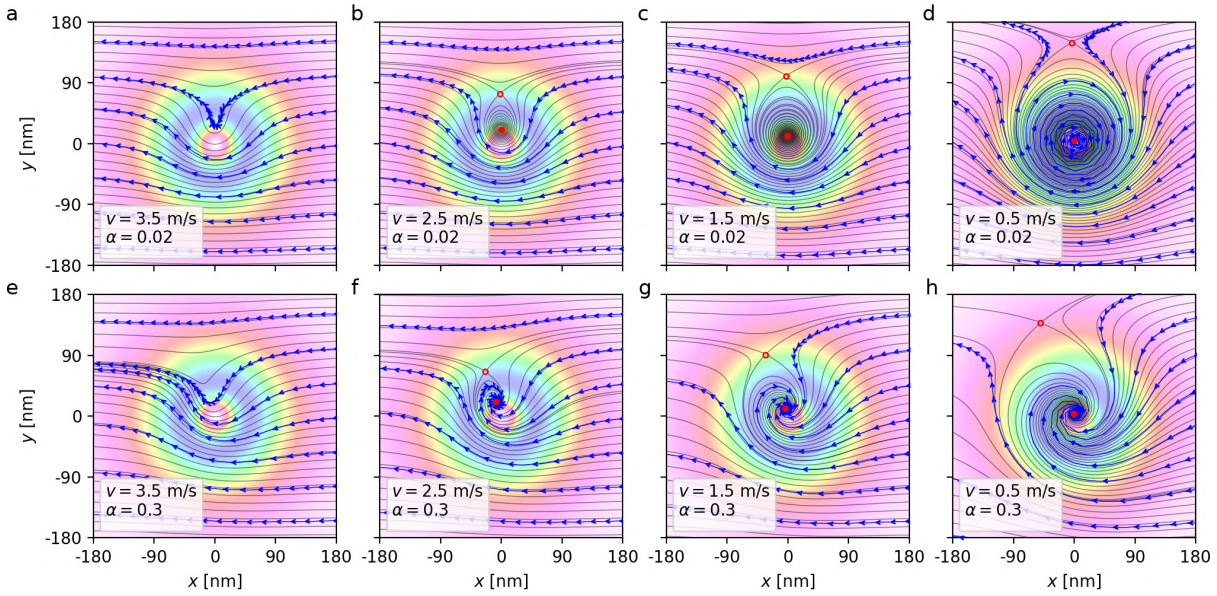

Figure 6.13 – Arrows show the skyrmion trajectories calculated in the micromagnetic simulations for different values of the vortex velocity, v, with $\alpha = 0.02$ (a-d) and 0.3 (e-h), plotted in the frame of reference of the moving vortex. Thin lines are the corresponding trajectories calculated from the Thiele equation. Dots show the fixed points, where open dots indicate saddle points and closed dots represent stable spiral points. Background colors show the z component of the magnetization induced in the absence of a skyrmion, as shown in Fig. 6.9(d).

with respect to the vortex core position. Notice that each point of the coordinate space belongs to a unique and well defined trajectory which converges to a fixed point or to infinity. Such dynamical behavior can be described in the Thiele formalism by the equation of motion for the center of mass of the skyrmion (see Sec. 6.8.2). In this frame of reference, the magnetic system is moving with velocity $-v\hat{x}$ with respect to the vortex and the skyrmion dynamics can be equivalently described by the situation where a spin-polarized current is applied into the ferromagnetic film along the $\hat{x}$ direction in the particular case where $\alpha = \beta$, and the vortex is at rest. In this case, in regions far from the vortex core, where $\partial V/\partial r = 0$, the skyrmion velocity is given by $\dot{\boldsymbol{r}}_{\rm sk} = \boldsymbol{v} = -v\hat{x}$. As the skyrmion approaches the vortex, its trajectory can be attracted by one of the fixed points, $\{\mathbf{r}^*\}$, which can be calculated by setting $\dot{\mathbf{r}}^*_{\rm sk} = 0$ in Eq. (6.9). In cylindrical coordinates,

$$\varphi^* = \arctan\left(\frac{\mathcal{G}}{\alpha\mathcal{D}}\right) + n\pi \quad (\text{for } v \neq 0), \tag{6.15a}$$

$$\left.\frac{\partial V}{\partial r}\right|_{r^*} = \pm\sigma_{\alpha\alpha} v, \tag{6.15b}$$

where $n = 0,1,2,\ldots$ represent the solutions for both vortex ($-\frac{\partial V}{\partial r} < 0$) and antivortex ($-\frac{\partial V}{\partial r} > 0$) if n is odd or even respectively. Comparing Eq. (6.15b) with the skyrmion-vortex interaction force in Fig. 6.11 (insets), there can be 0, 1 or 2 fixed points for $v > v_c$, $v = v_c$, and $v < v_c$ respectively, where $v_c = F_{\rm sv}^{\rm max}/\sigma_{\alpha\alpha}$ is the critical velocity. The stability of the fixed points can be calculated either analytically, by the linearization of the

equation of motion near the fixed points, or numerically, by iterating Eqs. (6.9) in discrete steps of time. Here we apply the second approach, where we take $\alpha = \beta$, $v_x = -v$, $v_y = 0$, and force $\mathbf{F}_{sv}$ as calculated in Sec. 6.8.3.3. The value of $\mathcal{D}$ was calculated as explained in Appendix B. The corresponding trajectories and fixed points calculated from the Thiele equation are shown in Fig. 6.13 as lines and dots, respectively, with the open dots representing saddle points and the closed dots representing stable spirals. Notice that the trajectories obtained from the micromagnetic simulations (blue lines) follow the shape of the neighbouring trajectories calculated from the Thiele approach (black lines) without crossing them (albeit with weak deviations), which indicates a good agreement between both solutions. A direct comparison between both solutions is also shown by the dash-dotted lines in Fig. 6.12 (a) and (b). Also notice that with increasing the vortex velocity the fixed points approach until they annihilate around the region of maximal background canting due to the vortex field.

6.8.4.3 Feedback effect of the skyrmion dynamics on the driven vortex

As a next step in the analysis, we introduce the feedback effect of the skyrmion dynamics on the driven vortex dynamics by taking into account the vortex-skyrmion interaction in the vortex equation of motion. For simplicity, here we consider the limit $d_s \ll \lambda$, where the currents in the superconducting film can be averaged over the film thickness and the vortex-core dynamics can be approximated as one of a point particle.

The Bardeen-Stephen equation [249] describes the overdamped motion of the vortex core, with terminal velocity $\dot{\mathbf{r}}_v$ given by the force balance: $\eta\dot{\mathbf{r}}_v = \mathbf{F}$, where η is a viscosity coefficient and $\mathbf{F}$ comprises all other forces acting on the vortex core. In this study we neglect the effects of vortex pinning in the superconductor, as well as the intrinsic vortex Hall effect (negligible outside the superclean limit [250, 251]), and write the force acting on the vortex core as $\mathbf{F} = \mathbf{F}_L - \mathbf{F}_{sv}$, with $\mathbf{F}_L = d_s\phi_0\mathbf{j}_{SC} \times \hat{z}$ the Lorentz force due to the current density $\mathbf{j}_{SC}$ applied into the superconductor and $\mathbf{F}_{sv}$ the skyrmion-vortex interaction force. Therefore, for the case of $\mathbf{F}_L = F_L\hat{x}$, the equation of motion for the vortex core can be separated as

$$\begin{aligned} \dot{x}_v &= \frac{1}{\eta}(F_L - F_{sv}^x), \\ \dot{y}_v &= -\frac{1}{\eta}F_{sv}^y. \end{aligned} \tag{6.16}$$

The threshold current applied into the superconductor that breaks the skyrmion-vortex pair (SVP) is reached when the vortex attains the critical velocity, i.e, $\eta v_c = |\mathbf{F}| = \sqrt{(F_L - F_{sv}^x)^2 + (F_{sv}^y)^2}$. The critical value of F_L then reads

$$F_L^c = \max\left[|F_{sv}^x| + \sqrt{(\eta v_c)^2 - (F_{sv}^y)^2}\right]. \tag{6.17}$$

Here $v_c = F_{\mathrm{sv}}^{\max}/\sigma_{\alpha\alpha}$, and we obtain

$$F_{\mathrm{L}}^{c} = \left(1 + \frac{\eta}{\sigma_{\alpha\alpha}}\right) F_{\mathrm{sv}}^{\max}. \tag{6.18}$$

Above this value, the fixed points of our dynamical system annihilate, and the skyrmion is left behind when the vortex moves. On the other hand, for $F_{\mathrm{L}} < F_{\mathrm{L}}^{c}$, the SVP remains bound, and after a transient oscillatory motion, the pair reaches a steady state (the dynamical system finds the stable fixed point), where the skyrmion and vortex move with the same velocity, i.e., $\dot{x}_{\mathrm{sk}} = \dot{x}_{\mathrm{v}} = v_x$ and $\dot{y}_{\mathrm{sk}} = \dot{y}_{\mathrm{v}} = v_y$, with v_x and v_y constant. By substituting that into Eqs. (6.9) and (6.16), one can calculate the resulting net angle (direction) of the SVP motion with respect to the $\hat{x}$ direction as $\Omega \equiv \arctan(v_y/v_x)$. For the case where there are no currents applied into the ferromagnetic film, i.e, $\nu_x = \nu_y = 0$, one obtains

$$\Omega = \arctan\left(-\frac{\mathcal{G}}{\alpha\mathcal{D} + \eta}\right). \tag{6.19}$$

In the previous section we have shown that the dynamics of the center-of-mass of the skyrmion, described by the Thiele formalism, is in good agreement with the micromagnetic simulations for the considered range of parameters where the skyrmion size is weakly affected by the vortex field. Therefore, from here on, in all remaining calculations, we assume the situation where the Thiele formalism correctly describes the skyrmion motion and the skyrmion dynamics can be represented by its center of mass. We perform a series of molecular dynamics simulations of the combined skyrmion-vortex system by numerically integrating the coupled Thiele [Eq. (6.9)] and Bardeen-Stephen [Eq. (6.16)] equations. However, since we are now considering a thin superconducting film, i.e. $d_{\mathrm{s}} \ll \lambda$, the monopole approximation is no longer accurate [240, 246] and we numerically integrate Eqs. (6.6a) and (6.6b) to obtain the vortex stray field. The interaction force is calculated as in Sec. 6.8.3.3 (see Appendix A.4). For the simulations we consider $\lambda = 50$ nm and $d_{\mathrm{s}} = 10$ nm, however, the results presented in this section can be easily generalized to other values of the parameters of the superconducting film. We initialize the system with the skyrmion and vortex concentric and apply a constant Lorentz force $\mathbf{F}_{\mathrm{L}} = F_{\mathrm{L}}\hat{x}$ to the vortex, i.e, an uniform current density $\mathbf{j}_{\mathrm{SC}} = -j_{\mathrm{SC}}\hat{y}$ is applied into the superconductor. Panels (c-r) in Fig. 6.14 show the trajectories obtained in the simulations, where Eq. (6.18) is used as reference for the considered parameters, as indicated in Fig. 6.14(a). Fig. 6.14(b) shows that the observed angle of the resultant motion of the SVP agrees with Eq. (6.19). Notice that now the skyrmion can experience many different transient motions and follow different directions, depending on the material parameters and Lorentz force. For high values of η, the dynamical system converges to the one considered in the last section, where Ω goes to zero and the vortex moves straight along the Lorentz force direction. For the limit of low viscosity of

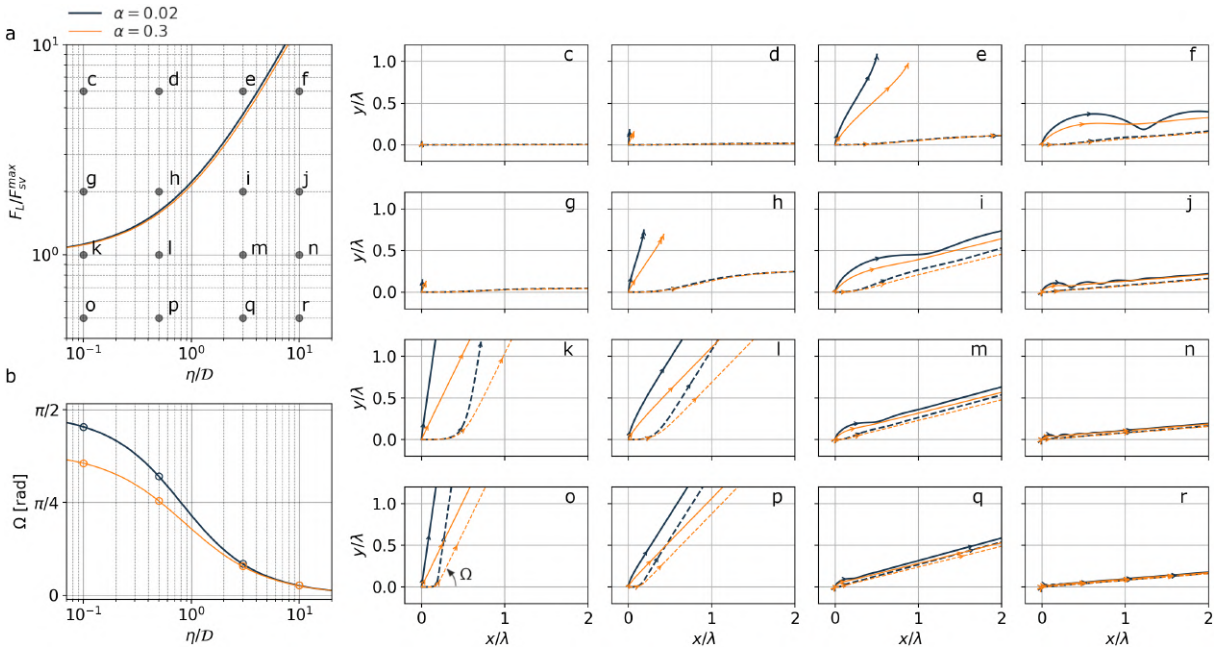

Figure 6.14 – (a) The critical force calculated from Eq. (6.18), for $\alpha = 0.02$ and $\alpha = 0.3$. The labeled points represent the parameters (F_L,η) considered in the simulations. (b) Resultant direction (angle Ω) of the SVP motion with respect to the $\hat{x}$ direction. The open dots indicate the angle calculated from the simulations and solid lines are given by Eq. (6.19). (c-r) Molecular dynamics simulations for labeled choices of parameters in (a), with the vortex trajectories represented by dashed lines and the skyrmion trajectories by solid lines.

the superconductor and ferromagnet, the SVP motion approaches the direction of the current applied into the superconductor, i.e, perpendicular to the Lorentz force!

Typical experimental values of the viscous drag coefficient for thin films of conventional superconducting materials are $\eta/d_s \sim 10^{-8}$–10^{-6} Ns/m^2. [250, 252, 253] Comparing these values with the skyrmion dissipative-tensor $\mathcal{D} \approx 2 \times 10^{-16}$ Ns/m calculated in Appendix B for the considered FM film, one finds $\eta/\mathcal{D} \sim 0.5$–$500$ for a superconducting film of thickness $d_s \sim 10$–100 nm. Notice that, once the material has been chosen, the relation $\eta/\mathcal{D}$ can still be tuned by changing the thickness of both FM and SC films, as well as by changing the heavy metal capping layer, which in turn affects the DMI and the skyrmion size. This allows for a high degree of controllability over the angle $\pi/2 - \Omega$ between the SVP motion and the current applied into the superconductor, and thereby, over the different dynamical regimes shown in Fig. 6.14.

6.8.4.4 Guiding magnetic skyrmions by vortex-screened Hall effect

In this section we analyze the full potential for guiding magnetic skyrmions by tuning the skyrmion-vortex Hall effect in FM-SC heterostructures. For that purpose, we now consider that independent currents are applied into both FM and SC films. As in the previous section, if one assumes that after a transient oscillatory motion the

SVP reaches the steady dynamic state, where skyrmion and vortex move with the same constant velocity, the angle of the SVP motion with respect to the $\hat{x}$ direction, now with v_x,$v_y \neq 0$, becomes

$$\tan\Omega = \frac{\mathcal{G}}{\alpha\mathcal{D}+\eta}\left[\frac{\Xi_1(v_x + \frac{\beta\mathcal{D}}{\eta}v_y)}{\Xi_2 v_x + \Xi_3 v_y + (\alpha\mathcal{D}+\eta)F_{\rm L}} - 1\right], \tag{6.20}$$

where

$$\begin{aligned}\Xi_1 &= \sigma_{\alpha\alpha}^2 + 2\alpha\mathcal{D}\eta + \eta^2,\\ \Xi_2 &= \sigma_{\alpha\beta}^2 + \beta\mathcal{D}\eta,\\ \Xi_3 &= \mathcal{G}\mathcal{D}(\beta - \alpha - \eta/\mathcal{D}).\end{aligned}$$

The above equation describes the terminal motion of the SVP in a general situation where currents are applied into both FM and SC films. Notice that the direction of the terminal motion does not depend on the strength of the skyrmion-vortex interaction, it depends only on the material parameters and the applied currents. The skyrmion-vortex interaction will nevertheless define the critical forces under which the pair remains connected. Similar expression has been obtained in Ref. [224] by a different approach, where Lorentz force due to currents applied into the superconductor was not considered. At this point, we call for attention to three different scenarios in Eq. (6.20). (i) *The current is applied only into the SC film*. In this case we recover Eq. (6.19) by substituting $v_x = v_y = 0$ into Eq. (6.20), and $0 < \Omega < \pi/2$, as verified in Fig. 6.14(b). (ii) *The current is applied only into the FM film*. This case is obtained by choosing $F_{\rm L} = 0$ in Eq. (6.20), where the case of $v_x > 0$ and $v_y = 0$ results in $-\pi/2 < \Omega < \Omega_0$, with $\Omega_0 = \tan^{-1}[\mathcal{G}\mathcal{D}(\alpha-\beta)/\sigma_{\alpha\beta}^2]$ the skyrmion Hall angle in the absence of the vortex. In other words, the SVP Hall-angle with respect to currents applied into the ferromagnetic film, $\theta_{\rm H}^{j_{\rm FM}} = \Omega$, is always greater than that observed in the absence of superconducting vortices. (iii) *The current is applied into both FM and SC films*. In this case we explore two different situations of the spin-polarized current, $\boldsymbol{v} \parallel \mathbf{F}_{\rm L}$ and $\boldsymbol{v} \perp \mathbf{F}_{\rm L}$. The Lorentz force, $F_{\rm L}^*$, that compensates the SHE, i.e, that makes the skyrmion move straight along the current direction, is obtained by setting ($\Omega = 0$, $v_x = v$, $v_y = 0$) and ($\Omega = \pi/2$, $v_x = 0$, $v_y = v$) in Eq. (6.20) for $\boldsymbol{v} \parallel \mathbf{F}_{\rm L}$ and $\boldsymbol{v} \perp \mathbf{F}_{\rm L}$ respectively:

$$F_{\rm L}^* = \frac{\Xi_1 - \Xi_2}{\alpha\mathcal{D}+\eta}v, \quad \text{for } (\boldsymbol{v} \parallel \mathbf{F}_{\rm L}), \tag{6.21a}$$

$$F_{\rm L}^* = -\frac{\Xi_3}{\alpha\mathcal{D}+\eta}v, \quad \text{for } (\boldsymbol{v} \perp \mathbf{F}_{\rm L}). \tag{6.21b}$$

Figs. 6.15 (a) and (b) show the trajectories calculated in the molecular dynamics simulations for $\boldsymbol{v} \parallel \mathbf{F}_{\rm L}$ and $\boldsymbol{v} \perp \mathbf{F}_{\rm L}$ respectively, where we assume the typical values

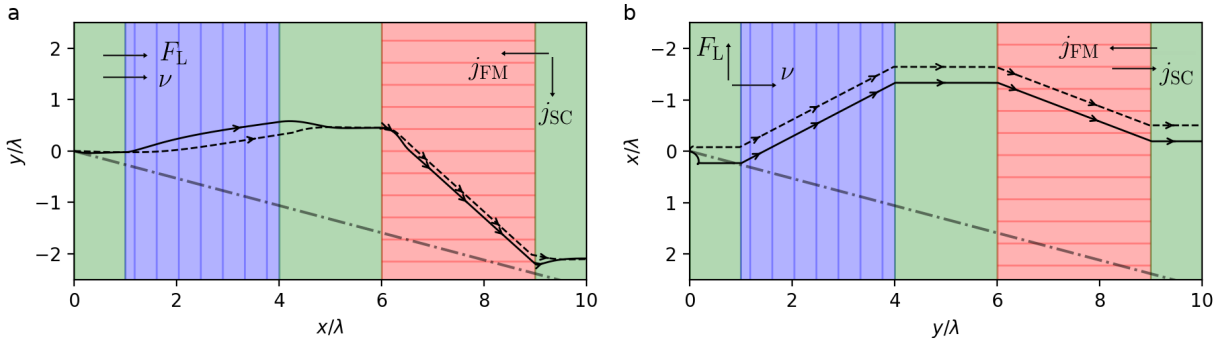

Figure 6.15 – Trajectories calculated in the molecular dynamics simulations for (a) $\boldsymbol{\nu} \parallel \mathbf{F}_L$, and (b) $\boldsymbol{\nu} \perp \mathbf{F}_L$, where dashed and solid lines represent the vortex and skyrmion trajectories respectively, for $F_L = F_L^*$ ((green) solid shaded region), $F_L = F_L^* + \delta F_L$ ((blue) vertically striped region) and $F_L = F_L^* - \delta F_L$ ((red) horizontally striped region). The dash-dotted line represents the skyrmion Hall angle in the absence of the vortex. Taken parameters are $\alpha = 0.3$, $\beta = \alpha/4$, $\eta = 2\mathcal{D}$ and $|\boldsymbol{\nu}| = 200 v_0 \approx 1\,\mathrm{ms}^{-1}$, with $v_0 \equiv F_{sv}^{max}/(\alpha\mathcal{D} + \eta)$. We use $\delta F_L = 160 F_{sv}^{max}$ in (a) and $\delta F_L = 3.2 F_{sv}^{max}$ in (b).

for Co/Pt samples $\alpha = 0.3$, $\beta = \alpha/4$, and $\eta = 2\mathcal{D}$ for the superconducting film, with $|\boldsymbol{\nu}| = 200 v_0 \approx 1\ \mathrm{ms}^{-1}$, with characteristic velocity $v_0 \equiv F_{sv}^{max}/(\alpha\mathcal{D} + \eta)$. Notice that for $F_L = F_L^*$ (solid shaded (green) regions in Fig. 6.15) the SHE is indeed canceled and the SVP moves straight along the current direction. Also notice that by tuning the Lorentz force one can control the direction of motion. By assuming the special cases of Eqs. (6.21a) and (6.21b) in the expression for the SVP terminal velocity, one finds

$$v_{pair}^* = \nu, \quad \text{for } (\boldsymbol{\nu} \parallel \mathbf{F}_L), \tag{6.22a}$$

$$v_{pair}^* = \frac{\beta}{\alpha + \eta/\mathcal{D}}\nu, \quad \text{for } (\boldsymbol{\nu} \perp \mathbf{F}_L), \tag{6.22b}$$

where v_{pair}^* is the SVP velocity along the direction of applied current. The maximal velocity for which the SVP remains bound together is obtained by substituting Eqs. (6.21a) and (6.21b) into Eq. (6.17), with ν given by the critical limit of Eqs. (6.22a) and (6.22b), yielding

$$v_c^* = \frac{F_{sv}^{max}}{\mathcal{D}(\alpha - \beta)}, \quad \text{for } (\boldsymbol{\nu} \parallel \mathbf{F}_L), \tag{6.23a}$$

$$v_c^* = \frac{\beta\mathcal{D}F_{sv}^{max}}{\Xi_3 - \beta\mathcal{D}\eta}, \quad \text{for } (\boldsymbol{\nu} \perp \mathbf{F}_L). \tag{6.23b}$$

Fig. 6.16 shows that the above expressions are indeed in agreement with the results obtained in the numerical simulations.

Notice that the stability of the SVP is directly related to the maximal value of the interaction force, F_{sv}^{max}. Therefore, we expect the threshold values to be enhanced for: i) smaller penetration depth λ of the superconducting film, which concentrates the magnetic flux in smaller regions, thus increasing the SVP interaction; ii) reduced thickness of the insulating layer, which increases the magnetic field of the vortex acting

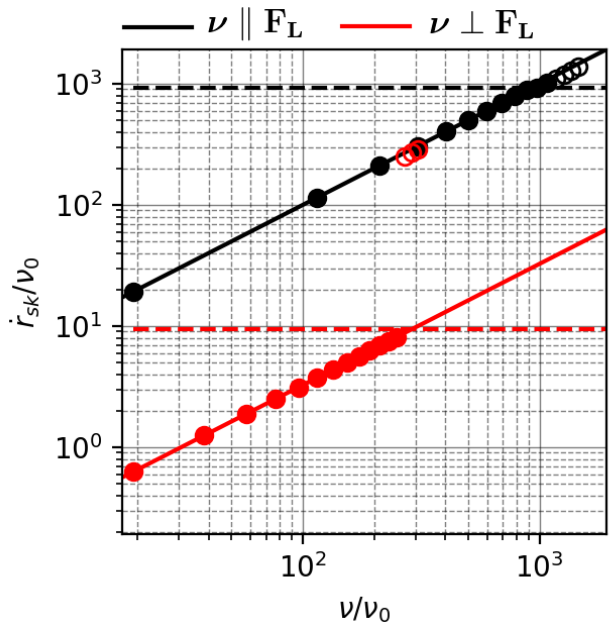

Figure 6.16 – Skyrmion terminal velocity as a function of the applied polarized current, for $\boldsymbol{\nu} \parallel \mathbf{F}_\mathrm{L}$ (black) and $\boldsymbol{\nu} \perp \mathbf{F}_\mathrm{L}$ (red), with F_L given by Eqs. (6.21a) and (6.21b) so as to compensate the skyrmion Hall effect. Solid lines indicate the expected SVP velocity from Eqs. (6.22a) and (6.22b). Dots show the results obtained from the simulation, where open dots indicate that the SVP has been broken and the skyrmion motion is no longer aligned with current direction. Dashed lines denote the critical velocities calculated from Eqs. (6.23a) and (6.23b).

on the FM plane; iii) stronger DMI in the FM film, which enlarges the core of the skyrmion, thus aligns the magnetization of the core with the stray field of the vortex, thereby increasing the SVP interaction.

6.9 Conclusion of the chapter

Precisely controlled dynamics of magnetic skyrmions in chiral ferromagnets has become of great relevance for cutting-edge memory devices and information technology applications. In this chapter, we have shown that skyrmion stray fields can nucleate stable antivortices in engineered chiral magnet-superconductor heterostructures and that the coexistence of these hybrid magnetic skyrmions with superconducting vortices creates a complex yet controllable environment for exploring unique emergent flux dynamics. We have demonstrated that such a hybrid system enables multiple possibilities for manipulating the skyrmion-vortex pair, that are not possible for either constituent separately. We analyzed the dependence of the skyrmion-vortex coupled motion on the effective material viscosities, the exerted Lorentz-like force on vortices, and magnetic torques acting on a skyrmion, and determined the threshold values of external drives for which the skyrmion-vortex pair remains bound. Futhermore, we have calculated the Hall-angle of the skyrmion-vortex pair with respect to currents applied into either,

or both superconducting and ferromagnetic films, and have thereby demonstrated the unprecedented tunability of the direction of motion for skyrmions in this hybrid system. Bearing in mind the plethora of known manners for manipulating fluxonics in superconductors by nanostructuring [254], and possibilities for similar manipulations of skyrmions [81, 255–258], the results presented in this section opens a research direction of hybridized dynamics in SC-CM systems that holds promise to reveal rich fundamental phases and applicable effects.

Part III

Magnonics and spin-textures in two-dimensional magnetic materials

7 The role of suppressed nearest-neighbor exchange in magnetic monolayers

High tunability of two dimensional magnetic materials (by strain, gating, heterostructuring or otherwise) provides unique conditions for studying versatile magnetic properties and controlling emergent magnetic phases. Expanding the scope of achievable magnetic phenomena in such materials is important for both fundamental and technological advances. In this chapter, we perform atomistic spin-dynamics simulations to explore the (chiral) magnetic phases of atomic monolayers in the limit of suppressed first-neighbors exchange interaction. We report the rich phase diagram of exotic magnetic configurations, obtained for both square and honeycomb lattice symmetries, comprising coexistence of ferromagnetic and antiferromagnetic spin-cycloids, as well as multiple types of magnetic skyrmions. We perform a minimum-energy path analysis for the skyrmion collapse to evaluate the stability of such topological objects, and reveal that magnetic monolayers could be good candidates to host the antiferromagnetic skyrmions that are experimentally evasive to date.

The results presented in this chapter are published in Physical Review B, **101**, 214429. (2020).

7.1 Motivation

Magnetism in two dimensions (2D) has recently drawn immense attention of both theoretical and experimental research, due to its fundamental significance and promising technological applications[259, 260]. Magnetic 2D atomic crystals present a diapason of possibilities for controlling magnetic interactions by different composition and structural arrangements[261–264], as well as engineering techniques[265, 266]. The competition between the magnetic interactions in such 2D materials, e.g., crystalline anisotropy, exchange, dipole-dipole, Dzyaloshinskii-Moriya interaction[73, 88] (DMI), etc., is likely to lead to a wide range of physical phenomena and novel magnetic phases.

It is well known that the exchange interaction between neighboring spins of a magnetic system plays a determinant role in resulting magnetic configurations. Interestingly, the exchange coupling of magnetic monolayers can be tuned in a multitude of ways. For example, a manganese monolayer presents ferromagnetic (FM) order when grown on the (001) surface of tungsten substrate[267], but presents antiferromagnetic (AFM) order when grown on tungsten (110)[268]. Ref. [261] claimed based on first-principles calculations that the nearest-neighbor (NN) exchange interaction of an iron monolayer on the (001) surface of a Ta_xW_{1-x} alloy can be continuously tuned from FM to AFM coupling by varying the Ta concentration in the substrate, and that in the situation of weak NN exchange nontrivial magnetic configurations can be achieved. Similarly, Ref. [269] showed that the ground state of a Fe monolayer on top of different 4d and 5d nonmagnetic metals can be continuously manipulated from FM to AFM by in-plane biaxial and uniaxial strain on the substrates. Ref. [263] demonstrated tunability of the exchange interaction by changing the stacking order of Fe/5d bilayers on Rh(001). The exchange interaction can also be tuned by strain in magnetic 2D monolayer chromium trihalides CrX_3 (with X = I, Cl and Br), continuously from FM to AFM one[266].

In addition to this (symmetric) exchange interaction, the asymmetric DMI plays an important role in the ordering of a magnetic system. As discussed in Sec. 2.3.3, instead of (anti)parallel spins, DMI favors the rotation of magnetization at short length scales, giving rise to chiral spin structures, such as cycloids and magnetic skyrmions. DMI can be tuned in 2D magnets by breaking inversion symmetry, e.g., in Janus structures of chromium trihalides [264] and manganese dichalcogenides[270], or at the interface of the magnetic monolayer with a heavy-metal substrate[271].

In spite of the many possibilities for tuning exchange interactions in 2D magnets, the resultant magnetic states of such systems remain scarcely investigated. Therefore, in this chapter we explore the magnetic phases of chiral magnetic monolayers, such as Fe monolayer and CrX_3 lattices, in the limit of suppressed NN exchange interaction. We present the rich phase diagram obtained for both square and honeycomb symmetries, where exotic magnetic configurations can be stabilized. There we reveal states with coexisting FM and AFM spin-cycloids and magnetic skyrmions, as well as the novel p-AFM skyrmion state, and explore stability of magnetic skyrmions when dominated either by NN or second-nearest-neighbor (SNN) exchange coupling.

7.2 Theoretical modeling

In the following sections we perform atomistic spin simulations to capture possible magnetic phases of the considered magnetic monolayers. The simulations are primarily based on the simulation package *Spirit* [38]. The extended Heisenberg

Hamiltonian of the considered classical system of spins, in absence of applied magnetic field, is given by [see Sec. 3.1.2]

$$\begin{aligned}\mathcal{H} = & - \sum_{<i,j>_{\text{sd}}} J_{ij}\mathbf{n}_i \cdot \mathbf{n}_j - \sum_{<i,j>_{\text{st}}} \mathbf{D}_{ij} \cdot (\mathbf{n}_i \times \mathbf{n}_j) \\ & - \frac{1}{2}\mathcal{D}_{\text{ddi}} \sum_{i,j\neq i} \frac{3(\mathbf{n}_i \cdot \hat{\boldsymbol{r}}_{ij})(\mathbf{n}_j \cdot \hat{\boldsymbol{r}}_{ij}) - (\mathbf{n}_i \cdot \mathbf{n}_j)}{(r_{ij}/r_0)^3} \\ & - K \sum_i (\mathbf{n}_i \cdot \hat{\boldsymbol{z}})^2, \end{aligned} \tag{7.1}$$

where $\mathbf{n}_i = \boldsymbol{\mu}_i/\mu$ is the i^{th} spin orientation, with $\boldsymbol{\mu}_i$ the magnetic moment of the i^{th} atomic site and $|\boldsymbol{\mu}_i| = \mu$. J_{ij} is the exchange coupling, where we define J_1 and J_2 as the NN and SNN exchange coupling respectively; $\mathbf{D}_{ij} = D(\hat{\boldsymbol{r}}_{ij} \times \hat{\boldsymbol{z}})$ is the DMI vector, with D the DMI strength and $\boldsymbol{r}_{ij}$ the vector connecting spins i and j. K is the perpendicular magnetic anisotropy and $\mathcal{D}_{\text{ddi}} = \mu_0\mu^2/(4\pi r_0^3)$ defines the magnitude of the dipole-dipole interaction (DDI), with r_0 the nearest-neighbor distance and μ_0 the vacuum permeability. $<>_{\text{st}}$ and $<>_{\text{sd}}$ denote summation up to first and second-neighbors sites respectively. For the dipole-dipole interaction we make use of fast Fourier transforms and the convolution theorem [272] adapted to treat arbitrary spin lattice configurations, as implemented in *Spirit*, which reduces significantly the computational effort. Moreover, a direct summation of dipoles has been performed in order to verify selected results. Although thermal fluctuations play an important role in the stability of any spin texture, in this chapter we describe all the fundamental states emerging from the competing interactions due to tuned exchange terms and leave the limitations brought by thermal effects for a separate study. The energy minimization is performed using a Verlet-like velocity projection method [38, 132], which accelerates convergence towards local minima and avoids overstepping due to momentum considered in the standard LLG equation [167, 168].

When constructing the equilibrium phase diagram of a spin system in the space of two relevant parameters in Eq. 7.1 (e.g. J_1 and J_2), the spin-relaxation simulations are performed for a uniform 10×10 matrix of values within the parametric range of the phase diagram. For each selected point of the phase diagram the spin system is initialized from a random configuration and the energy is minimized numerically for a sufficient number of different initial states in order to identify the configurations of lowest energy. In the following step, the energies of all found configurations were evaluated on a high-density grid in the parametric space (typically a 200×200 grid) and compared with each other in order to obtain the phase boundaries. In the simulations, a spin lattice with 102×102 unit cells is considered, with one and two spins per unit cell for the cases of square and honeycomb lattices respectively, unless otherwise specified. Periodic boundary conditions are considered along the two dimensions of the system.

For DDI calculations, four images of the spin system are considered along the two dimensions. In the case of incommensurate phases such as cycloids, we ensured that the considered system size is much larger than the periodicity of the final state.

7.3 Competing exchange interactions

In this chapter we are interested in magnetic configurations that emerge in the limit of vanishing nearest-neighbor exchange interaction. In order to be able to systematically discern effects from different types of interactions, we remove DMI and anisotropy and examine purely the effects of tuning the exchange coupling between both nearest-neighbor and second-nearest-neighbor sites, with dipole-dipole interactions taken into account.

7.3.1 Square lattice

We first consider a square lattice of spin sites, representative of e.g. Fe monolayer on a substrate [261]. Fig. 7.1 (A) shows the ground-state phase diagram obtained in the numerical experiments based on Eq. 7.1. The corresponding minimal energy configurations belonging to different regions of the phase diagram in Fig. 7.1 (A) are depicted in Fig. 7.1 (B-D). For dominating nearest-neighbor exchange interaction ($|J_1| > 2|J_2|$), only two states can occur, the FM state [Fig. 7.1 (B)] for $J_1 > 0$, and the checkerboard c(2x2)-AFM state [Fig. 7.1 (C)], also referred to as c-AFM, for $J_1 < 0$. Notice that dipole-dipole interaction favors in-plane spin configurations except for the c-AFM phase, where the “head-to-head" arrangement of spins is not energetically favored, forcing the system to align out of plane. However, if $J_2 < -|J_1|/2$ the exchange term in Eq. 7.1 favors the so-called p(2x1)-AFM ordering [see Fig. 7.1 (D)], also referred to as p-AFM. The p-AFM state is a degenerate solution of the Heisenberg Hamiltonian with respect to rotation of consecutive spins by an angle of $\pm\Omega$, with exchange energy $\mathcal{E}_{\text{ex}} = 4J_2$ per spin. Ferriani *et al.*[261] demonstrated that such degeneracy can be lifted by higher-order interactions such as four-spin and biquadratic ones, where noncollinear states, i.e. with $\Omega \neq 0$, are favored. Here we observed that the presence of dipole-dipole interactions favors collinear configurations. However, for dominating exchange energy, even small fluctuations of the spin configurations can overcome the dipolar ineractions so that noncollinear domains can coexist with the collinear ones. In such conditions, even though the state shown in Fig. 7.1 (C) remains the ground state of the system, the states similar to the one shown in Fig. 7.1 (E) become increasingly stable and frequently appearing. Such AFM states are similar to those obtained for pure dipolar systems on a square lattice[273].

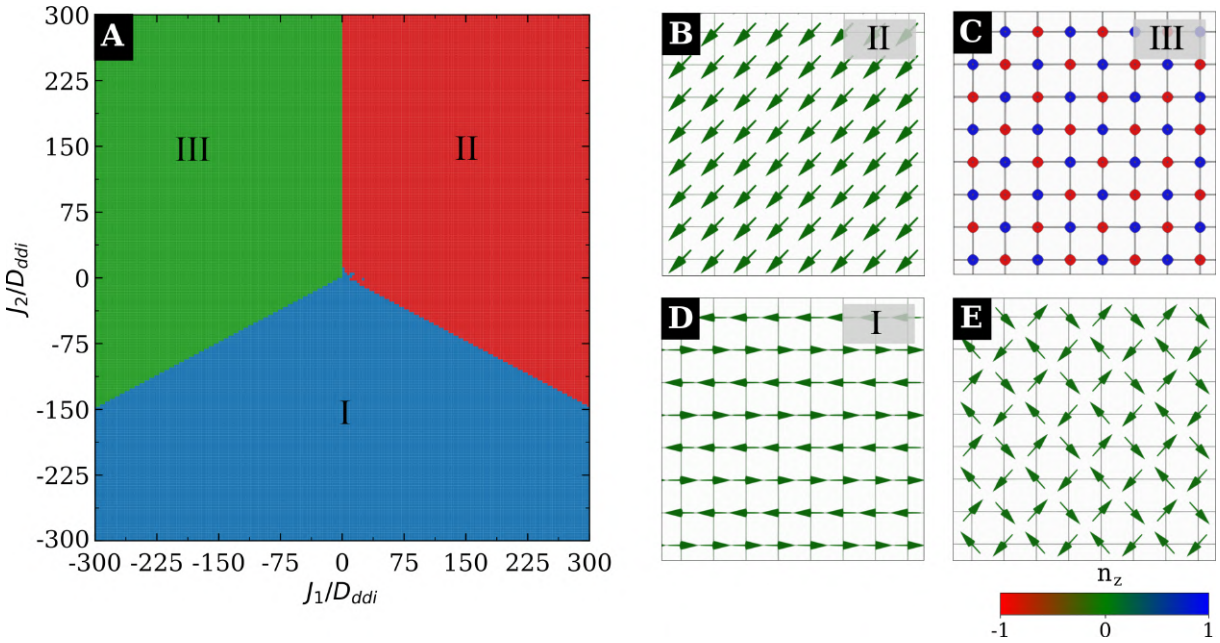

Figure 7.1 – (A) Phase diagram for a square monolayer lattice for different values of exchange couplings J_1 and J_2, in the presence of dipole-dipole interactions, for $K = D = 0$. (B-D) Ground-state magnetic phases, corresponding to nomenclature indicated in (A). Note that in case of dominating exchange interaction the non-collinear and collinear states become nearly energetically degenerate within phase I, so that states similar to the one shown in panel (E) frequently appear as stable.

7.3.2 Honeycomb lattice

In Fig. 7.2 (A) we show the phase diagram for the honeycomb lattice symmetry, analogous to the one of Fig. 7.1 (A) obtained for the square lattice. In the honeycomb case, the non-trivial structure, as well as the mismatch in the number of NN and SNN bonds of the honeycomb lattice give rise to several more magnetic phases. Furthermore, one should note that the SNN bonds form a triangular lattice, which is intrinsically frustrated under AFM coupling, which can lead to non-trivial spin textures. For the case of $J_2 > 0$, the FM and AFM states (phases II and III in Fig. 7.2) are analogous to the ones observed in the square lattice. On the other hand, for dominating $J_2 < 0$ two degenerate lattices of spin-loops are obtained, shown in Fig. 7.2 (B) and (C). Such magnetic phases are similar to those found for multiferroic hexagonal compounds[274, 275], which in that case are associated to the Γ_1 and Γ_3 irreducible representations of the $P6_3cm$ space group[276]. In our system the spin-loop configurations are also favored by the dipole-dipole interactions[277]. By increasing the magnitude of $|J_1|$, the competing NN and SNN coupling give rise to spin cycloids (phases IV and VII in Fig. 7.2), collinear AFM states (phases V and VIII in Fig. 7.2) and vortex-like configurations (lattice of FM vortices in phase VI and a lattice of AFM antivortices in phase IX, see Fig. 7.2). We notice that for $J_1 > 0$ the spins tend to form pairs of rows with same orientation [see e.g. Fig. 7.2 (H)] due to the FM NN coupling and the cycling of the spins in the cycloidal

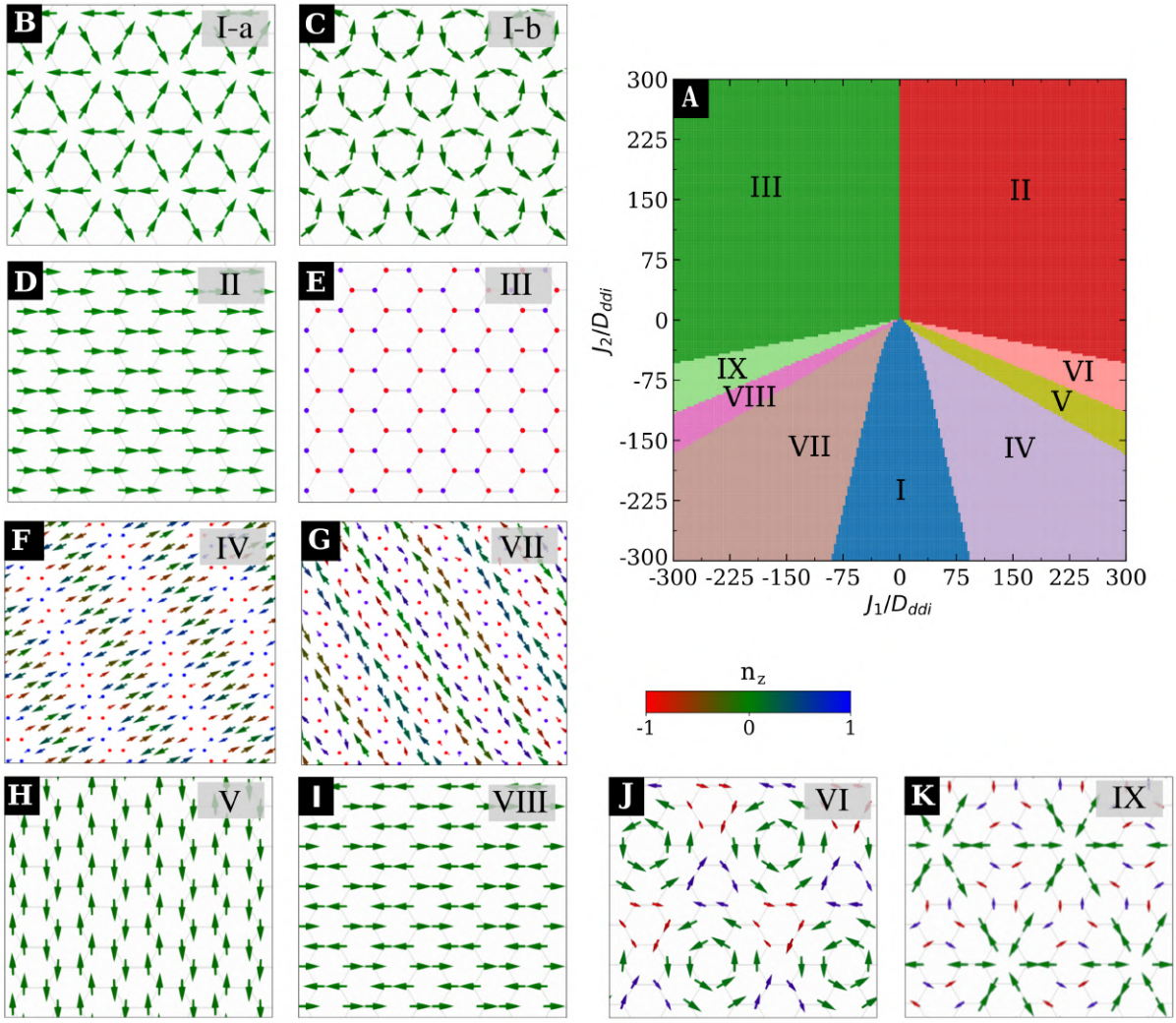

Figure 7.2 – (A) Phase diagram for a honeycomb monolayer lattice for different values of exchange couplings J_1 and J_2, in the presence of dipole-dipole interactions, for $K = D = 0$. (B-K) Ground-state magnetic phases, corresponding to labeling indicated in panel (A).

phase [Fig. 7.2 (F)] is of the Néel type. In contrast, for $J_1 < 0$, the spins are aligned in single rows and the cycloids are of the Bloch type.

7.4 Suppressed nearest-neighbor exchange in the square lattice

Having understood the competing effects between the nearest-neighbor and second-nearest-neighbor exchange and dipolar interactions, we proceed to examine spin configurations in the limit of vanishing NN exchange interaction. We start with the square lattice, which, due to its simpler geometry, allows for a more illuminating analysis of cycloids and skyrmions induced by suppressed NN exchange. Moreover, as will be shown, the square lattice encompasses all the main ingredients behind the

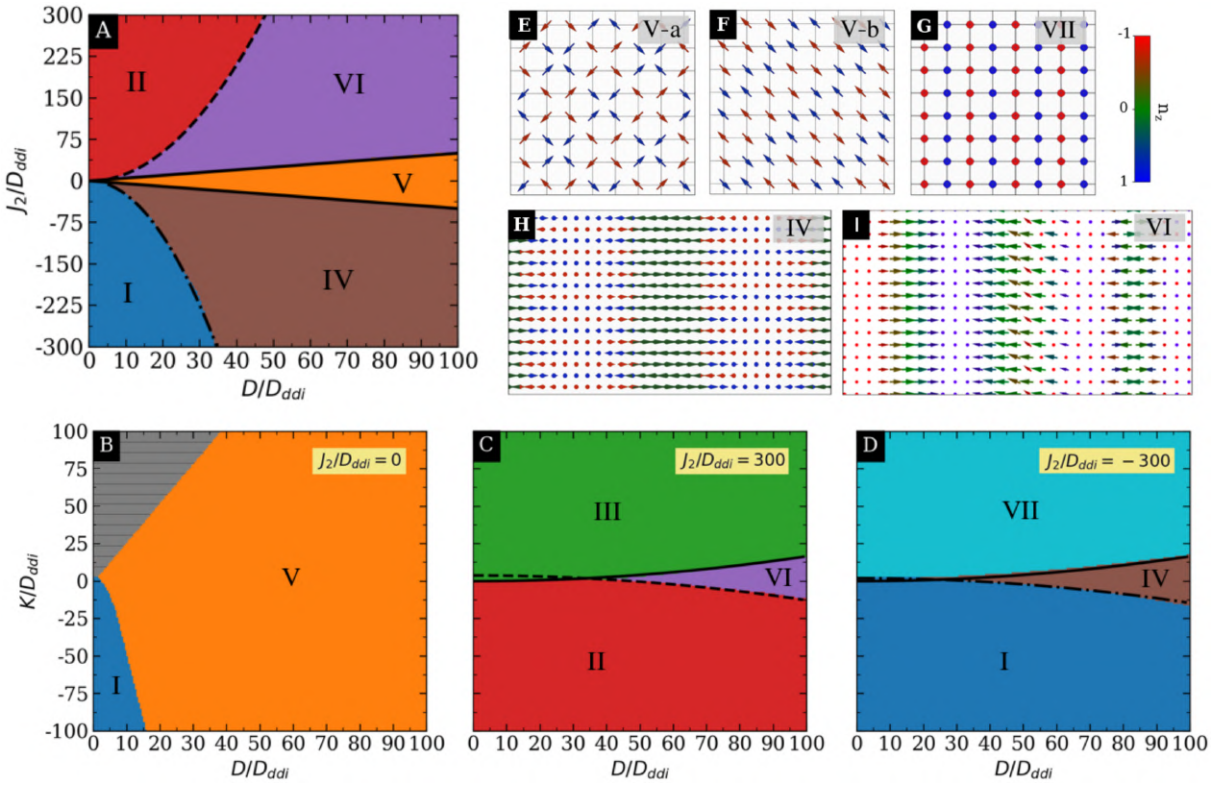

Figure 7.3 – Phase diagram for a square monolayer lattice for vanishing nearest-neighbor exchange interaction. (A) As a function of the second-nearest-neighbor exchange J_2 and the DMI strength D, for $K = 0$. (B-D) As a function of magnetic anisotropy K and DMI strength D, for $J_2 = 0$ (B), $J_2 = 300D_{\mathrm{ddi}}$ (C) and $J_2 = -300D_{\mathrm{ddi}}$ (D). The patterned region in (B) indicates disordered configurations. (E-I) Spin configurations corresponding to phases indicated in (A-D). Solid lines in panels (A), (C, (D) represent analytical solutions for the phase boundaries of the cycloidal states derived in Sec. 7.4.1.

physics of the chiral magnetic textures in the 2D limit. Supplementary notes on the honeycomb lattice case are given in subsection 7.5.

In Fig. 7.3 (A) we show the phase diagram for the square lattice, obtained for $J_1 = 0$, as a function of J_2 but also as a function of increasing DMI. For negative values of J_2, increasing DMI strength favors the formation of p-AFM spin-cycloids, shown in Fig. 7.3 (H), while for positive J_2 we report the coexistence of FM and c-AFM spin-cycloids with *opposite chiralities* [Fig. 7.3 (I)]. Notice that when neglecting the DDI term in the Hamiltonian [Eq. 7.1], the FM and c-AFM states are energetically degenerate for the case of $J_1 = 0$ and $J_2 > 0$ (see also Fig 7.10 for a better visualization of the coexisting FM and c-AFM domains). For the case of dominating DMI energy, all spins are forced orthogonal to each other, driving a transition to an emergent spin-ice type of state (V-a), of checkerboard symmetry with four spins pointing in or four spins pointing out of a same tetragon, or a degenerated striped state (V-b), shown respectively in Fig. 7.3 (E) and Fig. 7.3 (F). The effects of anisotropy interaction (parameter K in the Hamiltonian) are shown in Fig. 7.3 (B-D) for $J_2 = 0, 300D_{\mathrm{ddi}}$ and $-300D_{\mathrm{ddi}}$ respectively. For $J_2 = 0$ the

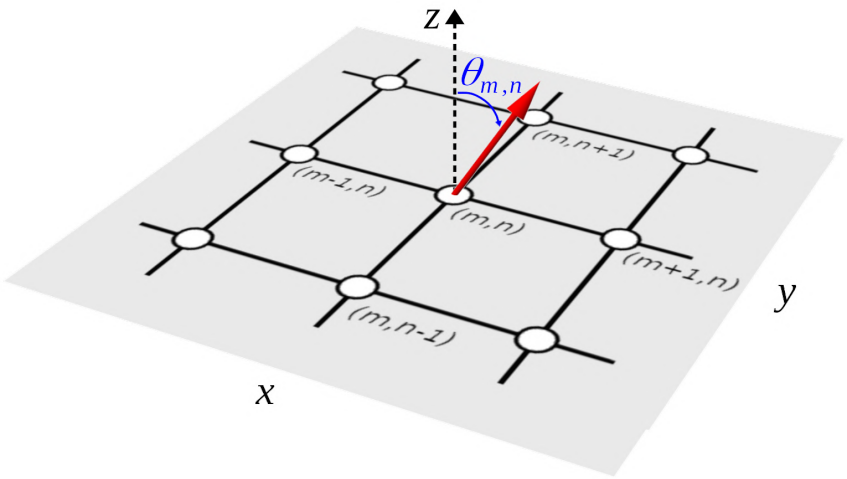

Figure 7.4 – Schematic representation of the lattice indices and spin angle θ considered in the calculations in Sec. 7.4.1.

in-plane order of state V is preserved and the z component of the spins are continuously deformed by anisotropy interaction. For $J_2 > 0$, the out-of-plane (in-plane) anisotropy favors the c-AFM (FM) state, while for $J_2 < 0$ the out-of-plane anisotropy gives rise to the out-of-plane p-AFM state, shown in Fig. 7.3 (G).

7.4.1 Phase boundaries

As will be shown in this section, analytical expressions can be derived for most of the phase boundaries in Fig. 7.3. In that derivation we consider the extended Heisenberg Hamiltonian in Eq. 7.1 with suppressed NN exchange interaction, and initially neglect the dipole-dipole interaction. For a simplified analysis, we assume the cycloidal phases are characterized by uniform rotation of the spins along one easy axis, say x. Accordingly, the angle θ of a spin in the cycloid with respect to the $\hat{z}$ axis is modelled as

$$FM \qquad \theta_{m,n} = \frac{2\pi m}{N_p}, \tag{7.2}$$

$$c\text{-AFM} \qquad \theta_{m,n} = -\frac{2\pi m}{N_p} - \pi[1-(-1)^{m+n}], \tag{7.3}$$

$$p\text{-AFM} \qquad \theta_{m,n} = \frac{2\pi m}{N_p} - \pi[1-(-1)^{n}], \tag{7.4}$$

where index m (n) counts spin rows parallel (perpendicular) to the x axis (see Fig. 7.4) and N_p is the number of spins involved in one period of the cycloid, which is to be determined after minimization of the free energy.

The DMI contribution to the energy of the system can easily be calculated by noticing that in all the above described cycloidal configurations only spins linked along the x direction have nonzero DMI energy. In this case $D_{ij} = -\hat{y}D$, $n_i \times n_j = -\hat{y}\sin(\theta_{m+1,n} - \theta_{m,n}) = -\hat{y}\sin(2\pi/N_p)$, and thereby the total DMI energy is $E_{DMI} =$

$-ND\sin(2\pi/N_p)$. For the total SNN exchange energy E_{J2}, we sum up terms like $n_i \cdot n_j = -\cos(\theta_{m\pm1,n} - \theta_{m,n}) = \sigma\cos(2\pi/N_p)$, where $\sigma = 1$ for positive exchange interaction (phases FM and c-AFM) and $\sigma = -1$ for negative exchange interaction (phase p-AFM). Therefore, for all three cases, $E_{J2} = -2|J_2|\cos(2\pi/N_p)$. Finally, the contribution of anisotropy to the total energy is given by $E_K = -K\sum_{m,n}\cos^2\theta_{m,n}$, which, by assuming that N/N_p is an integer, leads to $E_K = -\frac{1}{2}NK$. The total energy of the cycloidal phases is then given by $E/N = -2|J_2|\cos(2\pi/N_p) - D\sin(2\pi/N_p) - K/2$. Minimizing the energy with respect to N_p yields

$$N_p = \frac{2\pi}{\tan^{-1}(D/2|J_2|)} \tag{7.5}$$

and

$$\frac{E}{N} = -\sqrt{4|J_2|^2 + D^2} - \frac{K}{2}. \tag{7.6}$$

Similar expressions can be obtained for the case of dominating NN exchange interaction, leading to the well-known dependence of the cycloid period on the ratio D/J[278, 279]. In order to delineate the boundaries of the cycloidal phases, we compare Eq. 7.6 with other (non-cycloidal) candidates to ground-state configuration. First, we consider phase V (see Fig. 7.3). This phase is dominated by DMI interactions, where all neighboring spins are orthogonal to each other, so that $E_{J2} = 0$. The DMI and anisotropy contribution to the energy can be calculated trivially, resulting in a total energy per spin $E/N = -\sqrt{2}D - K/2$. The critical DMI value, calculated by comparing this result with Eq. 7.6, is given by $D_c = 2|J_2|$ [see solid black lines in Fig. 7.3 (A)], irrespective of the anisotropy parameter K. Below this value, the cycloidal phases are favored against the homogeneous configuration V.

As shown in Fig. 7.3 (C) and (D), the cycloidal phases also become unstable above a certain value of the anisotropy parameter. For positive K, the c-AFM phase (III) is potentially favored for $J_2 > 0$, while for $J_2 < 0$, the p-AFM (VII) becomes the potential candidate. Their energy per spin is simply $E/N = -2|J_2| - K$. Comparing with Eq. 7.6, we get $K_c = 2\sqrt{4|J_2|^2 + D^2} - 4|J_2|$ (see solid black lines in Fig. 7.3 (C) and (D)).

For $K \leq 0$, the cycloids decay into phases I and II, which are significantly influenced by the dipole-dipole interaction. For those cases, the demagnetizing energy can be approximated by an in-plane contribution to the effective anisotropy[16] $K_{\text{eff}} = K - K_{\text{ddi}}$, and the critical curves for $K \leq 0$ are simply shifted by a factor of K_{ddi} (see dashed and dashed-dotted lines in Fig. 7.3 (C) and (D)). The same curves can be plotted for the case $K = 0$ as shown in Fig. 7.3 (A), where we used $K_{\text{ddi}} = 3.8D_{\text{ddi}}$ and $2D_{\text{ddi}}$ for the phase boundaries II-VI and I-IV respectively.

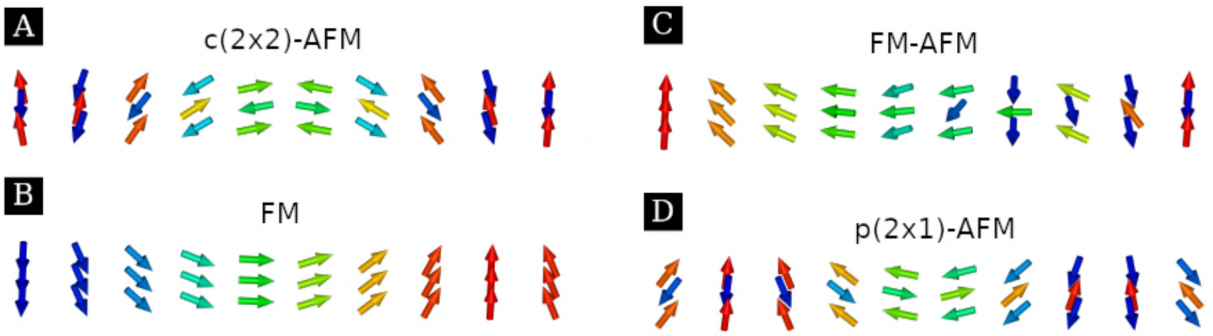

Figure 7.5 – Néel Domain wall structure for the c(2x2)-AFM state (A), FM state (B), between FM and AFM states (C) and p(2x1)-AFM state (D).

7.4.2 Domain walls and magnetic skyrmions

Domain walls (DW) and magnetic skyrmions are promising candidates for technological applications, especially for spin-based information processing and memory devices. In this section we look for such magnetic configurations in the limit of suppressed NN exchange coupling. Fig. 7.5 summarizes different types of domain walls obtained in our simulations. For $J_2 > 0$ the well-known c-AFM DW [Fig. 7.5 (A)] and FM DW [Fig. 7.5 (B)] are found. However, since the FM and c-AFM states can coexist in this region of the phase diagram, a DW between the two phases is necessary to stabilize the spin system, as shown in Fig. 7.5 (C). In this case, only one sublattice of the c-AFM structure is rotated to form the FM state. For $J_2 < 0$ the p-AFM DW [Fig. 7.5 (D)] is the only one found. Due to such possibilities for different types of DW one also expects a variety of magnetic skyrmions in this system. Isolated magnetic skyrmions are expected to be (meta)stable for the combination of microscopic parameters that yields $K > K_c$, where the background magnetization, either FM or AFM, is aligned out of plane. Fig. 7.6 (A) shows an example of FM and c-AFM skyrmions coexisting for $J_2 > 0$ (see also Fig 7.10 for a better visualization of the coexisting FM and c-AFM skyrmions), and Fig. 7.6 (B) shows the p-AFM skyrmion obtained for $J_2 < 0$ - which to our knowledge is the first such skyrmion reported in literature. One should note that the FM-AFM DW [as shown in Fig. 7.5 (C)] can not form a stable topological object by enclosing itself (contrary to its FM or AFM counterparts, since in this case only half of the spins would rotate across the domain wall and the resultant net topological charge is non-integer).

Now, let us compare the influence of both NN and SNN exchange on the skyrmion stability. For that purpose we analyze the energy of an isolated c-AFM skyrmion, which can be stabilized by both J_1 and J_2. In Fig. 7.6 (C) we show the c-AFM skyrmion energy calculated for (i) $J_1 = 0$, $J_2 = J$, and (ii) $J_1 = -J$, $J_2 = 0$, where we fixed the parameters $K = 3$ meV and $D = 5$ meV in such a way that the skyrmion can be stabilized for $|J_2|$ similar to that obtained in Refs. [261, 269], where $|J_1| \approx 0$. Notice that in case (i) one can stabilize skyrmions with equivalent energy but for smaller values of J when compared

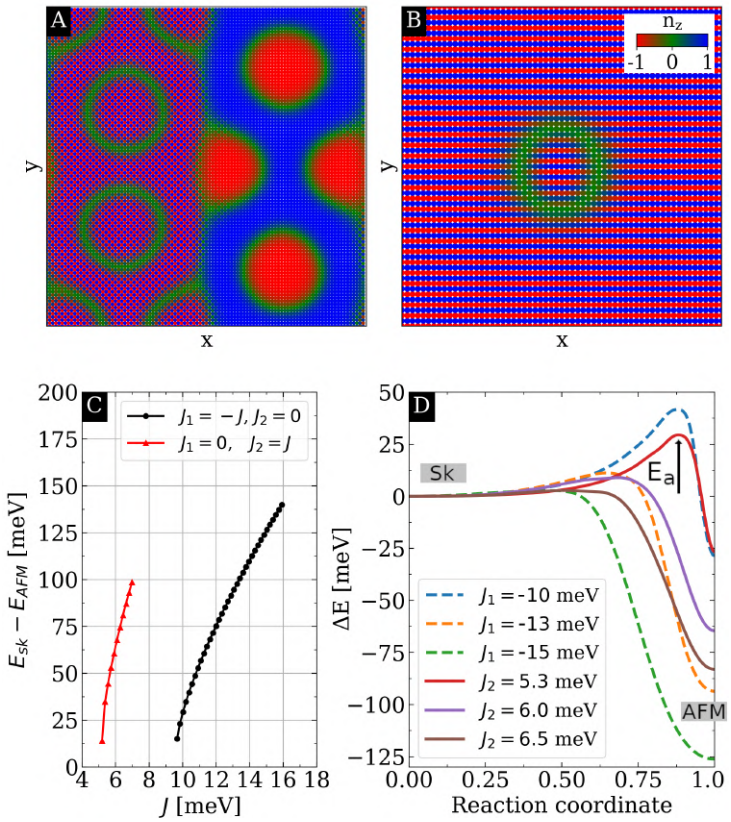

Figure 7.6 – (A) State with coexisting FM and c-AFM skyrmions, obtained for $J_2 > 0$. (B) The p-AFM skyrmion, obtained for $J_2 < 0$. (C) Skyrmion energy as a function of exchange coupling for (i) $J_1 = 0$, $J_2 = J$, and (ii) $J_1 = -J$, $J_2 = 0$, both with $K = 3$ meV and $D = 5$ meV. (D) Minimal-energy-path calculations for the isotropic collapse of the c-AFM skyrmion in both cases (i) and (ii). Here, the reaction coordinate defines the normalized (geodesic) displacement along the formation path and the activation energy E_a is defined by the highest-energy point along the path.

to the case (ii), which indicates that SNN exchange can dominate the skyrmion energy over small values of J_1. Fig. 7.6 (D) shows the minimal-energy-path calculations for the isotropic collapse of the c-AFM skyrmion in both cases (i) and (ii), where the activation energy, E_a, is calculated by the geodesic nudged elastic band method [132, 151] with the help of a climbing image method [134], both implemented in the simulation package *Spirit*, allowing an accurate determination of the highest-energy saddle point along the minimal energy path connecting the two states. Notice that, for both cases (i) and (ii), the activation energies have the same order of magnitude, which indicates that the skyrmions stabilized by dominating SNN exchange interaction present similar stability, and consequently similar lifetime[151, 280], to those stabilized by dominating NN exchange coupling. Notice that even though for some parameters the energy difference between initial and final states can be the same for both cases (i) and (ii), the skyrmion profiles are not identical (e.g., the domain wall width depends on exchange), which may cause the difference in the activation energy. Finally, the stability of the p-AFM skyrmion was found to be the same as the stability of the c-AFM skyrmion, as long as

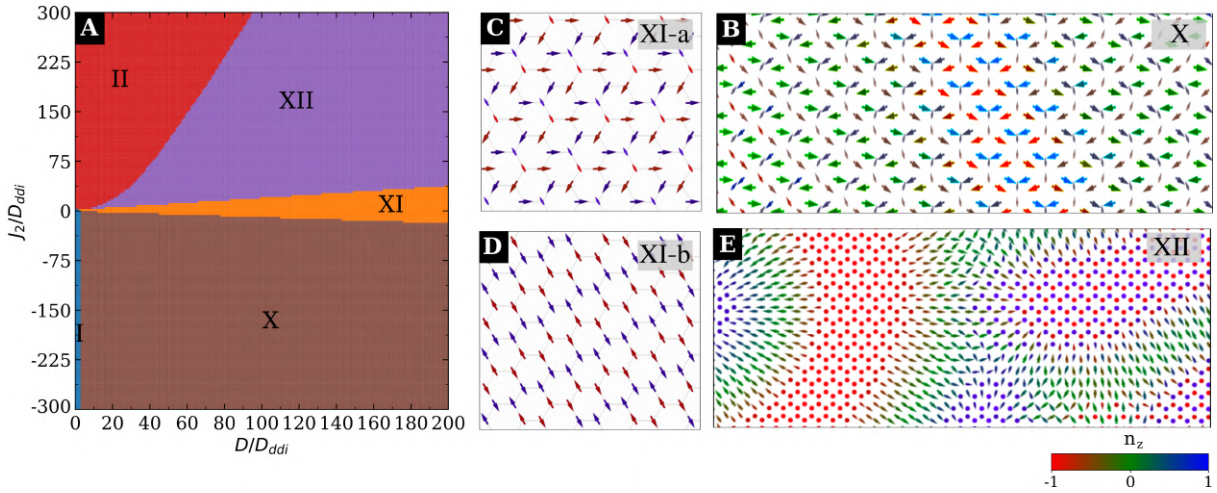

Figure 7.7 – (A) Phase diagram for the honeycomb lattice for varied second-nearest-neighbor exchange J_2 and DMI strength D, for vanishing nearest-neighbor exchange and $K = 0$. (B-E) The spin textures corresponding to the characteristic magnetic phases in panel (A).

the same values of $|J_2|$ are considered.

7.5 Suppressed nearest-neighbor exchange in the honeycomb lattice

The honeycomb lattice symmetry is representative of a variety of magnetic 2D materials, and is hence of particular recent interest. Notice that for a complete description of truly 2D magnetic materials (such as monolayer CrI_3) one should consider more magnetic interactions in the Hamiltonian, such as the Kitaev interaction [281]. In the present consideration, for simplicity and clarity, but also in order to provide a fair comparison between square and honeycomb lattice symmetry, we do not include those additional magnetic interactions in our spin system. Fig. 7.7 (A) exhibits the phase diagram obtained for the honeycomb lattice, for zeroed NN exchange coupling (J_1) and anisotropy (K), in the presence of dipole-dipole interactions, and for varied SNN exchange (J_2) and DMI strength (D). Similarly to the square lattice, for $J_2 > 0$, increasing DMI favors FM and AFM spin cycloids (see Fig. 7.7 (E), and also Fig. 7.10 for a better visualization of the coexisting FM and AFM states). For dominating DMI interaction all spins are forced orthogonal to each other, as shown in Fig. 7.7 (C) and Fig. 7.7 (D) (phase XI). Since in the honeycomb lattice the SNN bonds form a triangular lattice, which is frustrated under AFM coupling, the analogous forms of the p-AFM state and the p-AFM skyrmion found in the square lattice can not be obtained for $J_2 < 0$. Instead, for $J_2 < 0$ we obtained frustrated AFM spin cycloids (shown in Fig. 7.7 (B), also in Fig. 7.11 (A)). In Fig. 7.8 (A) we show that this configuration can actually be decomposed into six sublattices, each of which exhibiting a cycloidal behavior - as seen in the orientation

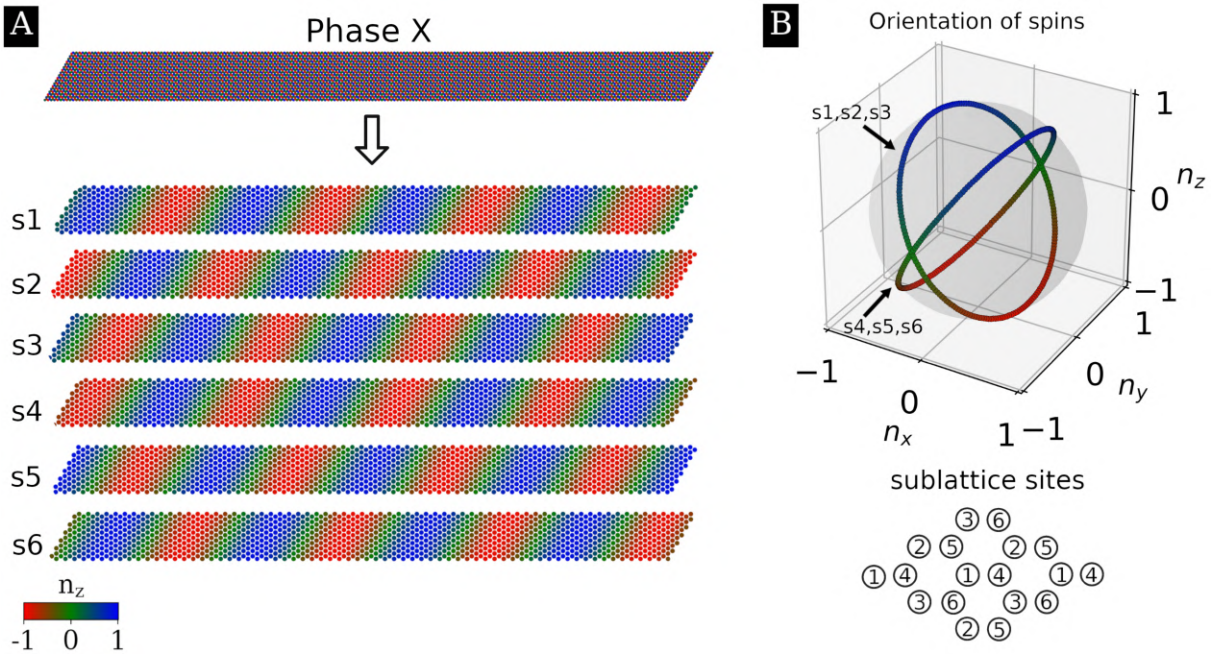

Figure 7.8 – (A) Decomposition of phase X (obtained in the phase diagram for the honeycomb lattice for $J_1 = 0$, $J_2 < 0$ and $D > 0$) into six spin-sublattices (s1-s6). (B) Orientation of spins around the unit sphere, demonstrating the sublattice-specific cycloidal behavior.

of spins shown in Fig. 7.8 (B). Due to the honeycomb symmetry of the lattice, the anti-parallel AFM coupling between the SNN spins can not be satisfied at all bonds and the system is therefore frustrated, causing this unique cycloidal spin state.

Such frustrated cycloid presents the same period in each one of the six spin-sublattices (named s_1 to s_6), but its oscillations are not in-phase, as shown in Fig. 7.8 (A). In addition, the cycloid rotation is not unidirectional, with three sublattices (s1, s2, s3) rotating across the other three (s4, s5, s6), as seen in the orientation of spins shown in Fig. 7.8 (B). In the Fig. 7.11 (B) we show the optimized cycloid period λ, after we found the minimum in the average energy density as a function of the cycloid period for different values of the DMI strength D. As expected for the conventional spin-cycloids (see, e.g, Eq. 7.5), one sees there that increasing the DMI favors the rotation of the magnetization in shorter periods.

To conclude the comparison to our previous findings for the square lattice, in Fig. 7.9 (A) we show an example of FM and c-AFM skyrmions coexisting for $J_2 > 0$ in the honeycomb lattice symmetry. Similarly to the analysis made in the preceding section, we have calculated the energy of an isolated AFM skyrmion and performed minimal-energy-path calculations to evaluate the influence of both NN and SNN exchange to the skyrmion stability. As in the square lattice, both kinds of skyrmions have equivalent energies [see Fig. 7.9 (C)] but their stability falls in different ranges of the exchange intensity $|J|$, with the SNN-stabilized skyrmion occurring at considerably smaller values

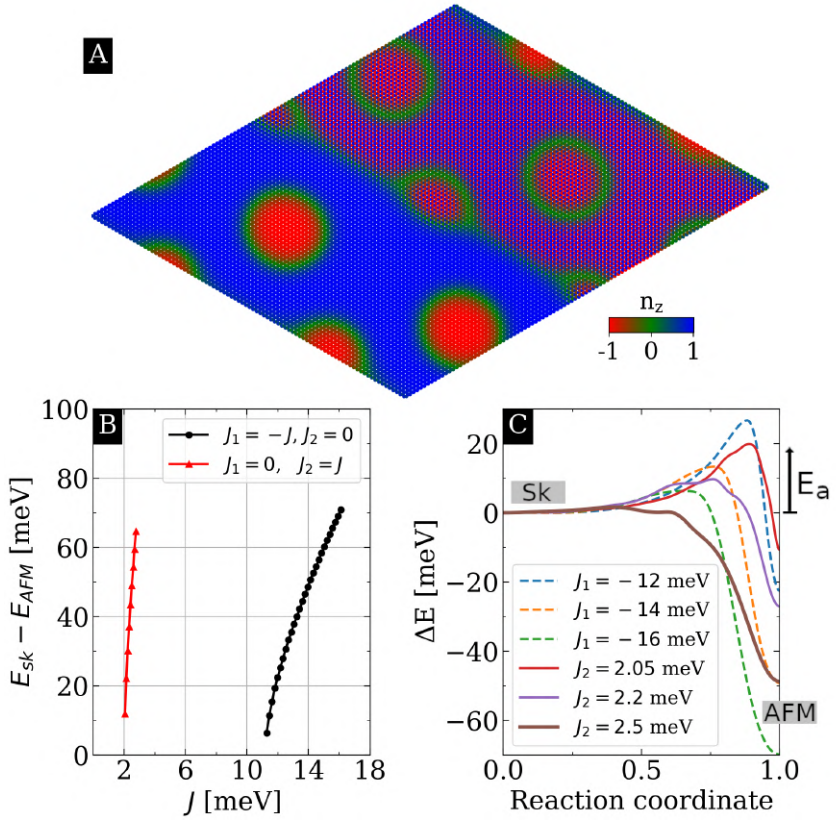

Figure 7.9 – (A) State with coexisting FM and AFM skyrmions, obtained for $J_2 > 0$ in the honeycomb symmetry. (B) Skyrmion energy as a function of exchange coupling for (i) $J_1 = 0$, $J_2 = J$, and (ii) $J_1 = -J$, $J_2 = 0$, both with $K = 3$ meV and $D = 5$ meV. (D) Minimal-energy-path calculations for the isotropic collapse of the AFM skyrmion in both cases (i) and (ii). Here, the reaction coordinate defines the normalized (geodesic) displacement along the formation path and the activation energy E_a is defined by the highest-energy point along the path.

of $|J|$. Finally we note again that, contrary to the square-lattice case, skyrmions with a p-AFM background are not possible in the honeycomb lattice because, as discussed above, AFM ordering is frustrated on a triangular lattice of second-nearest neighbors.

7.6 Conclusion of the chapter

The advent of monolayer materials over the last decade, freestanding or deposited, raises questions whether such systems can harbor unique magnetic properties and potential for technological applications. It is primarily the vast tunability of magnetic interactions in such magnetic monolayers that can lead to unexpected physical phenomena and magnetic phases. Here, we have given a step in that direction, revealing the rich magnetic phase diagram for both square and honeycomb symmetries of a magnetic monolayer, in the limit of suppressed nearest-neighbor exchange interaction. With underlying expectation of degenerate ferromagnetic and antiferromagnetic states promoted by the absence of the nearest-neighbor exchange, the competition between

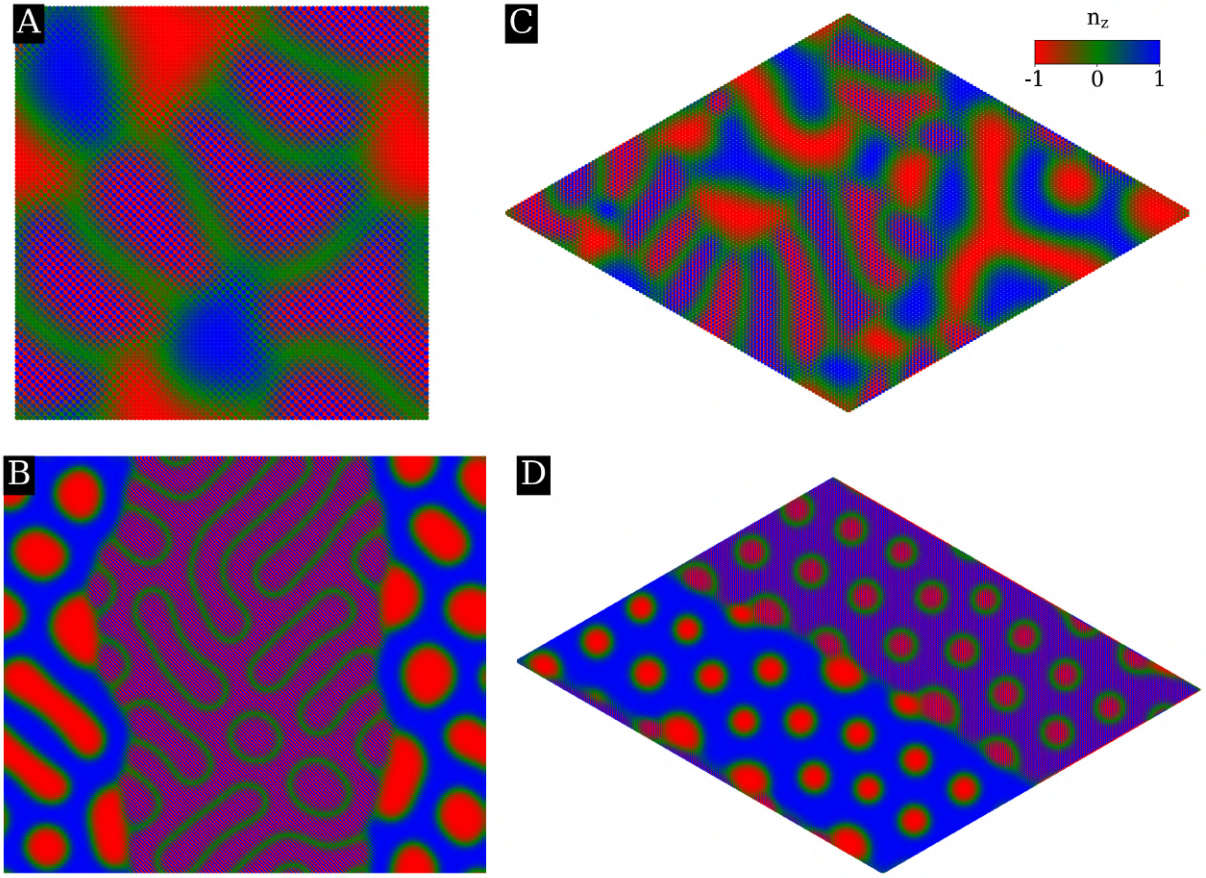

Figure 7.10 – Larger visualization of coexisting FM and AFM spin textures. (A) An example of the state with coexisting FM and AFM domains, obtained in the square lattice for $J_2 = 300D_{\text{ddi}}$, $K = 0$ and $D = 80D_{\text{ddi}}$ (phase VI in Fig. 7.3). (B) State with coexisting FM and AFM skyrmions obtained in the square lattice for $J_2 = 300D_{\text{ddi}}$, $K = 25D_{\text{ddi}}$ and $D = 100D_{\text{ddi}}$. (C) A state with coexisting FM and AFM domains obtained in the honeycomb lattice for $J_2 = 300D_{\text{ddi}}$, $K = 0$ and $D = 180D_{\text{ddi}}$ (phase XII in Fig. 7.7). (D) State with coexisting FM and AFM skyrmions obtained in the honeycomb lattice for $J_2 = 300D_{\text{ddi}}$, $K = 25D_{\text{ddi}}$ and $D = 200D_{\text{ddi}}$. Notice that the diamond shape of the textures shown in (C) and (D) is the actual shape of the unit cell in the calculations for the honeycomb lattice symmetry. In these simulations we have considered a spin lattice of 102×102 spins for (A) and (C) and 200×200 spins for (B) and (D).

the second-nearest-neighbor exchange, DMI, and dipolar interactions leads to several unique cycloidal, checkerboard, row-wise and spin-ice states, unattainable otherwise. Moreover, coexisting FM and AFM skyrmions are found, as well as novel types of chiral domain walls and skyrmions (such as the p-AFM ones). With several existing *ab initio* predictions that exchange interactions in elemental magnetic monolayers can be varied depending on the substrate[261–263, 269], the phases mapped out in this chapter can help the experimental validation of such claims, although influence of a broader range of interactions can be expected than considered here [282]. Last but not least, the interactions in the recently realized 2D magnetic materials can also be broadly manipulated by e.g. strain engineering[266] (as we shall see in the chapter 8), where the results

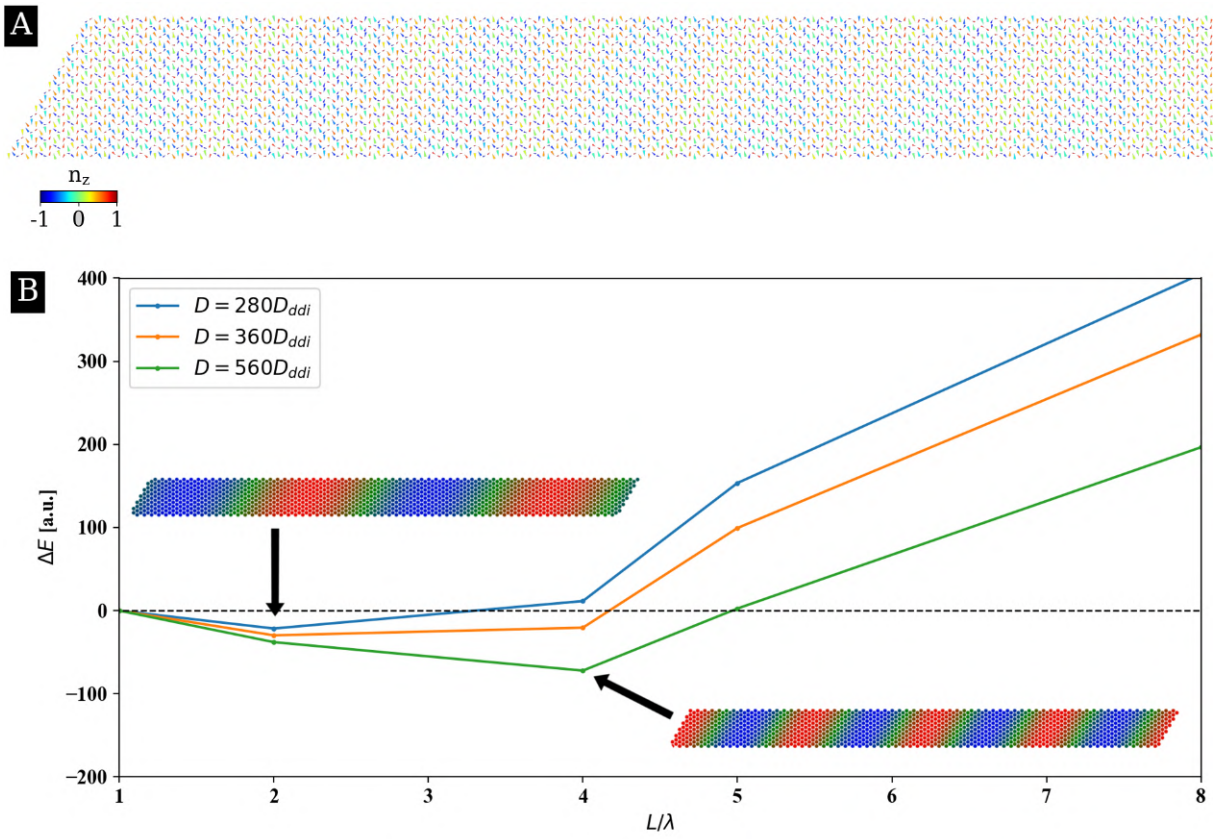

Figure 7.11 – (A) Example of a frustrated AFM cycloid state obtained in the honeycomb lattice for $J_1 = 0$, $J_2 < 0$ and $D > 0$ (corresponding to phase X in Fig. 7.7). Here a supercell of 204×18 spins is considered. (B) Energy of the frustrated AFM cycloid as a function of the cycloid period λ, for fixed size of the system ($L = 204$ spin sites, with periodic boundary conditions), for different DMI strength ($J_1 = 0$, $J_2 = -300D_{\text{ddi}}$, $K = 0$), revealing the energetically optimal period of the cycloid.

presented in this chapter can provide basic expectations and understanding before the more detailed calculations (including additional anisotropic exchange couplings such as Kitaev one[283]) are performed.

8 Magnonics in two-dimensional magnetic materials

Monolayer chromium-trihalides, the archetypal two-dimensional (2D) magnetic materials, are established as a promising platform for high-frequency magnonics. In this chapter, we detail the spin-wave properties of monolayer $CrBr_3$ and CrI_3, using spin-dynamics simulations parametrized from first principles. We reveal that their spin-wave dispersion can be tuned in a broad range of frequencies by strain, paving the way towards flexo-magnonic applications. We further show that ever-present halide vacancies in these monolayers host sufficiently strong Dzyaloshinskii–Moriya interaction to scatter spin-waves, which can be turned useful in design of spin-wave guides by defect engineering. Finally we discuss the spectra of spin-waves propagating across a moiré-periodic modulation of magnetic parameters in a van der Waals heterobilayer, and show that the several nanometer small moiré periodicities in such samples are ideal for realization of a magnonic crystal in the terahertz frequency range. Recalling the additional tunability of magnetic 2D materials by gating, we conclude that these systems are a front-runner for prospective terahertz magnonic applications.

The results presented in this chapter are published in arXiv:2111.14305 (2021).

8.1 Motivation

Two-dimensional (2D) magnetic materials, such as monolayer chromium trihalides and manganese dichalcogenides, have recently drawn immense attention of both theoretical and experimental research, due to its fundamental significance and promising technological applications. The high tunability of the magnetic parameters in such materials, e.g., by lattice straining [34, 284], electric gating [265, 285], layer stacking [286–288], among other techniques, is key for the manipulation of magnetic textures, such as domain-walls, spin-waves (SWs) and magnetic skyrmions, thus opening a field of possibilities for new device concepts [289]. Particularly, some chromium trihalides have been shown able to host terahertz SW modes [290] and are promising candidates

for ultra-fast information transport and processing based on magnons.

In a chromium trihalide monolayer CrX_3 (with X = I, Br or Cl), the plane of Cr atoms form a honeycomb structure and is sandwiched between two atomic planes of the halogen atoms, as illustrated in Fig. 8.1. The ferromagnetic super-exchange across the Cr-X-Cr bonds are anisotropic, and together with the weak single-ion anisotropy of Cr spins, results in ferromagnetic order with off-plane easy axis [281, 291]. In addition to the symmetric exchange, the antisymmetric exchange, also known as the Dzyaloshinskii–Moriya interaction (DMI), can be induced in such systems in the presence of structural symmetry break of the atomic lattice, e.g., in Janus structures [264] or in the presence of applied electric fields [292, 293].

In this chapter we investigate the SW propagation in monolayer $CrBr_3$ and CrI_3 as representative of 2D magnetic materials. We take magnetic parameters from first-principle calculations of the considered structures, as reported in literature [34, 41], and perform spin-dynamics simulations of the SW propagation. We calculate the SW dispersion relation in the chromium trihalides on both its pristine form and under uniform strain, thus showing the tunability of SW properties in the 2D materials, and reveal the possibility of manipulating the SWs by strain-engineering. We further analyse the SW propagation in the presence of lattice defects (halide vacancies) in the chromium trihalides. We show that the lattice defects induce local DMI in the magnetic monolayer, which can strongly affect the SW dynamics in such materials, and that a designed pattern of defects can confine the SWs and may serve as a SW guide in the CrX_3 monolayers. Lastly, we investigate the spectra of SWs propagating across periodic modulation of the magnetic parameters, induced by moiré pattern in van der Waals heterostructures [294, 295]. We show that such structure can work as a magnonic crytal [63] for the high-frequency SWs, which exhibit features such as band gaps where SWs are not allowed to propagate. The wide range of manipulations available in 2D materials therefore suggests these systems as promising candidates for terahertz magnonics.

8.2 Theoretical modeling

8.2.1 Atomistic spin model

We consider a spin system arranged in a honeycomb structure in order to simulate the magnetic moments of Cr atoms in the chromium trihalide monolayer. For that purpose we consider the quadratic Heisenberg spin Hamiltonian, which is given by [see Sec. 2.3]

$$\mathcal{H} = \frac{1}{2}\sum_{i,j} \mathbf{S}_i \mathcal{J}_{ij} \mathbf{S}_j + \sum_i \mathbf{S}_i \mathcal{A}_i \mathbf{S}_i, \tag{8.1}$$

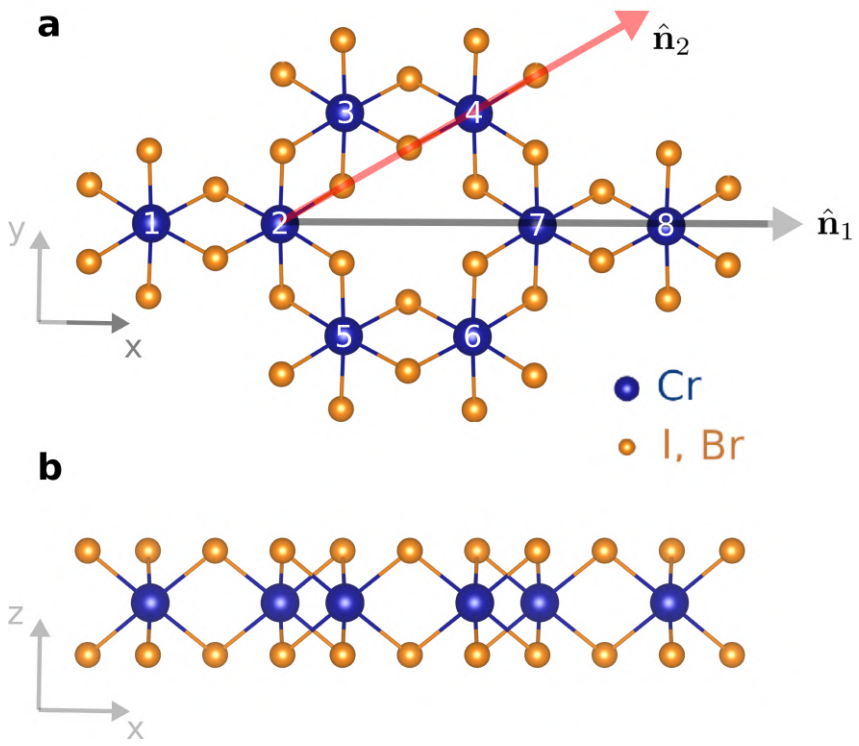

Figure 8.1 – (a) Top view of the CrX_3 lattice. $\hat{\mathbf{n}}_1$ and $\hat{\mathbf{n}}_2$ represent the main symmetry axis discussed in Sec. 8.3. (b) Side view of the CrX_3 monolayer.

where $\mathcal{J}_{ij}$ and $\mathcal{A}_i$ are the exchange and single ion anisotropy (SIA) matrices, respectively, and $\mathbf{S}_i = (S_i^x, S_i^y, S_i^z)$ is the spin vector at the i^{th} site. We consider $S = 3/2$ for the Cr^{3+} ions, with three unpaired valence electrons and quenched orbital moment ($L = 0$), which yields a magnetic moment of $\sim 3\mu_B$ per Cr atom, in agreement with the observed in such materials[281, 291, 296]. The sum over i in Eq. 8.1 runs over all Cr sites, while the sums over i, j run over all nearest-neighbor Cr pairs. The exchange matrix can be further decomposed into a symmetric exchange J and the antisymmetric DMI vector $\mathbf{D}$. The Hamiltonian then becomes

$$\begin{aligned}\mathcal{H} =& \frac{1}{2}\sum_{i,j}\Big[J_\alpha S_i^\alpha S_j^\alpha + J_\beta S_i^\beta S_j^\beta + J_\gamma S_i^\gamma S_j^\gamma \\ &+ \mathbf{D}_{ij}\cdot(\mathbf{S}_i \times \mathbf{S}_j)\Big] \\ &+ \sum_i \Big[\mathcal{A}_{\alpha'}(S_i^{\alpha'})^2 + \mathcal{A}_{\beta'}(S_i^{\beta'})^2 + \mathcal{A}_{\gamma'}(S_i^{\gamma'})^2\Big],\end{aligned} \tag{8.2}$$

where $\{\alpha\beta\gamma\}$ and $\{\alpha'\beta'\gamma'\}$ are the local bases of eigenvectors that diagonalize J and $\mathcal{A}$, respectively. $S_i^u = \frac{\mathbf{u}\cdot\mathbf{S}_i}{\mathbf{u}\cdot\mathbf{u}}$ is the projection of the i^{th} spin along the vector $\mathbf{u}$. For simplicity, and since in this work we are interested in high frequency SWs, which are dominated by the short-range exchange interactions, we neglect the contributions of dipole-dipole interactions. Notice that the above Hamiltonian is not limited to isotropic exchange interactions, and can be applied to different atomic structures, such as in the presence of lattice defects, where the bases of eigenvectors can change for specific bonds. For either

	pair (i-j)	J^{xx} (meV)	J^{yy} (meV)	J^{zz} (meV)	J^{xy} (meV)	J^{xz} (meV)	J^{yz} (meV)	Δ (meV)	$\mathcal{A}^{zz}$ (meV)
CrI_3								-0.22	-0.07
	(1-2)	-5.10	-3.72	-4.63	0.00	0.00	0.84		
	(2-3)	-4.07	-4.76	-4.63	-0.60	0.72	-0.42		
	(2-5)	-4.07	-4.76	-4.63	0.60	-0.72	-0.42		
	$\langle J \rangle$	-4.41	-4.41	-4.63	0.00	0.00	0.00		
$CrBr_3$								-0.04	-0.01
	(1-2)	-3.45	-3.29	-3.42	0.00	0.00	0.10		
	(2-3)	-3.33	-3.41	-3.42	-0.07	0.08	-0.05		
	(2-5)	-3.33	-3.41	-3.42	0.07	-0.08	-0.05		
	$\langle J \rangle$	-3.37	-3.37	-3.42	0.00	0.00	0.00		

Table 3 – Magnetic parameters for pristine CrI_3 and $CrBr_3$ obtained from first-principle calculations [see Ref. bacaksiz2021distinctive for details]. J^{xx}, J^{yy}, and J^{zz} are diagonal elements, and $J^{xy} = J^{yx}$, $J^{xz} = J^{zx}$, $J^{yz} = J^{zy}$ the off-diagonal elements of the exchange matrix. $\langle J \rangle$ is the average exchange over the three nearest-neighbour pairs and $\Delta = \langle J^{xx} \rangle - \langle J^{zz} \rangle$ is the out-of-plane anisotropy. $\mathcal{A}^{zz}$ is SIA parameter, same for each Cr site. Pairs (i-j) are indicated in Fig. 8.1 (a).

considered structure, corresponding exchange and SIA matrices for different Cr pairs are obtained from first principles calculations. Table 9 lists the magnetic parameters obtained for pristine CrI_3 and $CrBr_3$ monolayers [34]. Parameters obtained for other specific cases considered in this chapter will be shown where needed.

The dynamics of the magnetic spins is governed by the Landau-Lifshitz-Gilbert (LLG) equation [Eq. 2.15]. In this chapter, the LLG spin dynamics simulations are primarily based on the simulation package *Spirit* [38], adapted to accommodate our Hamiltonian [Eq. 8.2].

8.3 Spin-wave propagation in pristine and strained CrX_3

The magnetic interactions in 2D materials are very sensitive to deformation in the atomic lattice. In particular, it has been shown that exchange interactions in CrI_3 and $CrBr_3$ are significantly affected by either tensile or compressive strain [34]. Therefore, in this section, we investigate how straining the 2D material can affect the propagation of SWs in such systems. For the simulations, we consider both $CrBr_3$ and CrI_3 monolayers on their pristine form as well as under uniform biaxial strain. The SW beams are artificially created by a sinusoidal in-plane oscillating field $\mathbf{B}_{\text{input}} = b_0 \sin(2\pi f_{\text{in}} t)\hat{k}$ applied in a narrow rectangular region, where f_{in} is the input frequency; b_0 the field amplitude and $\hat{k}$ is the SW propagation direction. For the simulations we consider $b_0 = 0.1$ T and damping parameter $\alpha = 0.001$. The SW frequency f and wavelength λ are calculated by fitting a sine function to the magnetization oscillations [see e.g. Fig.8.2 (a)] as a function of time and space respectively. Fig. 8.2 (b,c) shows the dispersion relation,

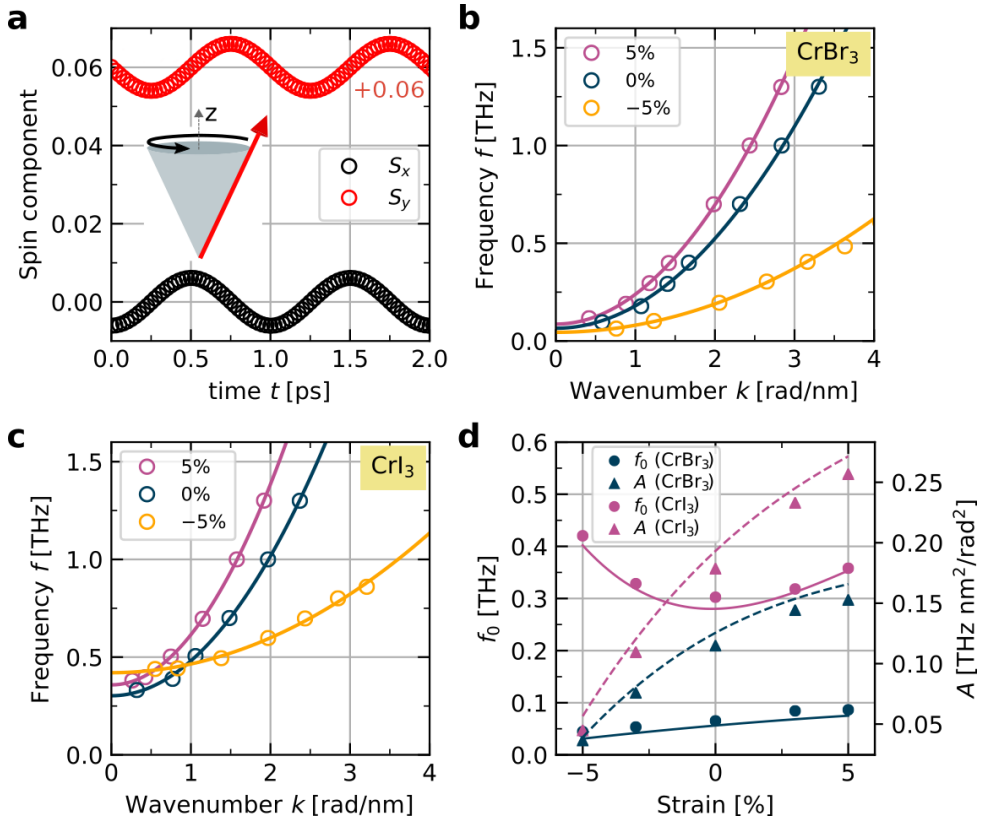

Figure 8.2 – (a) Spin components as a function of time for the case of 1 THz SW. The S_y spin component is shifted for better visualization. (b,c) Spin-wave dispersion relation obtained in the simulations for $CrBr_3$ (b) and CrI_3 (c), under different strain. Solid lines show the numerical fit to the quadratic expression $f(k) = Ak^2 + f_0$. (d) The values of the fitted parameters A and f_0 obtained as a function of strain. Solid and dashed lines are the analytical expressions (obtained from Eq. (8.4)) for f_0 and A, respectively.

i.e., the relation between the SW frequency and the wavenumber $k = 2\pi/\lambda$ for $CrBr_3$ and CrI_3, respectively, obtained in the simulations under different strain. The calculated dispersion curves correspond to the lower-energy magnon modes. Notice that the SW dispersion can be tuned throughout a wide range of frequencies by performing strain on the honeycomb structure, which demonstrates the ease of tuning magnonics in such 2D materials. Solid lines in Fig. 8.2 (b,c) depict the fit of the quadratic expression $f(k) = Ak^2 + f_0$ to the numerical data. The values of the fitting parameters A and f_0 as a function of strain are shown in Fig. 8.2 (d). One can clearly notice the distinct response of the parameter f_0, which corresponds to the zero-momentum SW mode, to strain in $CrBr_3$ and CrI_3. As discussed below, this behaviour is directly related to the out-of-plane exchange anisotropy, whose magnitude for CrI_3 increases for either tensile or compressive strain, while for $CrBr_3$ it has linear dependence on strain [see, e.g, Fig 8.3]. The corresponding energy gaps at $k = 0$, given by $\Delta E = h f_0$, where h is the Plank constant, varies in the range of 1.25 to 1.74 meV for CrI_3 and from 0.18 to 0.36 meV for $CrBr_3$, under the −5 to 5 % range of strain. Those values have the same

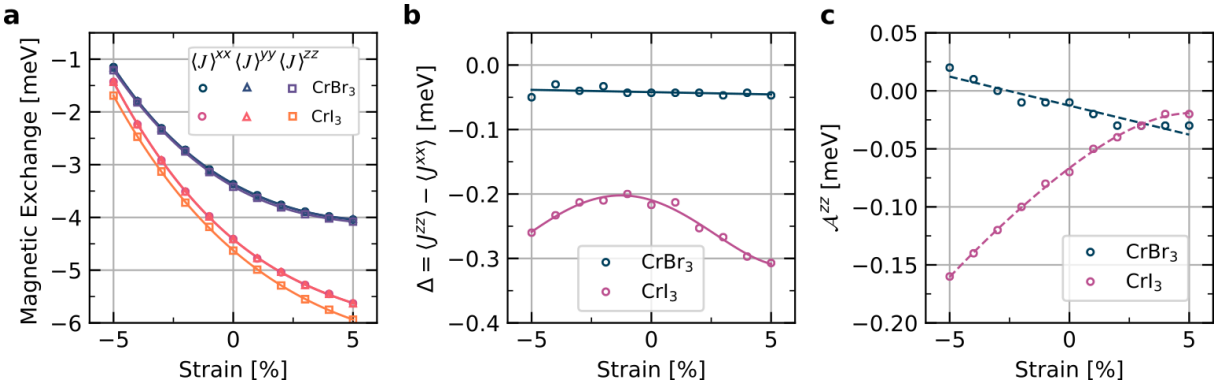

Figure 8.3 – Magnetic parameters for $CrBr_3$ and CrI_3 as a function of strain, for (a) Average exchange (b) Out-of-plane exchange anisotropy, and (c) Single-ion-anisotropy.

order of magnitude, but are significantly smaller than that measured for the case of few layer CrI_3 in Ref. [290] (9.4 meV) and Ref. [297] (3 meV). We expect that such strain dependency of spin excitations in the 2D magnets can be further investigated experimentally by means of different spectroscopy techniques [57, 61, 290, 297, 298].

The SW dispersion can be obtained analytically in the limit of small SW amplitude by solving the linearized LLG equation [32]. For that purpose, let us simplify the Hamiltonian [Eq. (8.2)] as follows. First notice that, due to the symmetry of the lattice, the DMI contribution is null, and the only finite term of SIA matrix is $\mathcal{A}^{zz}$, such that the SIA contribution to the energy of the i^{th} spin becomes $\mathcal{A}^{zz}(S_i^z)^2$. Assuming that both $CrBr_3$ and CrI_3 have strong out-of-plane anisotropy, the exchange energy might be rewritten in terms of an isotropic exchange $J_0 = \langle J^{xx} \rangle$, and the anisotropic term $\Delta = \langle J^{zz} \rangle - \langle J^{xx} \rangle$, where $\langle ... \rangle$ represents the average over the three nearest-neighbour pairs. The lattice symmetry guarantees that $\langle J^{yy} \rangle = \langle J^{xx} \rangle = J_0$ and $\langle J^{ab} \rangle = 0$ for $a \neq b$ [see, e.g., Table 9]. The Hamiltonian for the i^{th} spin takes the simple form of the XXZ model [291, 299, 300]

$$\mathcal{H}_i = J_0 \sum_j \mathbf{S}_i \cdot \mathbf{S}_j + \Delta \sum_j S_i^z S_j^z + \mathcal{A}^{zz}(S_i^z)^2, \tag{8.3}$$

where the sum in j runs over the three nearest-neighbours of the i^{th} spin. The SW dispersion is then calculated by assuming the linearized solution $\hat{S}^z \approx 1$, $\hat{S}^x \approx A_0 e^{i(\mathbf{k}\cdot\mathbf{r}-\omega t)}$ and $\hat{S}^y \approx iA_0 e^{i(\mathbf{k}\cdot\mathbf{r}-\omega t)}$, where $A_0 \ll 1$ represents the SW amplitude; ω is the SW angular frequency and $\mathbf{r}$ is the position of the considered spin. Substituting that into the LLG equation [Eq. (2.15)], with the effective field derived from Eq. (8.3), we obtain [see Appendix B.1]

$$\omega(k) = \frac{\gamma S^2}{(1+\alpha^2)\mu} \left[3\Delta + 2\mathcal{A}^{zz} + J_0 g(\mathbf{k}) \right], \tag{8.4}$$

where,

$$\begin{aligned} g(\mathbf{k}) &= 3 - \cos(ka) - 2\cos(ka/2), \quad \text{if } \mathbf{k} \parallel \hat{\mathbf{n}}_1, \\ g(\mathbf{k}) &= 2 - 2\cos(ka\sqrt{3}/2), \quad \text{if } \mathbf{k} \parallel \hat{\mathbf{n}}_2, \end{aligned} \tag{8.5}$$

where a is the distance between nearest-neighbour pairs, and $\hat{\mathbf{n}}_1$ and $\hat{\mathbf{n}}_2$ are the main symmetry axis of the honeycomb lattice, as shown in Fig. 8.1.

Notice that, in the limit of small ka, Eq. (8.5) can be approximated as $g(\mathbf{k}) \approx \frac{3a^2}{4}k^2$ for both $\mathbf{k} \parallel \hat{\mathbf{n}}_1$ and $\mathbf{k} \parallel \hat{\mathbf{n}}_2$. The SW frequency $f = \omega/2\pi$ then assumes quadratic dependence on the wavenumber k. The solid and dashed lines in Fig. 8.2 (d) show the analytical solutions (with $\alpha^2 \ll 1$) for the zero-momentum SW frequency $f_0 = \frac{\gamma S^2}{2\pi\mu}(3\Delta + 2\mathcal{A}^{zz})$ and the quadratic coefficient $A = \frac{\gamma S^2}{2\pi\mu}\frac{3a^2 J_0}{4}$, respectively, which are in good agreement with the numbers obtained in the simulations. The values of Δ, $\mathcal{A}^{zz}$ and J_0 as a function of strain are shown in Fig. 8.3. Notice that the XXZ model [Eq. (8.3)] is shown to be a good approximation to describe SWs in uniform CrI_3 and $CrBr_3$ 2D magnets.

In the case where the CrX_3 lattice experiences non-zero DMI, such as in Janus structures [264] or in the presence of out-of-plane applied electric fields [292, 293], the linearized solution for the SW dispersion [Eq. (8.4)] results in an extra term that has linear dependence on the wavevector k. [301] The strongest effect of DMI to the SW dispersion is observed when the background magnetization lies in the same plane of the DMI vectors. Detail on the calculation of SW dispersion with uniform DMI included can be found in Appendix B.1.

8.4 Flexo-magnonics

The strong response of SW properties to strain in the 2D material suggests the possibility of flexo-magnonic applications. In fact, 2D materials are flexible and strain engineering can be realized in numerous ways. For example, localized strain can be induced by growing the 2D material on top of a patterned substrate [302, 303] or by placing it onto a prestrained elastometric substrate, whose compression produces buckling-induced delamination of the 2D material, such as wrinkles and buckles [303–305]. In addition, bubbles and tents can be formed in the 2D material by trapping water, gas or solid nanoparticles at the interface between the magnetic layer and the substrate [306, 307].

To study the interaction of SWs with localized strain we simulate the SW propagation in the presence of a wrinkle in the CrI_3 monolayer. Fig. 8.4 (a) illustrates the considered system. In such a configuration, the position of a generic Cr atom in the curved structure can be parametrized as $\mathbf{r}' = \mathbf{r} + \mathbf{u}(\mathbf{r})$, where $\mathbf{r} = (x, y, 0)$ is the atom position in the pristine lattice and $\mathbf{u}(\mathbf{r}) = (u_x(\mathbf{r}), u_y(\mathbf{r}), h(\mathbf{r}))$ the position displacement. Here, u_x and u_y represent the in-plane displacement and $h(\mathbf{r})$ is a scalar field accounting for out-of-plane deformations. The red and blue shades in Fig. 8.4 (a) illustrate the expected regions of tensile and compressive strain respectively [308]. In addition to

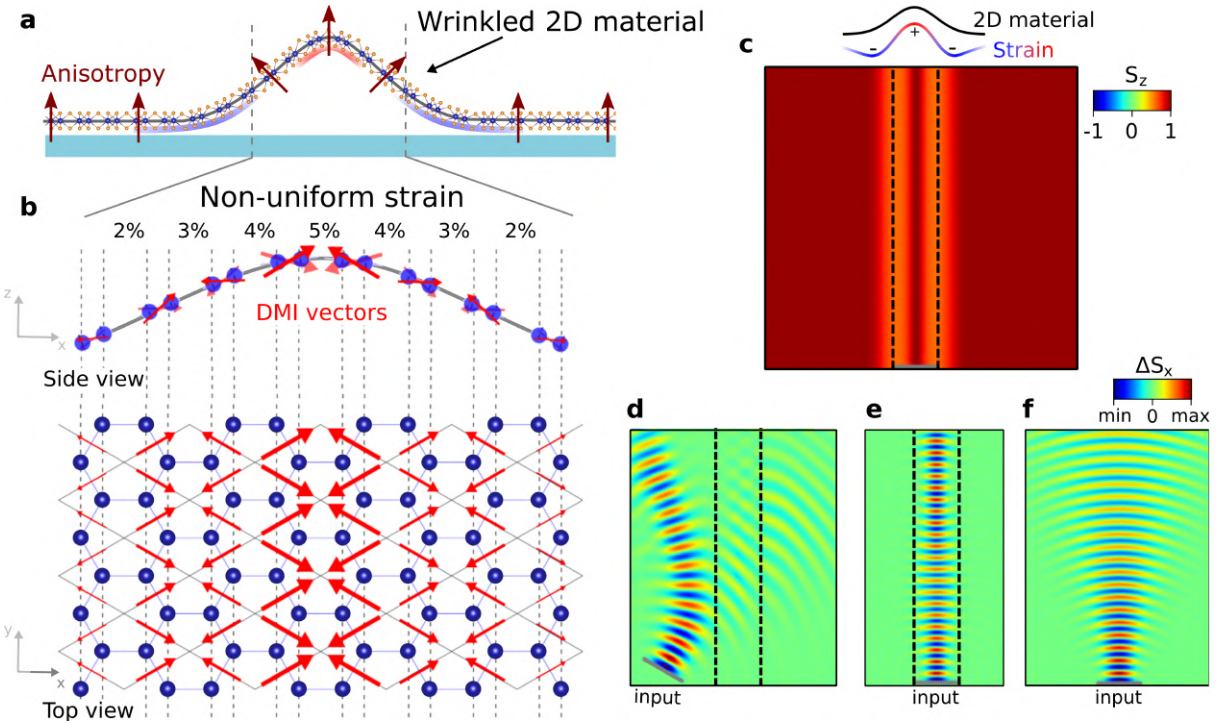

Figure 8.4 – (a) Schematic of wrinkled 2D magnetic material. The curvature induces nonuniform strain in the 2D material and the magnetic anisotropy points normal to the film surface. Here, the red shade stands for tensile strain and the blue shade represents the region of compressive strain. (b) Illustration of the DMI pattern expected in the case of nonuniform strain in the CrX_3 monolayer. (c) Snapshot of simulated magnetic ground state in the presence of a wrinkle in the 2D material. The dashed lines indicate the regions of maximum slope in the 2D material. (d-e) Snapshots of SW simulation propagating (d) across and (e) along a wrinkle in CrI_3, with $f = 0.5$ THz. (f) Snapshot of the SW simulation corresponding to (e) for the case of pristine film.

the local strain, the curvature also induces a rotation in the direction of the magnetic anisotropy, which points normal to the surface of the magnetic film [Fig. 8.4 (a)]. Moreover, due to the non-uniform deformation, a symmetry break also emerges giving rise to localized DMI. Figure 8.4(b) illustrates the expected DMI vectors in the case of a non-uniform uniaxial strain in the wrinkled CrX_3 monolayer. DFT calculations performed for a flat system show that the DMI increases linearly with uniaxial strain, with relatively small magnitude of up to $D = 0.08$ meV for 6% of local strain [41].

First principles calculations of such curved material are rather complicate and a relaxation of the atomic structure is required before calculating the magnetic parameters. However, as a first step in understanding the interaction of SWs in such systems, here we model the material curvature by rotating the local bases of eigenvectors of the magnetic Hamiltonian [Eq. (8.2)] accordingly to the surface normal, and the magnitude of interactions are modeled by including a strain profile. Observe that the considered magnetic Hamiltonian is completely determined by the exchange and anisotropy matrices and the angle between neighbouring spins, therefore, local deformations can be

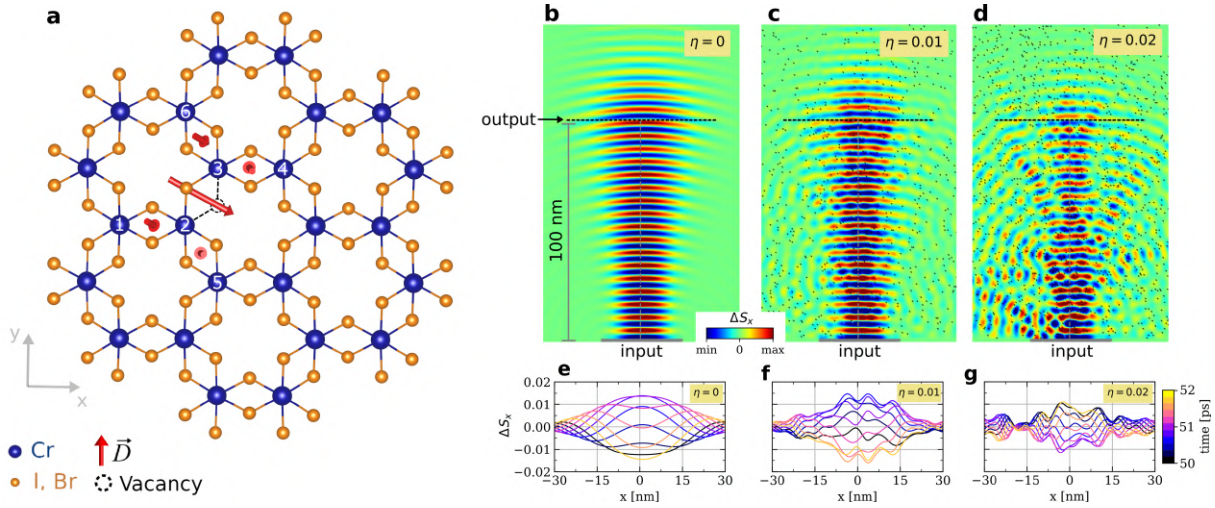

Figure 8.5 – (a) Illustration of CrX_3 lattice in the presence of a single halide vacancy. Induced DMI vectors are illustrated as red arrows. (b-d) Snapshots of SW simulations in the presence of randomly distributed defects in CrI_3, for defect densities $\eta = 0$, $\eta = 0.01$, $\eta = 0.02$ vacancies per Cr atom, respectively. The input SW frequency is 0.5 THz. (e-g) Correspondent output SW amplitudes for the cases in (b-d), respectively, measured at a distance of 100 nm from the SW source. Colors in (e-g) correspond to different time steps along the 2 ps SW period.

modeled by modifying the interaction matrices instead of the precise atomic positions. Fig. 8.4 (c) shows the magnetic ground state obtained in the simulations for a single wrinkle of Gaussian shape $h(\mathbf{r}) = h_0 e^{-\frac{x^2}{w^2}}$, where $h_0 = 20$ nm and $w = 15$ nm define the height and width of the wrinkle, respectively. The considered strain profile has maximal deformation of $\epsilon = 5\%$ on top of the wrinkle and satisfies $\epsilon(x) \propto \partial^2 h(\mathbf{r})/\partial x^2$. Notice that the curvature induces a canting in the ground state magnetization. Fig. 8.4 (d-f) shows snapshots of the simulation of a 0.5 THz SW propagating (d) across and (e) along the wrinkle, where the SW can either be reflected by or confined along the flexed region, in comparison with the case of a pristine film (f). In this way, and recalling the wide range of possibilities for manipulating the 2D material, this suggests these systems as candidates for flexo-magnonic applications.

Furthermore, although we have considered an uniform damping parameter (α) in our calculations, the value of α may also be affected by local strain in the vicinity of the wrinkle [309]. Further studies are needed to understand the effect of the strain-induced α nonuniformity on the SW propagation.

8.5 Interaction of spin-waves with lattice defects

8.5.1 Randomly distributed defects

Vacancies are the most commonly observed defect in nanomaterials. They not only naturally appear when the material is synthesized under harsh conditions, but

can also be artificially induced by vacancy engineering [310, 311]. In this section we investigate the interaction of SWs with randomly distributed defects (halides vacancies) in CrX_3 lattice. The symmetry break around the lattice defect results in DMI interaction between the neighboring Cr atoms, as illustrated in Fig.8.5 (a). It is well known that SWs are strongly affected by the DMI interaction and can even be reflected by an interface where DMI changes[312, 313]. In the case of lattice defects, *ab initio* calculations show DMI vectors of magnitudes up to $D = 5.57$ meV for CrI_3 and $D = 2.57$ meV for $CrBr_3$ in the vicinity of halide vacancies [41]. Such strong variations of the local magnetic interactions can therefore scatter the SW propagation in the 2D magnetic materials.

In this section we quantify the SW scatter in $CrBr_3$ and CrI_3 under different density

Isolated defect	pair (i-j)	D^x (meV)	D^y (meV)	D^z (meV)	$\|D\|$ (meV)
CrI_3					
	(1-2)	0.29	-0.20	-0.53	0.64
	(2-3)	4.05	-2.33	-0.39	4.69
	(2-5)	0.17	0.09	-0.46	0.50
	(3-4)	0.01	0.11	-0.06	0.12
	(3-6)	0.01	-0.38	0.19	0.42
$CrBr_3$					
	(1-2)	-0.05	-0.13	0.26	0.29
	(2-3)	2.24	-1.31	-0.08	2.60
	(2-5)	0.00	0.06	-0.04	0.07
	(3-4)	0.02	0.03	0.07	0.08
	(3-6)	-0.09	-0.14	0.07	0.18
Line of defects	pair (i-j)	D^x (meV)	D^y (meV)	D^z (meV)	$\|D\|$ (meV)
CrI_3					
	(1-2)	0.01	-0.43	0.06	0.44
	(2-3)	-0.05	-0.55	2.42	2.48
	(2-5)	3.61	-0.27	4.23	5.57
	(3-4)	-0.09	0.03	-0.23	0.25
	(3-6)	3.61	-0.27	4.23	5.57
$CrBr_3$					
	(1-2)	0.00	-0.09	0.01	0.09
	(2-3)	0.12	0.14	0.47	0.50
	(2-5)	2.09	-0.02	1.50	2.57
	(3-4)	-0.04	-0.03	0.01	0.05
	(3-6)	2.09	-0.02	1.50	2.57

Table 4 – Induced DMI parameters at an isolated defect (halide vacancy) and at a line of such defects in CrI_3 and $CrBr_3$, obtained from first-principle calculations [41]. Pairs (i-j) are indicated in Fig. 8.5 (a) and Fig. 8.7 (a).

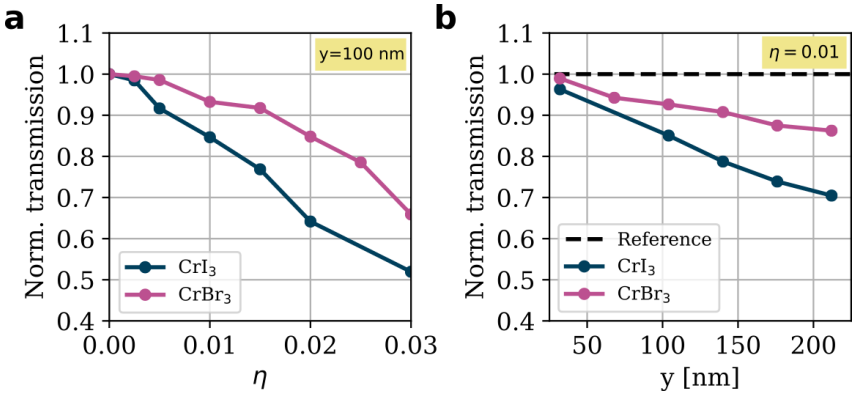

Figure 8.6 – (a) SW normalized transmission as a function of the density of defects, η, measured at a distance of $y = 100$ nm from the SW source, with $f = 0.5$ THz. (b) SW transmission as a function of the output distance, with $\eta = 0.01$ and $f = 0.5$ THz. Here, the transmission amplitudes are normalized with respect to the case of $\eta = 0$, measured at the same distance from the SW source.

of defects η, which we define as the number of vacancies per Cr atom. Fig.8.5 (b-d) shows the snapshots of SW simulations when propagating through the CrI_3 monolayer for $\eta = 0$, 0.01 and 0.02, respectively. The corresponding output SW amplitudes, measured at a distance of 100 nm from the SW source [Fig.8.5 (e-g)], reveal that the transmitted wave is strongly affected in the case of high density of defects. In order to quantify the SW transmission under the different defect densities, we integrate the output SW amplitudes along the direction perpendicular to the SW propagation and normalize it with respect to the case without defects, i.e., $\eta = 0$. Fig.8.6 (a) shows the normalized transmission for the 0.5 THz SWs in $CrBr_3$ and CrI_3. Notice that SWs in CrI_3 are strongly affected by the halide vacancies when compared to $CrBr_3$. We relate this property to the large DMI interactions induced in CrI_3, which are more than twice as large as in the $CrBr_3$ sample.

The defect-induced scattering as a function of distance may be important when designing new magnonic devices. Fig.8.6 (b) shows the SW transmission as a function of the output distance, normalized with respect to the case of $\eta = 0$, measured at the same distance from the SW source. Notice that the normalized transmission decreases linearly as a function of the output distance, where the transmission in CrI_3 decreases in a rate of approximately twice as fast as that of $CrBr_3$, for $\eta = 0.01$, thus emphasizing the stronger response of SWs to defects in CrI_3. Lastly, we did not observe any significant frequency dependence (for the range of 0.3–1.5 THz) in the results presented in this section.

8.5.2 Line of defects

In this section we investigate the interaction of SWs with a row of consecutive defects (halides vacancies) in CrX_3 lattices as a possible way of controlling the SW propagation direction in such systems. As demonstrated in the previous section, the

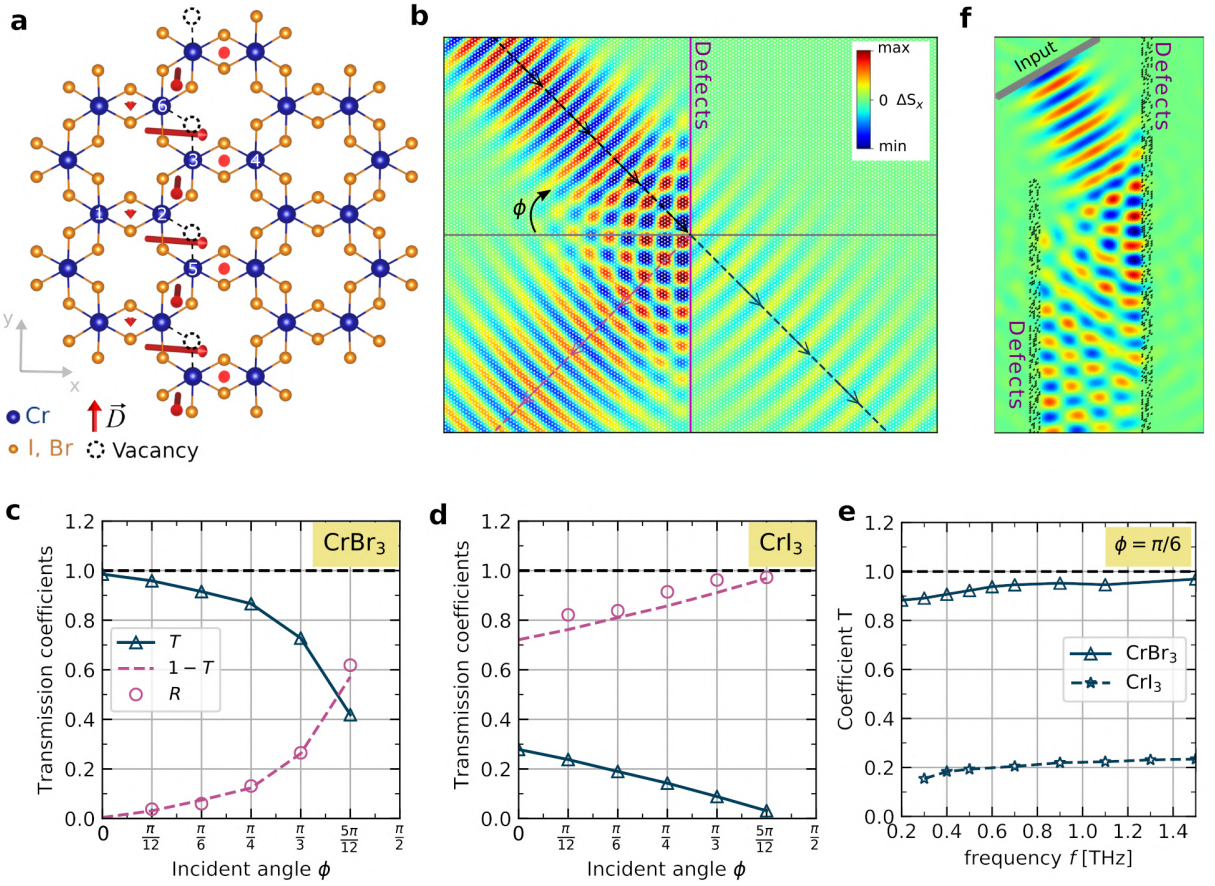

Figure 8.7 – (a) Illustration of CrX_3 lattice in the presence of defect line (halides vacancies). Induced DMI vectors are illustrated as red arrows. (b) Reflection of SW by defect line. Snapshot of spin-wave simulation for a 0.5 THz SW reaching the defect line in an incident angle of $\phi = \pi/4$ in CrI_3. Arrows indicate the SW propagation direction. (c-d) Transmission and reflection coefficients as a function of incident angle ϕ for $CrBr_3$ (c) and CrI_3 (d), obtained for SW frequency $f = 0.5$ THz and $\alpha = 0.001$. (e) Frequency dependency of the transmission coefficient T for both $CrBr_3$ and CrI_3 at fixed incident angle $\phi = \pi/6$. (f) Snapshot of the simulations for the SW confinement between two defect lines in the magnetic material.

induced fluctuations in magnetic parameters around the lattice defects strongly affect the SW propagation. Therefore, a designed pattern of defects, such as a row of consecutive defects, may be able to confine the SWs and serve as a waveguide. Magnetic parameters of the considered structure, which is illustrate in Fig.8.7 (a), are given in table 4 and in the Appendix B.2, where the magnitudes of the DMI are similar to that obtained in the vicinity of isolated defects. Fig. 8.7 (b) shows a snapshot of the simulation for a SW propagating across the defect line in CrI_3, where we consider a 0.5 THz SW reaching the defect line with an incident angle of $\phi = \pi/4$. Notice that only a fraction of the SW is able to cross the defect line while the other part is reflected. In Fig. 8.7 (c-d) we show the transmission coefficients, defined as [314, 315]

$$T = \left(\frac{\Delta_T}{\Delta_0}\right)^2, R = \left(\frac{\Delta_R}{\Delta_0}\right)^2, \tag{8.6}$$

where Δ_T and Δ_R are the amplitudes of the transmitted and reflected waves, respectively, and Δ_0 is the corresponding SW amplitude in the absence of defects, calculated at the same distance from the SW source. The reflection and transmission coefficients are defined to satisfy the relation $R = 1 - T$. In Fig. 8.7 (c-d) the transmission and reflection coefficients are shown as a function of incident angle ϕ for $CrBr_3$ [Fig. 8.7 (c)] and CrI_3 [Fig. 8.7 (d)]. Notice that, SWs experience large reflection by the defect line for the case of CrI_3 while most part of the SW is transmitted across defect line in $CrBr_3$. We relate this property to the large DMI interactions induced in CrI_3. Similar to an interface where DMI changes [312], the reflected part of the SW increases as we increase the incident angle from $\phi = 0$ to $\phi = \pi/2$. However, total reflection is not obtained in our simulations, which may be a consequence of the potential barrier induced by defects being composed of a single atomic line rather than an interface. Fig. 8.7 (e) shows the frequency dependency of the transmission coefficient T for both $CrBr_3$ and CrI_3 at fixed incident angle $\phi = \pi/6$, which shows a slight increase on transmission by increasing SW frequency.

Note that such precise pattern of defects can be difficult to reproduce experimentally by vacancy engineering the 2D material [310, 311]. However, a defected region could be induced, e.g., by electron-beam lithography [310] or by scratching the material with a tip. The induced defects would not be in a perfect line, but randomly placed along the scratch. In Fig. 8.7 (f) we show the snapshot of the simulation for the SW propagating across a distribution of defects in CrI_3, randomly placed along narrow regions of six lattice constants width, in order to simulate scratches in the magnetic material. Notice that such a pattern of defects can also confine the SWs. Moreover, the necessary ingredient for confining the SWs in such systems is the variation of the magnetic parameters locally, which can also be induced, for example, by electric gating [292] or strain-engineering the 2D material, as demonstrated in Sec. 8.4.

8.6 Magnonic crystals

The spectra of SWs can be significantly affected by the magnetic media in which the wave propagates. Magnonic crystals are artificial materials designed in such a way that the magnetic properties of the media are characterized by periodic lateral variation[63]. The SW spectra in such materials exhibit features such as band gaps, where the waves are not allowed to propagate. Magnonic crystals have potential application in magnonics, such as information transport and processing based on magnons. Periodic variations of the magnetic parameters in the 2D magnetic materials can be induced in multiple ways, for example, by periodic electric gating [316], strain engineering [303, 305, 307], or by growing the 2D material on top of a patterned substrate [302]. However, a magnonic crystal for THz frequencies requires a modulation

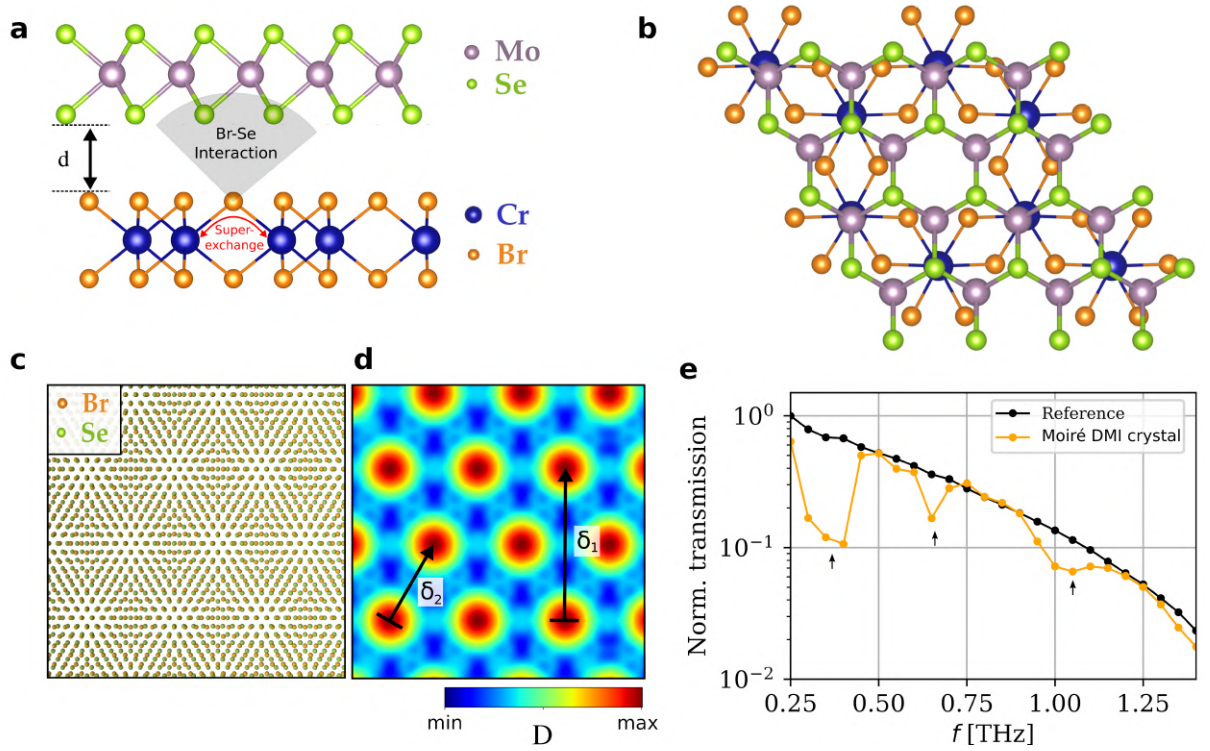

Figure 8.8 – Example of moiré-like magnonic crystal. (a-b) Illustration of $CrBr_3/MoSe_2$ heterostructure, from side (a) and top (b) views. (c) moiré pattern created between Br and Se layers. (d) Correspondent DMI profile calculated from the moiré pattern in (c) [see text]. Here, δ_1 and δ_2 are the two main periodicities of the system. (e) Simulated SW transmission spectra after crossing the moiré-like magnonic crystal, in comparison with the reference waveguide (pristine film), where we consider the incident SW propagating parallel to the δ_1 direction. Black arrows indicate the critical frequencies where the SW suffer destructive interference. Here we consider $D_0 = 3\exp(d/r_0)$ meV and $r_0 = 0.2$ Å, such that the maximum magnitude of DMI is 3 meV.

period of few nanometers [61] [see, e.g., SW dispersion relation in Fig. 8.2], which may be difficult to achieve with the methods mentioned above. Here we propose a moiré pattern as the source of periodic modulation in magnetic parameters for the design of magnonic crystals in the high-frequency regime. It is known that a moiré pattern can induce periodic variation in the magnetic parameters of the 2D material [294, 295]. Therefore, let us now consider the case where the CrX_3 monolayer is stacked with a non-magnetic material in order to produce a moiré pattern. For instance, consider the van der Waals heterostructure $CrBr_3/MoSe_2$ as illustrated in Fig. 8.8 (a-b). The superexchange interaction between Cr atoms, mediated by the Cr-Br-Cr bonds, will be affected by the Br-Se interaction, which in turn depends on the local stacking throughout the moiré pattern. The periodicity of the moiré structure is then reflected in a periodic modulation in magnetic parameters. Fig. 8.8 (c) shows the moiré pattern created between the Br layer (which form a hexagonal lattice, with lattice constant $a_{Br} = 3.698$ Å, different from the lattice constant of $CrBr_3$ suppercell) and the Se layer (which form a hexagonal

lattice, with lattice constant $a_{Se} = 3.289$ Å) [317]. The symmetry axes of both hexagonal lattices are considered to be aligned, which corresponds to an angle of 30° between $CrBr_3$ and $MoSe_2$ suppercells [318]. The mismatch in the lattice constants creates the moiré pattern.

The interaction between the layers can be modeled as a function of the distance between Br and Se atoms [295]. Since there is a lack of inversion symmetry in the heterostructure, and the transition metal dichalcogenide (TMD) monolayer $MoSe_2$ hold strong spin-orbit coupling [319, 320], one can expect a periodic modulation in the DMI parameter throughout the magnetic layer. As a first step in understanding the magnonics in such a complex system, and since the DMI strongly interact with SWs, here we consider a periodic modulation only in the DMI parameter, and assume the other magnetic parameters to be unchanged. Fig. 8.8 (d) shows the DMI profile extracted from the moiré pattern, according to the expression $D = D_0 \exp(-\sqrt{r^2 + d^2}/r_0)$, where r is the lateral distance between Br and Se atoms, $d = 3.5$ Å is the separation between the layers [318] [see Fig. 8.8 (a)] and D_0 and r_0 are constants that define the DMI magnitude. Here we consider $D_0 = 3\exp(d/r_0)$ meV and $r_0 = 0.2$ Å, such that the maximum magnitude of DMI is 3 meV. The small value of r_0 represents the short range interaction between neigbouring orbitals, such that the maximal interaction is given when Se atoms are on top of Br ones. Notice that, a SW propagating in such a system will experience different periodic modulations, depending on the propagation direction. The two main periodicities in the system are $\delta_1 \approx 5.13$ nm and $\delta_2 \approx 2.96$ nm, as indicated in Fig. 8.8 (d). Such short periodicities found in the moiré heterostructures are, therefore, capable of interacting with high frequency SWs and can be adjusted, for example, by changing the rotation angle between the layers or replacing the TMD layer with another material with a different lattice constant and/or different lattice structure.

Fig. 8.8 (e) shows the simulated SW transmission spectra after crossing the moiré-like magnonic crystal, in comparison with the reference waveguide (pristine film), where we consider the incident SW propagating parallel to the δ_1 direction. Notice that the transmission spectrum of the moiré system significantly differs from the pristine medium, and three valleys of prohibited frequencies are visible. Such spectrum is typical of magnonic crystals[63]. Fig. 8.9 (a-b) shows the snapshots of SW simulation for the 0.5 and 0.65 THz SWs propagating across the DMI pattern, where in the second case the SW suffer destructive interference and do not propagate.

Lastly, the hexagonal symmetry in the modulation of magnetic parameter results in anisotropic dispersion of the SW. Fig. 8.9 (c) shows the snapshots of SW simulation for the 0.4 THz SW propagating across the moiré pattern. The SW is created at the center of the sample and it propagates along the radial direction. Notice that the SW is filtered along the δ_1 directions, as expected from the transmission spectra in Fig. 8.8 (e), but it

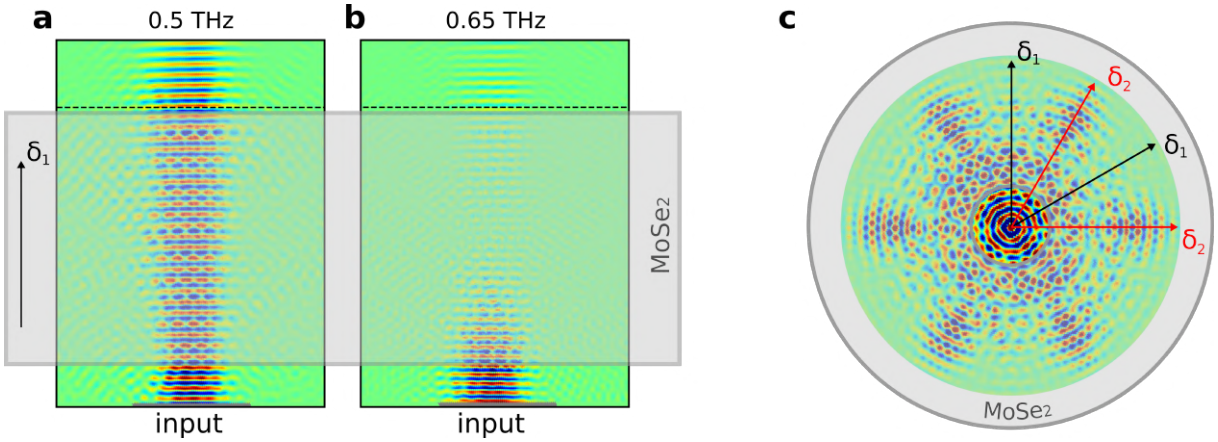

Figure 8.9 – (a-b) Snapshots of SW simulation for the 0.5 and 0.65 THz SWs propagating across the moiré pattern. The incident SW propagates parallel to the δ_1 direction. (c) Snapshots of SW simulation for the 0.4 THz SW propagating across the moiré pattern in the radial direction. The SW is filtered along the δ_1 directions, but can propagate along δ_2.

can propagate along δ_2 direction, thus demonstrating the anisotropic SW dispersion characteristic of such systems.

8.7 Conclusions of the chapter

In summary, we presented the SW properties in monolayer chromium trihalides $CrBr_3$ and CrI_3, under different possibilities for tuning magnonics in such 2D materials. We reveal that the SW dispersion relation can be tuned in a large range of frequencies by straining the 2D magnet, and that the SW dispersion has different response to strain in $CrBr_3$ when compared to CrI_3, which is directly related to their out-of-plane anisotropy. We reveal the possibility of controlling the SW propagation by strain-engineering the 2D material, paving the way towards flexo-magnonic applications. Next, we investigate the SW propagation in the presence of structural defects (halide vacancies) in the chromium trihalides. Our calculations show that the lattice defects induce large enough DMI to strongly affect the SW dynamics in the magnetic monolayers, with larger effects observed for the case of CrI_3. We show that a designed pattern of defects is able to confine SWs and may serve for SW-guides. Lastly, we show the spectra of SWs propagating across periodic modulation of the magnetic parameters, induced by moiré pattern in a van der Waals heterostructure, that indicate such structures hold the necessary nanometric modulation period to work as a magnonic crystal for the terahertz SWs. The wide range of possibilities for manipulating SWs in 2D materials therefore suggests these systems as a front-runner for terahertz magnonics.

9 Conclusions

The precise control of skyrmionics and magnonics in magnetic materials is key to the development of novel spin-based information technology applications. In this thesis, we revealed multiple alternatives for the manipulation of skyrmions and spin-waves in different materials, such as bulk chiral magnets, heterochiral structures, magnet-supperconductor hybrids and two-dimentional magnetic materials. We have made use of a multi-scale model, as described in **Chapter 3**, to numerically simulate the magnetic states at each considered material, from micromagnetic to atomistic control, together with minimum energy path analysis of magnetic transitions involving skyrmions. The spin dynamics simulations were performed with the help of the simulation packages *Mumax*^{3} [129] and *Spirit* [38], in some cases modified by us to accommodate the magnetic structures considered in our work.

The results of our work were presented in Chapters 4 to 8. First, in **Chapter 4** we have studied the dynamics of skyrmion nucleation from the conical phase in helical magnets and showed how the skyrmion lattice is formed progressively in small domains. The preferential nucleation mechanisms of magnetic skyrmions is reveled, under minimal energy path analysis, to follow a rod-like (one-dimensional) nucleation of chiral bobbers from the film surface, in agreement with experimental observations reported in literature, and with an activation barrier of several eV per skyrmion for the case of MnSi. Furthermore, we demonstrated the interesting blinking (creation-annihilation) behavior of skyrmions close to the phase boundary between the conical and SkL phases.

Next, in **Chapter 5** we demonstrated the manipulation of magnetic skyrmions in heterochiral magnets, for both the ferromagnetic (FM) and antiferromagnetic (AFM) cases. We demonstrated that a local canting of the magnetization, characteristic for the heterochiral interface, can strongly deflect the trajectory of FM skyrmions, which is very useful for the controlled manipulation of skyrmion chains in skyrmion-based devices, such as switches, logic gates and memory elements. In addition, we revealed that such deflection is completely absent in the AFM case, and that the AFM skyrmion achieves

much higher velocities and stronger confinement in nanoengineered heterochiral tracks when compared to its FM counterpart, thus reinforcing AFM skyrmions as a favorable choice for skyrmion-based devices.

In **Chapter 6**, we showed the coupling of magnetic skyrmions with supperconducting vortices in hybrid magnet-superconductor materials, which were revealed as promising platform for skyrmion manipulation. We demonstrated the nucleation of the skyrmion-vortex pairs (SVPs) in the hybrid sample, based on experimental observations, and studied in details the manipulation of a single SVP in case of current applied to either magnetic or superconducting parts, where we combined micromagnetic and molecular dynamics simulations to investigate the behavior of skyrmions and vortices simultaneously. The skyrmion Hall-angle with respect to current applied into the magnetic film is shown to be always greater than the one observed in the absence of vortices, and the possibility of compensating the skyrmion Hall effect in such systems is shown by applying combined currents into both constituents of the heterostructure. The precise control of the SVP in such topological hybrid materials, as demonstrated in Chapter 6, holds promise to reveal rich fundamental phenomena and applicable effects in skyrmionics.

In **Chapter 7** we discussed the effects of suppressing nearest-neighbour exchange in magnetic monolayers. Recalling the high tunability of magnetic parameters in two-dimentional magnets (by strain-engineering, gating, heterostructuring, etc.), we reported the rich phase diagram of exotic magnetic configurations obtained for both square and honeycomb lattice symmetries in the case of suppressed nearest-neighbour exchange interaction in the magnetic monolayers. We showed that several unique cycloidal, checkerboard, row-wise and spin-ice states are stabilized by the competition between the second-nearest-neighbor exchange, DMI, and dipolar interactions. In addition, the coexistence of FM and AFM skyrmions and cycloids are found (resulting from degenerate FM and AFM states promoted by the absence of the nearest-neighbor exchange), as well as novel types of skyrmions and chiral domain walls, such as the p-AFM ones. The magnetic monolayers are also shown to be good candidates to host the AFM skyrmions, experimentally evasive to date. The results presented in this chapter expanded the scope of magnetic phases achievable in such monolayer materials, crucial for both fundamental and technological advances.

Lastly, in **Chapter 8** we presented the spin-wave (SW) properties in two-dimensional (2D) chromium-trihalides CrI_3 and $CrBr_3$, which are established in the literature as a promising platform for high-frequency magnonics. We revealed that the SW dispersions in such 2D materials are highly sensitive to strain-engineering, and can be tuned in a broad range of frequencies, thus paving the way towards flexo-magnonic applications. We demonstrated the possibility of controlling the SW propagation by

both strain- and defect-engineering the 2D material, where structural defects (halide vacancies) induce large enough DMI to strongly affect the SW dynamics in the magnetic monolayers. Finally, we showed the spectra of SWs propagating across a moiré-periodic modulation of magnetic parameters in a van der Waals heterobilayer, where the nanometric periodicities found in such samples are ideal for the realization of a magnonic crystal in the terahertz frequency range. In this way, the results presented in this chapter reinforce these systems as front-runners for prospective terahertz magnonic applications.

Bibliography

[1] Rob Lavinsky and irocks.com. Picture of magnetite. https://www.mindat.org/photo-118736.html.

[2] Shutterstock. Ancient chinese compass. https://www.shutterstock.com/pt/image-photo/reproduction-ancient-chinese-compass-which-points-26572642.

[3] Wikimedia commons. Locator map of magnesia. https://commons.wikimedia.org/wiki/File:Locator_map_of_Magnesia_(constituency).svg#globalusage.

[4] Vecteezy. Earth's magnetic field. https://www.vecteezy.com/vector-art/1542586-earth-s-magnetic-field-or-geomagnetic-field-for-education.

[5] V. Sluka, T. Schneider, R. A Gallardo, A. Kákay, M. Weigand, T. Warnatz, R. Mattheis, A. Roldán-Molina, P. Landeros, V. Tiberkevich, et al. Emission and propagation of 1d and 2d spin waves with nanoscale wavelengths in anisotropic spin textures. *Nature Nanotechnology*, 14(4):328–333, 2019.

[6] A. V. Chumak, A. A. Serga, B. Hillebrands, and M. P. Kostylev. Scattering of backward spin waves in a one-dimensional magnonic crystal. *Applied Physics Letters*, 93(2):022508, 2008.

[7] S. Mühlbauer, B. Binz, F. Jonietz, C. Pfleiderer, A. Rosch, A. Neubauer, R. Georgii, and P. Böni. Skyrmion lattice in a chiral magnet. *Science*, 323(5916):915–919, 2009.

[8] P. Milde, D. Köhler, J. Seidel, L. M. Eng, A. Bauer, A. Chacon, J. Kindervater, S. Mühlbauer, C. Pfleiderer, S. Buhrandt, et al. Unwinding of a skyrmion lattice by magnetic monopoles. *Science*, 340(6136):1076–1080, 2013.

[9] N. Romming, C. Hanneken, M. Menzel, J. E. Bickel, B. Wolter, K. von Bergmann, A. Kubetzka, and R. Wiesendanger. Writing and deleting single magnetic skyrmions. *Science*, 341(6146):636–639, 2013.

[10] X. Z. Yu, Y. Onose, N. Kanazawa, J. H. Park, J. H. Han, Y. Matsui, N. Nagaosa, and Y. Tokura. Real-space observation of a two-dimensional skyrmion crystal. *Nature*, 465(7300):901–904, 2010.

[11] A. P. Petrović, M. Raju, X. Y. Tee, A. Louat, I. Maggio-Aprile, R. M. Menezes, M. J. Wyszyński, N. K. Duong, M. Reznikov, Ch. Renner, et al. Skyrmion-(anti) vortex coupling in a chiral magnet-superconductor heterostructure. *Physical Review Letters*, 126(11):117205, 2021.

[12] A. Fert, N. Reyren, and V. Cros. Magnetic skyrmions: advances in physics and potential applications. *Nature Reviews Materials*, 2(7):1–15, 2017.

[13] S. Luo, M. Song, X. Li, Y. Zhang, J. Hong, X. Yang, X. Zou, N. Xu, and L. You. Reconfigurable skyrmion logic gates. *Nano letters*, 18(2):1180–1184, 2018.

[14] W. Kang, B. Wu, X. Chen, D. Zhu, Z. Wang, X. Zhang, Y. Zhou, Y. Zhang, and W. Zhao. A comparative cross-layer study on racetrack memories: Domain wall vs skyrmion. *ACM Journal on Emerging Technologies in Computing Systems (JETC)*, 16(1):1–17, 2019.

[15] C. Psaroudaki and C. Panagopoulos. Skyrmion qubits: A new class of quantum logic elements based on nanoscale magnetization. *Physical Review Letters*, 127(6):067201, 2021.

[16] John MD Coey. *Magnetism and magnetic materials*. Cambridge university press, 2010.

[17] Claas Willem Abert. *Discrete Mathematical Concepts in Micromagnetic Computations*. PhD thesis, Staats-und Universitätsbibliothek Hamburg Carl von Ossietzky, 2013.

[18] V. V. Kulish and W. Huang. Single-layer metal halides MX 2 (X= Cl, Br, I): stability and tunable magnetism from first principles and monte carlo simulations. *Journal of Materials Chemistry C*, 5(34):8734–8741, 2017.

[19] A. Fert, V. Cros, and J. Sampaio. Skyrmions on the track. *Nature Nanotechnology*, 8(3):152–156, 2013.

[20] Tu Le M., José A. P. B., J. H. E. Hernández, and J. M. H. López. Correlation between barkhausen noise and magnetocrystalline anisotropy energy. In *Barkhausen Noise for Non-Destructive Testing and Materials Characterization in Low Carbon Steels*, pages 147–182. Elsevier, 2020.

[21] S. Blundell. *Magnetism in condensed matter*. OUP Oxford, 2001.

[22] T. Y. Ou-Yang, G. J. Shu, J.-Y.n Lin, C. D. Hu, and F. C. Chou. Mn vacancy defects, grain boundaries, and a-phase stability of helimagnet mnsi. *Journal of Physics: Condensed Matter*, 28(2):026004, 2015.

[23] S. Wang, J. Tang, W. Wang, L. Kong, M. Tian, and H. Du. Electrical detection of magnetic skyrmions. *Journal of Low Temperature Physics*, 197(3):321–336, 2019.

[24] Illustration of skyrmion. https://fr.wikipedia.org/wiki/Skyrmion.

[25] N. Nagaosa and Y. Tokura. Topological properties and dynamics of magnetic skyrmions. *Nature Nanotechnology*, 8(12):899–911, 2013.

[26] P. Barla, V. K. Joshi, and S. Bhat. Spintronic devices: a promising alternative to cmos devices. *Journal of Computational Electronics*, 20(2):805–837, 2021.

[27] W. Jiang, G. Chen, K. Liu, J. Zang, S. G. E. Te-Velthuis, and A. Hoffmann. Skyrmions in magnetic multilayers. *Physics Reports*, 704:1–49, 2017.

[28] G. Chen. Skyrmion hall effect. *Nature Physics*, 13(2):112–113, 2017.

[29] W. Jiang, X. Zhang, G. Yu, W. Zhang, X. Wang, M. B. Jungfleisch, J. E. Pearson, X. Cheng, O. Heinonen, K. L. Wang, et al. Direct observation of the skyrmion hall effect. *Nature Physics*, 13(2):162–169, 2017.

[30] J. Barker and O. A. Tretiakov. Static and dynamical properties of antiferromagnetic skyrmions in the presence of applied current and temperature. *Physical Review Letters*, 116(14):147203, 2016.

[31] P. Gruszecki, C. Banerjee, M. Mruczkiewicz, O. Hellwig, A. Barman, and M. Krawczyk. The influence of the internal domain wall structure on spin wave band structure in periodic magnetic stripe domain patterns. *Solid State Physics*, 70:79–132, 2019.

[32] S. M. Rezende. *Fundamentals of Magnonics*, volume 969. Springer, 2020.

[33] C. Etz, L. Bergqvist, A. Bergman, A. Taroni, and O. Eriksson. Atomistic spin dynamics and surface magnons. *Journal of Physics: Condensed Matter*, 27(24):243202, 2015.

[34] C. Bacaksiz, D. Šabani, R. M. Menezes, and M. V. Milošević. Distinctive magnetic properties of cr i 3 and cr br 3 monolayers caused by spin-orbit coupling. *Physical Review B*, 103(12):125418, 2021.

[35] M.-A. Bisotti, D. Cortés-Ortuño, R. A. Pepper, Weiwei Wang, Marijan Beg, Thomas Kluyver, and Hans Fangohr. Fidimag–a finite difference atomistic and micromagnetic simulation package. *arXiv preprint arXiv:2002.04318*, 2020.

[36] RHEOMAN: Nudged elastic band. http://umet.univ-lille1.fr/Projets/RheoMan/en/to-learn-more-about/nudged-elastic-band.php.

[37] I. A. Nosikov, M. V. Klimenko, P. F. Bessarab, and G. A. Zhbankov. Application of the optimization method to the point-to-point radio wave ray-tracing problem. *URSI Radio Science Bulletin*, 2017(361):14–19, 2017.

[38] G. P. Müller, M. Hoffmann, C. Dißelkamp, D. Schürhoff, S. Mavros, M. Sallermann, N. S. Kiselev, H. Jónsson, and S. Blügel. Spirit: Multifunctional framework for atomistic spin simulations. *Physical Review B*, 99(22):224414, 2019.

[39] A. W. D. Leishman, R. M. Menezes, G. Longbons, E. D. Bauer, M. Janoschek, D. Honecker, L. DeBeer-Schmitt, J. S. White, A. Sokolova, M. V. Milošević, et al. Topological energy barrier for skyrmion lattice formation in mnsi. *Physical Review B*, 102(10):104416, 2020.

[40] R. M. Menezes. Nonuniform vortex distributions in superconductors: from critical state to conformal crystals. Master's thesis, Universidade Federal de Pernambuco, 2017.

[41] D. Sabani, C. Bacaksiz, and M. V. Milosevic. Releasing latent chirality in magnetic two-dimensional materials. *arXiv preprint arXiv:2009.03421*, 2020.

[42] P. F. O'grady. *Thales of Miletus: the beginnings of western science and philosophy*. Routledge, 2017.

[43] R. T. Merrill and M. W. McElhinny. *The Earth's magnetic field: Its history, origin and planetary perspective*, volume 401. Academic Press London, 1983.

[44] W. Gilbert. *On the Loadstone and Magnetic Bodies, and on the Great Magnet the Earth: A New Physiology, Demonstrated with Many Arguments and Experiments*. Wiley, 1893.

[45] J. Bostock and H. T. Riley. Pliny the elder: The natural history. *Perseus at Tufts*, 1855.

[46] P. Peregrinus. *The Letter of Petrus Peregrinus on the Magnet, AD 1269*, volume 1. Library of Alexandria, 2020.

[47] R. M. Brain, R. S. Cohen, and O. Knudsen. *Hans Christian Ørsted and the romantic legacy in science: Ideas, disciplines, practices*, volume 241. Springer Science & Business Media, 2007.

[48] D. C. Mattis. History of magnetism. In *The Theory of Magnetism I*, pages 1–38. Springer, 1981.

[49] J.-B. Biot and F. Savart. Note sur le magnetisme de la pile de volta. *Ann. Chem. Phys*, 15:222, 1820.

[50] S. Chatterjee. Michael faraday: Discovery of electromagnetic induction. *Resonance*, 7(3):35–45, 2002.

[51] J. Clerk Maxwell. On faraday's lines of force. *Transactions of the Cambridge Philosophical Society*, 10:27, 1864.

[52] F. Bloch. Zur theorie des ferromagnetismus. *Zeitschrift für Physik*, 61(3-4):206–219, 1930.

[53] N. W. Ashcroft, N. D. Mermin, et al. *Solid state physics*. holt, rinehart and winston, new york London, 1976.

[54] T. Holstein and H. Primakoff. Field dependence of the intrinsic domain magnetization of a ferromagnet. *Physical Review*, 58(12):1098, 1940.

[55] F. J. Dyson. General theory of spin-wave interactions. *Physical Review*, 102(5):1217, 1956.

[56] K. Zakeri. Elementary spin excitations in ultrathin itinerant magnets. *Physics Reports*, 545(2):47–93, 2014.

[57] L. Chen, J.-H. Chung, B. Gao, T. Chen, M. B. Stone, A. I. Kolesnikov, Q. Huang, and P. Dai. Topological spin excitations in honeycomb ferromagnet cri 3. *Physical Review X*, 8(4):041028, 2018.

[58] P. Grünberg, M. G. Cottam, W. Vach, C. Mayr, and R. E. Camley. Brillouin scattering of light by spin waves in thin ferromagnetic films. *Journal of Applied Physics*, 53(3):2078–2083, 1982.

[59] J. Cenker, B. Huang, N. Suri, P. Thijssen, A. Miller, T. Song, T. Taniguchi, K. Watanabe, M. A McGuire, D. Xiao, et al. Direct observation of two-dimensional magnons in atomically thin cri 3. *Nature Physics*, 17(1):20–25, 2021.

[60] C. Kittel. Excitation of spin waves in a ferromagnet by a uniform rf field. *Physical Review*, 110(6):1295, 1958.

[61] H. J. Qin, S. Tsurkan, A. Ernst, and Kh. Zakeri. Experimental realization of atomic-scale magnonic crystals. *Physical Review Letters*, 123(25):257202, 2019.

[62] A. Barman, G. Gubbiotti, S. Ladak, A. O. Adeyeye, M. Krawczyk, J. Gräfe, C. Adelmann, S. Cotofana, A. Naeemi, V. I. Vasyuchka, et al. The 2021 magnonics roadmap. *Journal of Physics: Condensed Matter*, 2021.

[63] A. V. Chumak, A. A. Serga, and B. Hillebrands. Magnonic crystals for data processing. *Journal of Physics D: Applied Physics*, 50(24):244001, 2017.

[64] H. Qin, R. B. Holländer, L. Flajšman, F. Hermann, R. Dreyer, G. Woltersdorf, and S. van Dijken. Nanoscale magnonic fabry-pérot resonator for low-loss spin-wave manipulation. *Nature Communications*, 12(1):1–10, 2021.

[65] G. Csaba, A. Papp, and W. Porod. Perspectives of using spin waves for computing and signal processing. *Physics Letters A*, 381(17):1471–1476, 2017.

[66] B. Rana and Y. Otani. Voltage-controlled reconfigurable spin-wave nanochannels and logic devices. *Physical Review Applied*, 9(1):014033, 2018.

[67] P. Pirro, V. I Vasyuchka, A. A. Serga, and B. Hillebrands. Advances in coherent magnonics. *Nature Reviews Materials*, pages 1–22, 2021.

[68] B. Rana and Y. Otani. Towards magnonic devices based on voltage-controlled magnetic anisotropy. *Communications Physics*, 2(1):1–12, 2019.

[69] T. H. R. Skyrme. A unified field theory of mesons and baryons. *Nuclear Physics*, 31:556–569, 1962.

[70] A. O. Leonov, I. E. Dragunov, U. K. Rößler, and A. N. Bogdanov. Theory of skyrmion states in liquid crystals. *Physical Review E*, 90(4):042502, 2014.

[71] S. L. Sondhi, A. Karlhede, S. A. Kivelson, and E. H. Rezayi. Skyrmions and the crossover from the integer to fractional quantum hall effect at small zeeman energies. *Physical Review B*, 47(24):16419, 1993.

[72] U. Al-Khawaja and H. Stoof. Skyrmions in a ferromagnetic bose–einstein condensate. *Nature*, 411(6840):918–920, 2001.

[73] T. Moriya. Anisotropic superexchange interaction and weak ferromagnetism. *Physical Review*, 120(1):91, 1960.

[74] W. Münzer, A. Neubauer, T. Adams, S. Mühlbauer, C. Franz, F. Jonietz, R. Georgii, P. Böni, B. Pedersen, M. Schmidt, et al. Skyrmion lattice in the doped semiconductor fe 1- x co x si. *Physical Review B*, 81(4):041203, 2010.

[75] W. Jiang, P. Upadhyaya, W. Zhang, G. Yu, M. B. Jungfleisch, F. Y. Fradin, J. E. Pearson, Y. Tserkovnyak, K. L. Wang, O. Heinonen, et al. Blowing magnetic skyrmion bubbles. *Science*, 349(6245):283–286, 2015.

[76] K. Hamamoto, M. Ezawa, and N. Nagaosa. Purely electrical detection of a skyrmion in constricted geometry. *Applied Physics Letters*, 108(11):112401, 2016.

[77] O. Boulle, J. Vogel, H. Yang, S. Pizzini, D. de Souza C., A. Locatelli, T. O. Menteş, A. Sala, L. D. Buda-Prejbeanu, O. Klein, et al. Room-temperature chiral magnetic skyrmions in ultrathin magnetic nanostructures. *Nature Nanotechnology*, 11(5):449, 2016.

[78] F. Ma, Y. Zhou, H. B. Braun, and W. S. Lew. Skyrmion-based dynamic magnonic crystal. *Nano Letters*, 15(6):4029–4036, 2015.

[79] X. Zhang, M. Ezawa, and Y. Zhou. Magnetic skyrmion logic gates: conversion, duplication and merging of skyrmions. *Scientific reports*, 5(1):1–8, 2015.

[80] M. Carpentieri, R. Tomasello, R. Zivieri, and G. Finocchio. Topological, non-topological and instanton droplets driven by spin-transfer torque in materials with perpendicular magnetic anisotropy and dzyaloshinskii–moriya interaction. *Scientific Reports*, 5(1):1–8, 2015.

[81] R. M. Menezes, J. Mulkers, C. C. de Souza Silva, and M. V. Milošević. Deflection of ferromagnetic and antiferromagnetic skyrmions at heterochiral interfaces. *Physical Review B*, 99(10):104409, 2019.

[82] R. M. Menezes, J. F. S. Neto, C. C. de Souza Silva, and M. V. Milošević. Manipulation of magnetic skyrmions by superconducting vortices in ferromagnet-superconductor heterostructures. *Physical Review B*, 100(1):014431, 2019.

[83] R. M. Menezes, C. C. de Souza Silva, and M. V. Milošević. Spin textures in chiral magnetic monolayers with suppressed nearest-neighbor exchange. *Physical Review B*, 101(21):214429, 2020.

[84] D. J. Griffiths. *Introduction to electrodynamics*. American Association of Physics Teachers, 2005.

[85] K. Huang. *Introduction to statistical physics*. Chapman and Hall/CRC, 2009.

[86] J. J. Sakurai. *Advanced quantum mechanics*. Pearson Education India, 2006.

[87] T. L. Gilbert. A lagrangian formulation of the gyromagnetic equation of the magnetization field. *Phys. Rev.*, 100:1243, 1955.

[88] I. Dzyaloshinsky. A thermodynamic theory of "weak" ferromagnetism of antiferromagnetics. *Journal of Physics and Chemistry of Solids*, 4(4):241–255, 1958.

[89] I. Dzyaloshinskii. Theory of helicoidal structures in antiferromagnets. i. nonmetals. *Sov. Phys. JETP*, 19(4):960–971, 1964.

[90] A. Thiaville, S. Rohart, E. Jué, V. Cros, and A. Fert. Dynamics of dzyaloshinskii domain walls in ultrathin magnetic films. *EPL (Europhysics Letters)*, 100(5):57002, 2012.

[91] O. Nakanishi, A. Yanase, A. Hasegawa, and M. Kataoka. The origin of the helical spin density wave in mnsi. *Solid State Communications*, 35(12):995–998, 1980.

[92] A. A. Abrikosov. The magnetic properties of superconducting alloys. *Journal of Physics and Chemistry of Solids*, 2(3):199–208, 1957.

[93] R. Tomasello, E. Martinez, R. Zivieri, L. Torres, M. Carpentieri, and G. Finocchio. A strategy for the design of skyrmion racetrack memories. *Scientific Reports*, 4:6784, 2014.

[94] C. Jin, C. Song, J. Wang, and Q. Liu. Dynamics of antiferromagnetic skyrmion driven by the spin Hall effect. *Applied Physics Letters*, 109(18):182404, 2016.

[95] X. Zhang, Y. Zhou, and M. Ezawa. Magnetic bilayer-skyrmions without skyrmion Hall effect. *Nature Communications*, 7:10293, 2016.

[96] W. Jiang, X. Zhang, G. Yu, W. Zhang, X. Wang, M. B. Jungfleisch, J. E. Pearson, X. Cheng, O. Heinonen, K. L. Wang, et al. Direct observation of the skyrmion hall effect. *Nature Physics*, 13(2):162, 2017.

[97] S. Zhang and Z. Li. Roles of nonequilibrium conduction electrons on the magnetization dynamics of ferromagnets. *Physical Review Letters*, 93(12):127204, 2004.

[98] L. Liu, O. J. Lee, T. J. Gudmundsen, D. C. Ralph, and R. A. Buhrman. Current-induced switching of perpendicularly magnetized magnetic layers using spin torque from the spin Hall effect. *Physical Review Letters*, 109(9):096602, 2012.

[99] N. Perez, L. Torres, and E. Martinez-Vecino. Micromagnetic modeling of Dzyaloshinskii–Moriya interaction in spin Hall effect switching. *IEEE Transactions on Magnetics*, 50(11):1–4, 2014.

[100] J. C. Slonczewski. Current-driven excitation of magnetic multilayers. *Journal of Magnetism and Magnetic Materials*, 159(1-2):L1–L7, 1996.

[101] J. Xiao, A. Zangwill, and M. D. Stiles. Boltzmann test of Slonczewski's theory of spin-transfer torque. *Physical Review B*, 70(17):172405, 2004.

[102] E. H. Hall et al. On a new action of the magnet on electric currents. *American Journal of Mathematics*, 2(3):287–292, 1879.

[103] K. Litzius, I. Lemesh, B. Krüger, P. Bassirian, L. Caretta, K. Richter, F. Büttner, K. Sato, O. A Tretiakov, J. Förster, et al. Skyrmion hall effect revealed by direct time-resolved x-ray microscopy. *Nature Physics*, 13(2):170–175, 2017.

[104] A. A. Thiele. Steady-state motion of magnetic domains. *Physical Review Letters*, 30(6):230, 1973.

[105] J. Iwasaki, W. Koshibae, and N. Nagaosa. Colossal spin transfer torque effect on skyrmion along the edge. *Nano Letters*, 14(8):4432–4437, 2014.

[106] X. Zhang, Y. Zhou, and M. Ezawa. Antiferromagnetic skyrmion: stability, creation and manipulation. *Scientific Reports*, 6:24795, 2016.

[107] H. Xia, C. Jin, C. Song, J. Wang, J. Wang, and Q. Liu. Control and manipulation of antiferromagnetic skyrmions in racetrack. *Journal of Physics D: Applied Physics*, 50(50):505005, 2017.

[108] L. Shen, J. Xia, G. Zhao, X. Zhang, M. Ezawa, O. A. Tretiakov, X. Liu, and Y. Zhou. Dynamics of the antiferromagnetic skyrmion induced by a magnetic anisotropy gradient. *Physical Review B*, 98(13):134448, 2018.

[109] C. Kittel. Interpretation of anomalous larmor frequencies in ferromagnetic resonance experiment. *Physical Review*, 71(4):270, 1947.

[110] P. Hohenberg and W. Kohn. Inhomogeneous electron gas. *Physical Review*, 136(3B):B864, 1964.

[111] R. G. Parr. Density functional theory of atoms and molecules. In *Horizons of quantum chemistry*, pages 5–15. Springer, 1980.

[112] H. Xiang, C. Lee, H.-J. Koo, X. Gong, and M.-H. Whangbo. Magnetic properties and energy-mapping analysis. *Dalton Transactions*, 42(4):823–853, 2013.

[113] K. Terakura, A. R. Williams, T. Oguchi, and J. Kübler. Transition-metal monoxides: band or mott insulators. *Physical Review Letters*, 52(20):1830, 1984.

[114] K. Terakura, T. Oguchi, A. R. Williams, and J. Kübler. Band theory of insulating transition-metal monoxides: Band-structure calculations. *Physical Review B*, 30(8):4734, 1984.

[115] S. L. Dudarev, G. A. Botton, S. Y. Savrasov, C. J. Humphreys, and A. P. Sutton. Electron-energy-loss spectra and the structural stability of nickel oxide: An lsda+ u study. *Physical Review B*, 57(3):1505, 1998.

[116] G. Kresse and J. Furthmüller. Efficient iterative schemes for ab initio total-energy calculations using a plane-wave basis set. *Physical Review B*, 54(16):11169, 1996.

[117] FLEUR: The jülich FLAPW code family. http://www.flapw.de/pm/index.php.

[118] X. Gonze, B. Amadon, P.-M. Anglade, J.-M. Beuken, F. Bottin, P. Boulanger, F. Bruneval, D. Caliste, R. Caracas, M. Côté, et al. Abinit: First-principles approach to material and nanosystem properties. *Computer Physics Communications*, 180(12):2582–2615, 2009.

[119] P. Giannozzi, S. Baroni, N. Bonini, M. Calandra, R. Car, C. Cavazzoni, D. Ceresoli, G. L Chiarotti, M. Cococcioni, I. Dabo, et al. Quantum espresso: a modular and open-source software project for quantum simulations of materials. *Journal of physics: Condensed matter*, 21(39):395502, 2009.

[120] J. M. Soler, E. Artacho, J. D. Gale, A. García, J. Junquera, P. Ordejón, and D. Sánchez-Portal. The siesta method for ab initio order-n materials simulation. *Journal of Physics: Condensed Matter*, 14(11):2745, 2002.

[121] P. Blaha, K. Schwarz, G. K. H. Madsen, D. Kvasnicka, J. Luitz, et al. An augmented plane wave+ local orbitals program for calculating crystal properties. 2001.

[122] X. He, N. Helbig, M. J. Verstraete, and E. Bousquet. Tb2j: a python package for computing magnetic interaction parameters. *Computer Physics Communications*, 264:107938, 2021.

[123] K. E. Atkinson. *An introduction to numerical analysis*. John wiley & sons, 2008.

[124] J. C. Butcher. *The numerical analysis of ordinary differential equations: Runge-Kutta and general linear methods*. Wiley-Interscience, 1987.

[125] U. Nowak. Thermally activated reversal in magnetic nanostructures. *Annual Reviews Of Computational PhysicsIX*, pages 105–151, 2001.

[126] J. H. Mentink, M. V. Tretyakov, A. Fasolino, M. I. Katsnelson, and Th. Rasing. Stable and fast semi-implicit integration of the stochastic landau–lifshitz equation. *Journal of Physics: Condensed Matter*, 22(17):176001, 2010.

[127] R. F. L. Evans, W. J. Fan, P. Chureemart, T. A. Ostler, M. O. A. Ellis, and R. W. Chantrell. Atomistic spin model simulations of magnetic nanomaterials. *Journal of Physics: Condensed Matter*, 26(10):103202, 2014.

[128] B. Skubic, J. Hellsvik, L. Nordström, and O. Eriksson. A method for atomistic spin dynamics simulations: implementation and examples. *Journal of Physics: Condensed Matter*, 20(31):315203, 2008.

[129] A. Vansteenkiste, J. Leliaert, M. Dvornik, M. Helsen, F. Garcia-Sanchez, and B. Van Waeyenberge. The design and verification of mumax3. *AIP Advances*, 4(10):107133, 2014.

[130] M. J. Donahue and M. J. Donahue. *OOMMF user's guide, version 1.0*. US Department of Commerce, National Institute of Standards and Technology, 1999.

[131] T. Jourdan, A.n Marty, and F. Lancon. Multiscale method for heisenberg spin simulations. *Physical Review B*, 77(22):224428, 2008.

[132] P. F. Bessarab, V. M. Uzdin, and H. Jónsson. Method for finding mechanism and activation energy of magnetic transitions, applied to skyrmion and antivortex annihilation. *Computer Physics Communications*, 196:335–347, 2015.

[133] G. A. Korn and T. M. Korn. *Mathematical handbook for scientists and engineers: definitions, theorems, and formulas for reference and review*. Courier Corporation, 2000.

[134] G. Henkelman and H. Jónsson. Improved tangent estimate in the nudged elastic band method for finding minimum energy paths and saddle points. *The Journal of chemical physics*, 113(22):9978–9985, 2000.

[135] G. Henkelman, B. P. Uberuaga, and H. Jónsson. A climbing image nudged elastic band method for finding saddle points and minimum energy paths. *The Journal of chemical physics*, 113(22):9901–9904, 2000.

[136] A Fert, N Reyren, and V Cros. Magnetic skyrmions: advances in physics and potential applications. *Nat. Rev. Mater.*, 2:17031, 2017.

[137] S Mühlbauer, B Binz, F Jonietz, C Pfleiderer, A Rosch, A Neubauer, R Georgii, and P Boni. Skyrmion Lattice in a Chiral Magnet. *Science*, 323:915–919, 2009.

[138] A Bauer and C Pfleiderer. Magnetic phase diagram of MnSi inferred from magnetization and ac susceptibility. *Phys. Rev. B*, 85:214418, 2012.

[139] E Moskvin, S Grigoriev, V Dyadkin, H Eckerlebe, M Baenitz, M Schmidt, and H Wilhelm. Complex Chiral Modulations in FeGe Close to Magnetic Ordering. *Phys. Rev. Lett.*, 110:077207, 2013.

[140] K Karube, J S White, N Reynolds, J L Gavilano, H Oike, A Kikkawa, F Kagawa, Y Tokunaga, H M Rønnow, Y Tokura, and Y Taguchi. Robust metastable skyrmions and their triangular-square lattice structural transition in a high-temperature chiral magnet. *Nat. Mater.*, 15:1237–1242, 2016.

[141] K Makino, J D Reim, D Higashi, D Okuyama, T J Sato, Y Nambu, E P Gilbert, N Booth, S Seki, and Y Tokura. Thermal stability and irreversibility of skyrmion-lattice phases in Cu_2OSeO_3. *Phys. Rev. B*, 95:134412, 2017.

[142] L J Bannenberg, F Qian, R M Dalgliesh, N Martin, G Chaboussant, M Schmidt, D L Schlagel, T A Lograsso, H Wilhelm, and C Pappas. Reorientations, relaxations, metastabilities and domains of skyrmion lattices. *Phys. Rev. B*, 96:184416, 2017.

[143] H Oike, A Kikkawa, N Kanazawa, Y Taguchi, M Kawasaki, Y Tokura, and F Kagawa. Interplay between topological and thermodynamic stability in a metastable magnetic skyrmion lattice. *Nat. Phys.*, 12:62–66, 2016.

[144] T Nakajima, H Oike, A Kikkawa, E P Gilbert, N Booth, K Kakurai, Y Taguchi, Y Tokura, F Kagawa, and T Arima. Skyrmion lattice structural transition in MnSi. *Sci. Adv.*, 3:e1602562, 2017.

[145] K Karube, Jonathan S White, D Morikawa, Marek Bartkowiak, A Kikkawa, Y Tokunaga, T Arima, Henrik M Rønnow, Y Tokura, and Y Taguchi. Skyrmion formation in a bulk chiral magnet at zero magnetic field and above room temperature. *Phys. Rev. Mater.*, 1:074405, 2017.

[146] J Wild, T N G Meier, S Pöllath, M Kronseder, A Bauer, A Chacon, M Halder, M Schowalter, A Rosenauer, J Zweck, J Müller, A Rosch, C Pfleiderer, and C H Back. Entropy-limited topological protection of skyrmions. *Sci. Adv.*, 3:e1701704, 2017.

[147] M T Birch, R Takagi, S Seki, M N Wilson, F Kagawa, A Štefančič, G Balakrishnan, R Fan, P Steadman, C J Ottley, M Crisanti, R Cubitt, T Lancaster, Y Tokura, and P D Hatton. Increased lifetime of metastable skyrmions by doping. *Phys. Rev. B*, 100:014425, 2019.

[148] M N Wilson, M Crisanti, C Barker, A Štefančič, J S White, M T Birch, G Balakrishnan, R Cubitt, and P D Hatton. Measuring the formation energy barrier of skyrmions in zinc-substituted Cu_2OSeO_3. *Phys. Rev. B*, 99:174421, 2019.

[149] S Rohart, J Miltat, and A Thiaville. Path to collapse for an isolated Néel skyrmion. *Phys. Rev. B*, 93:214412, 2016.

[150] I S Lobanov, H Jónsson, and V M Uzdin. Mechanism and activation energy of magnetic skyrmion annihilation obtained from minimum energy path calculations. *Phys. Rev. B*, 94:174418, 2016.

[151] D Stosic, J Mulkers, B Van Waeyenberge, T B Ludermir, and M V Milošević. Paths to collapse for isolated skyrmions in few-monolayer ferromagnetic films. *Phys. Rev. B*, 95:214418, 2017.

[152] B Heil, A Rosch, and J Masell. Universality of annihilation barriers of large magnetic skyrmions in chiral and frustrated magnets. *Phys. Rev. B*, 100:134424, 2019.

[153] T.-H. Kim, H. Zhao, B. Xu, B. A. Jensen, A. H. King, M. J. Kramer, C. Nan, L. Ke, and L. Zhou. Mechanisms of skyrmion and skyrmion crystal formation from the conical phase. *Nano Letters*, 20(7):4731–4738, 2020.

[154] T.-H. Kim, H. Zhao, P.-V. Ong, B. A Jensen, B. Cui, A. H. King, L. Ke, and L. Zhou. Kinetics of magnetic skyrmion crystal formation from the conical phase. *Nano Letters*, 21(13):5547–5554, 2021.

[155] S Mühlbauer, D Honecker, È A Pèrigo, F Bergner, S Disch, A Heinemann, S Erokhin, D Berkov, C Leighton, M R Eskildsen, and A Michels. Magnetic small-angle neutron scattering. *Rev. Mod. Phys.*, 91:015004, 2019.

[156] G Bertotti. *Hysteresis in Magnetism: for Physicists, Materials Scientists, and Engineers*. Academic Press, 1998.

[157] J Iwasaki, M Mochizuki, and N Nagaosa. Universal current-velocity relation of skyrmion motion in chiral magnets. *Nat. Commun.*, 4:1463, 2013.

[158] J. Iwasaki, M. Mochizuki, and N. Nagaosa. Current-induced skyrmion dynamics in constricted geometries. *Nature Nanotechnology*, 8(10):742, 2013.

[159] P Bak and M H Jensen. Theory of helical magnetic structures and phase transitions in MnSi and FeGe. *J. Phys. C*, 13(31):L881–L885, 1980.

[160] S. V. Maleyev. Cubic magnets with Dzyaloshinskii-Moriya interaction at low temperature. *Phys. Rev. B*, 73:174402, 2006.

[161] S. V. Grigoriev, S. V. Maleyev, A. I. Okorokov, Yu. O. Chetverikov, P. Böni, R. Georgii, D. Lamago, H. Eckerlebe, and K. Pranzas. Magnetic structure of MnSi under an applied field probed by polarized small-angle neutron scattering. *Phys. Rev. B*, 74:214414, 2006.

[162] T Jeong and W E Pickett. Implications of the B20 crystal structure for the magnetoelectronic structure of MnSi. *Phys. Rev. B*, 70:075114, 2004.

[163] P Milde, D Köhler, J Seidel, L M Eng, A Bauer, A Chacon, J Kindervater, S Mühlbauer, C Pfleiderer, S Buhrandt, C Schütte, and A Rosch. Topological unwinding of a Skyrmion lattice by magnetic monopoles. *Science*, 340:1076–1080, 2013.

[164] Ch Schütte and A Rosch. Dynamics and energetics of emergent magnetic monopoles in chiral magnets. *Phys. Rev. B*, 90:174432, 2014.

[165] F N Rybakov, A B Borisov, S Blügel, and N S Kiselev. New Type of Stable Particlelike States in Chiral Magnets. *Phys. Rev. Lett.*, 115:117201, 2015.

[166] G G Lonzarich and L Taillefer. Effect of spin fluctuations on the magnetic equation of state of ferromagnetic or nearly ferromagnetic metals. *J. Phys. C*, 18:4339–4371, 1985.

[167] L. Landau and E. Lifshitz. On the theory of the dispersion of magnetic permeability in ferromagnetic bodies. In *Perspectives in Theoretical Physics*, pages 51–65. Elsevier, 1992.

[168] T. L. Gilbert. A phenomenological theory of damping in ferromagnetic materials. *IEEE Transactions on Magnetics*, 40(6):3443–3449, 2004.

[169] A. O. Leonov and K. Inoue. Homogeneous and heterogeneous nucleation of skyrmions in thin layers of cubic helimagnets. *Physical Review B*, 98(5):054404, 2018.

[170] F. Zheng, F. N. Rybakov, A. B. Borisov, D. Song, S. Wang, Z.-A. Li, H. Du, N. S. Kiselev, J. Caron, A. Kovács, et al. Experimental observation of chiral magnetic bobbers in b20-type fege. *Nature nanotechnology*, 13(6):451–455, 2018.

[171] A. N. Kolmogorov. Statistical theory of phase transformation. *Bull. Acad. Sci. USSR, Ser. Math*, 3:355–359, 1937.

[172] M. Avrami. Kinetics of phase change. ii transformation-time relations for random distribution of nuclei. *The Journal of Chemical Physics*, 8(2):212–224, 1940.

[173] J. Hagemeister, N. Romming, K. Von Bergmann, E. Y. Vedmedenko, and R. Wiesendanger. Stability of single skyrmionic bits. *Nature Communications*, 6(1):1–7, 2015.

[174] I. Dzyaloshinsky. A thermodynamic theory of "weak" ferromagnetism of antiferromagnetics. *Journal of Physics and Chemistry of Solids*, 4(4):241–255, 1958.

[175] T. Moriya. Anisotropic superexchange interaction and weak ferromagnetism. *Physical Review*, 120(1):91, 1960.

[176] A. Crépieux and C. Lacroix. Dzyaloshinsky–Moriya interactions induced by symmetry breaking at a surface. *Journal of Magnetism and Magnetic Materials*, 182(3):341–349, 1998.

[177] A. Bogdanov and A. Hubert. Thermodynamically stable magnetic vortex states in magnetic crystals. *Journal of Magnetism and Magnetic Materials*, 138(3):255–269, 1994.

[178] A. N. Bogdanov and U. K. Rößler. Chiral symmetry breaking in magnetic thin films and multilayers. *Physical Review Letters*, 87(3):037203, 2001.

[179] M. Ezawa. Compact merons and skyrmions in thin chiral magnetic films. *Physical Review B*, 83(10):100408, 2011.

[180] N. S. Kiselev, A. N. Bogdanov, R. Schäfer, and U. K. Rößler. Chiral skyrmions in thin magnetic films: new objects for magnetic storage technologies? *Journal of Physics D: Applied Physics*, 44(39):392001, 2011.

[181] S. S. P. Parkin, M. Hayashi, and L. Thomas. Magnetic domain-wall racetrack memory. *Science*, 320(5873):190–194, 2008.

[182] A. Fert, V. Cros, and J. Sampaio. Skyrmions on the track. *Nature Nanotechnology*, 8(3):152, 2013.

[183] N. Nagaosa and Y. Tokura. Topological properties and dynamics of magnetic skyrmions. *Nature nanotechnology*, 8(12):899, 2013.

[184] A. N. Bogdanov and D. A. Yablonskii. Contribution to the theory of inhomogeneous states of magnets in the region of magnetic-field-induced phase transitions. mixed state of antiferromagnets. *Zh. Eksp. Teor. Fiz*, 96:253–260, 1989.

[185] H. D. Rosales, D. C. Cabra, and P. Pujol. Three-sublattice skyrmion crystal in the antiferromagnetic triangular lattice. *Physical Review B*, 92(21):214439, 2015.

[186] S. Rohart and A. Thiaville. Skyrmion confinement in ultrathin film nanostructures in the presence of Dzyaloshinskii-Moriya interaction. *Physical Review B*, 88(18):184422, 2013.

[187] J. Mulkers, M. V. Milošević, and B. Van Waeyenberge. Cycloidal versus skyrmionic states in mesoscopic chiral magnets. *Physical Review B*, 93(21):214405, 2016.

[188] C. P. Chui, F. Ma, and Y. Zhou. Geometrical and physical conditions for skyrmion stability in a nanowire. *AIP Advances*, 5(4):047141, 2015.

[189] C. Navau, N. Del-Valle, and A. Sanchez. Analytical trajectories of skyrmions in confined geometries: Skyrmionic racetracks and nano-oscillators. *Physical Review B*, 94(18):184104, 2016.

[190] J. Mulkers, B. Van Waeyenberge, and M. V. Milošević. Effects of spatially engineered Dzyaloshinskii-Moriya interaction in ferromagnetic films. *Physical Review B*, 95(14):144401, 2017.

[191] D. Stosic, T. B. Ludermir, and M. V. Milošević. Pinning of magnetic skyrmions in a monolayer co film on pt (111): Theoretical characterization and exemplified utilization. *Physical Review B*, 96(21):214403, 2017.

[192] D. Stosic, J. Mulkers, B. Van Waeyenberge, T. B. Ludermir, and M. V. Milošević. Paths to collapse for isolated skyrmions in few-monolayer ferromagnetic films. *Physical Review B*, 95(21):214418, 2017.

[193] A. L. Balk, K. W. Kim, D. T. Pierce, M. D. Stiles, J. Unguris, and S. M. Stavis. Simultaneous control of the Dzyaloshinskii-Moriya interaction and magnetic anisotropy in nanomagnetic trilayers. *Physical Review Letters*, 119(7):077205, 2017.

[194] A. W. J. Wells, P. M. Shepley, C. H. Marrows, and T. A. Moore. Effect of interfacial intermixing on the Dzyaloshinskii-Moriya interaction in Pt/Co/Pt. *Physical Review B*, 95(5):054428, 2017.

[195] A. Vansteenkiste, J. Leliaert, M. Dvornik, M.s Helsen, F. Garcia-Sanchez, and B. Van Waeyenberge. The design and verification of MuMax3. *AIP Advances*, 4(10):107133, 2014.

[196] P. J. Metaxas, J. P. Jamet, A. Mougin, M. Cormier, J. Ferré, V. Baltz, B. Rodmacq, B. Dieny, and R. L. Stamps. Creep and flow regimes of magnetic domain-wall motion in ultrathin Pt/Co/Pt films with perpendicular anisotropy. *Physical Review Letters*, 99(21):217208, 2007.

[197] J. Sampaio, V. Cros, S. Rohart, A. Thiaville, and A. Fert. Nucleation, stability and current-induced motion of isolated magnetic skyrmions in nanostructures. *Nature Nanotechnology*, 8(11):839, 2013.

[198] H. V. Gomonay and V. M. Loktev. Spin transfer and current-induced switching in antiferromagnets. *Physical Review B*, 81(14):144427, 2010.

[199] H. V. Gomonay, R. V. Kunitsyn, and V. M. Loktev. Symmetry and the macroscopic dynamics of antiferromagnetic materials in the presence of spin-polarized current. *Physical Review B*, 85(13):134446, 2012.

[200] S. Mizukami, Y. Ando, and T. Miyazaki. The study on ferromagnetic resonance linewidth for NM/80NiFe/NM (NM= Cu, Ta, Pd and Pt) films. *Japanese journal of applied physics*, 40(2R):580, 2001.

[201] M. Oogane, T. Wakitani, S. Yakata, R. Yilgin, Y. Ando, A. Sakuma, and T. Miyazaki. Magnetic damping in ferromagnetic thin films. *Japanese journal of applied physics*, 45(5R):3889, 2006.

[202] S. Ikeda, K. Miura, H. Yamamoto, K. Mizunuma, H. D. Gan, M. Endo, S. Kanai, J. Hayakawa, F. Matsukura, and H. Ohno. A perpendicular-anisotropy CoFeB–MgO magnetic tunnel junction. *Nature Materials*, 9(9):721, 2010.

[203] M. Oogane, T. Kubota, Y. Kota, S. Mizukami, H. Naganuma, A. Sakuma, and Y. Ando. Gilbert magnetic damping constant of epitaxially grown co-based heusler alloy thin films. *Applied Physics Letters*, 96(25):252501, 2010.

[204] See Supplemental Material at https://www.dropbox.com/sh/38yc4vjozvmws4m/AACTkUjHcRmphUtBeilQDXV2a?dl=0 for the animation of the transition between Con and SkL states presented in Fig. 5(d).

[205] A. N. Bogdanov, U. K. Rößler, M. Wolf, and K.-H. Müller. Magnetic structures and reorientation transitions in noncentrosymmetric uniaxial antiferromagnets. *Physical Review B*, 66(21):214410, 2002.

[206] R. Khoshlahni, A. Qaiumzadeh, A. Bergman, and A. Brataas. Ultrafast generation and dynamics of isolated skyrmions in antiferromagnetic insulators. *arXiv preprint arXiv:1809.08306*, 2018.

[207] P. F. Bessarab, D. Yudin, D. R. Gulevich, P. Wadley, M. Titov, and O. A. Tretiakov. Stability and lifetime of antiferromagnetic skyrmions. *arXiv preprint arXiv:1709.04454*, 2017.

[208] CF. Pai, L. Liu, Y. Li, H. W. Tseng, D. C. Ralph, and R. A. Buhrman. Spin transfer torque devices utilizing the giant spin Hall effect of tungsten. *Applied Physics Letters*, 101(12):122404, 2012.

[209] M. G. Blamire and J. W. A. Robinson. The interface between superconductivity and magnetism: understanding and device prospects. *Journal of Physics: Condensed Matter*, 26(45):453201, 2014.

[210] F. S. Bergeret, A. F. Volkov, and K. B. Efetov. Odd triplet superconductivity and related phenomena in superconductor-ferromagnet structures. *Reviews of Modern Physics*, 77(4):1321, 2005.

[211] M. Eschrig. Spin-polarized supercurrents for spintronics: a review of current progress. *Reports on Progress in Physics*, 78(10):104501, 2015.

[212] A. I. Buzdin. Proximity effects in superconductor-ferromagnet heterostructures. *Reviews of Modern Physics*, 77(3):935, 2005.

[213] J. Linder and J. W. A. Robinson. Superconducting spintronics. *Nature Physics*, 11(4):307, 2015.

[214] G. B. Halász, J. W. A. Robinson, J. F. Annett, and M. G. Blamire. Critical current of a josephson junction containing a conical magnet. *Physical Review B*, 79(22):224505, 2009.

[215] M. S. Kalenkov, A. D. Zaikin, and V. T. Petrashov. Triplet superconductivity in a ferromagnetic vortex. *Physical Review Letters*, 107(8):087003, 2011.

[216] T. Yokoyama and J. Linder. Josephson effect through magnetic skyrmions. *Physical Review B*, 92(6):060503(R), 2015.

[217] M. Alidoust and K. Halterman. Proximity induced vortices and long-range triplet supercurrents in ferromagnetic josephson junctions and spin valves. *Journal of Applied Physics*, 117(12):123906, 2015.

[218] M. A. Zorro, T. Saraiva, and C. C. de Souza Silva. Nucleation of superconductivity in multiply connected superconductor–ferromagnet hybrids. *Superconductor Science and Technology*, 27(5):055002, 2014.

[219] S. S. Pershoguba, S. Nakosai, and A. V. Balatsky. Skyrmion-induced bound states in a superconductor. *Physical Review B*, 94(6):064513, 2016.

[220] K. Björnson and A. M. Black-Schaffer. Skyrmion spin texture in ferromagnetic semiconductor–superconductor heterostructures. *Physical Review B*, 89(13):134518, 2014.

[221] L. E. Helseth. Interaction between superconducting films and magnetic nanostructures. *Physical Review B*, 66(10):104508, 2002.

[222] V. L. Vadimov, M. V. Sapozhnikov, and A. S. Mel'nikov. Magnetic skyrmions in ferromagnet-superconductor (f/s) heterostructures. *Applied Physics Letters*, 113(3):032402, 2018.

[223] N. Del-Valle, S. Agramunt-Puig, A. Sanchez, and C. Navau. Imprinting skyrmions in thin films by ferromagnetic and superconducting templates. *Applied Physics Letters*, 107(13):133103, 2015.

[224] K. M. D. Hals, M. Schecter, and M. S. Rudner. Composite topological excitations in ferromagnet-superconductor heterostructures. *Physical Review Letters*, 117(1):017001, 2016.

[225] S. M. Dahir, A. F. Volkov, and I. M. Eremin. Interaction of skyrmions and pearl vortices in superconductor-chiral ferromagnet heterostructures. *Physical Review Letters*, 122(9):097001, 2019.

[226] S. Nakosai, Y. Tanaka, and N. Nagaosa. Two-dimensional p-wave superconducting states with magnetic moments on a conventional s-wave superconductor. *Physical Review B*, 88(18):180503, 2013.

[227] W. Chen and A. P. Schnyder. Majorana edge states in superconductor-noncollinear magnet interfaces. *Physical Review B*, 92(21):214502, 2015.

[228] G. Yang, P. Stano, J. Klinovaja, and D. Loss. Majorana bound states in magnetic skyrmions. *Physical Review B*, 93(22):224505, 2016.

[229] U. Güngördü, S. Sandhoefner, and A. A. Kovalev. Stabilization and control of majorana bound states with elongated skyrmions. *Physical Review B*, 97(11):115136, 2018.

[230] S. Rex, I. V. Gornyi, and A. D. Mirlin. Majorana bound states in magnetic skyrmions imposed onto a superconductor. *Physical Review B*, 100(6):064504, 2019.

[231] M. Garnier, A. Mesaros, and P. Simon. Topological superconductivity with deformable magnetic skyrmions. *Communications Physics*, 2(1):1–8, 2019.

[232] T. Zhou, N. Mohanta, J. E. Han, A. Matos-Abiague, and I. Žutić. Tunable magnetic textures in spin valves: From spintronics to majorana bound states. *Physical Review B*, 99(13):134505, 2019.

[233] S. Rex, I. V. Gornyi, and A. D. Mirlin. Majorana modes in emergent-wire phases of helical and cycloidal magnet-superconductor hybrids. *Physical Review B*, 102(22):224501, 2020.

[234] T. Posske, C.-K. Chiu, and M. Thorwart. Vortex majorana braiding in a finite time. *Physical Review Research*, 2(2):023205, 2020.

[235] X. Ma, C. J. O. Reichhardt, and C. Reichhardt. Braiding majorana fermions and creating quantum logic gates with vortices on a periodic pinning structure. *Physical Review B*, 101(2):024514, 2020.

[236] Y.-L. Wang, X. Ma, J. Xu, Z.-L. Xiao, A. Snezhko, R. Divan, L. E. Ocola, J. E. Pearson, B. Janko, and W.-K. Kwok. Switchable geometric frustration in an artificial-spin-ice–superconductor heterosystem. *Nature Nanotechnology*, 13(7):560–565, 2018.

[237] N. Romming, A. Kubetzka, C. Hanneken, K. von Bergmann, and R. Wiesendanger. Field-dependent size and shape of single magnetic skyrmions. *Physical Review Letters*, 114(17):177203, 2015.

[238] A. Yagil, A. Almoalem, A. Soumyanarayanan, A. K. C. Tan, M. Raju, C. Panagopoulos, and O. M. Auslaender. Stray field signatures of néel textured skyrmions in ir/fe/co/pt multilayer films. *Applied Physics Letters*, 112(19):192403, 2018.

[239] M. Tinkham. *Introduction to superconductivity*. Courier Corporation, 2004.

[240] G. Carneiro and E. H. Brandt. Vortex lines in films: fields and interactions. *Physical Review B*, 61(9):6370, 2000.

[241] A. Soumyanarayanan, M. Raju, A. L. G. Oyarce, A. K. C. Tan, M.-Y. Im, A. P. Petrović, P. Ho, K. H. Khoo, M. Tran, C. K. Gan, et al. Tunable room-temperature

magnetic skyrmions in ir/fe/co/pt multilayers. *Nature Materials*, 16(9):898–904, 2017.

[242] S. Rohart and A. Thiaville. Skyrmion confinement in ultrathin film nanostructures in the presence of dzyaloshinskii-moriya interaction. *Physical Review B*, 88(18):184422, 2013.

[243] J. Müller and A. Rosch. Capturing of a magnetic skyrmion with a hole. *Physical Review B*, 91(5):054410, 2015.

[244] S.-Z. Lin, C. Reichhardt, C. D. Batista, and A. Saxena. Particle model for skyrmions in metallic chiral magnets: Dynamics, pinning, and creep. *Physical Review B*, 87(21):214419, 2013.

[245] J. Mulkers, B. Van Waeyenberge, and M. V. Milošević. Effects of spatially engineered dzyaloshinskii-moriya interaction in ferromagnetic films. *Physical Review B*, 95(14):144401, 2017.

[246] L. Thiel, D. Rohner, M. Ganzhorn, P. Appel, E. Neu, B. Müller, R. Kleiner, D. Koelle, and P. Maletinsky. Quantitative nanoscale vortex imaging using a cryogenic quantum magnetometer. *Nature Nanotechnology*, 11(8):677, 2016.

[247] Y.-H. Liu and Y.-Q. Li. A mechanism to pin skyrmions in chiral magnets. *Journal of Physics: Condensed Matter*, 25(7):076005, 2013.

[248] C. Wang, D. Xiao, X. Chen, Y. Zhou, and Y. Liu. Manipulating and trapping skyrmions by magnetic field gradients. *New Journal of Physics*, 19(8):083008, 2017.

[249] J. Bardeen and M. J. Stephen. Theory of the motion of vortices in superconductors. *Physical Review*, 140(4A):A1197, 1965.

[250] B. Parks, S. Spielman, J. Orenstein, D. T. Nemeth, F. Ludwig, J. Clarke, P. Merchant, and D. J. Lew. Phase-sensitive measurements of vortex dynamics in the terahertz domain. *Physical Review Letters*, 74(16):3265, 1995.

[251] L. P. Gor'kov and N. B. Kopnin. Vortex motion and resistivity of type-ll superconductors in a magnetic field. *Soviet Physics Uspekhi*, 18(7):496, 1975.

[252] L. Embon, Y. Anahory, Ž. L. Jelić, E. O. Lachman, Y. Myasoedov, M. E. Huber, G. P. Mikitik, A. V. Silhanek, M. V. Milošević, A. Gurevich, and E. Zeldov. Imaging of super-fast dynamics and flow instabilities of superconducting vortices. *Nature Communications*, 8(1):85, 2017.

[253] R. Alexandre and D. Guy. *Coherence In High Temperature Superconductors*. World Scientific, 1996.

[254] V. Moshchalkov, R. Woerdenweber, and W. Lang. *Nanoscience and engineering in superconductivity*. Springer Science & Business Media, 2010.

[255] C. Reichhardt, D. Ray, and C. J. Olson Reichhardt. Quantized transport for a skyrmion moving on a two-dimensional periodic substrate. *Physical Review B*, 91(10):104426, 2015.

[256] I. L. Fernandes, J. Bouaziz, S. Blügel, and S. Lounis. Universality of defect-skyrmion interaction profiles. *Nature Communications*, 9(1):4395, 2018.

[257] C. Reichhardt and C. J. Olson Reichhardt. Shapiro steps for skyrmion motion on a washboard potential with longitudinal and transverse ac drives. *Physical Review B*, 92(22):224432, 2015.

[258] C. Reichhardt, D. Ray, and C. J. O. Reichhardt. Magnus-induced ratchet effects for skyrmions interacting with asymmetric substrates. *New Journal of Physics*, 17(7):073034, 2015.

[259] M. Gibertini, M. Koperski, A. F. Morpurgo, and K. S. Novoselov. Magnetic 2d materials and heterostructures. *Nature Nanotechnology*, 14:408–419, 2019.

[260] K. S. Burch, D. Mandrus, and J.-G. Park. Magnetism in two-dimensional van der waals materials. *Nature*, 563(7729):47, 2018.

[261] P. Ferriani, I. Turek, S. Heinze, G. Bihlmayer, and S. Blügel. Magnetic phase control in monolayer films by substrate tuning. *Physical Review Letters*, 99(18):187203, 2007.

[262] B. Hardrat, A. Al-Zubi, P. Ferriani, S. Blügel, G. Bihlmayer, and S. Heinze. Complex magnetism of iron monolayers on hexagonal transition metal surfaces from first principles. *Physical Review B*, 79(9):094411, 2009.

[263] S. Meyer, B. Dupé, P. Ferriani, and S. Heinze. Dzyaloshinskii-moriya interaction at an antiferromagnetic interface: First-principles study of Fe/Ir bilayers on Rh(001). *Physical Review B*, 96(9):094408, 2017.

[264] C. Xu, J. Feng, S. Prokhorenko, Y. Nahas, H. Xiang, and L. Bellaiche. Topological spin texture in janus monolayers of the chromium trihalides Cr(I, X)$_3$. *Physical Review B*, 101(6):060404(R), 2020.

[265] B. Huang, G. Clark, D. R. Klein, D. MacNeill, E. Navarro-Moratalla, K. L. Seyler, N. Wilson, M. A McGuire, D. H. Cobden, D. Xiao, et al. Electrical control of 2d magnetism in bilayer CrI_3. *Nature nanotechnology*, 13(7):544, 2018.

[266] L. Webster and J.-A. Yan. Strain-tunable magnetic anisotropy in monolayer $CrCl_3$, $CrBr_3$, and CrI_3. *Physical Review B*, 98(14):144411, 2018.

[267] P. Ferriani, K. Von Bergmann, E. Y. Vedmedenko, S. Heinze, M. Bode, M. Heide, G. Bihlmayer, S. Blügel, and R. Wiesendanger. Atomic-scale spin spiral with a unique rotational sense: Mn monolayer on W(001). *Physical Review Letters*, 101(2):027201, 2008.

[268] P. Sessi, N. P. Guisinger, J. R. Guest, and M. Bode. Temperature and size dependence of antiferromagnetism in Mn nanostructures. *Physical Review Letters*, 103(16):167201, 2009.

[269] L. Tan, L. Wang, and T. Min. Tunable magnetic ground states of iron monolayer on nonmagnetic metallic substrates by small in-plane strains. *RSC Advances*, 9(70):41099–41106, 2019.

[270] J. Liang, M. Chshiev, A. Fert, and H. Yang. Very large dzyaloshinskii-moriya interaction in two-dimensional janus manganese dichalcogenides and its application to realize field-free skyrmions. *arXiv preprint arXiv:1906.00648*, 2019.

[271] A. N. Bogdanov and U. K. Rößler. Chiral symmetry breaking in magnetic thin films and multilayers. *Physical Review Letters*, 87(3):037203, 2001.

[272] N. Hayashi, K. Saito, and Y. Nakatani. Calculation of demagnetizing field distribution based on fast fourier transform of convolution. *Japanese Journal of Applied Physics*, 35(12R):6065, 1996.

[273] K. De'Bell, A. B. MacIsaac, I. N. Booth, and J. P. Whitehead. Dipolar-induced planar anisotropy in ultrathin magnetic films. *Physical Review B*, 55(22):15108, 1997.

[274] X. Fabrèges, S. Petit, I. Mirebeau, S. Pailhès, L. Pinsard, A. Forget, M. T. Fernandez-Diaz, and F. Porcher. Spin-lattice coupling, frustration, and magnetic order in multiferroic $R\mathrm{MnO_3}$. *Physical Review Letters*, 103(6):067204, 2009.

[275] H. Tan, C. Xu, M. Li, S. Wang, B. Gu, and W. Duan. Pressure and strain effects of hexagonal rare-earth manganites: A first-principles study. *Journal of Physics: Condensed Matter*, 28(12):126002, 2016.

[276] W. Wang, J. Zhao, W. Wang, Z. Gai, N. Balke, M. Chi, H. N. Lee, W. Tian, L. Zhu, X. Cheng, et al. Room-temperature multiferroic hexagonal $\mathrm{LuFeO_3}$ films. *Physical Review Letters*, 110(23):237601, 2013.

[277] G. O. Zimmerman, A. K. Ibrahim, and F. Y. Wu. Planar classical dipolar system on a honeycomb lattice. *Physical Review B*, 37(4):2059, 1988.

[278] A. M. Belemuk and S. M. Stishov. Phase transitions in chiral magnets from monte carlo simulations. *Physical Review B*, 95(22):224433, 2017.

[279] S. Buhrandt and L. Fritz. Skyrmion lattice phase in three-dimensional chiral magnets from monte carlo simulations. *Physical Review B*, 88(19):195137, 2013.

[280] P. F. Bessarab, D. Yudin, D. R. Gulevich, P. Wadley, M. Titov, and O. A. Tretiakov. Stability and lifetime of antiferromagnetic skyrmions. *Physical Review B*, 99(14):140411(R), 2019.

[281] C. Xu, J. Feng, H. Xiang, and L. Bellaiche. Interplay between kitaev interaction and single ion anisotropy in ferromagnetic CrI3 and CrGeTe3 monolayers. *npj Computational Materials*, 4(1):1–6, 2018.

[282] R. Wieser, E. Y. Vedmedenko, and R. Wiesendanger. Entropy driven phase transition in itinerant antiferromagnetic monolayers. *Physical Review B*, 77(6):064410, 2008.

[283] A. Kitaev. Anyons in an exactly solved model and beyond. *Annals of Physics*, 321(1):2–111, 2006.

[284] S. I. Vishkayi, Z. Torbatian, A. Qaiumzadeh, and R. Asgari. Strain and electric-field control of spin-spin interactions in monolayer CrI3. *Physical Review Materials*, 4(9):094004, 2020.

[285] S. Jiang, L. Li, Z. Wang, K. F. Mak, and J. Shan. Controlling magnetism in 2d cri 3 by electrostatic doping. *Nature nanotechnology*, 13(7):549–553, 2018.

[286] W. Chen, Z. Sun, Z. Wang, L. Gu, X. Xu, S. Wu, and C. Gao. Direct observation of van der waals stacking–dependent interlayer magnetism. *Science*, 366(6468):983–987, 2019.

[287] N. Sivadas, S. Okamoto, X. Xu, C. J. Fennie, and D. Xiao. Stacking-dependent magnetism in bilayer cri3. *Nano Letters*, 18(12):7658–7664, 2018.

[288] J. Shang, X. Tang, X. Tan, A. Du, T. Liao, S. C. Smith, Y. Gu, C. Li, and L. Kou. Stacking-dependent interlayer magnetic coupling in 2d cri3/crgete3 nanostructures for spintronics. *ACS Applied Nano Materials*, 3(2):1282–1288, 2019.

[289] C. Gong and X. Zhang. Two-dimensional magnetic crystals and emergent heterostructure devices. *Science*, 363(6428), 2019.

[290] W. Jin, H. Ho Kim, Z. Ye, S. Li, P. Rezaie, F. Diaz, S. Siddiq, E. Wauer, B. Yang, C. Li, et al. Raman fingerprint of two terahertz spin wave branches in a two-dimensional honeycomb ising ferromagnet. *Nature communications*, 9(1):1–7, 2018.

[291] J. L. Lado and J. Fernández-Rossier. On the origin of magnetic anisotropy in two dimensional CrI3. *2D Materials*, 4(3):035002, 2017.

[292] J. Liu, M. Shi, J. Lu, and M. P. Anantram. Analysis of electrical-field-dependent dzyaloshinskii-moriya interaction and magnetocrystalline anisotropy in a two-dimensional ferromagnetic monolayer. *Physical Review B*, 97(5):054416, 2018.

[293] A. K. Behera, S. Chowdhury, and S. R. Das. Magnetic skyrmions in atomic thin cri3 monolayer. *Applied Physics Letters*, 114(23):232402, 2019.

[294] F. Xiao, K. Chen, and Q. Tong. Magnetization textures in twisted bilayer cr x 3 (x= br, i). *Physical Review Research*, 3(1):013027, 2021.

[295] Q. Tong, F. Liu, J. Xiao, and W. Yao. Skyrmions in the moiré of van der waals 2d magnets. *Nano Letters*, 18(11):7194–7199, 2018.

[296] D. Šabani, C. Bacaksiz, and M. V. Milošević. Ab initio methodology for magnetic exchange parameters: Generic four-state energy mapping onto a heisenberg spin hamiltonian. *Physical Review B*, 102(1):014457, 2020.

[297] D. R. Klein, D. MacNeill, J. L. Lado, D. Soriano, E. Navarro-Moratalla, K. Watanabe, T. Taniguchi, S. Manni, P. Canfield, J. Fernández-Rossier, et al. Probing magnetism in 2d van der waals crystalline insulators via electron tunneling. *Science*, 360(6394):1218–1222, 2018.

[298] Y.-J. Chen, Kh. Zakeri, A. Ernst, H. J. Qin, Y. Meng, and J. Kirschner. Group velocity engineering of confined ultrafast magnons. *Physical Review Letters*, 119(26):267201, 2017.

[299] S. Zhang, R. Xu, N. Luo, and X. Zou. Two-dimensional magnetic materials: structures, properties and external controls. *Nanoscale*, 13(3):1398–1424, 2021.

[300] D. Torelli, K. S. Thygesen, and T. Olsen. High throughput computational screening for 2d ferromagnetic materials: the critical role of anisotropy and local correlations. *2D Materials*, 6(4):045018, 2019.

[301] D. Cortés-Ortuño and P. Landeros. Influence of the dzyaloshinskii–moriya interaction on the spin-wave spectra of thin films. *Journal of Physics: Condensed Matter*, 25(15):156001, 2013.

[302] K. Wang, A. A Puretzky, Z. Hu, B. R. Srijanto, X. Li, N. Gupta, H. Yu, M. Tian, M. Mahjouri-Samani, X. Gao, et al. Strain tolerance of two-dimensional crystal growth on curved surfaces. *Science advances*, 5(5):eaav4028, 2019.

[303] Z. Peng, X. Chen, Y. Fan, D. J. Srolovitz, and D. Lei. Strain engineering of 2d semiconductors and graphene: from strain fields to band-structure tuning and photonic applications. *Light: Science & Applications*, 9(1):1–25, 2020.

[304] A. Castellanos-Gomez, R. Roldán, E. Cappelluti, M. Buscema, F. Guinea, H. S. J. van-der Zant, and G. A. Steele. Local strain engineering in atomically thin mos2. *Nano letters*, 13(11):5361–5366, 2013.

[305] Y. Sun and K. Liu. Strain engineering in functional 2-dimensional materials. *Journal of Applied Physics*, 125(8):082402, 2019.

[306] E. Khestanova, F. Guinea, L. Fumagalli, A. K. Geim, and I. V. Grigorieva. Universal shape and pressure inside bubbles appearing in van der waals heterostructures. *Nature Communications*, 7(1):1–10, 2016.

[307] Z. Dai, L. Liu, and Z. Zhang. Strain engineering of 2d materials: issues and opportunities at the interface. *Advanced Materials*, 31(45):1805417, 2019.

[308] J. Quereda, P. San-Jose, V. Parente, L. Vaquero-Garzon, A. J. Molina-Mendoza, N. Agraït, G. Rubio-Bollinger, F. Guinea, R. Roldán, and A. Castellanos-Gomez. Strong modulation of optical properties in black phosphorus through strain-engineered rippling. *Nano letters*, 16(5):2931–2937, 2016.

[309] W. K. Peria, X. Wang, H. Yu, S. Lee, I. Takeuchi, and P. A. Crowell. Magnetoelastic gilbert damping in magnetostrictive fe 0.7 ga 0.3 thin films. *Physical Review B*, 103(22):L220403, 2021.

[310] J. Jiang, T. Xu, J. Lu, L. Sun, and Z. Ni. Defect engineering in 2d materials: precise manipulation and improved functionalities. *Research*, 2019, 2019.

[311] B. Schuler, D. Y. Qiu, S. Refaely-Abramson, C. Kastl, C. T. Chen, S. Barja, R. J. Koch, D. F. Ogletree, S. Aloni, A. M. Schwartzberg, et al. Large spin-orbit splitting of deep in-gap defect states of engineered sulfur vacancies in monolayer ws 2. *Physical Review Letters*, 123(7):076801, 2019.

[312] J. Mulkers, B. Van W., and M. V. Milošević. Tunable snell's law for spin waves in heterochiral magnetic films. *Physical Review B*, 97(10):104422, 2018.

[313] Z. Wang, B. Zhang, Y. Cao, and P. Yan. Probing the dzyaloshinskii-moriya interaction via the propagation of spin waves in ferromagnetic thin films. *Physical Review Applied*, 10(5):054018, 2018.

[314] S. Macke and D. Goll. Transmission and reflection of spin waves in the presence of néel walls. In *Journal of Physics: Conference Series*, volume 200, page 042015. IOP Publishing, 2010.

[315] X-G Wang, G-H Guo, G-F Zhang, Y-Z Nie, and Q-L Xia. Spin-wave resonance reflection and spin-wave induced domain wall displacement. *Journal of Applied Physics*, 113(21):213904, 2013.

[316] F.t K de Vries, E. Portolés, G. Zheng, T. Taniguchi, K. Watanabe, T. Ihn, K. Ensslin, and P. Rickhaus. Gate-defined josephson junctions in magic-angle twisted bilayer graphene. *Nature Nanotechnology*, pages 1–4, 2021.

[317] X. Wang, Q. Weng, Y. Yang, Y. Bando, and D. Golberg. Hybrid two-dimensional materials in rechargeable battery applications and their microscopic mechanisms. *Chemical Society Reviews*, 45(15):4042–4073, 2016.

[318] K. Zollner, P. E. F. Junior, and J. Fabian. Proximity exchange effects in mose 2 and wse 2 heterostructures with cri 3: Twist angle, layer, and gate dependence. *Physical Review B*, 100(8):085128, 2019.

[319] Z. Y. Zhu, Y. C. Cheng, and U. Schwingenschlögl. Giant spin-orbit-induced spin splitting in two-dimensional transition-metal dichalcogenide semiconductors. *Physical Review B*, 84(15):153402, 2011.

[320] J. A. Reyes-Retana and F. Cervantes-Sodi. Spin-orbital effects in metal-dichalcogenide semiconducting monolayers. *Scientific Reports*, 6(1):1–10, 2016.

A

Supporting information for Part II-Skyrmionics in thin film heterostructures

A.1 Micromagnetic model and the antiferromagnetic state

The mumax[3] software was originally developed for simulations of ferromagnetic (FM) systems in the continuous field approximation. However, in micromagnetic simulations we do not work with a continuous field. Instead we discretize the field on a grid. Therefore, for the case of an antiferromagnetic (AFM) system, which comprises two sublattices of reversely-aligned spins, each cell of the mesh grid is now understood as one single spin, and we end up performing an atomistic simulation, with the grid separation now representing the lattice parameter.

The exchange energy density $\mathcal{E}_{\text{ex}} = A\left[(\partial_x \mathbf{m})^2 + (\partial_y \mathbf{m})^2\right]$ is the continuous analogue form of the classical Heisenberg Hamiltonian $E_{ij} = -J\mathbf{S}^i \cdot \mathbf{S}^j$, which models the exchange interaction between neighbouring spins $\mathbf{S}^i$ and $\mathbf{S}^j$ in atomistic spin systems. This analogy can be observed by considering, e.g., the first-order finite-difference approximation of the energy density due to variations of the magnetization along the x direction, i.e.,

$$A\left(\frac{\mathbf{m}^{i+1} - \mathbf{m}^i}{\Delta x}\right)^2 = \frac{2A}{(\Delta x)^2}(1 - \mathbf{m}^i \cdot \mathbf{m}^{i+1}), \tag{A.1}$$

where $\mathbf{m}^i$ and $\mathbf{m}^{i+1}$ are the magnetizations of adjacent grid cells, with grid separation Δx along the x direction. Notice that the energy changes with the dot product of the magnetization in neighbouring cells, which is mathematically equivalent to the classical Heissenberg Hamiltonian. Similar to the exchange interaction, the Dzyaloshinskii-Moriya interaction (DMI) $\mathcal{E}_{\text{dmi}} = -D\left[m_x\partial_x m_z - m_z\partial_x m_x + m_y\partial_y m_z - m_z\partial_y m_y\right]$ is the continuous analogue of the classical Heisenberg-like Hamiltonian $E_{ij} = \mathbf{D} \cdot (\mathbf{S}^i \times \mathbf{S}^j)$, which models the DMI between neighbouring spins $\mathbf{S}^i$ and $\mathbf{S}^j$ with DMI vector $\mathbf{D}$. Again, considering only variations of the magnetization along the x direction, the

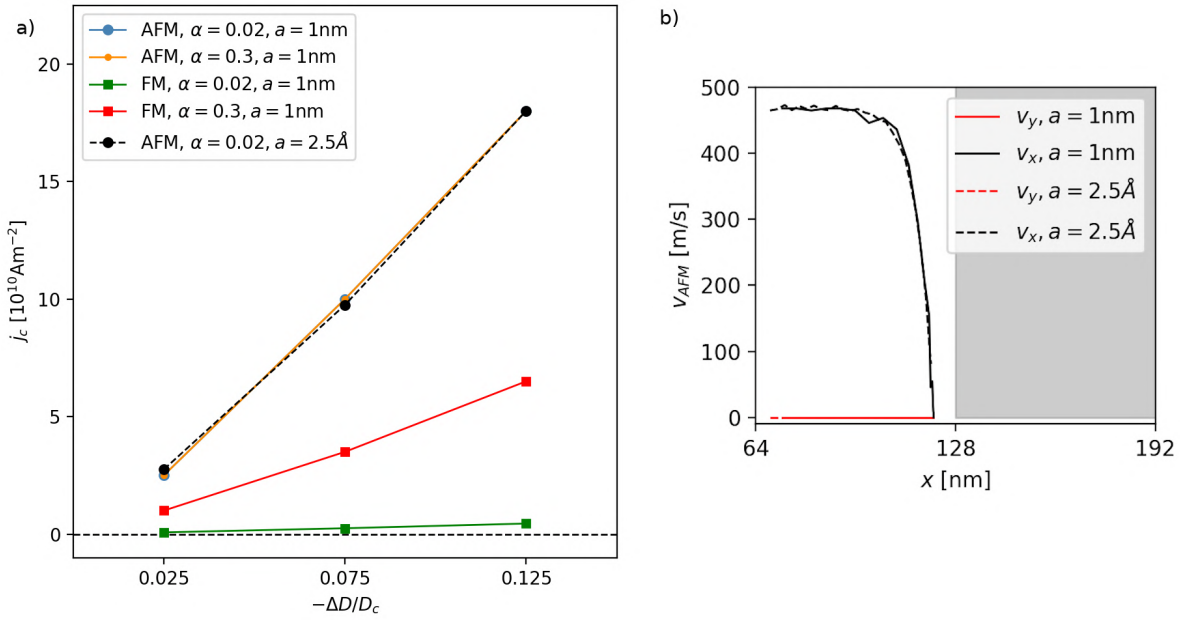

Figure A.1 – Comparison of the results obtained in Fig. 5.8 and Fig. 5.9 of chapter 4 with those obtained for the ultra-small grid separation of $a = 2.5$Å. (a) Critical current for the skyrmion to overcome a heterochiral interface in the AFM and FM cases, as a function of ΔD, with $D_1 = 0.8D_c$ fixed. (b) Center-of-mass velocities of the AFM skyrmion during motion shown in Fig. 8 (a) of the main text.

finite-difference approximation yields

$$-D\left[m_x^i\frac{m_z^{i+1}-m_z^i}{\Delta x}-m_z^i\frac{m_x^{i+1}-m_x^i}{\Delta x}\right]=\frac{D}{\Delta x}\hat{e}_y\cdot(\mathbf{m}^i\times\mathbf{m}^{i+1}), \tag{A.2}$$

with $\mathbf{m}^i$ and $\mathbf{m}^{i+1}$ the magnetizations of adjacent grid cells. This expression is also equivalent to the classical Heissenberg Hamiltonian for the DMI.

Therefore, to perform the atomistic simulation one needs to consider an ultra-small mesh grid with grid separation of the order of the atomic distances. In order to check our results, we reproduced Fig. 5.8 and 5.9 of chapter 4 for the antiferromagnetic system, now with a grid separation of $a = 2.5$Å, which is a typical value for the lattice constant considered in atomistic simulations[127, 206]. Fig. A.1 compares the results of Figs. 5.8 and 5.9 of chapter 4 with those obtained for the ultra-small grid separation of $a = 2.5$Å. Notice that the results do not change considerably by changing the grid separation, which indicates that the AFM simulations presented in the main text can be understood as atomistic simulations on a square lattice.

A.2 Calculation of the dissipative tensor

The dissipative tensor can be calculated by considering a single magnetic skyrmion with its center located at the origin $r = 0$. The components of the dissi-

pative tensor are defined as

$$\mathcal{D}_{ij} = \frac{dM_s}{\gamma} \int d^2 r \partial_i \mathbf{m} \cdot \partial_j \mathbf{m}. \tag{A.3}$$

The azimuthal symmetry of the spin configuration leads to $\mathcal{D}_{xx} = \mathcal{D}_{yy} = \mathcal{D}$ and $\mathcal{D}_{xy} = \mathcal{D}_{yx} = 0$, and reduces the problem to a 1D integral

$$\mathcal{D} = \frac{dM_s}{\gamma} \pi \int_0^\infty r dr \left[\left(\frac{d\theta(r)}{dr} \right)^2 + \frac{\sin^2 \theta(r)}{r^2} \right], \tag{A.4}$$

where we used $\mathbf{m}(\mathbf{r}) = \sin[\theta(r)]\hat{r} + \cos[\theta(r)]\hat{z}$ in Eq. (A.3) for the case of a Néel skyrmion. Here $r = \sqrt{x^2 + y^2}$ is the distance from the skyrmion core. Eq. (A.4) can be discretized in the simulation as follows

$$\mathcal{D} = \frac{dM_s}{\gamma} \pi \sum_{i=1}^{N} i \left[\left(\frac{\theta(i+1) - \theta(i-1)}{2} \right)^2 + \frac{\sin^2 \theta(i)}{i^2} \right], \tag{A.5}$$

where $r = ia$, with a the lattice separation. N is such that $\xi_{sk} \ll Na$, with ξ_{sk} the skyrmion radius.

For the range of parameters considered in chapter 4 we calculate $\mathcal{D}/(\frac{dM_s}{\gamma}) \approx 4\pi$–$8\pi$.

For the results presented in Sec. 6.8.4 of chapter 5 we have calculated $\mathcal{D} \approx 2 \times 10^{-16}$ N/ms^{-1}, for the skyrmion at rest in the absence of applied fields, with $D = 0.8 D_c$ and the remaining FM parameters as given in Sec. 6.8.1.

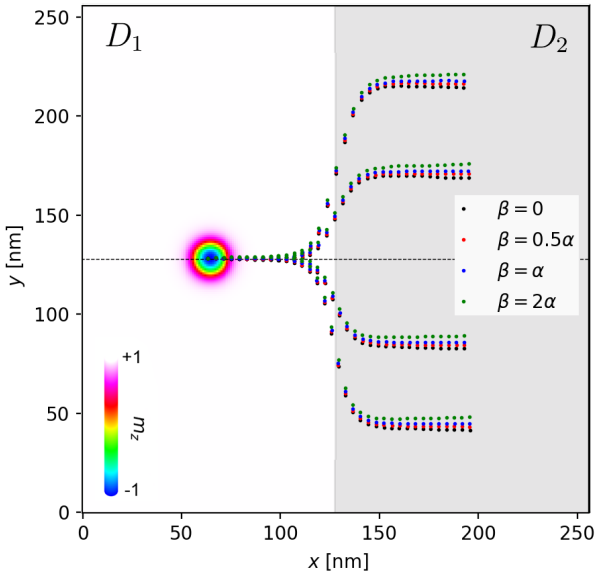

Figure A.2 – The skyrmion is initialized on the left side of the diagram. Depending on the difference of the DMI strengths across the interface, D_1 and D_2, the skyrmion deflection is positive ($\Delta y > 0$) or negative ($\Delta y < 0$). The dots show the respective trajectories of the skyrmion and the colors indicates the value of β considered, for $j = 2 \times 10^{11}$Am^{-2} and $\Delta D/D_c = 0.05, 0.025, -0.025, -0.05$, respectively top-to-bottom.

A.3 Effects of the non-adiabatic spin transfer torque

Fig. A.2 shows the effects of the non-adiabatic spin transfer torque to the skyrmion trajectories with a fixed damping parameter $\alpha = 0.02$. The value of β does not affect the deflection induced by the interface, but induces a small constant velocity transverse to the applied current, as expected for a single skyrmion moving in the free space.

A.4 Skyrmion-vortex interaction for superconducting films of arbitrary thicknesses

In order to calculate the stray field of the vortex in a superconducting film of an arbitrary thickness d_{sc}, we integrate Eqs. (6.6a) and (6.6b) numerically. Figs. A.3 (a) and (b) show the obtained stray fields for different values of d_{SC}, with $\lambda = 50$ nm and $d_{\mathrm{I}} = 10$ nm fixed, where we consider a finite vortex core by inserting the cutoff factor $\exp(-\xi^2 k^2)$, with $\xi = 10$ nm in Eqs. (6.6a) and (6.6b). Fig. A.3 (c) and (d) show the skyrmion-vortex interaction energy and interaction force, respectively, calculated as in Sec. 6.8.3.3 of the main text, for $D = 0.8D_c$. The dashed lines in Fig. A.3 (d) show the pure-Zeeman component of the interaction force. Notice that even though for the

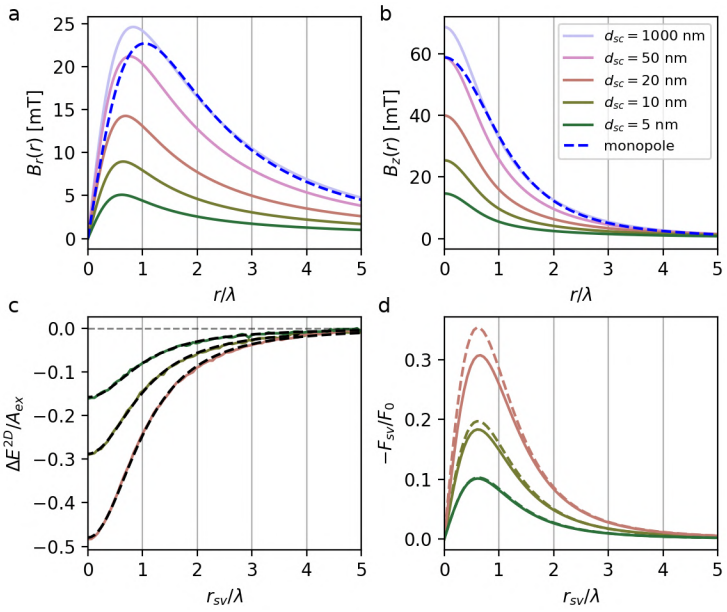

Figure A.3 – (a,b) Stray magnetic field of the vortex for different thickness of the superconducting film, calculated in the plane of the FM film within the considered SC-FM hybrid. (c) Skyrmion-vortex interaction energy calculated in the micromagnetic simulations as a function of the distance between the skyrmion and the vortex cores, for $d_{\mathrm{SC}} = 5$, 10 and 20 nm. Here the energy curves were fitted by $E = a/(r_{\mathrm{sv}}^2 + b\lambda^2)^c$, with a, b, c the fitting parameters (yielding black dashed lines). (d) Corresponding interaction force calculated by the derivative of the fitted curves in (c), the dashed lines denote the pure-Zeeman component of the interaction force. In all calculations we take $\lambda = 50$ nm, $d_{\mathrm{I}} = 10$ nm and $D = 0.8D_c$.

considered parameters the skyrmion size is weakly affected by the presence of the vortex field, small changes in the skymion shape can still result in a non-negligible contribution of the non-Zeeman energy terms to the total skyrmion-vortex interaction.

B

Supporting information for Part III-Magnonics and spin-textures in two-dimensional magnetic materials

B.1 Spin wave dispersion relation in $CrBr_3$ and CrI_3

The precession of the i^{th} spin is given by the first term in the Landau-Lifshitz-Gilbert (LLG) equation [Eq. 2.15], where the effective field acting on the i^{th} spin is given by $\mathbf{B}_i^{\text{eff}} = -\partial\mathcal{H}_i/\partial\hat{\mathbf{S}}_i$. From Eq. (8.3) we obtain

$$\mathbf{B}_i^{\text{eff}} = S^2\left[J_0\sum_j \hat{S}_j + \Delta\sum_j \hat{S}_j^z\hat{z} + 2\mathcal{A}^{zz}\hat{S}_i^z\hat{z}\right] \tag{B.1}$$

where the sum in j runs over the three nearest-neighbours of the i^{th} spin [see Fig. B.1]. The SW dispersion is calculated by assuming the linearized solution $\hat{S}^z \approx 1$, $\hat{S}^x \approx A_0 e^{i(\mathbf{k}\cdot\mathbf{r}-\omega t)}$ and $\hat{S}^y \approx iA_0 e^{i(\mathbf{k}\cdot\mathbf{r}-\omega t)}$, where $A_0 \ll 1$ represents the SW amplitude; ω is the SW angular frequency and $\mathbf{r}$ is the position of the considered spin. Substituting that into the LLG equation,

$$\frac{\partial\hat{S}_i^x}{\partial t} = -\frac{\gamma}{(1+\alpha^2)\mu}\left[\hat{S}_i^y(\mathbf{B}_i^{\text{eff}})^z - \hat{S}_i^z(\mathbf{B}_i^{\text{eff}})^y\right], \tag{B.2}$$

with the effective field given by Eq. (B.1), we obtain

$$\omega = \frac{\gamma S^2}{(1+\alpha^2)\mu}\left[3\Delta + 2\mathcal{A}^{zz} + 3J_0 - J_0\,\text{Re}\left(\sum_j \exp(i\mathbf{k}\cdot(\mathbf{r}_j-\mathbf{r}_i))\right)\right], \tag{B.3}$$

where,

$$\text{Re}\left(\sum_j \exp(i\mathbf{k}\cdot(\mathbf{r}_j-\mathbf{r}_i))\right) = \begin{cases}\text{Re}\left(e^{-ika} + 2e^{\frac{ika}{2}}\right) = \cos(ka) + 2\cos\left(\frac{ka}{2}\right), & \text{if } \mathbf{k} \parallel \hat{\mathbf{n}}_1,\\ \text{Re}\left(1 + e^{\frac{-ik\sqrt{3}a}{2}} + e^{\frac{ik\sqrt{3}a}{2}}\right) = 1 + 2\cos\left(\frac{ka\sqrt{3}}{2}\right), & \text{if } \mathbf{k} \parallel \hat{\mathbf{n}}_2,\end{cases} \tag{B.4}$$

which results in Eqs. (8.3) and (8.5) of the main text.

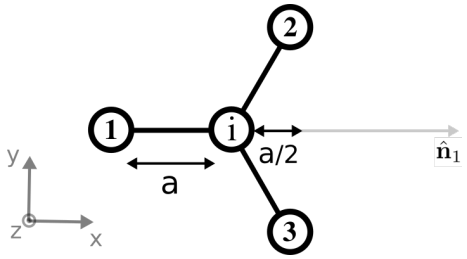

Figure B.1 – Illustration of spin sites. $j = 1, 2$ and 3 are the three nearest-neighbours of the i^{th} spin, and a the distance between nearest-neighbour Cr atoms.

B.1.1 DMI contribution

In the case where the CrX_3 lattice experience non-zero DMI, the Hamiltonian for the i^{th} spin has the DMI contribution

$$\mathcal{H}_i^{dmi} = \sum_j \mathbf{D}_{ij} \cdot (\mathbf{S}_i \times \mathbf{S}_j) = DS^2 \hat{\mathbf{S}}_i \cdot \sum_j (\hat{\mathbf{S}}_j \times \hat{\mathbf{D}}_{ij}), \tag{B.5}$$

which results in the DMI field,

$$\mathbf{B}_i^{\text{dmi}} = DS^2 \sum_j (\hat{\mathbf{S}}_j \times \hat{\mathbf{D}}_{ij}). \tag{B.6}$$

Considering a symmetry break along the out-of-plane ($\hat{z}$) direction, such as that in Janus structures [264] or in the presence of out-of-plane applied electric fields [292, 293], the induced DMI vectors point along the directions $\hat{\mathbf{D}}_{ij} = \hat{z} \times \hat{\mathbf{r}}_{ij}$, where $\hat{\mathbf{r}}_{ij}$ is the vector connecting spins i and j. The DMI field becomes

$$\mathbf{B}_i^{\text{dmi}} = DS^2 \sum_j [\hat{\mathbf{S}}_j \times (\hat{z} \times \hat{\mathbf{r}}_{ij})] = DS^2 \sum_j (\hat{\mathbf{S}}_j \cdot \hat{\mathbf{r}}_{ij}) \cdot \hat{z} - DS^2 \sum_j \hat{S}_j^z \hat{\mathbf{r}}_{ij}. \tag{B.7}$$

For a SW propagating along the $\hat{\mathbf{n}}_1$ ($\hat{x}$) direction, the spins at sites $j = 2$ and $j = 3$ [see Fig. B.1] point in the same direction, i.e., $\hat{S}_2 = \hat{S}_3$. In this way, Eq. (B.7) becomes

$$\mathbf{B}_i^{\text{dmi}} = DS^2[\hat{S}_2^x - \hat{S}_1^x] \cdot \hat{z} - DS^2[\hat{S}_2^z - \hat{S}_1^z] \cdot \hat{x}. \tag{B.8}$$

Considering the continuum approximation

$$\hat{\mathbf{S}}_2 \approx \hat{\mathbf{S}}_i + \frac{a}{2}\frac{\partial \hat{\mathbf{S}}_i}{\partial x}, \tag{B.9a}$$

$$\hat{\mathbf{S}}_1 \approx \hat{\mathbf{S}}_i - a\frac{\partial \hat{\mathbf{S}}_i}{\partial x}, \tag{B.9b}$$

the DMI field becomes

$$\mathbf{B}_i^{\text{dmi}} \approx DS^2 \frac{3a}{2} \left[\frac{\partial \hat{S}_i^x}{\partial x} \cdot \hat{z} - \frac{\partial \hat{S}_i^z}{\partial x} \cdot \hat{x} \right]. \tag{B.10}$$

For the background magnetization lying in the yz-plane [see Fig. B.1], the linearized solution for the SW can be written as

$$\hat{\mathbf{S}} \approx 1\hat{n} + A_0 e^{i(\mathbf{k}\cdot\mathbf{r}-\omega t)}\hat{x} + iA_0 e^{i(\mathbf{k}\cdot\mathbf{r}-\omega t)}\hat{e}_\perp, \tag{B.11}$$

where $\hat{n}$ is the direction of the magnetization; $\hat{e}_\perp = \hat{n} \times \hat{x}$; $A_0 \ll 1$ represents the SW amplitude; ω is the SW angular frequency and $\mathbf{r}$ is the position of the considered spin. Substituting Eqs. (B.10) and (B.11) into the LLG equation

$$\frac{\partial \hat{S}_i^x}{\partial t} = -\frac{\gamma}{(1+\alpha^2)\mu}\left[\hat{S}_i^{e_\perp}(\mathbf{B}_i^{\mathrm{dmi}})^n - \hat{S}_i^n(\mathbf{B}_i^{\mathrm{dmi}})^{e_\perp}\right], \tag{B.12}$$

we obtain

$$i\omega\hat{S}_i^x = \frac{\gamma D S^2}{(1+\alpha^2)\mu}\frac{3a}{2}ik\hat{S}_i^x\hat{z}\cdot\hat{e}_\perp + O(A_0^2). \tag{B.13}$$

Therefore, the linearized solution for the SW dispersion relation is

$$\omega_{DM} = \frac{\gamma S^2}{(1+\alpha^2)\mu}\frac{3aD\sin\theta_M}{2}k, \tag{B.14}$$

where θ_M is the angle between the magnetization direction and the $\hat{z}$ direction.

B.2 Magnetic parameters for $CrBr_3$ and CrI_3

CrI_3 |	Strain (%)	J^{xx} (meV)	J^{yy} (meV)	J^{zz} (meV)	J^{xy} (meV)	J^{xz} (meV)	J^{yz} (meV)
Pair (1-2)							
	-5	-1.95	-0.91	-1.69	0.00	0.00	0.74
	-4	-2.79	-1.68	-2.47	0.00	0.00	0.76
	-3	-3.51	-2.32	-3.13	0.00	0.00	0.79
	-2	-4.13	-2.89	-3.72	0.00	0.00	0.79
	-1	-4.62	-3.34	-4.18	0.00	0.00	0.81
	0	-5.10	-3.72	-4.63	0.00	0.00	0.83
	1	-5.49	-4.06	-4.99	0.00	0.00	0.83
	2	-5.81	-4.26	-5.29	0.00	0.00	0.86
	3	-6.09	-4.47	-5.55	0.00	0.00	0.88
	4	-6.30	-4.60	-5.75	0.00	0.00	0.90
	5	-6.52	-4.74	-5.94	0.00	0.00	0.91
Pair (2-3)							
	-5	-1.17	-1.69	-1.69	-0.45	0.64	-0.37
	-4	-1.96	-2.51	-2.47	-0.48	0.66	-0.38
	-3	-2.62	-3.21	-3.13	-0.52	0.68	-0.40
	-2	-3.20	-3.82	-3.72	-0.54	0.68	-0.40
	-1	-3.66	-4.30	-4.18	-0.55	0.70	-0.41
	0	-4.07	-4.76	-4.63	-0.60	0.72	-0.42
	1	-4.42	-5.13	-4.99	-0.62	0.72	-0.42
	2	-4.65	-5.42	-5.29	-0.67	0.74	-0.43
	3	-4.88	-5.69	-5.55	-0.70	0.76	-0.44
	4	-5.03	-5.88	-5.75	-0.74	0.78	-0.45
	5	-5.19	-6.08	-5.94	-0.77	0.79	-0.46
Pair (2-5)							
	-5	-1.17	-1.69	-1.69	0.45	-0.64	-0.37
	-4	-1.96	-2.51	-2.47	0.48	-0.66	-0.38
	-3	-2.62	-3.21	-3.13	0.52	-0.68	-0.40
	-2	-3.20	-3.82	-3.72	0.54	-0.68	-0.40
	-1	-3.66	-4.30	-4.18	0.55	-0.70	-0.41
	0	-4.07	-4.76	-4.63	0.60	-0.72	-0.42
	1	-4.42	-5.13	-4.99	0.62	-0.72	-0.42
	2	-4.65	-5.42	-5.29	0.67	-0.74	-0.43
	3	-4.88	-5.69	-5.55	0.70	-0.76	-0.44
	4	-5.03	-5.88	-5.75	0.74	-0.78	-0.45
	5	-5.19	-6.08	-5.94	0.77	-0.79	-0.46

Table 5 – Exchange parameters for biaxial strain in CrI_3 obtained from first-principle calculations [see Ref. [34] for details]. J^{xx}, J^{yy}, and J^{zz} are diagonal elements, and $J^{xy} = J^{yx}$, $J^{xz} = J^{zx}$, $J^{yz} = J^{zy}$ the off-diagonal elements of the exchange matrix. A_{ii} is SIA parameter, same for each Cr site. Pairs (*i*-*j*) are indicated in Fig. 8.1 (a).

$CrBr_3$ |	Strain (%)	J^{xx} (meV)	J^{yy} (meV)	J^{zz} (meV)	J^{xy} (meV)	J^{xz} (meV)	J^{yz} (meV)
Pair (1-2)							
	-5	-1.24	-1.06	-1.21	0.00	0.00	0.08
	-4	-1.87	-1.72	-1.81	0.00	0.00	0.09
	-3	-2.39	-2.23	-2.35	0.00	0.00	0.08
	-2	-2.79	-2.65	-2.75	0.00	0.00	0.10
	-1	-3.18	-3.01	-3.14	0.00	0.00	0.10
	0	-3.45	-3.29	-3.42	0.00	0.00	0.09
	1	-3.67	-3.50	-3.63	0.00	0.00	0.10
	2	-3.85	-3.68	-3.81	0.00	0.00	0.09
	3	-3.98	-3.80	-3.94	0.00	0.00	0.09
	4	-4.07	-3.89	-4.02	0.00	0.00	0.10
	5	-4.13	-3.94	-4.08	0.00	0.00	0.10
Pair (2-3)							
	-5	-1.11	-1.20	-1.21	-0.08	0.07	-0.04
	-4	-1.76	-1.83	-1.81	-0.06	0.08	-0.05
	-3	-2.27	-2.35	-2.35	-0.07	0.07	-0.04
	-2	-2.69	-2.76	-2.75	-0.06	0.09	-0.05
	-1	-3.05	-3.14	-3.14	-0.07	0.09	-0.05
	0	-3.33	-3.41	-3.42	-0.07	0.08	-0.05
	1	-3.54	-3.63	-3.63	-0.07	0.09	-0.05
	2	-3.72	-3.81	-3.81	-0.07	0.08	-0.05
	3	-3.85	-3.94	-3.94	-0.08	0.08	-0.05
	4	-3.94	-4.03	-4.02	-0.08	0.09	-0.05
	5	-3.99	-4.08	-4.08	-0.08	0.09	-0.05
Pair (2-5)							
	-5	-1.11	-1.21	-1.20	0.08	-0.07	-0.04
	-4	-1.76	-1.81	-1.83	0.06	-0.08	-0.05
	-3	-2.27	-2.35	-2.35	0.07	-0.07	-0.04
	-2	-2.69	-2.75	-2.76	0.06	-0.09	-0.05
	-1	-3.05	-3.14	-3.14	0.07	-0.09	-0.05
	0	-3.33	-3.42	-3.41	0.07	-0.08	-0.05
	1	-3.54	-3.63	-3.63	0.07	-0.09	-0.05
	2	-3.72	-3.81	-3.81	0.07	-0.08	-0.05
	3	-3.85	-3.94	-3.94	0.08	-0.08	-0.05
	4	-3.94	-4.02	-4.03	0.08	-0.09	-0.05
	5	-3.99	-4.08	-4.08	0.08	-0.09	-0.05

Table 6 – Exchange parameters for biaxial strain in $CrBr_3$ obtained from first-principle calculations [see Ref. [34] for details]. J^{xx}, J^{yy}, and J^{zz} are diagonal elements, and $J^{xy} = J^{yx}$, $J^{xz} = J^{zx}$, $J^{yz} = J^{zy}$ the off-diagonal elements of the exchange matrix. A_{ii} is SIA parameter, same for each Cr site. Pairs (*i*-*j*) are indicated in Fig. 8.1 (a).

Strain (%)	$\mathcal{A}^{zz}$ (CrI_3) (meV)	$\mathcal{A}^{zz}$ ($CrBr_3$) (meV)
-5	-0.16	0.02
-4	-0.14	0.01
-3	-0.12	0.00
-2	-0.10	-0.01
-1	-0.08	-0.01
0	-0.07	-0.01
1	-0.05	-0.02
2	-0.04	-0.03
3	-0.03	-0.03
4	-0.02	-0.03
5	-0.02	-0.03

Table 7 – SIA parameter for biaxial strain in CrI_3 and $CrBr_3$ obtained from first-principle calculations [see Ref. [34] for details]. $\mathcal{A}^{zz}$ is the same for each Cr site.

	pair (i-j)	J^{xx} (meV)	J^{xy} (meV)	J^{xz} (meV)	J^{yx} (meV)	J^{yy} (meV)	J^{yz} (meV)	J^{zx} (meV)	J^{zy} (meV)	J^{zz} (meV)
CrI_3										
	(1-2)	-4.3	0.53	-0.03	1.6	-3.82	1.4	-0.43	0.83	-3.47
	(2-3)	-11.65	-5.31	1.55	-4.53	-11.31	4.49	-3.11	-3.61	-13.42
	(2-5)	-4.09	0.09	-0.62	1.01	-4.47	-0.06	-0.44	-0.4	-4.24
	(3-4)	-4.6	-0.34	-0.15	-0.22	-3.66	0.63	0.06	0.61	-4.12
	(3-6)	-4.03	0.46	-0.18	0.08	-4.09	-0.11	-0.94	-0.13	-4.12
$CrBr_3$										
	(1-2)	-2.91	-0.08	0.11	-0.59	-2.8	0.03	-0.14	0.13	-2.91
	(2-3)	-32.73	-2.41	1.23	-2.26	-32.75	2.29	-1.39	-2.19	-33.08
	(2-5)	-2.93	-0.02	-0.13	0.06	-2.91	-0.09	-0.02	-0.09	-2.92
	(3-4)	-3.12	0.02	-0.05	-0.11	-2.88	0.11	0.01	0.08	-2.92
	(3-6)	-2.81	0.1	0.05	-0.03	-2.9	-0.11	-0.23	0.07	-2.9

Table 8 – Total exchange parameters for the case of isolated defect (halide vacancy) in CrI_3 and $CrBr_3$, obtained from first-principle calculations [41]. Pairs (i-j) are indicated in Fig. 8.5 (a).

	pair (i-j)	J^{xx} (meV)	J^{xy} (meV)	J^{xz} (meV)	J^{yx} (meV)	J^{yy} (meV)	J^{yz} (meV)	J^{zx} (meV)	J^{zy} (meV)	J^{zz} (meV)
CrI_3										
	(1-2)	-4.49	0.32	0.01	0.2	-3.99	-0.32	-0.86	-0.33	-4.35
	(2-3)	-1.82	1.58	-1.16	-3.26	-1.1	-1.15	-2.25	-1.06	-4.08
	(2-5)	-12.71	4.2	-0.03	-4.27	-12.13	3.76	-0.57	-3.47	-9.85
	(3-4)	-4.81	0.11	-0.34	0.56	-4.24	-0.68	-0.29	-0.52	-4.59
	(3-6)	-12.71	4.2	-0.03	-4.27	-12.13	3.76	-0.57	-3.47	-9.85
$CrBr_3$										
	(1-2)	-3.46	0.05	-0.09	0.03	-3.3	0.1	-0.27	0.1	-3.42
	(2-3)	-2.61	0.37	-0.4	-0.57	-2.42	0.07	-0.12	-0.17	-2.61
	(2-5)	-19.89	1.5	-0.05	-1.5	-19.8	2.11	-0.09	-2.08	-19.91
	(3-4)	-3.25	0.03	0.01	0.01	-3.15	-0.11	-0.06	-0.04	-3.23
	(3-6)	-19.89	1.5	-0.05	-1.5	-19.8	2.11	-0.09	-2.08	-19.91

Table 9 – Total exchange parameters for the case of a line of defects in CrI_3 and $CrBr_3$, obtained from first-principle calculations [41]. Pairs (i-j) are indicated in Fig. 8.7 (a).

C

List of publications

Publications related to the thesis are indicated by asterisks (*).

1 **Raí M. Menezes** and Clécio C. de Souza Silva. Conformal Vortex Crystals. *Scientific Reports* 7, 12766. (2017)

2 **Raí M. Menezes**, Edson Sardella, Leonardo R E Cabral and Clécio C de Souza Silva. Self-assembled vortex crystals induced by inhomogeneous magnetic textures. *Journal of Physics: Condensed Matter* 31 175402. (2019)

3 * **Raí M. Menezes**, Jeroen Mulkers, Clécio C. de Souza Silva, and Milorad V. Milošević. Deflection of ferromagnetic and antiferromagnetic skyrmions at heterochiral interfaces.
Phys. Rev. B 99, 104409. (2019)

4 * **Raí M. Menezes**, José F. S. Neto, Clécio C. de Souza Silva, and Milorad V. Milošević. Manipulation of magnetic skyrmions by superconducting vortices in ferromagnet-superconductor heterostructures.
Phys. Rev. B 100, 014431. (2019)

5 * **Raí M. Menezes**, Clécio C. de Souza Silva, and Milorad V. Milošević. Spin textures in chiral magnetic monolayers with suppressed nearest-neighbor exchange.
Phys. Rev. B 101, 214429. (2020)

6 FCO Silva, **RM Menezes**, LRE Cabral, CC de Souza Silva. Formation and stability of conformal spirals in confined 2D crystals.
Journal of Physics: Condensed Matter 32 (50), 505401. (2020)

7 * A. W. D. Leishman, **R. M. Menezes**, G. Longbons, E. D. Bauer, M. Janoschek, D. Honecker, L. DeBeer-Schmitt, J. S. White, A.Sokolova, M. V. Milošević, and M. R. Eskildsen. Topological energy barrier for skyrmion lattice formation in MnSi.
Phys. Rev. B 102, 104416. (2020)

8 C. Bacaksiz, D. Šabani, **R. M. Menezes**, and M. V. Milošević. Distinctive magnetic properties of CrI_3 and $CrBr_3$ monolayers caused by spin-orbit coupling.
Phys. Rev. B 103, 125418. (2021)

9 * A. P. Petrović, M. Raju, X. Y. Tee, A. Louat, I. Maggio-Aprile, **R. M. Menezes**, M. J. Wyszyński, N. K. Duong, M. Reznikov, Ch. Renner, M. V. Milošević, and C. Panagopoulos. Skyrmion-(anti) vortex coupling in a chiral magnet-superconductor heterostructure.
Phys. Rev. Lett 126, 117205. (2021)

10 * **Raí M. Menezes**, D. Šabani, C. Bacaksiz, Clécio C. de Souza Silva, and Milorad V. Milošević. Tailoring high-frequency magnonics in two-dimensional Chromium trihalides.
(Manuscript submitted). *arXiv*:2111.14305 (2021).

11 **Raí M. Menezes**, Jeroen Mulkers, Clecio C. de Souza Silva, Bartel Van Waeyenberge, and Milorad V. Milošević. Spin waves guided by currents.
(Manuscript in preparation).

ABOUT THE AUTHOR

PERSONAL INFORMATION

Rai
Maciel de Menezes

Nationality: Brazilian
Email: Rai.MacieldeMenezes@uantwerpen.be
rai.menezes3@gmail.com

Web of Science ResearcherID: AAB-3655-2021
Scholar.google: Raí M. Menezes

EDUCATION

2017 – 2021 Joint Ph.D. in Physics.
University of Antwerp (UA) - Belgium,
and Federal University of Pernambuco (UFPE) - Brazil.
Advisors: Prof. Milorad V. Milosevic (UA)
and Prof. Clecio Clemente de Souza Silva (UFPE).
Subject: Skyrmionics and Magnonics in Chiral Ferromagnets:
from micromagnetic to atomistic control.

2015 - 2017 Master in Physics.
Federal University of Pernambuco - Brazil.
Advisor: Prof. Clecio Clemente de Souza Silva.
Subject: Nonuniform vortex distributions in type II superconductors:
from critical state to conformal crystals.

2011 - 2014 Bachelor in Physics.

Federal University of Pernambuco - Brazil.

RESEARCH INTERESTS

Magnetic materials, Multiscale Spin dynamics, Topological Spin textures, Magnetic skyrmions, Spin Waves, 2D magnetism.